POLYPUBLIE

Improved Microstructural Control of Ag Films for High Temperature and Environmental Stability of Low-Emissivity Coatings

Phillip Rumsby

Document en libre accès dans PolyPublie
Open Access document in PolyPublie

Date	2026
Type	Mémoire ou thèse / Dissertation or Thesis Thèse de doctorat/Ph.D. thesis
URL de PolyPublie PolyPublie URL	https://publications.polymtl.ca/73909/
Conditions d'utilisation Terms of use	© Tous droits réservés / All rights reserved
Référence Citation	Rumsby, P. (2026). Improved Microstructural Control of Ag Films for High Temperature and Environmental Stability of Low-Emissivity Coatings [Thèse de doctorat, Polytechnique Montréal]. PolyPublie. https://publications.polymtl.ca/73909/

Détails de la thèse
Thesis details

Directeurs de recherche Advisors	Ludvik Martinu, Jolanta-Ewa Sapieha
Programme Program	Génie physique

Ce fichier a été téléchargé à partir de PolyPublie, le dépôt institutionnel de Polytechnique Montréal
This file has been downloaded from PolyPublie, the institutional repository of Polytechnique Montréal
https://publications.polymtl.ca

POLYTECHNIQUE MONTRÉAL

affiliée à l'Université de Montréal

Improved microstructural control of Ag films for high temperature and environmental stability of low-emissivity coatings

PHILLIP RUMSBY

Département de génie physique

Thèse présentée en vue de l'obtention du diplôme de *Philosophiæ Doctor*

Génie Physique

Février 2026

© Phillip Rumsby, 2026.

POLYTECHNIQUE MONTRÉAL

affiliée à l'Université de Montréal

Cette thèse intitulée :

Improved microstructural control of Ag films for high temperature and environmental stability of low-emissivity coatings

présentée par **Phillip RUMSBY**

en vue de l'obtention du diplôme de *Philosophiæ Doctor*

a été dûment acceptée par le jury d'examen constitué de :

Stéphane KÉNA-COHEN, président
Ludvik MARTINU, membre et directeur de recherche
Jolanta-Ewa SAPIEHA, membre et codirectrice de recherche
Frédéric SIROIS, membre
Grégory ABADIAS, membre externe

ACKNOWLEDGEMENTS

I cannot start this section in any other way than by thanking my research supervisors, Professor Ludvik Martinu and Professor Jolanta-Ewa Klemberg Sapieha; none of this would have happened without them. Thank you for recognizing my potential, continuously supporting me to succeed, and for introducing me to the surface engineering research community.

At the complete other end of this journey, at its very end, I would like to thank the members of the jury. Professor Stéphane Kéna-Cohen, Professor Frédéric Sirois and Professor Grégory Abadias; thank you for accepting to participate in this pivotal moment of my studies.

Throughout the course of this degree, I've had the pleasure of working with a host of professionals from our industrial partner, Guardian Glass. I would like to thank Richard Vernhes, Yiwei Lu, Brent Boyce, Jim Hu, and Adam Tokarz, amongst others. My competence in all things low-E has benefitted through many insightful and animated discussions.

I've also benefitted from the unmatched support of a plethora of academic and technical professionals at Polytechnique. My thanks go out to our technicians, Francis Turcot, Francis Boutet and Sylvain Fleury, who've played a foundational role in the work of everyone in this lab, in addition to myself. In addition, my thanks go out to Pavel Pleskunov, Patricia Moraille, Josianne Lefebvre, Etienne Bousser and Jean-Philippe Masse who've lent me their expertise to obtain and interpret a number of results essential to the furtherance of this project. I'd also like to thank Oleg Zabeida, who has been instrumental in helping me develop my technical and practical knowledge of a host of deposition and measurement systems. More importantly, he has never let me settle for less than I've been capable of.

I've had the immense privilege of receiving the mentorship of Bill Baloukas; throughout the entirety of my time at the FCSEL he has been unwavering in his support, patience and good nature, constantly offering his time, effort and insight. I cannot emphasize enough how much impact he has had on my development here; any success I've had, he has been a part of.

Having worked at the FCSEL for nearly eight years now, between my master's degree and this one, I couldn't possibly name all the other brilliant students, post-docs and professionals whose contact I've benefitted from – my sincere apologies to everyone who I didn't include here. I'd like to thank Artem Shelemin, Zdeněk Krtouš, Jincheng Qian, Michael Mayerhofer, Mohammed

Ammari, and Oumar Touré, with whom I've collaborated with on Guardian research projects. It's been a pleasure to work alongside you all. I'd also like to thank Jacques Lengaigne, Louis Dubé-Riopel, Francis Blanchard, Rodrigue Beaini, Erika Jimenez, Martin Crouan, Massine Kadi, Marie-Andrée Dionne and Pedro Avila for brightening my time at the lab. Special thanks are owed to Aleksandra Pajak in this regard, for all the times spent either celebrating or commiserating, and for being my ally in honing the office coffee machine.

Finally, I want to thank all of my loved ones outside of the FCSEL, who've shaped my growth and supported me throughout the years, who've come and who've gone. I cannot name them all, but I need to underscore a few, such as Marieta, Ioana, Melis and Arda. My parents, Larry and Louise, and my brother John, who've believed in me every step of the way. Eli and Gabriel, who've been by my side since the very beginning of university; I'm proud to reach the end of this journey at your sides. Thank you to Florence, my wonderful partner, who has patiently supported me throughout the redaction of this thesis and with whom I find fun in the most mundane activities and the most exciting adventures.

RÉSUMÉ

Alors que le climat se réchauffe dû à l'augmentation continue des gaz à effet de serre, il devient de plus en plus important de réduire notre consommation d'énergie et d'efficacement contrôler la température des immeubles. Les revêtements de fenêtres à basse émissivité (low-E), font exactement cela. Cette technologie passive permet de réduire le transfert de chaleur radiatif à travers les fenêtres, l'un des principaux points faibles de l'isolation thermique des immeubles modernes, permettant ainsi de garder les immeubles frais en climats chauds (et vice-versa), améliorant le confort des occupants et réduisant l'énergie requise pour climatiser les immeubles. Pour ce faire, ces revêtements doivent intégrer des couches hautement conductives, et donc hautement réflectives dans l'infrarouge, tout en conservant la transparence et l'esthétique des fenêtres.

L'argent (Ag), déposé par pulvérisation magnétron, est le choix par excellence pour ce rôle, ayant la plus haute conductivité des métaux élémentaires ainsi que d'excellentes propriétés optiques, avec peu d'absorption dans le spectre visible. Cela étant dit, la fabrication de couches d'Ag suffisamment minces pour des applications optiques n'est pas triviale. L'Ag suit le mode de croissance Volmer-Weber lorsque déposé sur la plupart des matériaux diélectriques : à basse épaisseur des nanoparticules isolées se forment au lieu d'une couche continue et conductrice. Il y a plusieurs façons de mitiger ce comportement (par le contrôle de la cinétique de dépôt, en réduisant l'écart entre les énergies de surface et l'Ag et du substrat, avec l'ajout de dopants), cependant celles-ci mènent à la formation de cristallites, ou grains, plus petits au sein de la couche. De plus, l'Ag devient instable dans plusieurs types d'environnements, ce qui peut mettre en risque la fonctionnalité du revêtement. En plus d'être susceptible à la présence de plusieurs contaminants, la structure même de l'Ag peut changer de manière importante lorsque exposé à de hautes températures, et ce, même dans l'absence de contaminants. Ces changements peuvent être dramatiques, notamment menant à la séparation en ilots d'une couche continue, réduisant la proportion couverte du substrat; ce processus est le démouillage à l'état solide. Des couches comportant des petits grains d'Ag seront également prônes à croitre à haute températures, menant à des changements de leurs propriétés optiques et électriques.

Plusieurs couches diélectriques sont mises en place autour de la couche d'Ag pour minimiser ces processus, mais ils causent tout de même des problèmes importants lors de la production de verre

trempé. Dans ce cas, le verre revêtu doit être chauffé à une température de 650 °C, puis être rapidement refroidi afin de créer de fortes contraintes mécaniques résiduelles dans le verre. En plus des changements intrinsèques à l'Ag à haute température, tel que décrit plus haut, ceci permet aux contaminants présents dans l'atmosphère et le substrat de diffuser vers l'Ag beaucoup plus rapidement. Le contrôle de ces processus est donc d'un grand intérêt pour les manufacturiers de verre low-E. Afin de ce faire sans avoir recours au dopage de l'Ag, qui peut causer un déclin de la performance telle-que-revêtue, de nouvelles manières de contrôler la microstructure de l'Ag sont requises. L'objectif principal de cette thèse est donc d'enquêter les mécanismes par lesquels les revêtement low-E à base d'Ag se dégradent, et concevoir de nouvelles approches pour les mitiger, basées sur le contrôle de la microstructure de l'Ag. Les résultats principaux de cette enquête sont présentés sous la forme de trois articles soumis à des revues scientifiques avec évaluation par les pairs.

Le premier article se penche sur l'effet des contaminants sur la dégradation des low-E à hautes températures. Pour ce faire, des revêtements sont fabriqués avec différentes permutations de couches protectrices et la présence de contaminants est contrôlée en effectuant le recuit sous atmosphère d'argon, ainsi qu'en utilisant des substrats avec des différences de composition importantes. Ce faisant, l'effet de différents contaminants et de combinaisons de ceux-ci peut être évalué pour des revêtements qui sont autrement identiques. Des mesures optiques et électriques révèlent que la contamination par l'oxygène ou par le sodium peuvent tous les deux causer une dégradation importante de la performance; cependant, des observations par microscopie électronique révèlent que cette dégradation est causée par des mécanismes qualitativement différents. La dégradation à haute température d'égratignures à la surface du revêtement est aussi enquêtée, utilisant les mêmes méthodes pour contrôler l'apport de contaminants et isoler leur rôle. Il est trouvé que des craques dans la couche protectrice du haut permettant la diffusion de contaminants atmosphériques vers la couche d'Ag et la présence de délaminations au sein du revêtement mènent aux changements les plus importants, en causant la formation de nanoparticules hautement diffusives dans le revêtement.

Le second article démontre les améliorations potentielles du niveau de durabilité qui peuvent être obtenues en contrôlant la microstructure de la couche d'argent, mais dans le contexte de la résistance à la corrosion. Le dépôt de couches d'Ag minces et conductrices est effectué en utilisant l'azote comme surfactant ($Ag_{(N)}$). Cependant, ceci cause la formation de grains significativement

plus petits, menant à une dégradation encore plus rapide lorsque placé dans un environnement corrosif. Une couche d'oxide de zinc dopé à l'aluminium ($ZnO_{(Al)}$) est ajoutée avant le dépôt d'$Ag_{(N)}$ pour promouvoir la croissance de l'Ag en orientation (111), avec des grains plus larges et plus uniformes, et ce, peu importe la concentration d'azote. Il est découvert que, malgré qu'ils aient des grains de taille similaires, les revêtements d'$Ag_{(N)}$ déposés avec des faibles concentrations d'azote sont beaucoup plus résistants que ceux d'Ag pur. Cet effet est attribué à la réduction de zones vides à l'interface entre l'Ag et le substrat, tel que confirmé par des mesures par microscopie à force atomique. Ces mesures révèlent que les couches d'$Ag_{(N)}$ recouvrent une beaucoup plus grande proportion du substrat à basses épaisseurs, malgré qu'elles convergent vers une morphologie similaire à l'Ag pur lorsque déposées sur du $ZnO_{(Al)}$. Enfin, des couches ultra-minces d'$Ag_{(N)}$ sont utilisées pour produire des revêtements anti-reflet avec une stabilité chimique accrue.

Dans le troisième article, une étape d'amincissement post-dépôt est étudiée comme nouvelle méthode de fabrication, permettant le dépôt de couches minces d'Ag avec des microstructures contrôlées. Une fois qu'une couche continue est formée, l'amincissement de la couche via une gravure par plasma d'argon permet de réduire l'épaisseur de la couche en gardant une morphologie continue. Ceci d'éviter les morphologies discontinues qui découlent du mode croissance Volmer-Weber, sans avoir recours à des méthodes qui réduisent la taille des grains. L'article se concentre sur la dépendance des morphologies obtenues par gravure sur les conditions de dépôt et microstructures initiales. Pour ce faire, des techniques conventionnelles d'ellipsométrie *in situ* avec augmentation interférentielles sont utilisés pour identifier les épaisseurs auxquelles des couches continues d'Ag sont formées et une méthode sans dépendance sur les propriétés interférentielles du substrat est utilisée pour identifier les épaisseurs auxquelles les couches forment des réseaux conducteurs. Cette étude révèle que lors de la gravure, la formation de trous et le démouillage de la couche sont contrôlés par des mécanismes différents; ceux-ci sont attribués à des processus connus de démouillage à l'état solide, avec quelques subtilités propres à la gravure ionique. Des résultats additionnels, non-publiés, sont aussi présentés : des revêtements anti-reflet à haute conductivité sont fabriqués par amincissement post-dépôt et des simulations numériques à différences finies dans le domaine temporel sont utilisées pour identifier quelles morphologies de trous causent les plus de pertes en transmission de la lumière visible.

Enfin, l'amincissement post-dépôt est utilisé pour tenter d'obtenir des revêtements à haute stabilité thermique. Étant donné les limitations de la méthode, identifiées dans l'article précédent, l'addition

d’une étape de recuit additionnelle est utilisée pour déposer des revêtements épais mais stables, ajuster leur microstructure par recuit, puis sélectionner leur épaisseur finale par gravure plasma. L’Ag est substitué par de l’or pour ces expériences pour permettre de recuits rapides sous atmosphère ambiante, mais ces résultats préliminaires démontrent néanmoins une meilleure performance telle-que-revêtue et des améliorations prometteuses en termes de stabilité optique à hautes températures.

ABSTRACT

As global temperatures rise due to ever-increasing greenhouse gas emissions, it is becoming ever more important to efficiently manage building temperatures and reduce energy consumption. Low-emissivity (low-E) window coatings, do just this. By passively reducing radiative heat transfer through windows, one of the main weak points in the insulation of modern building envelopes, they allow to keep buildings cool in warm climates (and vice-versa), improving comfort and reducing the energy required to either heat or cool buildings. To do so, these coatings must integrate highly conductive, and thus infrared reflective, layers while remaining aesthetically pleasing and transparent.

Silver (Ag), deposited by magnetron sputtering, is the ubiquitous choice for this role, boasting the highest conductivity of all elemental metals as well as excellent optical properties, with low absorption in the visible spectrum. The fabrication of optically thin Ag films is not trivial, however. Ag follows a Volmer-Weber growth mode when deposited on most dielectric materials: at low thicknesses, isolated nanoparticles are formed instead of a continuous, conductive layer. While there a number of methods that can mitigate this (change of deposition kinetics, reduced surface energy mismatch with the substrate, usage of dopants) these typically result in the formation of smaller Ag crystallites, or grains, within the continuous Ag layer. Moreover, Ag presents environmental stability issues which present risks to coating integrity. In addition to being susceptible to degradation when exposed to a number of contaminants, the Ag microstructure is prone to change at high temperatures, even if isolated from said contaminants. These changes can manifest dramatically, enabling the Ag layer to revert into discontinuous islands with low surface coverage, in a process known as solid-state dewetting. Small Ag grains will also be prone to grow at high temperatures, leading to changes in the optical and electrical properties of the layer.

While a host of dielectric layers are put in place around the Ag layer to minimize these issues, they nevertheless cause significant issues in the production of tempered low-E glass. In this case, the coated glass must be heat-treated at a temperature of 650 °C before being rapidly cooled to induce high residual stresses in the glass. In addition to the changes intrinsic to Ag layers at high temperatures described above, this allows rapid diffusion of contaminants from the atmosphere and substrate. Managing these changes is thus of great interest to coated glass manufacturers. To do so without resorting to doping the Ag layer, which can result in lesser as-coated performance, new

methods of controlling the Ag microstructure are required. As a result, the main objective of this thesis is thus to investigate the mechanisms by which Ag-based low-E coatings degrade and devise new approaches to mitigate them based on microstructural control of the Ag layer. The main results of this investigation are presented in the form of three articles in peer-reviewed journals.

The first article investigates the effect of contaminants on low-E degradation at high temperatures. To do so, coatings are fabricated with various permutations of barrier layers, and the presence of contaminants is externally controlled by purging the tempering furnace with argon and by using substrates with starkly different compositions. In doing so, the effect of various contaminants and combinations thereof can be evaluated for otherwise identical coatings. Optical and electrical measurements reveal that exposure to oxygen or sodium both result in important degradation; however, electron microscopy reveals qualitatively different features underpinning these changes. The high-temperature degradation of scratches at the coating surface is also investigated, once again controlling the availability of contaminants to isolate their impact. It's found that cracks in the top barrier layers allowing diffusion of atmospheric contaminants and delamination within the low-E coating structure result in the most serious changes due to the formation of highly scattering nanoparticles within the coating.

The second article demonstrates the potential durability increases which can be obtained from appropriate control of the Ag microstructure, albeit in the context of corrosion resistance. The deposition of conductive Ag films at low thicknesses is enabled using nitrogen as surfactant ($Ag_{(N)}$). However, this comes at the price of much smaller grains, which results in accelerated degradation in a corrosive environment. Addition of a polycrystalline aluminum-doped zinc oxide ($ZnO_{(Al)}$) seed layer promotes (111) oriented Ag growth, with larger, more uniform grains, regardless of the nitrogen concentration. Although they have similar grain sizes, $Ag_{(N)}$ films deposited with modest nitrogen concentrations are found to have much higher durability than pure Ag. This is attributed to reduced interfacial voids, on the basis of atomic force microscopy measurements. These reveal that despite converging to similar continuous morphologies when deposited on $ZnO_{(Al)}$, $Ag_{(N)}$ films nonetheless show much greater coverage during the early wetting phases. Finally, ultra-thin $Ag_{(N)}$ films are used to produce highly anti-reflective coatings with superior chemical stability.

In the third article, post-deposition etching is investigated as a novel approach to fabricate thin Ag films with tailored microstructures. Once a continuous Ag film is formed, subsequent etching via

an argon plasma can allow one to reduce the film thickness while retaining a continuous morphology. In turn, this allows to circumvent the discontinuous morphologies arising from the Volmer-Weber growth mode without using deposition techniques which result in smaller grain sizes. Thus, the article focuses on the morphological dependence of etched Ag films on the deposition conditions and resulting microstructures. To do so, conventional interference-enhanced *in situ* ellipsometry is used to monitor the thickness at which continuous Ag films are formed, and a novel interference-agnostic method is used to monitor the thickness at which films form conductive networks. This reveals that during etching, hole formation and dewetting are driven by distinct mechanisms; these are attributed to known solid-state dewetting processes, with some subtleties arising from the ion etching process. Unpublished results are also presented: highly conductive antireflective coatings are fabricated by post-deposition etching and finite-difference time-domain simulations are used to identify the hole morphologies that result in the most visible transmission losses.

Finally, post-deposition etching is implemented to attempt to obtain low-E coatings with high optical stability at high temperatures. Given the limitations of post-deposition etching identified in the previous study, the addition of an additional annealing step is used to deposit thick, but stable films, then tailor their microstructure by annealing, and finally select their final thickness via etching. Although Ag is substituted with gold to enable annealing in atmosphere, the preliminary results nevertheless show improved as-coated performance and promising improvements to optical stability.

TABLE OF CONTENTS

ACKNOWLEDGEMENTS III

RÉSUMÉ V

ABSTRACT IX

TABLE OF CONTENTS XII

LIST OF TABLES XVII

LIST OF FIGURES XVIII

LIST OF SYMBOLS AND ABBREVIATIONS XXV

LIST OF APPENDICES XXX

CHAPTER 1 INTRODUCTION 1

1.1 Controlling the microstructure and stability of Ag films 2

1.2 Context of the research 5

1.3 Objectives 7

1.4 Publications 7

1.5 Outline 8

CHAPTER 2 LITERATURE REVIEW 10

2.1 Low-E coatings 10

2.1.1 Conventional coating archetypes 10

2.1.2 Alternative metals and Ag dopants 14

2.2 Ag film formation and deposition strategies 16

2.2.1 Physics of Ag film formation 16

2.2.2 Controlled deposition kinetics 25

2.2.3 Multi-step approaches 27

2.2.4 Seed layers and metallic seeding 30

2.2.5 Dopants and surfactants 33
2.3 Mechanisms of Ag film instability and their mitigation 36
2.3.1 Intrinsic Ag changes 36
2.3.2 Mitigating intrinsic Ag changes 42
2.3.3 Interdiffusion of film species and contaminants 47
2.3.4 Mitigating the effects and the diffusion of contaminants 52
CHAPTER 3 METHODOLOGY 56
3.1 Sample fabrication 56
3.1.1 Substrate cleaning and preparation 56
3.1.2 Coating deposition via magnetron sputtering 57
3.2 Film performance characterization methods 59
3.2.1 Spectrophotometry 59
3.2.2 Contactless sheet resistance monitoring 60
3.3 Stability characterization methods 61
3.3.1 High temperature stability 62
3.3.2 Stability of scratch defects 63
3.3.3 Corrosion stability 64
3.4 Materials characterization 65
3.4.1 Ellipsometry 65
3.4.2 Stylus profilometry and atomic force microscopy 68
3.4.3 X-ray diffraction 69
3.4.4 Wafer curvature stress measurements 70
3.4.5 Scanning electron microscopy 71
3.4.6 Transmission electron microscopy 72

3.4.7 X-ray photoelectron spectroscopy 72

CHAPTER 4 ARTICLE 1 : ROLE OF ATMOSPHERIC AND SUBSTRATE CONTAMINANTS ON THE DEGRADATION AND DEFECT VISIBILITY IN AG-BASED LOW-EMISSIVITY COATINGS 74

4.1 Foreword 74

4.2 Introduction 76

4.3 Methods 77

4.4 Results & discussion 81

4.4.1 Effects of contaminants and structural changes in the absence of defects 81

4.4.2 Defects and their evolution at high temperature 91

4.5 Conclusion 103

4.6 Acknowledgements 105

CHAPTER 5 ARTICLE 2 : ENHANCED DURABILITY AND ANTIREFLECTIVE PERFORMANCE OF AG-BASED TRANSPARENT CONDUCTORS ACHIEVED VIA CONTROLLED N-DOPING 106

5.1 Foreword 106

5.2 Introduction 108

5.3 Experimental details 110

5.3.1 Sample fabrication 110

5.3.2 Modeling 111

5.3.3 Corrosion durability and in situ optical monitoring 113

5.3.4 Other characterization methods 115

5.4 Results and discussion 116

5.4.1 AR design approach 116

5.4.2 Evaluation of Ag durability 120

5.4.3 Fabrication of Ag-based TCs with optimized AR performance and durability ... 127

5.5 Conclusions ... 130

5.6 Acknowledgements ... 131

CHAPTER 6 ARTICLE 3 : INVESTIGATING THE MORPHOLOGICAL EVOLUTION OF ION-THINNED AG FILMS VIA IN SITU ELLIPSOMETRY ... 133

6.1 Foreword ... 133

6.2 Introduction ... 135

6.3 Experimental methodology ... 137

6.4 Results & discussion ... 139

6.4.1 Monitoring the formation and breakdown of conductive networks via *in situ* ellipsometry ... 139

6.4.2 Effect of process parameters on Ag stability during etching ... 143

6.4.3 Proposed mechanisms and suggested changes for improved etching stability ... 149

6.5 Conclusions ... 155

6.6 Acknowledgements ... 155

6.7 Antireflective coatings produced with post-deposition etching ... 156

CHAPTER 7 GENERAL DISCUSSION: PERSPECTIVES FOR HIGH TEMPERATURE OPTICAL STABILITY IN LOW-EMISSIVITY COATINGS ... 164

7.1 Foreword ... 164

7.2 Multi-step Ag deposition processes for high temperature stability ... 164

7.2.1 Preliminary results ... 164

7.2.2 Improvements to the DAE approach ... 170

7.3 Stabilized dielectrics and improved stack architectures ... 172

CHAPTER 8 CONCLUSION AND OUTLOOK ... 175

REFERENCES ... 178

APPENDICES..... 204

LIST OF TABLES

Table 5.1: Summary of the sputtering conditions used for the deposition of the various films used in Chapter 5. 111

Table 6.1: Summary of the deposition conditions used for the different films in Chapter 6. 137

Table 6.2: Summary of the different substrate conditions used for IE-ISE monitoring, where r_q is the root-mean-square roughness obtained by AFM over a 1 μm × 1 μm area. 138

Table 7.1: Summary of the sputtering conditions used for the deposition of the various films used in Chapter 7. 166

Table B.1: Composition of the substrates used in Chapter 4, as measured by XPS. 213

Table B.2: Young's modulus (E), hardness (H), coefficient of thermal expansion (CTE) and transformation temperature (T_t) of SLG and BSG substrates. 214

Table B.3: Sheet resistance of low-E stacks and partial stacks produced on various substrates and annealed in different atmospheres, as-coated and heat-treated. 216

LIST OF FIGURES

Figure 1.1: Schematic illustrating the intended functionality of low-E coatings in different climates. 2

Figure 1.2: Images highlighting key challenges of Ag film fabrication and stability: Volmer-Weber growth mode, solid-state dewetting at high temperatures and corrosion. 3

Figure 1.3: Schematic example of a low-E coating, presenting typical thicknesses and materials used in this work, as well as their functional roles within the stack. 4

Figure 2.1: Comparison of the spectral dependence of the sensitivity of the human eye, the irradiance of the solar spectrum, and the thermal irradiance of a blackbody at 300 K to the simulated transmission curves of different low-E coatings. 11

Figure 2.2: Schematic representation of film material forming clusters in the capillary model, showing different degrees of film wetting. 18

Figure 2.3: Qualitative figure showing the total free energy ΔG of a spherical cluster of radius r, highlighting the contributions of various parameters. 20

Figure 2.4: Schematic overview of VW film formation processes, for different degrees of film coverage, and categorized under non equilibrium and equilibrium driven processes. 22

Figure 2.5: Schematic representation of an Ag adatom diffusing across a substrate and onto a Ag cluster and qualitative graph of the adatom energy along its path. 28

Figure 2.6: Schematic representation of the model proposed by Netterfield and Martin, describing the minimum thicknesses achievable via post-deposition etching. 29

Figure 2.7: Schematic representation of the change in grain size for a Ag film during grain growth and secondary grain growth with top-down view. 38

Figure 2.8: Schematic representation of the change in surface geometry for a Ag film during grain boundary (GB) grooving. 40

Figure 2.9: Change in energy resulting from the inclusion of holes in a thin film and stable radii towards which holes will converge. 41

Figure 2.10: Surface and grain boundary energies of Ag for different concentrations of oxygen and their effect on the Ag grain structure. 51

Figure 2.11: Schematic showcasing the effect of different grain structures on through-coating diffusion. 55

Figure 3.1: Schematic representation of the magnetron sputtering system used in this work. 58

Figure 3.2: Schematic representation of the spectrophotometer integrating sphere used in this work. 59

Figure 3.3: Schematic representation of the tube furnace and box furnace used in this work. ... 63

Figure 3.4: Interference-enhanced in situ ellipsometry measurements of a Ag film, compared to simulated results obtained with different modelling approaches. 68

Figure 4.1: Example of the image treatment process used to quantify scratch visibility. 81

Figure 4.2: Schematic overview of model stack architectures used in Chapter 4..... 82

Figure 4.3: Optical, electrical and microstructural observations of annealed GRAR-type stacks (with both diffusion barriers present). 83

Figure 4.4: Optical, electrical and microstructural observations of annealed GRAZ-type stacks (with no top diffusion barrier). 84

Figure 4.5: Optical, electrical and microstructural observations of annealed GZAR-type stacks (with no bottom diffusion barrier). 86

Figure 4.6: Optical, electrical and microstructural observations of annealed GZAZ-type stacks (with no diffusion barriers). 88

Figure 4.7: Schematic representation of the proposed model of fingering instability dewetting patterns caused by Na diffusion into Ag. 90

Figure 4.8: Optical microscope images of the main scratch morphologies. 92

Figure 4.9: As-coated (AC) visibility and defect types of scratches obtained for different scratch loads. 93

Figure 4.10: Scratch intensities and widths before and after annealing in different conditions. . 95

Figure 4.11: SEM images of tensile-type scratch defects annealed in different atmospheres. 98

Figure 4.12: Bright-field TEM cross-section imaging of tensile-type scratches annealed in different atmospheres. 99

Figure 4.13: Schematic overview of the main effects of O_2 and Na diffusion on undamaged coatings and coatings presenting scratch defects. 102

Figure 5.1: Example of the graphical user interface allowing one to plot R_V and T_V as a function of the thickness or refractive index of the mapped layers. 112

Figure 5.2: Schematic representation of the in situ corrosion monitoring setup and example of the resulting durability assessment. 114

Figure 5.3: Minimum modelled R_V and refractive indices at which it is achieved as a function of the Ag thickness in DMD coatings modelling. Mapping of the minimum modelled R_V as a function of the refractive indices of the dielectrics for a Ag thickness of 6 nm. 117

Figure 5.4: Schematic representation of the different filter architecture types used in Chapter 5, with their associated labels referred to throughout the text. 118

Figure 5.5: R_V^{FS}, T_V, and sheet resistance of samples with ARS and ARZ architectures, as a function of the N_2 concentration in the gas mixture during sputtering of $Ag_{(N)}$.. 119

Figure 5.6: *In situ* transmission monitoring and change in reflection obtained in low-severity and high-severity corrosion tests of coatings deposited in various architectures for different N_2 concentrations in the gas mixture during sputtering of $Ag_{(N)}$. 123

Figure 5.7: 1 µm × 1 µm AFM images of $Ag_{(N)}$:0% and $Ag_{(N)}$:5% films, with nominal thicknesses of 7.5 nm and 4 nm, deposited on 33 nm thick seed layers of Si_3N_4 or $ZnO_{(Al)}$, annotated with their root mean square roughness, r_q. 125

Figure 5.8: Front-side reflectance and transmittance of uncoated B270 glass and of durable AR coatings. Change of performance of these samples following 20 minutes of immersion in high severity corrosion testing. 128

Figure 6.1: SEM images of Ag films produced by deposition on $ZnO_{(Al)}$-coated Si substrates and subsequent etching. Examples of the comparative modelling approach identifying the percolation threshold in these samples 141

Figure 6.2: Validation of the comparative modelling approach via *in situ* sheet resistance measurements. 143

Figure 6.3: Example of critical thickness assessments with IE-ISE monitoring. 144

Figure 6.4: Critical thicknesses observed during deposition and etching as a function of the substrate and deposition conditions of Ag films. 146

Figure 6.5: Continuous film formation (breakdown) thickness as a function of percolation threshold thickness during deposition (etching). 150

Figure 6.6: Schematic representation of hole formation and subsequent dewetting. 151

Figure 6.7: Absorption, reflection and transmission of AR stacks, using Ag films deposited in different conditions, as well as post-deposition etching, compared to curves obtained from FDTD modelling using the same architecture and realistic Ag input geometries. 158

Figure 6.8: Hole size distributions and change in transmission attributable to their plasmonic resonances for hole morphologies derived from SEM imaging and inserted into FDTD simulations. 160

Figure 7.1: STM topography of Ag films deposited on amorphous Si before and after annealing for different initial film thicknesses and annealing temperatures. 165

Figure 7.2: As-coated transmission and sheet resistance measurements, *ex situ* change in transmission and in situ change in transmission 160 s into HT, for Au-based samples deposited with standard processes or the DAE approach. 168

Figure 7.3: Evaluation of the benefits achievable when annealing standard-deposited films, or thicker films, subsequently etched, following the DAE method. 169

Figure 7.4: Schematic outlining the different morphologies which may be obtained when encapsulating an Ag film prior to annealing and vice-versa, and describing their consequences on film stability during subsequent tempering. 170

Figure 7.5: Schema of the main changes resulting in optical changes during low-E tempering, excluding processes driven by Ag contamination and modelled change in transmission for each of these, compared to experimental results. 173

Figure A.1: Deposition rates, refractive indices and extinction coefficients of $ZnO_{(Al)}$ and $SiN_{(Al)}$ films deposited with different reactive gas ratios. 206

Figure A.2: ΔT following 7-minute HT of 3mm low-E glass samples for different combinations of substrate cleaning methods..... 207

Figure A.3: ΔT following 7-minute HT of 3 mm low-E glass samples with different modifications applied to the base layer. 208

Figure A.4: Stress changes of 40 nm $SiN_{(Al)}$ films as a function of temperature, measured via wafer curvature. 209

Figure A.5: Analysis of 40 nm thick $ZnO_{(Al)}$ and $SiN_{(Al)}$ layers deposited on fused silica substrates, as-coated and following 7 minutes of HT. 211

Figure A.6: Change in absorption following HT of a 40 nm single layer of $ZnO_{(Al)}$, a bilayer of $ZnO_{(Al)}$ and $SiN_{(Al)}$, and a low-E stack. 212

Figure B.1: Schematic representation of the darkfield scratch imaging set-up used in Chapter 4. 214

Figure B.2: As-coated (AC) optical transmission and reflection, as well as transmission change and reflection change for each of the partial stack designs used in Chapter 4. 215

Figure B.3: Optical transmission change of various partial stack types annealed in air and in argon. 217

Figure B.4: SEM image of a GZAZ-type stack deposited on BSG and annealed in air, and associated EDS mapping of Ag. 218

Figure B.5: Diffuse transmission of samples following heat treatment, for different partial stack designs, substrate types, and gas environments. 218

Figure B.6: Comparison of transmission curves of different annealed partial stacks to modelled curves obtained using the *CompleteEASE* software. 219

Figure B.7: Backscattered electron mode SEM images of GZAZ-type partial stacks annealed in air, highlighting the irregular edges of the holes in the Ag film. 220

Figure B.8: Residual scratch depth as a function of the applied load, measured by stylus profilometry. 221

Figure B.9: Optical microscope images of tensile and conformal cracks in full low-E stacks, and of the same samples following acid etching of all but the bottom rigid diffusion barrier layer. 221

Figure B.10: As-coated scratch width and defect types of scratches obtained at various constant loads on GRAR-type stacks. 222

Figure B.11: Average background intensity for each scratched sample, as-coated and following annealing in one of various controlled atmospheres. 222

Figure B.12: SEM images of tensile crack structures as-coated and annealed at 650 °C for 8 minutes in humid air. 223

Figure B.13: Number of spherical nanoparticles which can be formed per volume of Ag, scattering cross-section at 550 nm of an Ag nanoparticle, and scattering cross-section per unit volume of Ag dewet into nanoparticles, all as a function of the nanoparticles' radius. 224

Figure C.1: Crystallite size of 7.5 nm thick $Ag_{(N)}$ coatings deposited on $ZnO_{(Al)}$-coated and uncoated Si substrates as a function of the N_2 concentration in the $Ag_{(N)}$ sputtering gas mixture, obtained from XRD diffractograms. 225

Figure C.2: AFM images of 33-nm-thick Si_3N_4 and $ZnO_{(Al)}$ films. 226

Figure C.3: Threshold analysis of AFM images of 7.5 nm Ag films deposited on Si_3N_4 substrates. 227

Figure D.1: AFM images of IE-ISE substrates using different SiO_2 layers, bare or overcoated with 10 nm of $ZnO_{(Al)}$, and XRD diffractograms $ZnO_{(Al)}$-coated substrates. 228

Figure D.2: t_{cont}^{d} as a function of t_{perc}^{d} measured by IE-ISE on various substrates in different deposition conditions. 229

Figure D.3: t_{perc}^{e} and t_{cont}^{e} as a function of the Ag thickness etched between the end of deposition and initiation of breakdown. 231

Figure D.4: SEM image of a Ag film produced by deposition on a $ZnO_{(Al)}$-coated Si substrate and **s**ubsequent etching to a thickness of 7 nm. 232

Figure D.5: t_{perc}^{e} and t_{perc}^{d} obtained for Ag films deposited in Ar gas at floating potential, for different $ZnO_{(Al)}$ coated substrates. 233

Figure D.6: FDTD-simulated absorption, reflection and transmission of experimentally derived Ag film structures obtained from experimental images. 235

Figure D.7: Demonstration of the processing performed to evaluate the transmission loss attributable to the plasmonic behavior of holes patterns. 237

Figure D.8: Transmission loss due to plasmonic behavior of manually generated circular hole patterns. 238

Figure D.9: Absorption, reflection, transmission and sheet resistance of optical devices on $ZnO_{(Al)}$ or bare B270 glass substrates, using standard deposition or post-deposition etching. Modelled transmission values for each sample type. 239

Figure E.1: Comparison of different corrections accounting for the transmission changes of SLG at high temperatures. Comparison of the transmission of an industrial reference sample to the correction factor used. 242

Figure E.2: Evaluation of the feasibility of etching off Ag encapsulating layers post-HT via comparative modelling and proposed explanation for the rapid breakdown observed once etching of the Ag layer begins..... 243

LIST OF SYMBOLS AND ABBREVIATIONS

Materials and elements

Ag	Silver
$Ag_{(N)}$	Nitrogen-doped silver, silver deposited with nitrogen surfactant
Au	Gold
AZO	Aluminum-doped zinc oxide (see also: $ZnO_{(Al)}$)
Ca	Calcium
Cu	Copper
ITO	Indium-tin oxide
Mg	Magnesium
N	Nitrogen
Na	Sodium
Ni	Nickel
$NiCrO_x$	Nickel-chrome oxide
$NiCrN_x$	Nickel-chrome nitride
$SiN_{(Al)}$	Aluminum-doped silicon nitride
SiO_2	Silicon dioxide, silica
SnO_2	Tin oxide
TiO_2	Titanium oxide
ZnO	Zinc oxide
$ZnO_{(Al)}$	Aluminum-doped zinc oxide (see also: AZO)
ZrO_2	Zirconium oxide

Symbols

A	Absorption, absorptance
$a_{f,i,s,GB}$	Area associated to film, interface, substrate, grain boundary surfaces
β	Composite parameter concerning hole stability
C	Concentration
$D_{(0)}$	Diffusivity (prefactor)
Δ	Ellipsometry parameter; dephasing between p- and s-polarizations
$\Delta G_{(S,V)}$	Gibb's free energy change (associated to forming a surface, volume)
ΔG^*	Gibb's free energy change of forming a critical cluster
ΔT	Change in transmission
Δt_{GB}	Change in thickness (from the average film thickness) at a grain boundary groove
ε	Emissivity
E_D	Activation energy of diffusion
E_b	Surface energy of the bottom interface of a Ag film structure
E_{GB}	Grain boundary energy of a Ag film structure
E_t	Surface energy of the top interface of a Ag film structure
E_ε	Strain energy of a Ag film structure
E_T	Total energy of a Ag film structure
F	Particle deposition flux
F_D	Diffusion flux
$\gamma_{(f,s,i,GB)}$	Surface energy (of the film, substrate, interface, grain boundaries)
$\gamma_{q,n}$	Surface energy of the "q" interface of a given grain
k	Complex component of the refractive index, extinction coefficient
k_B	Boltzmann's constant

φ	Wetting contact angle
Ψ	Ellipsometry parameter; intensity ratio between p- and s-polarizations
Ω	Atomic volume
n	Real component of the refractive index, refractive index
$N_{(sat)}$	Island density (at saturation)
$p_{(0)}$	Pressure (at equilibrium)
R	Reflection, reflectance
$R_V^{(FS)}$	Visual reflectance (of the front surface of a sample)
R_{Sh}	Sheet resistance
$r^{(*)}$	(Critical) radius of a cluster or grain
r_h	Hole radius
r_q	Root mean square roughness
ρ	Resistivity
Φ_S	Spectral power distribution of the lighting/illuminant
θ	Equilibrium angle of grain boundary grooving
T	Transmission, transmittance
T_V	Visual transmittance
t	Film thickness
$t_{perc}^{(d,e)}$	Percolation threshold thickness (during deposition, etching)
$t_{cont}^{(d,e)}$	Continuous film formation thickness (during deposition, etching)
τ_{coal}	Critical time for cluster coalescence
υ	Density of diffusing atoms per surface area
ζ	Supersaturation
$\bar{y}$	Spectral sensitivity of the observer, spectral luminous efficiency

Abbreviations

AC	As coated, prior to heat treatment
AFM	Atomic force microscopy
AR	Antireflective
CIE	International Commission on Illumination
DAE	Deposit-anneal-etch, multi-step Ag deposition sequence
DI	De-ionized (water)
DMD	Dielectric-Metal-Dielectric
EDS	Energy dispersive X-ray spectroscopy
FIB	Focused ion beam (milling)
MIR	Mid infrared, in this work referring to wavelengths above 2.5 μm
FoM	Figure of merit, Haacke's figure of merit
HT	Heat treatment, heat-treated
(IE-)ISE	(Interference enhanced) *in situ* ellipsometry
GB	Grain boundary
Low-E	Low-emissivity (coatings, windows)
MSE	Mean square error
NIR	Near infrared, in this work referring to wavelengths between 780 nm and 2.5 μm
RDB	Rigid diffusion barrier (e.g. SiO_2, Al_2O_3, SiN, TiN)
SHGC	Solar heat gain coefficient
SEM	Scanning electron microscopy
TC	Transparent conductor
TEM	Transmission electron microscopy
VW	Volmer-Weber (growth mode), also 3-D or island growth mode

XPS	X-ray photoelectron spectroscopy
XRD	X-ray diffraction

LIST OF APPENDICES

APPENDIX A Obtaining basic optical performance and high temperature stability 204

APPENDIX B Supporting information for Chapter 4 213

APPENDIX C Supporting information for Chapter 5 225

APPENDIX D Supporting information for Chapter 6 228

APPENDIX E Additional details pertaining to Chapter 7 242

CHAPTER 1 INTRODUCTION

Faced with the responsibility to address the threats imposed by climate change, modern societies must embrace a multifaceted approach to achieve sustainability [1]. In its 2022 report on the mitigation of climate change, the Intergovernmental Panel on Climate Change identifies key areas where there is potential for emissions reductions and critically assesses them. Amongst these, is the building sector: the report evaluates that in 2019, this sector was responsible for 21% of global greenhouse gas emissions, 57% of which – roughly 10% of global emissions – were a result of supplying electricity and heating for buildings [2]. This presents dire risks, both for energy consumption and immediate health risks: namely, rising temperatures are expected to drive up energy consumption where they intersect with access to active cooling technologies (i.e. air conditioning), and to result in heatwave-related deaths where they are unavailable [2], [3]. Reducing the energy consumption required for space heating and cooling and, more broadly, improving thermal control by passive means can, therefore, offer significant benefits in terms of emissions reductions and human well-being.

One way of doing so is via low-emissivity, or low-E window coatings. Indeed, windows are one of the main weak points of the thermal insulation of buildings [4]. Although improvements in the insulation of window frames and the pursuit of vacuum-insulated glass units offer significant potential for improvement in regard to conductive and convective heat losses, they do not address the fundamentally weak resistance of typical window glass to radiative heat transfer [5], [6], [7].

By virtue of integrating a transparent and electrically conductive film, low-E coatings lend high infrared reflectance to glass, correcting this issue [6], [8]. Combined with effectively designed window assemblies, they can offer significant improvements in insulating buildings, both for mitigating heat loss in cold climates and vice-versa [2], [5], [6], [7], [8].

As the insulating ability of these coatings is intrinsically linked to the electrical conductivity of the materials used within them [6], [9], [10], silver (Ag) has emerged as the clear material of choice for this application [5], [6], [11]. Indeed, Ag has the highest electrical conductivity of all elemental metals [12], [13], in addition to presenting low visible absorption and excellent potential for their use in antireflective filters [11], [14], [15], [16], enabling it to offer high insulating performance while maintaining excellent transmission and aesthetics in the visible range [6], [11].

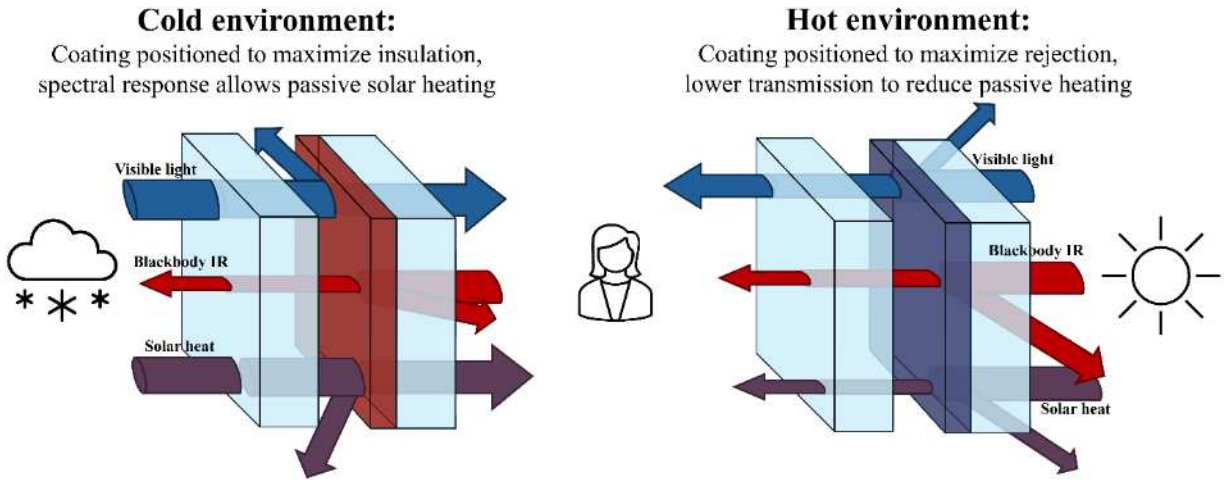


Figure 1.1: Schematic illustrating the intended functionality of low-E coatings in different climates. Modeled after [5].

However, fabricating the thin (< 15 nm) Ag films required for these applications presents specific challenges, as does imparting them with sufficient durability to maintain their performance throughout various processing steps and decades-long use. As these challenges are situated at the intersection of transparent, conductive, IR reflective and durable Ag-based coatings, they are of interest to a number of other fields. Thus, this work will gain insight from (and hopefully offer insight to) others who must contend with Ag's specific material challenges, in more fundamental work [17], [18], [19] or in other applications such as high durability Ag-based reflectors [20], [21], [22] or Ag-based transparent electrodes [23], [24], [25].

1.1 Controlling the microstructure and stability of Ag films

The difficulties encountered when working with ultra-thin Ag mainly stem from its relatively high surface energy and poor bonding to common oxide materials; as a result, surface free energy minimization constraints drives Ag towards morphologies that minimize its surface-to-volume ratio [26], [27].

During film deposition, this leads to a Volmer-Weber growth mode, in which Ag films form isolated islands at low thicknesses [26], [27], as shown in **Figure 1.2a**. In addition to inhibiting the

longe range conductivity necessary for effective infrared reflection, isolated Ag islands can induce significant optical absorption due to localized surface plasmon resonance [28], [29]. While these will coalesce into a fully continuous film as film deposition continues (**Figure 1.2a**), achieving this at relatively low thicknesses is required to maintain high visible transmission. As a result, controlling film coalescence is a key element when producing Ag based-devices. In addition, the coalescence dynamics will greatly influence the size of the grains, i.e. of areas in which consistent crystalline alignment is maintained, formed by the combination of differently oriented Ag clusters [19], [30]. This, in turn, will also impact coating performance, as the presence of rough external interfaces, defects, and boundaries between grains will impact the electrical and optical performance of Ag films [17], [31].

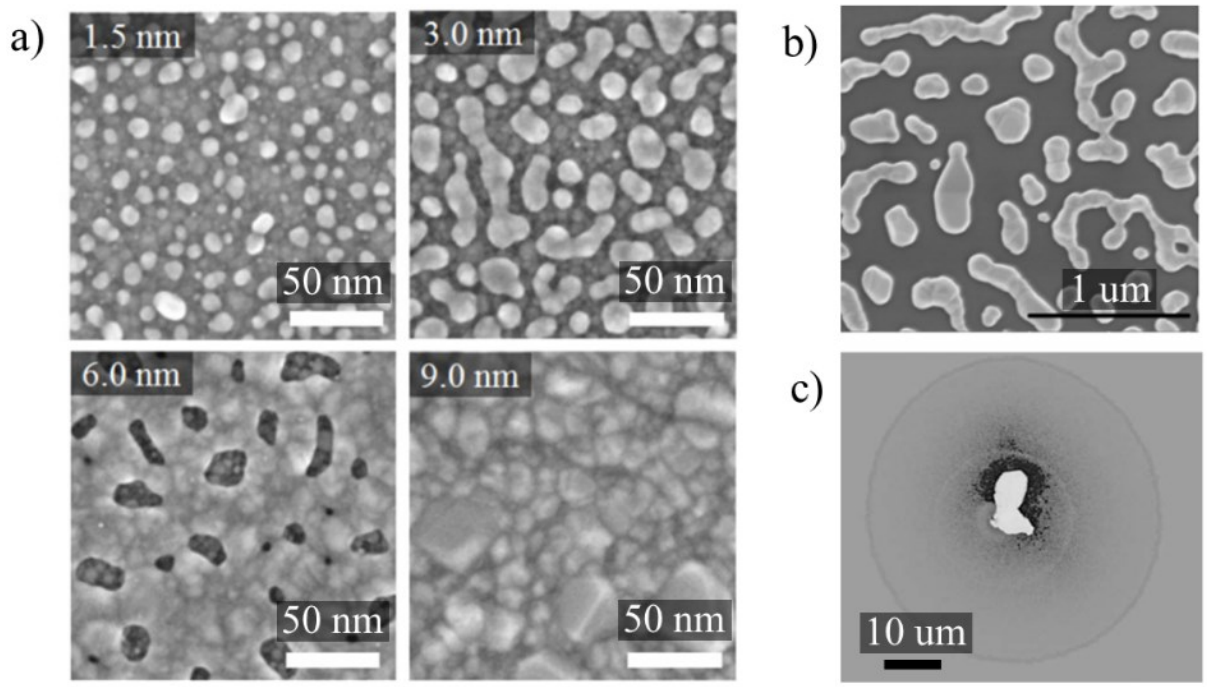


Figure 1.2: a) Deposited Ag film morphology as a function of nominal thickness, showcasing the Volmer-Weber growth mode. Adapted with permission from [23]. Copyright 2018 American Chemical Society. **b)** Solid-state dewetting of a 15 nm Ag film following annealing in N_2 at 300 °C. Adapted with permission from [32]. Copyright 2014 American Chemical Society. **c)** Backscattered electron image of a degradation feature resulting from exposure of a protected Ag film to a flowing gas mixture (H_2S, Cl_2, NO_2 and H_2O diluted in air), showing a large Ag-based nodule is surrounded by a Ag-depleted area. Adapted with permission from [20]. Copyright 2016 Optical Society of America.

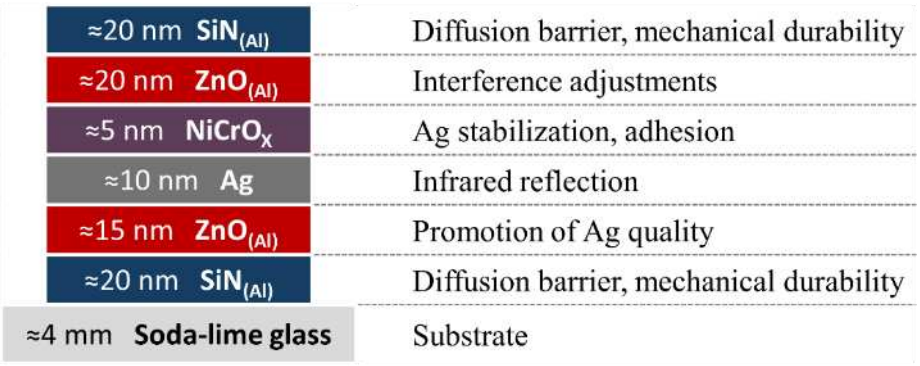


Figure 1.3: Schematic example of a low-E coating, presenting typical thicknesses and materials used in this work, as well as their functional roles within the stack.

By the same token of surface energy minimization, Ag films present issues in terms of their environmental stability: continuous layers may re-transition to discontinuous droplets, if such a morphology decreases total free energy and sufficient energy is available for Ag to reorganize. This is a commonly occurring issue when Ag layers are annealed at high temperature, enabled by increased Ag mobility, and is known as dewetting, or agglomeration [33], [34], [35], exemplified in **Figure 1.2b**. Finally, exposure to various contaminants can also drive Ag degradation, as presented in **Figure 1.2c**, either by forming chemical compounds [36], [37], or facilitating Ag reorganization into clusters [34], [38]. These effects can easily compound with one another, as high temperatures can increase the diffusivity of contaminants [39] or induce Ag microstructural changes that increase its susceptibility to chemical degradation [21], [38]. Conversely, exposure to oxygen is known to facilitate thermal dewetting and Ag diffusion [34], [40].

Low-E coatings manage these issues via the addition of other functional layers, as shown in **Figure 1.3**. Perhaps most importantly, a seed layer, i.e. a dielectric layer that promotes the formation of a continuous and high-quality Ag, will be deposited prior to the Ag film in order to improve its optical and electrical properties; this is commonly zinc oxide (ZnO), or a doped variation thereof [6], [27], [41], [42], [43]. The addition of a suitable dielectric layer above the Ag layer then allows to tune the optical response via optical interference, yielding improved visible transmission [6], [11], [41]. The resulting dielectric-metal-dielectric, or DMD, structure is quite possibly the simplest type of Ag-based architecture which can, nevertheless, yield high optical and electrical performance [24], [44], and as a result is very common in literature [45], but is not necessarily

durable. To correct this, diffusion barriers can be added at either extremity of the coating ($SiN_{(Al)}$ in **Figure 1.3**) in order to prevent contaminants from the atmosphere or substrate from reaching and degrading the Ag layer [6], [39], [41]. Finally, a protective layer which can be deposited in mild conditions may be inserted between the Ag layer and the dielectrics above it in order to protect Ag from more reactive or energetic deposition processes, as well as offering further stabilization of the Ag layer [6], [20], [46]. With all this in place, we now have a quite well-rounded and robust coating. Given the low thickness of the individual films, however, analysing their behavior can be challenging, requiring adapting the coating architectures or testing methodologies to emphasize specific properties.

1.2 Context of the research

Although the challenges described above can emerge for a number of applications in which thin Ag films are used, low-E window coatings present specific issues which warrant similarly specific investigation. This project was, therefore, performed in collaboration with Guardian Glass, one of the world's leading glass manufacturers, in order to ensure that it accurately addressed the challenges typical of coated glass products.

The durability requirements of low-E window coatings are somewhat unlike those of other devices, in that they have very little to do with the coating's operating conditions. Rather, they're defined by their fabrication process. Indeed, low-E coatings will typically be positioned on one of the inner faces of a multi-pane insulated glass unit, as shown in **Figure 1.1** [5], [6], [7]. Thus, they'll be sealed in a non-reactive gas, and a glass pane on either side will separate them from any mechanical contact. In addition, they'll only be exposed to temperatures somewhere in the range between room temperature and that of the environment they're insulating it from.

While conventional coatings deposited by magnetron sputtering do not need to be deposited immediately after glass fabrication, it is practical to deposit them onto standard full-size glass panes (≈ 6.0 m × 3.2 m) prior to other operations as this avoids needing to optimize the placement of a multitude of smaller panes of various shapes and sizes [6]. As a consequence, low-E coatings are often fabricated prior to a number of storage, transport, cutting, tempering and assembly steps, during which they can be exposed to various atmospheric contaminants, mechanical damage and high temperatures.

Namely, in order to obtain the improved mechanical properties required for architectural and safety applications, glass must be tempered, i.e. undergo heat treatment (HT) at ≈ 650 °C and subsequently quenched to induce high compressive stresses at the glass surfaces [47]. These cause the glass to be able to support much higher mechanical loads, but also to shatter into small pieces when broken. This latter point is useful as a safety feature but also means tempering the glass must take place after cutting it, and therefore, after coating it.

With an appropriate design, low-E coatings can undergo the requisite HT while maintaining or even improving their IR reflecting performance, but this nevertheless results in significant visible optical changes, even in the best-case scenario. Glass manufacturers aim to control this, attempting to develop "single stock" low-E coatings, meaning coatings that present the same visible and thermal properties following HT. This allows to temper only select panes while simultaneously obtaining uniform aesthetics and performance, all using glass from a single stock – hence the name [6]. However, these are currently restricted to a narrow portfolio of products.

This all assumes that the coating's protective layers are performing as intended, however. As shown back in **Figure 1.2c**, small flaws in an otherwise durable coating can lead to the formation of much more serious degradation features when exposed to contaminants. Namely, this can cause important production issues when defects are exposed to high temperatures. As tempered glass cannot be cut, prior to tempering, the glass must be cut, and its edges smoothed and reworked. These handling steps can easily result in the formation of small, barely visible scratches which, when heat-treated, become highly visible. This was identified as an issue of high importance by the industrial partner as these can lead to glass being discarded at the very end of the fabrication process, in turn leading to significant waste. However, the combination of mechanical defects, high temperatures, and the presence of multiple potential contaminants makes the explicit mechanism of scratch visibility intensification difficult to assess.

Last but not least, these challenges must be addressed while simultaneously maintaining or improving the as-coated performance of the coatings; a coating that is rejected by the consumers rather than the manufacturer is not much of an improvement. Dielectric barrier layers don't present any major issues in this regard, but it somewhat limits the approaches which can be taken to stabilize the Ag layer directly. Although doped Ag films can enable significant improvements in terms of deposition dynamics as well as chemical and thermal stability [32], [36], [48], these

typically have decreased as-coated performance, and show important changes following HT [49], [50]. The latter makes them particularly poor candidates for single-stock coatings. Thus, emphasis must be placed on the role of the Ag microstructure in determining its optical and electrical performance, as well as its durability.

1.3 Objectives

In order to improve the durability of low-E coatings to chemical and thermal degradation without compositionally changing the Ag layer, this work aims to control durability via modifying the Ag microstructure. Indeed, if Ag is susceptible to degradation because it is driven towards morphologies that decrease its surface free energy, one way of mitigating degradation would then be to generate Ag films presenting microstructures with less thermodynamic incentive to degrade. However, it is first necessary to develop a robust understanding of the different stack degradation mechanisms and assess their importance relative to purely temperature-driven changes. Given the numerous potential mechanisms which can result in Ag instability during HT, specific approaches allowing one to isolate the effect of different defect types, coating architectures and contaminants are required.

In response, the objectives of this PhD project can be categorized as follows:

1. Establish causal links between specific coating features, contaminant species and optical changes within low-E stacks during the tempering process and assess their impact on the accentuation of coating defects at high temperatures.
2. Modify the microstructure of Ag layers without altering their chemical composition, by using novel deposition techniques and approaches.
3. Fabricate low-E coatings with improved chemical and/or high temperature stability by leveraging Ag layers with tailored microstructures.

1.4 Publications

The work performed in the pursuit of the above objectives has led to the writing of three manuscripts, all of which have been published by, or submitted to, peer-reviewed scientific journals. In the following work, each chapter dedicated to results will present an integral copy of

one of these articles, as described in the following section. While this work also led to several oral or poster presentations at international conferences, these will not be discussed in this thesis.

1.5 Outline

With the key concepts and the specific objectives guiding this work introduced, the structure of the remainder of this thesis can now be presented.

Chapter 2 consists of a literature review which will, in a first part, offer additional details on the fundamental requirements of low-E coating performance, as well as further contextualise the choice of Ag as the IR reflector in these coatings. In a second part, the basic physics leading to the Ag layer's Volmer-Weber growth mode will be presented. Following this, various approaches allowing one to manipulate the film formation dynamics and resulting microstructures will be discussed. In a third and final part, the mechanisms that drive Ag microstructural changes will be presented starting with changes intrinsic to the Ag layer, then those resulting from the interaction with other coating layers or external contaminants.

Chapter 3 presents the tools and methodologies used in this work. Sample fabrication is presented first, followed by performance and durability assessment methods. Material characterization techniques used to investigate the specific mechanisms taking place during coating fabrication and degradation are then discussed.

Chapter 4 presents the first of three results chapters; here, the article titled "Role of atmospheric and substrate contaminants on the degradation and defect visibility in Ag-based low-emissivity coatings" is presented. In this article, the role of various contaminants on Ag degradation is investigated, establishing how they interact with the coating alone, in combination with one another, and with respect to modifications of the coating architecture. In particular, the role of sodium, which is underreported, is discussed. This allows to isolate the changes intrinsic to high temperature processing low-E coatings, which this thesis tries to mitigate in later chapters. Finally, the effect of these contaminants on the enhancement of scratch defect visibility during tempering is quantified and associated to distinct defect features and contaminant-driven mechanisms.

Chapter 5 presents an article titled "Enhanced Durability and Antireflective Performance of Ag-Based Transparent Conductors Achieved via Controlled N-Doping", in which nitrogen is used as

a surfactant to modify Ag growth dynamics without causing compositional changes, and the effect of the resulting changes in the film morphology are investigated, correlated to corrosion durability, and leveraged to produce highly durable films. While not addressing high temperature durability, this is used as a proof of concept to demonstrate how microstructural control of the Ag layer can result in improved coating stability.

In Chapter 6, post-deposition etching is explored as a method to fabricate Ag films with unconventional microstructures by decoupling the thickness at which a continuous film can be obtained from the microstructural features resulting from given deposition conditions. Thus, the morphological evolution of films deposited in various conditions and subsequently plasma etched is studied and correlated to their expected microstructural features. This is presented in an article titled “Investigating the Morphological Evolution of Ion-thinned Ag Films via In Situ Ellipsometry”. Subsequently, additional results are presented, in which this method is used to produce highly conductive antireflective filters and the effect of hole formation in the Ag layers on optical performance is investigated.

Chapter 7 offers a general discussion on the fabrication of single-stock low-E coatings. Notably, the application of post-deposition etching towards achieving high temperature stability of the Ag layer is studied. Some promising preliminary results are obtained, and pathways to further improve this approach are discussed.

Finally, Chapter 8 concludes the thesis by summarizing the findings herein and their outcomes, as well as sharing recommendations and suggestions for future work.

CHAPTER 2 LITERATURE REVIEW

2.1 Low-E coatings

Before exploring the particularities of Ag films – what influences their formation dynamics, their microstructures, their susceptibility or durability when exposed to given elements – it is worth exploring the contexts they are used in. Thus, this section will first present an overview of the functional requirements of low-E coatings used in different contexts, as well as give an overview of the main low-E archetypes. As part of this, the benefits and drawbacks of alternative metallic layers and Ag doping for low-E coatings are discussed, as, while this work focuses specifically on Ag-based coatings, these present significant potential for low-E coatings and other metal-based transparent conductors.

2.1.1 Conventional coating archetypes

The fundamental purpose of low-E window coatings is to address a problem with glass: it absorbs IR light and, more specifically, re-emits it [5], [6], [47]. With the exception of highly engineered non-reciprocal materials, Kirchoff's law of radiation states that at thermodynamic equilibrium, the absorption is equal to the emissivity ($A = \varepsilon$), spectrally and directionally [9], [51]. Conventional window glass is highly absorbing ($\varepsilon \approx 0.85$) and can be taken to have null IR transmittance ($T \approx 0$) [5], [6], [52]. Thus, if our goal is to obtain a window with low absorbance, conservation of energy ($R + T + A = 1$) demands that it have high IR reflectance (R) [6], [45], [52], [53].

The Hagen-Rubens relation, shown below, provides a relationship between a material's IR reflectance, R, and its conductivity, σ, (which for our purposes we may take as frequency independent), given ω, the frequency of the radiation, and ε_0, the permittivity of vacuum [8].

$$R \approx 1 - 2\sqrt{\frac{2\varepsilon_0\omega}{\sigma}} \qquad 2.1$$

The result is that the higher the conductivity of a material, the better it will be at reflecting IR radiation, and, following the previous discussion ($A = \varepsilon$; $T \approx 0$; $R + T + A = 1 \therefore R \approx 1 - \varepsilon$), the better it will perform in low-emissivity applications. While the most rudimentary requirement of a low-emissivity window coating is, therefore, that it include a conductive layer to reflect IR radiation

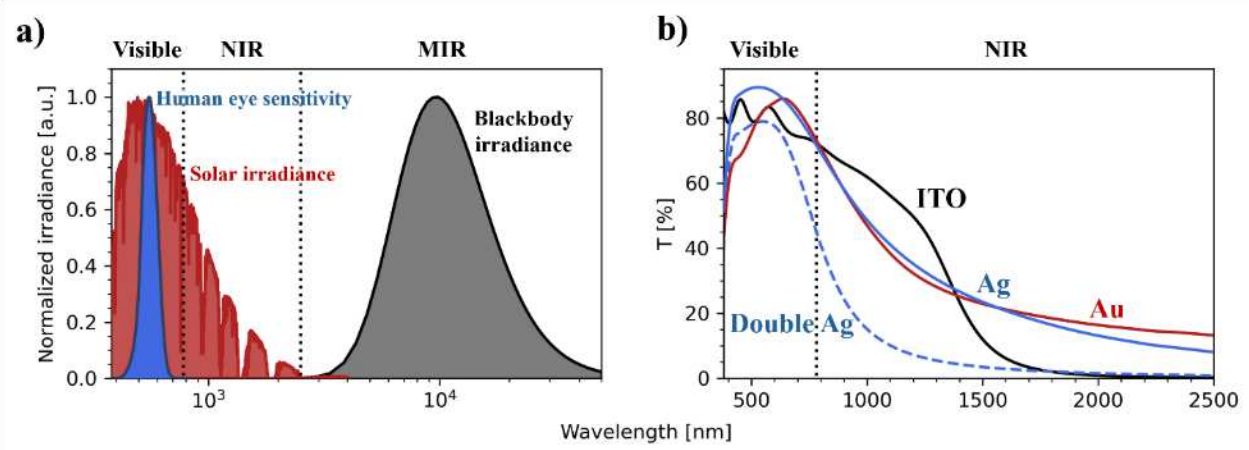


Figure 2.1: a) Comparison of the spectral dependence of the light sensitivity of the human eye (CIE-1931 observer [55]), the irradiance of the solar spectrum (ASTM G173 [56]), and the thermal irradiance of a blackbody at 300 K. **b)** Comparison of the simulated transmission curves of four different low-E coatings on a 3-mm-thick soda-lime glass substrate, with the following architectures: 500 nm ITO; 40 nm $ZnO_{(Al)}$ / 10 nm Ag / 40 nm $ZnO_{(Al)}$; 40 nm $ZnO_{(Al)}$ / 10 nm Au / 40 nm $ZnO_{(Al)}$; 40 nm $ZnO_{(Al)}$ / 10 nm Ag / 60 nm $ZnO_{(Al)}$ / 10 nm Ag / 40 nm $ZnO_{(Al)}$. Modeled after [54].

while simultaneously maintaining sufficient transparency to fulfill its role as a window, effective implementation requires more nuance.

Specifically, while the previous discussion did not make the distinction for the sake of simplicity, IR radiation should in no way be considered as monolithic. **Figure 2.1a**, highlights the two main categories that should be distinguished for the purposes of insulating against radiative heat transfer: solar or near-IR (NIR) radiation, and thermal blackbody radiation, in the mid-IR (MIR). These make for essential distinctions in application: in hot climates the priority is to reduce cooling requirements, and thus low-E coatings will aim to reject as much heat from the sun as possible, even reducing visible light transmission to this end; alternatively, in colder climates, benefiting from passive solar heating while insulating against thermal radiation losses is desired [5], [6], [45], [54]. This is particularly important as glass is actually highly transparent in the NIR, despite it being essentially opaque in the MIR, as previously discussed [6].

As a result, the optical and IR-insulating performance of low-E coatings are typically quantified using their visible transmittance (T_V) [6], [52], [57], i.e. the transmittance weighted to the sensitivity of the human eye , the solar heat gain coefficient (SHGC), which includes direct solar

transmission, in a similar fashion to T_V, while also accounting for absorption and re-emission of NIR radiation [54], [58], and the emissivity (ε), measured on a scale of one to zero, one being a perfect blackbody and 0 a perfect reflector [45]. The sheet resistance (R_{Sh}) can be linearly correlated to ε for a given material; therefore it is frequently used as a substitute for ε, although comparison between different materials should be taken with appropriate reserve [59]. Finally, the U-value goes beyond radiative considerations and offers a standardized measurement for the total heat transfer through a window unit, including convective and conductive contributions [6], [45], [54].

While other metrics exist [6], [45], we do not need to delve into these. Currently, it suffices to distinguish visible, NIR and MIR contributions, as well as non-radiative contributions, as this will allow to contextualize the main performance differences between different coating types, fabricated with different materials.

Hard low-E coatings, or pyrolytic coatings, refer to a class of coatings that are deposited by chemical vapor deposition (CVD) processes during glass fabrication, leveraging the high temperature of the glass to drive pyrolytic reactions [5], [45], [52]. These typically make use of a conductive metal oxide, doped to improve its optical and electrical performance [5], [6], [45], [52]. The resulting coating is embedded in the final glass product, resulting in much higher mechanical and chemical durability, allowing them to be used on single-pane windows as well as simplifying post-processing [45], [52]. The downside of these coatings is that, while they provide a decent decrease in emissivity, they display lower visible transparency than conventional coatings, as well as a high SHGC, making them a poor choice in most hot climates [6], [45]. Moreover, the reduction of convective and conductive heat transfer requires the usage of an insulating glass unit, a window configuration where two panes of glass are separated by a sealed cavity filled with an insulating gas [6], [7], [45]: in this case, more fragile coatings can be placed inside the cavity, protecting them from damage and greatly reducing the need for increased durability. This lowered return on their increased durability, coupled to their lower performance and tunability has, therefore, led these to lose favor.

Conventional coatings, sometimes referred to as soft coatings, typically incorporate conductive metal layers and are deposited by magnetron sputtering, independently from the glass fabrication process [5], [45], [54]. The coatings fabricated and studied in this work are soft coatings. While non-metallic transparent conductors, such as ITO [60], [61], aluminum-doped zinc oxide (AZO or

$ZnO_{(Al)}$) [62], or transition metal nitrides [45], [63], could also be deposited by magnetron sputtering, these seem to run into very much the same performance limitations as hard coatings, with some added cost and complexity. As a result, it should come as no surprise that these are almost exclusively metal-based.

As stated previously, Ag is the main metal used for this purpose. In addition to having the highest conductivity amongst metals [12], [13], it has the highest k/n ratio in the visible (where k and n are the complex and real parts the refractive index, respectively) [14], [15], which has been shown to enable greater interferential effects when integrated in an appropriate stack design [16]. Coupled with appropriate antireflective layers, coatings using a single thin Ag layer can simultaneously achieve lower emissivity, lower SHGC, and higher visible transmission than a pyrolytic coating [6]. On the other hand, alternative metals like gold or copper (which will be discussed in more detail shortly) can achieve similar results, but have interband transitions in the visible leading to poor visible aesthetics [11], [15], as shown in **Figure 2.1b**. This is not to say that all Ag films are made equal: as mentioned in Section 1.1, discontinuous Ag coatings will lack conductivity and generate plasmonic absorption features [27], [29]. Even for continuous films, the presence of grain boundaries, defects and roughness will all impact the electrical, and thus optical performance of Ag films [17], [30], motivating us to search for deposition conditions with which we can obtain smooth, large-grained films in Section 2.2.

There are limits to the conductivity of Ag films, even with tailored microstructures, of course: to obtain a steeper transition between the visible-transmitting and NIR-reflecting portions of the coating's optical response, double- or triple-Ag stacks which essentially repeat a similar "unit stack structure" are used [6], [11], [41]; an example is shown in **Figure 2.1b**. These stacks are obviously significantly more complex, and require more time and resources to produce; therefore, this work will limit itself to the investigation of single-Ag coatings, with the implicit assumption that the results obtained will offer useful insight for coatings with multiple Ag layers as well.

It should be mentioned that there are many more design features and functionalities that can be added to low-E coatings. For example, the addition of patterning to the Ag layers can allow the selective transmission of network communications [64], and the addition of thermochromic or electrochromic active coatings, which can modify their optical properties as a response to temperature changes or an applied voltage, can allow to fit their insulating properties to current

conditions [5], [65], [66]. We will not delve into these, however; an understanding of the standard passive coating archetypes is sufficient to contextualize this work.

2.1.2 Alternative metals and Ag dopants

The main metallic layers employed in low-E coatings, other than Ag, tend to be copper (Cu) or gold (Au), owing to their similar optical and electrical properties, yielding high IR reflectance [11], [12], [13], [14], [15]. These are not simply mild downgrades from Ag in terms of performance metrics; rather, while keeping similar overall behavior, they present specific advantages and disadvantages. Namely, Au benefits from much higher chemical stability, making it an attractive choice when oxidation durability is required [67], [68], [69], [70]. This advantage constitutes its own downside, however, resulting in poor adhesion to oxide substrates, due to similarly poor bonding between Au and oxygen, and thus Au commonly requires the implementation of adhesion layers which may decrease coating performance [71], [72], [73]. Furthermore, Au has historically been – and still is – significantly more expensive than Ag, with no obvious indication that this trend will change in the foreseeable future. On the other hand, the conductivity of Cu is second only to Ag's while being vastly less expensive and thus presents interesting opportunities for low-cost coatings. However, its absorption band extends well into the visible spectrum, resulting in poor aesthetics [11], [14]. Conversely to Au, Cu readily forms oxide bonds, which results in stronger adhesion [74], [75], [76], counterbalanced by its susceptibility to oxidation [76], [77].

While high performance devices have been fabricated with both materials, particularly when coupled with methods such as the usage of advanced deposition techniques, dopants, adhesion layers, seed layers, or stabilizing layers, these are (often quite literally) exactly the type of methods one might employ with Ag [32], [71], [77], [78], [79], [80], [81], [82], [83], [84]. Indeed, they present many of the same deposition dynamics [27], [85] and thermal instabilities [76], [86], [87], yielding insight that is easily transferrable to Ag films, but by the same token, these don't make either material stand out from Ag. Consequently, studies on these metals are relevant to this work and will be referred to in the following sections, but the properties distinguishing Au or Cu from Ag are insufficient to justify their widespread adoption in the experimental work.

Perhaps a more interesting option than substituting the Ag layer entirely is to dope it, in order to tune some of its properties while maintaining its overall character. This approach has elicited

enormous interest, with a wide variety of dopants being tested, including O [49], [84], Al [32], [50], [88], [89], Cu [44], [48], [90], Au [91], Ni [92], and more [36]. These can drastically improve the formation of well-coalesced films at low thickness [32], [48], [84], [89], and impart improved mechanical [90], chemical [32], [36], [49], [50], [90], [91], or thermal stability [32], [49], [50], [84], [89], [92], [93]. Very low concentrations result in minimal degradation of the optical properties, allowing excellent performance, particularly when using dopants with good optical and electrical properties, and when leveraging the improved film coalescence [44], [48], [50]. However, not only does increasing their concentration result in decreasing optoelectronic performance (at least when compared with films with comparable degrees of coalescence), their optical and electrical properties tend to change significantly during HT, making them a poor fit for an attempt at single-stock coatings [49], [50], [79], [89], [92]. These nevertheless constitute a tool with exceptional potential for improving Ag-based devices, including low-E coatings; their omission from the experimental part of this work should not be misconstrued as believing otherwise. Rather, an attempt will be made to identify the key beneficial changes these dopants induce and recreate them without said dopants. Before this can be discussed in more detail however, some more fundamental aspects of Ag film formation and stability must be introduced.

2.2 Ag film formation and deposition strategies

Now that we've established the importance of Ag in obtaining performant low-E coatings, we can turn to the challenges it presents. In this section, we will first address how to obtain continuous silver films, and how the used methods define the morphological features of the resulting coatings, before moving on to their durability.

Section 2.2.1 will begin by presenting the basic physics leading to the Volmer-Weber (VW) growth mode of Ag, in which discontinuous clusters form on the substrate surface rather than forming a continuous layer outright. This is fundamentally due to thermodynamic considerations, i.e. surface free energy minimization, and thus we can start by looking at things from a thermodynamic equilibrium perspective. While this is enlightening and helps intuitive understanding, film condensation from the vapor phase is very much not an equilibrium process; therefore, their competition with more kinetic processes will be explored. As such, the mechanisms by which we can control film formation will be highlighted.

The following subsections will discuss the practical embodiments by which this is achieved, separated as a function of the different implemented tools. Following the previous discussion on kinetic aspects of film deposition, a few straightforwardly leverageable parameters will be highlighted, followed by less conventional multi-step processes. Then, additional tools allowing to influence the deposition dynamics will be discussed, for example, selecting an appropriate substrate, and adding surfactants or dopants. Throughout these discussions, the effect on the grain size and roughness will be highlighted, as these will be important in defining performance and durability.

2.2.1 Physics of Ag film formation

The capillary model of film nucleation and its extensions are an intuitive way to approach the VW growth mode while nevertheless describing its relevant behaviors; as pointed out by Greene, this model is inexact is a number of ways, relying on convenient approximations, but it is just that – intuitive, descriptive and convenient [26]. Thus, while it should be taken with appropriate reserve, it will be extremely useful in the interpretation of experimental results.

If we ignore the tensorial properties of a crystalline material such as Ag, the Gibbs surface free energy, γ, is equivalent to the surface tension and can be seen as a force per unit length (1 J/m^2 = 1 N/m) [94]. We can then treat deposited atoms forming 3-D islands on a substrate the same way Young's equation describes liquid droplets beading up on a surface, with γ replacing the surface tension [26], [94], [95]. The contact angle φ between the film material and the substrate can then be predicted by the balance of the surface free energies of the deposited film material, the substrate, and their interface (γ_f, γ_s, γ_i, respectively).

$$\gamma_f \cos\varphi = \gamma_s - \gamma_i \qquad 2.2$$

Lüth goes on to add another term accounting for the free energy change resulting from condensation into a solid from the gas phase [94], but for the illustrative purposes here, the current form suffices; more nuance will be added later. Indeed, this expression is enough to describe the basic criteria defining VW growth. If γ_f is larger than ($\gamma_s - \gamma_i$), to satisfy equation 2.2, φ must be larger than zero. Thus, the film material will form into clusters rather than lying flat against the substrate. In the complete opposite case, if γ_s is dominant, there is a null contact angle, and the film "wets" the surface, growing layer by layer [26], [94]. This is known as Frank–van der Merwe growth. As imaged in **Figure 2.2**, the degree of wetting can manifest itself in a much wider range than simply 2-D growth or 3-D growth; not all VW growth is equivalent, and for practical purposes, simply decreasing the contact angle is a tangible improvement.

It should be noted that the image of rounded caps shown here isn't quite accurate at small scales; indeed, individual clusters will form as single-crystals with defined facets, which will grow rounder as they grow [19], [30]. However, the truncation of these crystals and their height to width ratios can vary in such a way that the image of the droplets remains representative, as shown by the 'crystal' shapes shown with dashed red lines in **Figure 2.2**. Indeed, the crystal shapes will nonetheless obey surface energy minimization, with low γ facets tending to occupy up a larger surface area. Assuming a smooth substrate that doesn't promote a specific crystal orientation, we could then expect Ag islands to present low-surface energy (111) facets parallel to the substrate surface [96].

Thus, the image of the rounded caps will be kept, regardless of scale, as it allows us to easily represent different film morphologies and identify mechanisms that can be used to control the Volmer-Weber growth mode: an appropriate substrate might have higher surface energy γ_s and/or

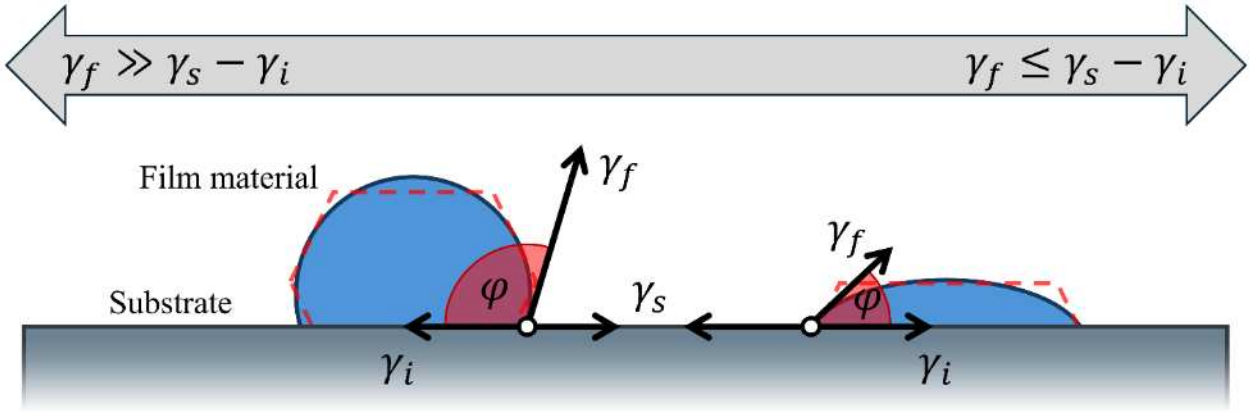


Figure 2.2: Schematic representation of film material forming clusters in the capillary model, following equation 2.2. Different degrees of film wetting resulting from higher or lower degrees of mismatch between γ_f and γ_s - γ_i, are shown. φ, γ_f, γ_s, γ_i are respectively the contact angle and the surface free energies of the deposited film material, the substrate, and their interface. Dashed red lines offer an approximation of the representative shapes of truncated single crystals for each wetting angle.

increase the interface binding energy, reducing γ_i,; this type of approach will be discussed in Section 2.2.4. Similarly, doping can be seen as a tool to decrease γ_f [18], which will be discussed in Section 2.2.5.

However, it is insufficient to only consider the geometry of the Ag clusters (or clusters of any other material growing in VW mode) at thermodynamic equilibrium; the factors determining how these clusters form, grow, and coalesce into a continuous film must also be discussed.

The formation of clusters is largely driven by the supersaturation, $\zeta = p/p_0$, where p and p_0 are the pressure of the deposited material in the vapor phase and its equilibrium pressure, respectively [26], [94]. This can also be expressed as a ratio between the flux of particles and an equivalent equilibrium value [26]; essentially, ζ is a measure of how far out of equilibrium the fluxes of material arriving from the vapor phase and desorbing from the surface are. This changes how thermodynamically advantageous it is for Ag in the vapor phase to condense into a solid, with supersaturation values above unity generating a decrease in free energy per atom condensed [94]. Assuming a constant atomic density, the net change in free energy ΔG associated to the formation of a spherical cluster of film material is then given by the following equation, where r is the radius

of the spherical cluster, k_B is Boltzmann's constant, T_K is the temperature and Ω is the atomic volume [26], [94].

$$\Delta G = 4\pi r^2 \gamma_f - \frac{4\pi r^3}{3}\frac{k_B T_K}{\Omega}\ln\zeta = \Delta G_S + \Delta G_V \qquad 2.3$$

Of course, the formation of a spherical cluster in vacuum is not what interests us, but it provides simplicity while illustrating the point well; if we average the different surface energies in a more complex geometry, we likewise get a positive terms scaling in r^2 associated to the surface, ΔG_S, and a negative term scaling in r^3 associated to the volume ΔG_V [26]. As ΔG must be negative for a process to take place, there is a critical cluster radius, r^*, that much be reached for a cluster to be stable. Note here, that r^* is not defined as the radius at which ΔG becomes negative for increasing cluster size, but at the maximum of ΔG, the point at which further growth of the cluster decreases its total free energy. This can be found by setting the first derivative in respect to r of equation 2.3 to zero, then isolating r, yielding equation 2.4 below.

$$r^* = 2\gamma_f \frac{\Omega}{k_B T_K}\frac{1}{\ln\zeta} \qquad 2.4$$

This shows, as imaged in **Figure 2.3**, that modifications to γ_f or ζ can increase or decrease both the activation barrier for nucleation, ΔG^*, and the critical radius. For a non-spherical cluster forming on a substrate it can still be understood without going into any detailed equations that similar increases or decreases in r^* can be obtained by modifying the overall change in surface energy: thus, as previously discussed, increasing the interfacial binding or substrate surface energy will have an effect similar to decreasing γ_f [26]. Thus, modifying the effective surface energy mismatch of increasing the flux of impinging film atoms (in turn increasing ζ) can decrease the critical radius of film clusters and promote their nucleation.

Now that we understand what controls the equilibrium shape of a cluster forming at the surface of a substrate and whether one will nucleate there, we simply need to piece together how kinetically competing processes and multiple clusters developing side-by-side will evolve throughout deposition. Indeed, if we kept ourselves to a single cluster, it would simply continue scaling up in size without appreciably changing its shape, with kinetics mainly limiting how close to an equilibrium structure that shape would be [97].

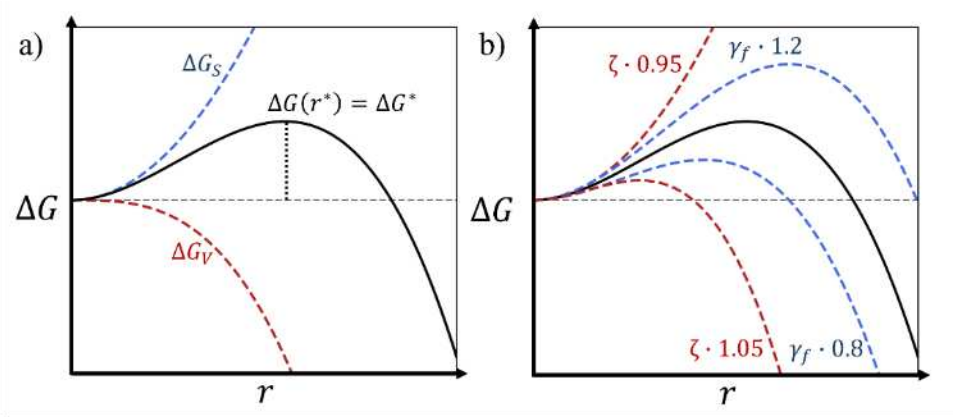


Figure 2.3: Qualitative figure showing the total free energy ΔG of a spherical cluster of radius r, highlighting in **a)** the individual contributions from the surface and volume free energies, ΔG_S and ΔG_V, and the critical cluster radius r^*, and in **b)** the effect of modifying the cluster surface free energy, γ_f, and the supersaturation, ζ on ΔG. Modelled after a combination of [26] and [94].

Categorizing the main competing mechanisms at different qualitative coverage levels allows for a simpler exposition; thus, we can start at the early stages of film growth, at which only a few clusters have formed at the surface. In such a case, the amount of film atoms impinging directly onto existing clusters is negligible, leaving adatoms to diffuse on the substrate surface, following equation 2.5 [19], [98].

$$D = D_0 e^{-(E_D/k_B T_K)} \qquad 2.5$$

Here, D is the diffusivity, in which D_0 is a prefactor that includes (amongst others) the average jump length and the frequency of jump attempts. E_D is the activation barrier for diffusion, which is found to be roughly one-tenth of the adatom binding energy [98]. T_K is the temperature, as previously, but given adatoms will quickly thermalize to the substrate, this can effectively be taken as the substrate temperature.

In the previous discussion, it was established that there was a critical size below which a cluster would not be stable. Thus, there can only be two scenarios in which the adatom remains stable on the surface: one where it encounters other adatoms and nucleates to form a new cluster, and one where it joins an existing one. The competition between these illustrates a general trend of non-equilibrium and equilibrium-seeking processes being in competition. As mentioned previously, increasing the flux of impinging film atoms, and therefore moving further away from equilibrium,

will increase the supersaturation; this will decrease the critical radius size and facilitate cluster nucleation, as can be seen from equation 2.4 and **Figure 2.3**. Alternatively, increasing the substrate temperature will allow particles (or clusters) to diffuse further, enabling them to reach positions that bring them closer to equilibrium, such as joining large existing clusters [19], [98], [99]. A schematic example is shown in the top row of **Figure 2.4**.

This competition self-limits itself to an extent: as the density of clusters increases, the chance of an adatom participating in the growth of existing clusters increases relative to its chance of nucleating a new one, leading to a saturation in the island density N, given by the expression below [19], [100].

$$N_{sat} \propto (F/D)^{\frac{i}{i+2}} \tag{2.6}$$

Here, N_{sat} is the saturated island density, F is the flux of impinging film atoms, and i is the critical cluster size, in number of atoms [19], [100]. While there are more dependencies to N_{sat} [100], and the exponent can change with the dimensionality of growth [101], the current expression is sufficient; indeed, the entire exponent can be replaced with a known ratio, under appropriate conditions [19]. It suffices that this equation illustrates the previous point (increasing F will lead to a higher island density, while increasing T, and thus D, will lead to a lower one), as well as indicating that the critical cluster size, will also affect N_{sat}.

As coverage increases and the island density approaches saturation, the nucleation of new islands becomes much less important, and the coalescence of existing islands takes over [19]. Upon contact, two clusters with equilibrium-defined shapes will begin to coalesce into a singular, larger, island with the same shape [19], [102]. The critical time τ_{coal} in which this happens is given by:

$$\tau_{coal} = r^4 \frac{k_B T_K}{D \gamma_f \Omega^2 \upsilon} \tag{2.7}$$

Where r is the radius of the smaller of the two clusters and υ is the density of diffusing atoms per surface area [102], [103]. Here, D is specifically the self-diffusion of the film atoms on cluster surfaces, i.e. it neglects externally driven diffusion such as electromigration, but as we will almost exclusively consider self-diffusion in this this work, we keep the previous notation.

As shown in **Figure 2.4**, this can again be characterized as a competition between a non-equilibrium (clusters connecting to form flatter, more worm-like structure) and equilibrium-seeking (connected clusters coalescing into a single cluster with equilibrium geometry)

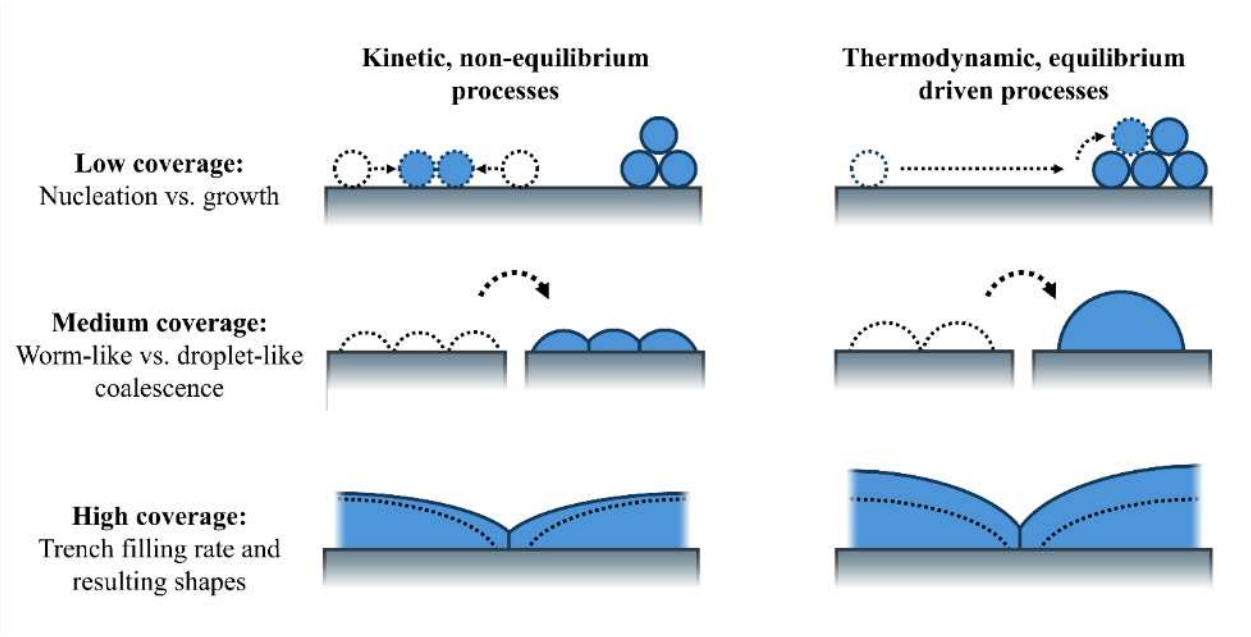


Figure 2.4: Schematic overview of VW film formation processes, broken down in terms of the main competing processes taking place at a given coverage, and categorized under the two main banners of kinetic, non equilibrium processes, and thermodynamic, equilibrium driven processes.

mechanism, which inevitably encounters a limit [19], [102]. Indeed, even if contacting clusters coalesce quickly at first, as the clusters increase in size, τ_{coal} will increase at a quartic rate, increasingly slowing the coalescence. The nominal thickness at which the connection of existing clusters leads to the onset of elongated worm-like islands across the substrate is referred to as the elongation thickness, t_{elong}; for a continuous flux of imping atoms, it has been found to scale as [19], [101], [104]:

$$t_{elong} \approx \left(\frac{1}{F}\frac{D\gamma_f \Omega^2 \upsilon}{k_B T_K}\right)^{1/3} \qquad 2.8$$

Here, the flux plays a similar role as for the saturated density of islands (see equation 2.6), promoting a high density of clusters, which makes them naturally more prone to undergo multiple connections and create a worm-like structure before coalescence into a droplet structure can take place. The second fraction is often simplified by defining it as a new variable, B, such that $t_{elong} \approx (B/F)^{1/3}$ and $\tau_{coal} = r^4/B$ [19], [101], [102], [103], [104], but it can be worth it to investigate the components within. Namely, there is the surface (self-)diffusivity of the cluster material, which

will vary with temperature (see equation 2.5), and above its activation energy, this term will vary much more quickly than the denominator, highlighting the impact not only of the temperature, but of surface diffusion on cluster coalescence into droplet shapes. Surface energy factors in, of course, being the thermodynamic driving force between droplet shapes in the first place. Finally, υ is sometimes described as the planar density of atoms [102]; however it was originally described as the surface density of *diffusing* atoms [103]. This might not be a meaningful distinction; however, it has been found that for equal flux, leading to equal nucleation density, alloyed Ag films show much lower thicknesses for the elongation threshold [105], [106]. There is not a clearly defined reason for this, however diffusion of dopants or surfactants to the outer surfaces of Ag films has been reported [18], [32], [107]; thus, in addition to the reduction of the surface energy [18], [106], control of the atoms available for surface diffusion may play a role. This would be consistent with the observation that immiscible elements have the best performance for this purpose, as they would more readily diffuse to the surface [105].

Taking the next step along the stages of film formation, once cluster elongation has settled in, films will begin to percolate, i.e. to form large-scale conductive networks of interconnected islands without forming a fully continuous film [19], [27], [85]. This is a key point in Ag film deposition, as it enables Ag to conduct across the plane of the coating, and the formation of these paths results in suppression of localized plasmon resonances which otherwise severely degrade optical transmission [27], [85], [108]. The thickness at which this process takes place, t_{perc}, as well as the thickness at which a fully continuous Ag film is formed, t_{cont}, are found to be linearly related to the elongation thickness [19]; thus the main factors appear to mostly be the same as which contribute to elongation.

It is, however, worth noting the behaviors in the presence of trenches formed between worm-like clusters; these have been shown to be surprisingly stable during deposition, and can perdure at quite high thicknesses [30]. Whereas in the early stages of deposition, where nucleation of new clusters was competing with the growth of existing ones, film adatoms were almost guaranteed to impinge on the substrate surface, here the opposite is true – by virtue of their limited area, only a small amount of adatoms will be deposited into the trenches. Unless the flux of incoming atoms is quite high or their diffusivity quite low, these will most likely diffuse to the trench edges and incorporate into larger islands before more deposited atoms incorporate them into a more stable structure [30]. Assuming these trenches are occurring close to coalescence, we can assume the

surrounding islands are well out of equilibrium, creating a thermodynamic pressure for diffusion up to the island centers [30]; an issue that is expected to be compounded by faceted sidewalls, which facilitate upwards diffusion [97]. Thus, γ_f and D remain important factors, consistent with equation 2.8, and the observation that t_{elong} scales with the continuous film formation thickness. Closure of trenches can be partially attributed to a phenomenon known as grain boundary zipping, in which closely separated clusters can elastically deform themselves to reduce the surface energy associated to the exposed trench sidewalls; to reduce the total film energy, the reduction in free energy must outweigh the increase in strain energy induced by the deformation [30], [109].

With this, we have reached a continuous film at last; the microstructure can continue to evolve as the thickness increases, as has been described in various structure-zone models (SZM) [26], [110], but the films that are of interest to this work should rarely get so far beyond continuous film formation that we would need to go over these in detail. It suffices to say that at typical deposition temperatures (room temperature and a few tens of kelvins above), cluster nucleation on existing Ag facets should be limited [97], leading to columnar growth starting from existing grains [26], [110].

Finally, some thought should be given to the crystalline microstructure resulting from these different processes. As discussed earlier, individual clusters will evolve as single-crystals; so when these coalesce into worm-like islands, these will form distinct grains in the resulting structures [19], [30]. Grain boundaries (GB) have their own associated embodied energy, and their formation is associated to film stresses, which carry their own strain energy; as a result, energy minimization constraints will shift and remove grains, and these will evolve throughout deposition [19], [30], [109]. Nevertheless, it's fairly easy to intuit, especially with **Figure 2.4** as a visual aid, that a larger density of clusters increases the odds of worm-like clusters with multiple grain boundaries forming, the presence of more initial grain boundaries will, in spite of surface energy minimization, result in more grain boundaries by the end of deposition, and the dynamics of filling trenches and grain reshaping will affect the film morphology around these grain boundaries. Thus, processes that promote earlier continuous film formation often intrinsically promote smaller grains, and vice-versa [26], [32], [92], [99], [105], [108], [111], [112], [113], [114], [115], [116], [117]. In the following subsections, particular attention will be given to the grain structures resulting from different deposition approaches: their initial structure will have important impacts on how they evolve at high temperatures, given the energy to seek out equilibrium structures.

2.2.2 Controlled deposition kinetics

At this point, it goes without saying that controlling the kinetics of deposition offers ways to control film growth. In fact, after the previous discussion, two controllable parameters should stand out readily: the flux of incident film-forming atoms and the diffusivity.

Increasing the deposition rate, i.e. F, straightforwardly decreases t_{perc} and t_{cont} as this promotes cluster nucleation and elongation [85], [99]. The atomic force microscopy (AFM) measurements on Ag and Cu films presented by Jamnig *et al*., as well as the grazing incidence small-angle X-ray scattering (GISAXS) measurements on Au films by Schwartzkopf *et al*., indeed show that this results in smoother film surfaces, although at the cost of forming smaller grains and/or clusters, which will reduce film conductivity [31], [99], [111]. Pulsed deposition can allow additional control via the deposition rate; low frequency pulses appear to result in more regular grains in Elofsson *et al*.'s AFM images, but t_{cont} is delayed and the grains are not appreciably larger [104]. As a result, deposition rates should be increased enough to obtain a continuous film at the thicknesses of interest, but no more.

Increasing the diffusivity can be achieved in different ways. In the simplest case, one can increase the substrate temperature: adatoms will become thermalized shortly after deposition, resulting in all the opposite behaviors that were described for increasing deposition rates; higher roughness, higher t_{cont}, larger grains. Indeed, this is what is observed [85], [99], [112]. While some interesting features are obtained, such as highly regular clusters in the early stages of deposition, or large, flat topped grains, these are only observed at temperatures well beyond those for which a continuous film can be obtained at a reasonable thickness (e.g. for Ag films deposited on substrates heated to 600 °C, which remain discontinuous at thicknesses exceeding 100 nm) [112]; ways to leverage these features will be addressed in the following subsection. In principle, active cooling of the substrate can yield interesting results in *decreasing* the substrate diffusivity [97], [118], but as similar changes could be obtained by increasing F relative to the diffusivity instead, this isn't sufficient to justify trying to implement it into a production setting.

Additional control of the diffusivity can be achieved by controlling the energy of the deposited particles; whereas the previous discussion only considered thermally activated diffusion, other techniques can be used to increase adatom mobility, including, but not limited to, ion beam

assistance [113], [118], [119], [120], substrate biasing [85], [121], and energetic deposition techniques such as high-power impulse magnetron sputtering (HiPIMS) [85], [121].

Supplying additional energy to adatoms via ionic means distinguishes itself from thermal processes in a few major ways. First, the magnitude of the involved energies is radically different: average thermal energies ($\approx k_B T$) will remain below 0.1 eV even at temperatures surpassing 500 K. On the other hand, ions can easily be accelerated to energies between a few eV and a few hundred eV, allowing to easily provoke diffusion and even penetrate the bulk of the underlying films [26], [110]. Second, this energy is temporary: as discussed earlier, adatoms will quickly thermalize to the substrate temperature, and thus additional energy imparted to adatoms will dissipate just as quickly. This can enable temporarily increased diffusivity, which does not result in long-term film reorganization [118]. Finally, this energy can be imparted to adatoms in different doses and at different stages of the film formation process: incident film atoms will benefit from higher initial diffusivity but quickly be thermalized, while irradiation of the substrate with an external ion beam can impart mobility to atoms that are already arranged in stable clusters and prompt their reorganization [118], [119]. This can be further tuned by changing the flux of ions relative to the flux of film atoms, as well as their angle of incidence, mass, and energy [26], [122].

Increasing the incident energy of film-forming atoms, which can be achieved via accelerating charged species or reducing operating pressures to increase the mean-free-path and decrease collisions [85], [110], [123], has been shown to reduce t_{cont} by promoting cluster nucleation and facilitating elongation [85], [121].

Control of film properties by irradiation with external ions has more parameters, which results both in higher complexity, but also the potential for more control. High energy incident ions (in the order of 100 eV) can cause film densification and implantation of the ion species, as well as generate compressive stress and coating defects; but this is not a monotonous trend, as local heating caused by the thermalization of high energy ions can induce localized annealing [26], [110], [113], [123]. Using lower energy ions (in the order of 20 eV) at higher fluxes (keeping a constant product of energy per ion and flux) has been shown to alleviate many of these issues, enabling higher density, control of the preferential grain orientation and more [26], [123]. Interconnectedness of these parameters (e.g. increased pressure decreases incident energies, but also changes the range of incident angles [123], different sputtering gases can lead to kinetic changes, but also changes in

gas incorporation [124]), as well as their interactions with other parameters (e.g. biasing during magnetron sputtering causes different effects on different substrates [121]) make it non-trivial to select optimal conditions for a given process. Thus, despite following relatively simple physical models, the kinetic parameters available to control film coalescence can lead to quite some complexity.

2.2.3 Multi-step approaches

The processes described in the previous subsection have been overarchingly uniform; fixed deposition rates, powers, temperatures – even pulsed depositions typically use fixed frequencies. Additional methods exist, however, in which characteristically different behaviors can be leveraged subsequently to obtain new results.

Although it concerns much thicker films, and is performed on substrates allowing epitaxial growth of Ag, the work of Rodionov *et al*. offers an excellent demonstration of this concept [17]. Previously, it was described that at high deposition temperatures, large, single-crystal Ag islands with smooth, flat tops could be obtained [112]. However, the deposition conditions that yield these features do not allow formation of a continuous film at reasonable thicknesses. The answer to this problem is to separate the deposition process into two steps: one in which these desirable features are obtained, and one in which the film is made continuous. Evaporation onto a high temperature substrate (350 °C) provides the first half, following which the substrate is cooled to room temperature and deposition resumes at a much lower rate. As highlighted by Lü *et al*., one of the key energetic barriers in Ag deposition is at the transition between Ag facets, at which there is significantly lower coordination [97]. Adatoms diffusing from the substrate towards Ag sidewalls also face an energetic barrier at its edge, where they have significantly higher coordination. This is shown schematically in **Figure 2.5**: at the sites (iii) and (v) an adatom respectively has more or less direct neighbors, creating important activation barriers for diffusion. Thus, adjusting the temperature to provide sufficient energy to bypass the low-coordination barrier at the island tops, but not enough to bypass the high-coordination barrier at their base allows to promote diffusion selectively to the sidewalls [17]; in the example of **Figure 2.5**, the temperature must be such that $E_2 < k_B T < E_1$. Note that this relies on the substrate properties to obtain a large enough barrier at the substrate-sidewall barrier; for instance, it fails on quartz substrates, a typical weakly-interacting

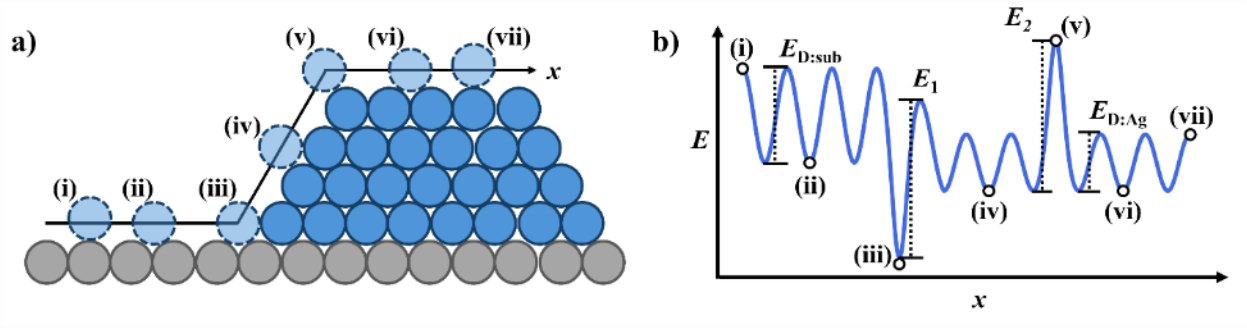


Figure 2.5: a) Schematic representation of an Ag adatom diffusing across a substrate and onto a Ag cluster, following a path x, with key locations shown by dotted outlined and numbers (i) through (vii). **b)** Qualitative graph of the adatom energy along the path x. The sites (i)-(vii) are marked with black circles. The diffusion activation barrier for diffusion on the substrate and on the Ag cluster (considered identical for both facets) are respectively denoted as $E_{D:sub}$ and $E_{D:Ag}$. The energy barriers encountered by an Ag adatom arriving to the cluster facet from the substrate and from the top of the facet are respectively denoted as E_1 and E_2. Modelled after [97].

substrate for Ag, consistent with other results [17], [97]. Coupled with the decreased deposition rate, which inhibits nucleation, this leads to something akin to a coalescence-free growth regime with atomistic island growth [101]. Following annealing to relax the intrinsic stresses developed during the high temperature deposition and cooling, the grains align themselves, and a singe-crystalline film is achieved, at much lower thicknesses than other epitaxial Ag depositions [17], [125].

While this technique is unsuitable for the applications of interest in this work (requiring specific substrates, requiring extended heating and cooling periods, producing optically thick Ag films), it highlights how previously explicited concepts can be combined in novel ways to break from their individual limitations. Moreover, it gives an example of how film microstructures can be tailored in different ways, at the expense of other metrics, such as t_{cont}.

Another way of segmenting Ag film fabrication into distinct steps, which could allow decoupling critical film formation thicknesses from the microstructure, is post-deposition ion etching. Indeed, once Ag clusters have begun to coalesce, their re-separation entails an increase in surface energy, as their GBs have much lower surface energy than exposed Ag surfaces [96], [126]. The result is that continuous films are metastable, and thus retain continuous morphologies at lower thicknesses than are achieved during deposition, when subsequently etched [82], [83], [127], [128]. Moreover,

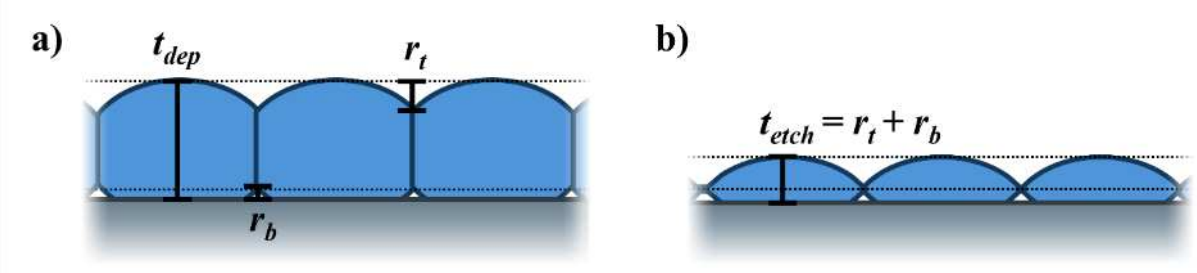


Figure 2.6: Schematic representation of the model proposed by Netterfield and Martin, describing the minimum thicknesses achievable via post-deposition etching. **a)** As-coated Ag film with roughnesses r_t and r_b at its top and bottom interfaces. **b)** Etched Ag film, with a minimum continuous thickness equal to the sum of the film roughnesses. Reproduced based on [127].

even once these films breakdown, the resulting island structures are qualitatively different than discontinuous films of the same equivalent thickness achieved by direct deposition [82], [128].

In principle, this could allow to deposit Ag films in such a manner to optimize the microstructure; the thickness at which it would be achieved would be irrelevant, if it could subsequently be etched to a desired value. However, the functional limitations of this method are unclear. While they produce extremely thin continuous Ag layer, Ma *et al*. leverage films with extremely fine grains to do so; thus, it offers an advantage in obtaining very thin films, but not necessarily in obtaining thin films with large grains [82]. Moreover, they attribute the stability of their films during etching to its partial implantation in the dielectric substrate layer. This seems highly unlikely, as the energy-dispersive X-ray spectroscopy (EDS) measurements they use to justify this hypothesis shows minimal overlap between Ag and the substrate material, which could be entirely attributable to electron beam broadening [129]; to make matters worse, they do not include the signal from the caping layer deposited above Ag, which could have provided a point of reference [82]. In addition to all this, other works report similar critical thicknesses via etching, despite using deposition techniques that could not reasonably cause implantation [83]. Thus, the simple model proposed by Netterfield and Martin in 1986, shown in **Figure 2.6**, appears to be the most consistent with the results of other works: this model straightforwardly supposes that the continuous film thickness obtainable during etching is limited by the total interfacial roughness, as this creates locally thinner areas in the coating which form holes at low enough thickness [127].

2.2.4 Seed layers and metallic seeding

So far, we have discussed approaches to obtain thin continuous Ag films that use clever kinetics or thermodynamic tricks but have only briefly touched upon the most fundamental approach: i.e., using substrates that alleviate the surface energy mismatch which causes the Volmer-Weber growth mode in the first place, commonly referred to as seed layers.

Equation 2.2, visually represented in **Figure 2.2**, allows to easily intuit two main properties with which we could base a selection of suitable substrates: a high surface energy, γ_s, and strong binding to Ag (meaning a highly negative γ_i). In addition to this, a crystal structure that is commensurate with that of Ag will promote the formation of well-ordered Ag crystals and reduce strain [43], [130]. Naturally, for the purpose of fabricating durable transparent conductors, this layer must also have appropriate mechanical and optical properties.

Despite the poor adhesion of Ag to most oxides, this nonetheless leaves a host of available materials, including ZnO (and doped variations thereof), titanium oxide (TiO_2), tin oxide (SnO_2), zirconium oxide (ZrO_2), ITO, and many more [27], [39], [43], [45]. Indeed, there are too many potential materials to discuss them all. Moreover, the functionality of a given material is dependant on its stoichiometry [43], [131], [132], composition [27], [132], and structure [43], [130], [133], making experimental comparison between materials tricky at best; differences in the optimization of the deposition conditions can easily be interpreted as differences in the material quality.

As a result, computational comparison can be quite advantageous. Cornil *et al*. compare the work of separation for various oxides, with different structures and Ag arrangements; while they also evaluate the commensurability of the different structures with Ag (111), they use supercell structures to alleviate important size mismatches between the unit cell sizes of Ag and of the different dielectric materials studied, in order to better focus on work of separation [43]. Thus, the strain induced by the lattice mismatch will depend on the chosen supercells, which does not guarantee that these will be representative of experimentally obtained structures.

They find that (001)-oriented ZnO – the common surface orientation for sputtered films of this material [134] – displays strong adhesion for multiple Ag configurations and relatively strong adhesion even in other orientations [43]. Its mismatch strain is dependant on the Ag configuration relative to ZnO, as reported elsewhere [43], [130]. Despite having a relatively high mismatch, low strain in Ag islands is found experimentally for Ag on (001)-oriented ZnO, which is attributed to

the formation of superstructures larger than those simulated by Cornil *et al*. [43], [130]. TiO_2 is found to have excellent lattice matching to Ag, but very poor adhesion which can be greatly improved by decreasing the surface oxidation [43], consistent with its frequent deposition as a sub-stoichiometric layer [82], [135], [136]. SnO_2 shows weak dependence of its work of separation on crystalline orientation; both of those evaluated, as well as those of TiO_2, are well below those of (001)-oriented ZnO [43]. It shows meaningful mismatch strain, but this is a bit of a moot point; SnO_2 films are frequently amorphous in their as-coated state, even at high thicknesses [137]. Finally, while ZrO_2 can show excellent adhesion given proper (100) orientation, its (111) orientation shows extremely weak adhesion [43].

While ITO layers are frequently employed to enable electrical contact with the metal layer without leaving it exposed [69], [138], [139], doped or sub-stoichiometric ZnO can also fulfill this role [140], [141]; moreover, in the context of low-E coatings, this is not a requirement. Thus, it should come as no surprise that (doped) ZnO is commonly chosen as a seed layer in a wide range of applications [6], [23], [25], [27], [41], [142], including this work. Accordingly, methods to improve seed layer performance will largely be discussed in the context of ZnO, although these could ostensibly be used to improve other layers.

Structural improvements can be made, in turn, by using appropriate growth templates for ZnO; deposition of thin ZnO layers on sapphire substrates, which are an epitaxial growth substrate for Ag, has been shown to enable nearly GB free Ag films despite said ZnO layers being highly polycrystalline [143]. Thus, it can be assumed that the ZnO lattice is deformed, and its grain boundaries defined, by its mismatch with the sapphire substrate, improving its commensurability with Ag. Additionally, it is proposed that this alleviates strain that would otherwise be accumulated during Ag heteroepitaxy directly on sapphire [143]. While using epitaxial substrates in the context of window coatings could not be realistically implemented, similar results can be achieved by depositing ZnO on a surface which nevertheless promotes the growth of a structure more commensurate with Ag; namely, the high commensurability of TiO_2 and Ag, discussed earlier, can be leveraged to this end [144], [145]. While this is not commonly seen in academic research, as simple designs minimizing the number of materials are often used [45], more technologically mature designs will typically integrate interlayers between the bottom barrier layers and the seed layer [142].

Modifying the composition of the seed layers offers another interesting route; as this will change the adhesion between Ag and the substrate [43], [132], and as the energy barrier for adatom diffusion is proportional to it [98], this can decrease Ag diffusion in addition to modifying the shape of equilibrium structures. Simulations of Ag-ZrO_2 interfaces found that modifying the stoichiometry of the ZrO_2 surface resulted in improved adhesion regardless of whether Zr or O_2 vacancies are introduced; in fact, as long as they are not in a stoichiometric ratio, a combination of both types results in improved adhesion [132]. This is consistent with other works, which show (apparent) contradictions: Lee *et al*. report *worse* Ag wetting when ZnO is exposed to an oxygen plasma [131], whereas Li *et al*. achieve *improved* Ag wetting by treating their ZnO seed layer with an oxygen plasma treatment[146]. In simulation, work of separation does not increase monotonously with increasing concentration of oxygen vacancies [132], and ostensibly the same could be true for metal vacancies. Thus, excessive oxygen treatment may be at cause. This is not to say that they are equivalent: simulation results show that metal vacancies increase the adhesion more strongly than oxygen vacancies. Analogously, substitutional metal dopants of both p- and n-type improve adhesion as well, with p-type dopants yielding the higher adhesion increase of the two [132]. For instance, aluminum doping is found to mildly reduce the $ZnO_{(Al)}$ lattice parameters, consistent with its smaller atomic radius, although not enough to appreciably reduce its mismatch with Ag; moreover, elevated dopant concentrations are found to result in rougher, less crystalline films [147]. As a result, increase of the binding energy level is probably best controlled by manipulating the film stoichiometry rather than its level of doping.

Finally, seed layers may be improved with further surface functionalization. Self-assembled monolayers (SAM) with strong adhesion to metals and their respective substrates have been shown to significantly improve wetting [27], [148], [149], [150]; as described earlier, increased adhesion has the dual benefit of suppressing diffusion in addition to promoting flatter equilibrium structures [26], [94], [98]. While these have been shown to offer benefit when self-assembled on glass, SiN, and ZnO substrates in separate studies, direct comparison of Ag deposited on self-assembled monolayerss with and without an underlying ZnO layer is not reported [148], [150]. Thus, it is not clear whether these can benefit from a templating effect of the crystalline structure of the underlying layer, as discussed previously. However, best results are reported for films applied via solution-based approaches rather than vapor-based ones, hindering industrial scale implementation [148], [150].

Metallic seeding offers a far simpler implementation; in this case, metallic films with nominal thicknesses of a few monolayers are deposited on the substrate prior to Ag deposition, which is straightforwardly implementable at larger scale [27], [114], [151]. To function appropriately, however, they must be deposited with appropriate control of the nominal thickness, as their benefit is both highly dependant on said thickness and does not scale with it monotonously [114], [151]. For example, Fukuda *et al*. find that metallic Ni seeding on $ZnO_{(Al)}$ will promote coalescence for a nominal thickness of 0.2 nm, but significantly hinder it for 0.5 nm [151]. In addition to the sensitivity to the nominal thickness of the metallic seed, important wetting improvements present commensurate decreases in the grain size [114], [115], [116], [117]. Finally, addition of metals with undesirable optical properties will decrease overall performance, similarly to doping, thus limiting the relevant candidates [105]; notably, Al and Au have been used to minimize such losses [27].

2.2.5 Dopants and surfactants

Modifying Ag film growth via the addition of metallic dopants presents significant overlap with the usage of metallic seeds; in the case of doping, the additional metal is simply deposited during Ag deposition rather than prior to it. That being said, studies that present the effect of varying the dopant concentration on film coalescence suggest that this process is less sensitive to the dopant concentration than metal seeds are to the nominal thickness. Indeed, once a certain concentration threshold is met, film coalescence appears to remains stable, with negative impact on coalescence only taking place at high concentrations [48], [88], [152].

Beyond this, however, many of the issues remain the same, with evidenced decreases in grain size [32], [48], [92], [105], as well as decreased optical and electrical properties [48], [50], [89], [90]. While Ewald *et al*. claim that films alloyed with Au present extended lateral grains, they support this on the basis of smooth areas being observed in very large AFM images; it seems more likely that these are in fact areas with very fine grains, consistent with the rest of the literature [91].

Two methods may alleviate the performance burdens placed by film dopants, however. The first is to use selective deployment of the dopants, i.e. only doping during the first steps of Ag deposition [48], [105], [108]. This approach yields significant improvements, wherein similar decreases of t_{cont} are obtained as during continuous doping, but film resistivity changes are decreased; in the

best cases, continuous film resistivity is even lower than that of pure Ag within certain thickness windows [105]. This can be attributed to changes in grain boundary reorganization speed [48], leading to earlier t_{elong}, which in turn is expected to determine later stages of film coalescence [19]. This is not to say that early growth stages are all-defining: beginning deposition with pure Ag and adding dopants later on still shows an effect on coalescence, albeit a less good one, and in some cases it delays coalescence significantly [48], [105]. Moreover, these all show higher resistivity than pure Ag films, highlighting that dopants must be used in a focused way to control growth, and otherwise avoided to achieve optimal optical and electrical performance [105].

The other method is to use a dopant that does not permanently modify the Ag chemistry, i.e. an immiscible material which does not remain in the Ag film following deposition; this may also be referred to as a surfactant. While metallic dopants with lower miscibility (Cu, Cr, Mo) may show better performance as dopants, these nonetheless remain in the film following deposition [105]. Alternatively, gaseous dopants could be used, then pumped out following deposition. Oxygen has shown strong potential in altering Ag growth; however as it can form an oxide with Ag, it is expected to remain in the film [84], [93], [106]. Nitrogen (N)-doped Ag ($Ag_{(N)}$) has been shown to enable such an effect however, strongly altering Ag coalescence with minimal residual N_2 detected in the resulting films [18], [23], [93], [108], [153]. In computational experiments, N is found to only remain stable when in the first nanometer of depth into Ag; thus, as deposition continues and the N becomes buried within the layer, it becomes unstable, leading it to "float out" and leaving pure Ag in the bulk of the film. The same simulations show that, increasing N surface concentration reduces the surface energy of Ag's different facets at different rates, which leads to (100) becoming the preferred Ag orientation at high N concentrations [18]. Together, these results explain much of the behavior observed for $Ag_{(N)}$ coatings. Deposition of $Ag_{(N)}$ with a constant N_2 addition will lead to increasing N concentration at the Ag surface, as N floats out to the surface from previous deposition in addition to impinging from the sputtering gas, promoting (100) surface orientation [18], [23]. This also explains the observation that the nitrogen concentration is highest at film interfaces, with other residual N likely being trapped at grain boundaries [18], [23], [108]. Resistivity of $Ag_{(N)}$ films deposited on silica (SiO_2) is significantly higher than pure Ag, although selective N_2 deployment during the start of deposition alleviates this effect while preserving improvements in continuous film formation, and vice versa, just as for metallic dopants [108]. As the amount of residual N_2 is so low, this appears to be almost entirely attributable to smaller grain

sizes observed for $Ag_{(N)}$ [108]. Although selective deployment is not as evident for a gaseous dopant due to pumping speed limitations [105], crystallographic measurements suggest that deposition of $Ag_{(N)}$ on ZnO may offer an alternative route to influencing their crystal structure [23].

It should be noted that the exact mechanisms taking place during improvement of Ag coalescence via doping remain unclear. Changes in surface energy as a function of the dopant concentration have similarly been found for Ag films with non-immiscible dopants [106], suggesting similar mechanisms as for N_2. While this is coherent with the observation that immiscible metal dopants also perform very well in reducing t_{cont} [105], the float out behavior found for N, and the resulting increase of surface concentration during deposition, does not explain how late introduction of dopants causes such negative effect in the electrical properties, worse than that of continuous deposition [105], [108]. Rather, this seems due to dopants changing how hole and trench filling proceeds during the later stages of continuous film formation, as suggested by Jamnig *et al.* [105]. Although there may be multiple competing interpretations, as previously, the measurable outcomes remain the same.

While the film microstructure will continue to change beyond continuous film formation, this concludes the overview of qualitative morphological changes specific to film deposition. How film morphologies will evolve beyond this point, especially at high temperatures, with ample energy available to reorganize, becomes a key factor for coating durability and this discussion will thus continue in the context of film stability.

2.3 Mechanisms of Ag film instability and their mitigation

The methods with which one can control the deposition dynamics and resulting microstructures of thing Ag films have been well-explicited; we can now proceed to the mechanisms by which this structure evolves, when exposed to high temperatures and or chemical contaminants. It bears repeating that these processes may very well occur during deposition as well, if sufficient energy is available, and thus they contribute not only to the evolution of the film during tempering, but also to the evolution of the microstructure throughout deposition.

While the changes taking place in a Ag film during annealing follow the familiar concept of seeking a thermodynamically advantageous state, the plethora of ways a film may reorganize to do this means we must still contend with different competing mechanisms. Thus, these will be categorized based on the main participant actors, and this section will be separated accordingly, discussing the mechanisms at play and the means of controlling them.

In Section 2.3.1 we will begin with changes intrinsic to the Ag layer, wherein thermal energy supplied to the Ag film allows it to reorganize into structures closer to equilibrium without significantly interacting with any other materials. Section 2.3.2 will present means to manage these changes. Following this, in Section 2.3.3, diffusion processes involving other film layers and external contaminants, will be discussed, and then Section 2.3.4 will once again address their mitigation. Throughout each section, an attempt will be made to discuss changes that do not explicitly involve the Ag layer, but which are relevant to the overall stability of low-E coatings.

2.3.1 Intrinsic Ag changes

As stated, we begin by studying the mechanisms that cause Ag microstructural changes by considering changes that are intrinsic to Ag. As discussed, these are changes which are the logical conclusion of the Ag film not having a structure that minimizes its free energy, and, at high temperatures, being given the energy to move towards one. Thus, we can start by considering the total energy embodied in a Ag film, E_T, given by equation 2.9 below:

$$E_T = \overbrace{a_f\gamma_f}^{E_t} + \overbrace{a_s\gamma_s + a_i\gamma_i}^{E_b} + \overbrace{a_{GB}\gamma_{GB}}^{E_{GB}} + E_\varepsilon \qquad 2.9$$

Where E_t, E_b, E_{GB} and E_ε are respectively the surface energy of the top and bottom film interfaces, the grain boundary energy, and the strain energy [30]. Here, each component represents the sum of the contributions of each grain, with different sizes, number of facets, orientations and surface energies, which would be arduous to consider for a realistic film morphology. Additionally, we consider that the surface energies (γ_f, γ_s, γ_i, γ_{GB}, respectively those of the film, substrate, interface, and GBs) are orientation independent averages, such that we only need to consider the total area associated with each (a_f, a_s, a_i and a_{GB}, respectively). For a continuous film, a_s will be zero until a hole in the Ag film causes the substrate to become exposed. Moreover, we will not investigate E_ε in detail; it suffices that we keep in mind that processes that reduce strain energy will be promoted.

It is worth noting that a continuous film is a highly metastable structure; that is, without embodying the global minimum of free energy, a continuous film without defects, anisotropic effects or stress will not dewet, even at high temperatures, unless a perturbation of the scale of the thickness (i.e. a sufficiently large hole) is generated within it [154]. Section 2.2.1 has already given us an intuitive grasp of why it is thermodynamically profitable for films to dewet; therefore, we can begin by discussing processes which can generate such perturbations.

Considering a continuous film with perfectly flat surfaces and uniform surfaces energies, a reduction of E_{GB} is categorically required to decrease the total film energy while maintaining a continuous film morphology. To achieve this, we must reduce the area associated to grain boundaries, a_{GB}, which is the product of the film thickness, t, and the total length of grain boundaries in the plane of the coating.

The latter can be straightforwardly decreased by transitioning to a structure with larger average grains, i.e. grain growth [155]. Similar processes will seek to remove other internal surfaces, such a small voids or pinholes, which also increase the total free energy, not unlike grain boundary "zipping" [30], [109]. That being said, there may be competing energetic incentives to close or expand such defects, particularly in the case of pinholes [154], [156].

Grain growth will occur via the consumption of small grains by larger ones, as they represent a larger expenditure of surface energy per volume, analogously to the discussion of cluster nucleation in Section 2.2.1. This primary mode of grain growth will stagnate once grains have columnar structures which extend to the Ag film interfaces, and lateral sizes a few times that of the film thickness [155].

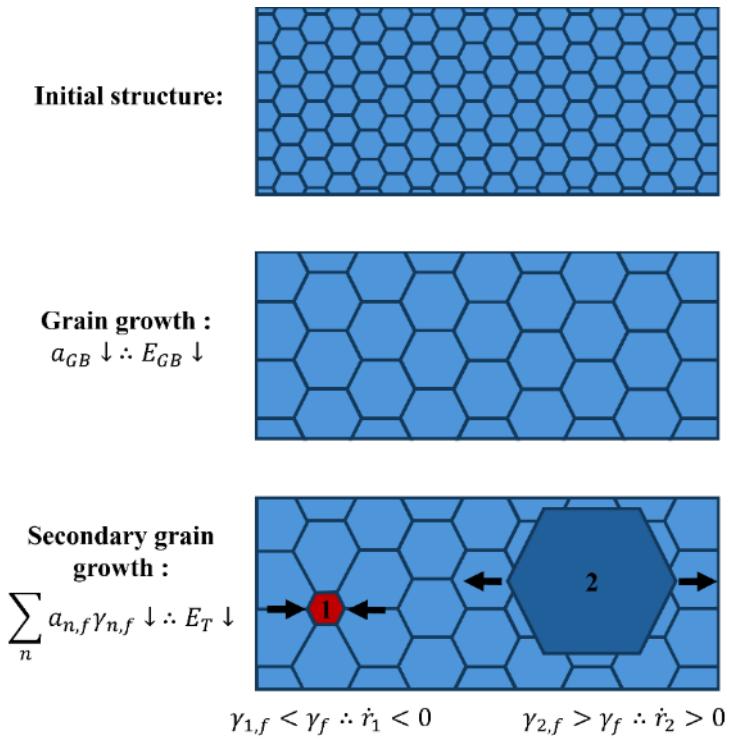


Figure 2.7: Schematic representation of the change in grain size for a Ag film during grain growth and secondary grain growth with top-down view.

Occurring beyond this point, secondary grain growth, also known as abnormal grain growth, will be prevalent; in this case, grains with energetically advantageous surface orientations will grow by consuming those with higher associated energy. This is shown schematically in **Figure 2.7**: grain "1" with higher surface energy than average, will shrink, whereas grain "2", with lower surface energy than average, will grow. This mode of grain growth is particularly important for this work: as-deposited Ag microstructures will often already meet the criteria for secondary grain growth, such as the Ag films deposited in Ar by Jamnig *et al.*, which show wide columnar grains extending through the full thickness of the coating and with a lateral size much larger than the thickness [108]. Even when films do not display such a structure as-coated, at high temperatures they are expected to rapidly reach this point [155]. The average growth rate of a given grain with in-plane radius r_n and orientation-dependent film and interface surface energies $\gamma_{f,n}$ and $\gamma_{i,n}$, is given by equation 2.10 below.

$$\dot{r_n} = M_{GB}\left(\frac{1}{t}\left(\left(\gamma_f - \gamma_{f,n}\right) + \left(\gamma_i - \gamma_{i,n}\right)\right) + \gamma_{GB}\left(\frac{1}{r} - \frac{1}{r_n}\right)\right) \quad 2.10$$

Where M_{GB} is the grain mobility, which is structured in the same way as the diffusivity in equation 2.5, r is the average grain radius, and γ_f, γ_i and γ_{GB} are the orientation-independent average energies used previously [155]. This equation is written such as to consider an un-encapsulated film, but it is a trivial substitution to replace the surface energy of the film with that of an upper Ag-encapsulating film interface.

While this appears benign at first glance, it will take its full importance in the context of other mechanisms. Indeed, if grain growth minimizes the in-plane density of GBs, reducing their out-of-plane size, i.e. the film thickness, may also decrease the total film energy.

More specifically, assuming a columnar film with grain boundaries that intersect the interfaces, locally thinning the film at said intersections will reduce a_{GB}; this is known as grain boundary grooving [26], [35], [154]. In order to maintain grain volume while accommodating a decrease in thickness at the grain boundary, hemispherical caps must form at the grain surfaces. In turn, these caps increase the film area and its associated surface energy; the resulting groove is in fact an equilibrium shape, which results from the balance between the film and grain surface energies, reducing the total energy. This is shown schematically in **Figure 2.8**, and detailed in equation 2.11 below [154].

$$\frac{\Delta t_{GB}}{r} = \left(\frac{2 - 3\cos\theta + \cos^3\theta}{3\sin^3\theta}\right) \approx 0.13\frac{\gamma_{GB}}{\gamma_f}, \text{ where } \sin\theta = \frac{\gamma_{GB}}{2\gamma_f} \quad 2.11$$

Here, Δt_{GB} is the difference between the thickness at the grooved boundary and the average film thickness, r is the radius of the film grains (for simplicity we assume a uniform average size), and θ is the angle of the grain surface at its intersection with the GB, relative to a flat film of average thickness t. Based on the surface and GB energy values of Ag reported by Tran, Zheng, and their collaborators [96], [126], we can assume the ratio between γ_{GB} and γ_f to be somewhere between 0.1 and 1. Plotting the term in parentheses of equation 2.11 as a function of this ratio, as shown in the inset of **Figure 2.8**, we find a roughly linear relationship. This allows for the approximated form of equation 2.11, in which Δt_{GB} can be found to increase linearly with the grain size as well as with the ratio of GB and surface energies.

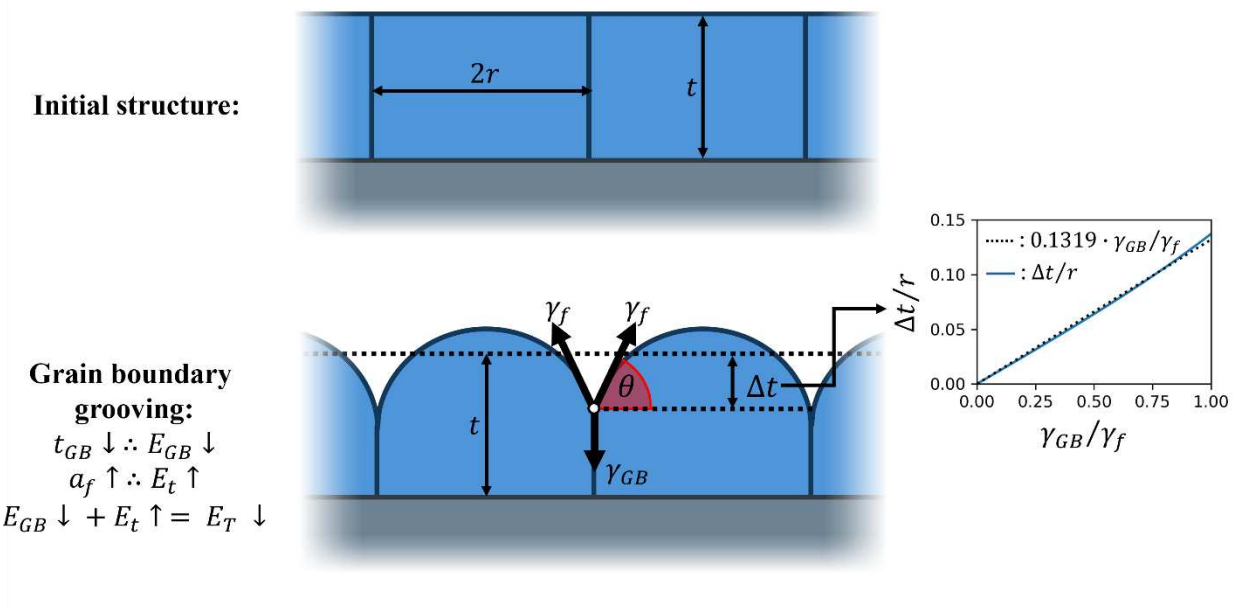


Figure 2.8: Schematic representation of the change in surface geometry for a Ag film during grain boundary (GB) grooving; the change in GB thickness relative to the grain radius is shown for the analytical and approximated formats given in equation 2.11. Modeled after [154].

The key point of this equation is that for a given ratio of GB and film surface energies, there exists a grain radius r for which Δt_{GB} will exceed t, leading to hole formation. For example, assuming a GB in a 10-nm-thick Ag film with $\gamma_{GB} = 0.71$ J/m^2 and $\gamma_f = 0.76$ J/m^2 [96], [126], GB grooving will generate a hole for $r \approx 82$ nm. This demonstrates the potential impact of secondary grain growth, in particular; whereas primary grain growth will typically stagnate for grains with lateral dimensions a few time larger than the thickness, secondary grain growth can lead to such larger radii [155].

It should be noted, however, that not all holes formed will lead to dewetting. Indeed, Srolovitz and Safran find that for a film with given t and γ_f, considering holes spaced $2r$ apart (equivalent to holes separated by grains of radius r), the change in energy associated to the formation of a hole of radius r_h will vary only as a function of r_h/r and the composite parameter β, shown below [154].

$$\beta = \left(\frac{r}{t}\right)^2 \left(1 + \frac{\gamma_i - \gamma_s}{\gamma_f}\right) \qquad 2.12$$

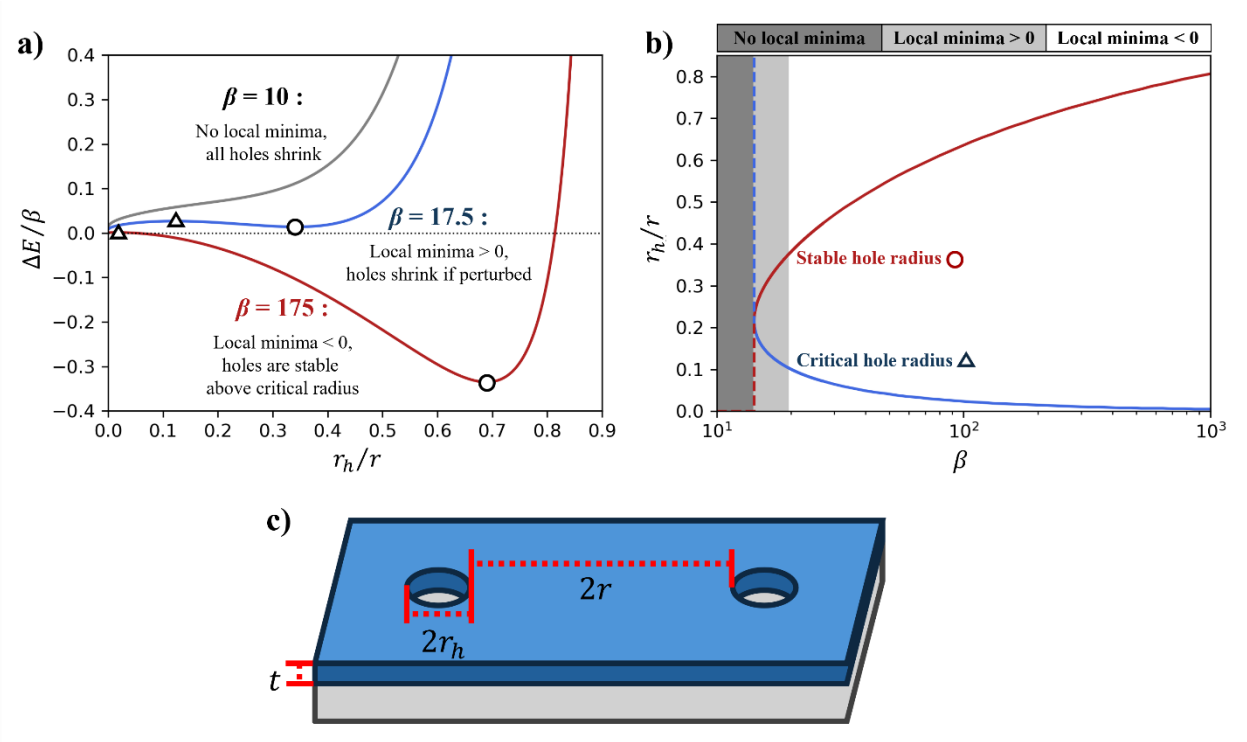


Figure 2.9: a) Change in energy resulting from the inclusion of holes of radius r_h in grains of radius r, for different values of the hole stability parameter β; local minima (circle markers) correspond to stable hole sizes that minimize total energy and local maxima (triangle markers) to critical hole sizes, below which holes will shrink. **b)** Stable radius towards which holes will converge, if their radius surpasses the associated critical hole radius, both as a function of β. Values for which all holes are unstable, or in which holes are merely metastable are indicated via shading. **c)** Schematic showing the main geometric parameters. Modeled after [154] and the discussion therein.

We can see that β varies with the ratio of the grain size and thickness, similar to the criteria for hole formation at grooves. In the second parenthesis, the energetic cost of exposing the substrate is balanced by removing interface and film area. **Figure 2.9a** shows the change in energy for different values of β with each result showing qualitatively distinct behaviors. At very low β (smaller than ≈14.5), no holes are stable, and they will shrink spontaneously. At intermediate β values (between ≈14.5 and ≈19.5), holes above a critical size will drift to a (meta)stable size but will shrink if displaced from the local minima of energy. Finally, for high values of β, holes larger than the critical size will be fully stable [154]. **Figure 2.9b** shows how the critical and stable hole radii evolve as a function of β.

A caveat to both expressions is that they only consider unencapsulated films. For the case of grooving, an expression considering both the exposed film and its substrate interface has been proposed, albeit it isn't particularly helpful: rather than accounting for the substrate becoming exposed, it assumes that the substrate deforms such as to maintain contact with the grooved film, leading to a similar behavior as for an exposed surface, but with some γ_i replacing γ_f [157]. In practice, with a rigid substrate, one would need to consider the energetic cost of creating new exposed substrate and film surfaces, akin to the criteria for hole formation. For hole formation, we would need to consider the change in energy associated to reducing the top interface area and exposing the surface of the encapsulating layer, rather than simply decreasing the exposed film area. In fact, the formation of the hole's sidewalls will increase the film area, albeit it ought to scale roughly linearly with the hole radius, rather than quadratically.

Finally, it should be noted that while equation 2.12 and **Figure 2.9** give insight into how certain parameters affect the size threshold holes must overcome to generate a dewetting front, and how energetically favorable hole expansion will be, they do not describe the qualitative morphology of dewetting. Depending on the context, this may lead to the formation of a high density of small islands, or large dewetting fronts with highly irregular patterns [35]. We won't dwell on this, as in the context of this work we are mainly seeking to prevent dewetting. For those desiring a more complete accounting of these behaviours, Thompson describes this following a capillary model with isotropic film properties [35], as we have for most of this work; this is well complemented by the work of Jacquet *et al*., which gives insight into how the grain structure affects dewetting [34].

2.3.2 Mitigating intrinsic Ag changes

From equations 2.11 and 2.12, one could (correctly) surmise that depositing a coating with very small grains could help prevent dewetting. Indeed, larger grains will lead to deeper GB grooves, which will be more likely to generate holes, and they will increase the energetic incentive of hole formation. However, there are a number of reasons that make small-grained Ag films undesirable in the context of this work. Namely, a smaller average grain size will result in a worse as-coated performance [17], [31], and accelerate the rate of grain growth, as highlighted in the second term of equation 2.10. Moreover, this will make it difficult to limit the total change in grain size, resulting in important optical and electrical performance changes, which makes this particularly

unfit in the context of obtaining single-stock window coatings [6]. Additionally, incorporation of grain boundaries with lower atomic density during grain growth can lead to the development of tensile stress [30], [158]. Grain thinning can then occur as a means to alleviate this stress [159], and locally thinning the film in this way may then facilitate hole formation [35].

Instead, we can consider ways of stabilizing the grain size. Changing the film thickness or decreasing the GB mobility via lowering the temperature, while straightforward, is not a realistic option for many applications. Thus, the main morphological tools offered by equation 2.10 are the generation of grains with uniform sizes and surface energies, with additional benefit from a larger average grain size. As discussed in Section 2.2.4, an appropriate seed layer such as (doped) ZnO can promote these traits, and accordingly these have been employed to reduce dewetting and optical changes at high temperatures [142], [160]. Both the Ag-substrate and Ag-encapsulating layer interfaces contribute to a grain's energetic balance, and low energy at one interface may offset an otherwise poorly aligned grain; usage of appropriate encapsulating top layers thus also helps, although these must be deposited in conditions that do not degrade the Ag film [161].

Interestingly, despite that it results in a locally thinner film at the grain boundaries (which could plausibly affect the first term in the parentheses of equation 2.10), GB grooving is known to slow down grain growth [155], [162], [163], [164]. The geometrical argument proposed by Mullins relies on the idea that GB motion centered about a groove would result in an increase of its associated thickness, t_{GB}, which would increase the associated area, a_{GB}, and energy, E_{GB}. [164]. Further supporting this, simulations wherein grooves are manually inserted at different points during annealing show rapid stagnation of grain growth [162]. The results of Dannenberg *et al*. suggest GB mobility is restricted by surface diffusion in the presences of grooves, although diffusion at the grain boundaries is the likely mechanism otherwise [86]. Holm and Foiles indicate that at increasing temperatures, a higher proportion of GBs becomes destabilized, allowing their motion in spite of limiting effects, suggesting that as temperatures increase, management of surface diffusion will be insufficient [163].

Finally, dopants may allow to reduce grain growth by targeting diffusion at GBs; reduction of the GB mobility is commonly referred to as solute drag, in which dopants, initially present or accumulating at the grain boundaries during grain growth, mitigate reorganization around the GBs [92], [155], [163], [165]. However, as discussed earlier, the addition of dopants is consistently

reported to result in the formation of smaller grains [32], [48], [92], [105]. This is a direct consequence of their ability to slow GB motion, as it also impacts the cluster coalescence dynamics (see equation 2.7) during film formation, as discussed in Section 2.2.1. Thus, while many dopants have been shown to yield higher stability to dewetting and/or smaller final grain sizes [32], [49], [50], [84], [89], [92], [93], the grain growth (and other reorganization processes) that does take place is amply enough to cause significant optical and electrical changes [49], [50], [79], [89], [92]. While this is typically presented as beneficial, (rightfully so, for most applications) for the purpose of minimizing optical and electrical changes, it is an inconvenience. Chi and Bassim bypass the apparent restrictions doping places on the initial grain size by doping films via ion implantation after deposition is complete: Si-doped Ag films produced in this way show essentially the same initial grain size as pure Ag, but with much less grain growth [165]. While this is not straightforwardly implementable in conventional coating production, it demonstrates that dopants may offer further benefits if implemented appropriately.

Given the desirability of large grains, and the inherent difficulty associated to imposing small grain sizes on a film throughout high temperature processing, there is somewhat of a shortage of tools available to control the equilibrium shape of GB grooves; indeed, the balance between grain boundary and surface energies will depend largely on the chosen material [96], [126], and as discussed above, the film thickness will depend on the desired coating functionality. Moreover, as demonstrated in the previous section, the grain sizes resulting from normal grain growth are typically well below the critical threshold at which grooving causes hole formation, so management of abnormal grain growth remains the focus on that front [35].

Indeed, the equilibrium structures of GB grooves, in idealized films for which grain growth is well-managed, are not the main issue causing dewetting. Instead, we must consider what coating features can exacerbate grooving enough to cause hole formation, and what recourse we have to stop holes from inducing widespread dewetting.

Amongst said features is the film stress: as discussed in the context of equation 2.9, given film reorganization mechanisms can be promoted if they relieve strain energy. Previously it was discussed that separated islands could elastically deform themselves to close a grain boundary, if the resulting increase in strain energy was lower than the decrease in surface energies [30], [109]. Intuitively, we can see how the opposite may also be true: relief of this tensile stress may facilitate

splitting the GB. Thouless develops this further in the context of creep, i.e. diffusive stress relaxation, demonstrating that tensile stress applied at the grain boundaries will result in deeper grooves at equilibrium, and lead to faster groove formation [166]. This effect can be exacerbated by grain growth, as larger grains lead to deeper equilibrium grooves, but also because the removal of low-density GBs from the film structure can generate tensile stress [30], [158]. This is not to say that films should be in as much compressive stress as possible; in excess, this may lead to films forming blisters or hillocks to relieve the excess strain energy, both of which promote hole formation [35], [166]. Finally, while the discussion here is very much focused on the Ag layer, it should be noted that stress in adjoining layers can cause similar issues, by cracking or delaminating under their own internal stresses, or applying strain to the Ag layer, exacerbating existing issues [109], [158], [167].

In terms of structure, triple boundaries, i.e. the boundary formed at the junction of three grains, will also promote hole formation; these have been shown to strongly impede grain boundary motion regardless of the presence of grooves [168], as well as to result in deeper grooves [35], [154]. *In situ* transmission electron microscopy (TEM) measurements performed by Dannenberg *et al*. demonstrate that holes preferentially nucleate at these triple boundaries, showing thinner areas both at and around the groove [86]. Consistent with Holm and Foiles, they find that the average grain size is largely determined by the temperature, with temperatures of 600 °C leading to sufficient grain growth for these triple boundaries to induce dewetting in their 80 nm thick films [86], [163]. While stress, density and defects in the film can be controlled via the deposition kinetics [26], [113], [123], [124], there is no simple recourse to removing triple boundaries; we must impede the film's transition towards their equilibrium shape instead.

This is a relatively straightforward endeavor, as GB grooving and dewetting are mediated by surface diffusion [34], [35], [86], [154], [166], [169]. Indeed, these require mass transport out and away from the GBs, meaning GBs cannot contribute, and even at high temperatures, as considered in this work, bulk diffusion will be negligible next to either GB or surface diffusion [170], [171]. Thus, control of these processes can be performed by controlling Ag's external surfaces; something much easier than controlling its internal ones.

The addition of encapsulating layers thus allows to straightforwardly mitigate grooving and hole expansion; for example Smith and Gurev found that the addition of a silica encapsulating layer

allowed hole closing processes to compete with their formation, at least for given durations and temperatures [156]. On the other hand, Folgner *et al*. find that $NiCrN_x$ interlayers reduce diffusion at a Ag/SiN interface in chemical exposure tests, which they attribute to Ni interdiffusion at the Ag surface [20]. This is consistent with the common usage of NiCr-based interface layers being used in Ag coatings requiring high-temperature stability [22], [142], [172], [173], [174]; although other layers are also used for high temperature stability [161], [175], the improvements in chemical and mechanical durability offered by NiCr further popularise it [20], [46], [176], [177], [178]. Kumar *et al*. report that the activation energies required for diffusion at interfaces of a given material will scale roughly with the work of adhesion at that interface [169], analogous to the previous observation that activation energy for surface diffusion scales with the adatom binding energy [98]. Thus, any encapsulating layer strongly adhering to Ag will also suppress grooving and dewetting processes, as well as the other advantages discussed previously. Finally, in addition to adhesion, conformality and rigidity of the encapsulating layers should also be pursued [35]; simply enough, dewetting and grooving require meaningful coating volume to be displaced, and these traits will respectively limit the existing free space and limit how difficult it is to generate new space. Intuitively, we see that these must be coupled to good adhesion as well, lest they simply delaminate from the Ag film instead. Thus, atomic layer deposition (ALD) thin films, which present exceptional conformality, can significantly improve resistance to dewetting and other structural changes [179], [180], [181], [182], [183].

Finally, when discussing equation 2.8 in Section 2.2.1, it was mentioned that dopants may suppress surface diffusion; they could thus improve resistance to grooving and dewetting via this mechanism as well, consistent with the high temperature stability improvements reported for dopants discussed previously [32], [49], [50], [84], [89], [92], [93], [165]. The resulting effect is unarguable, but as previously, the interconnectedness of the physics determining equilibrium shapes and film reorganization kinetics make it difficult to attribute this effect to a specific mechanism, controlled by a specific parameter. An overlooked aspect of dopants and their role in improving temperature stability is their effect on as-coated morphology. We have focused on mechanisms that leads to the formation of holes in continuous films, but this is for naught if holes of critical size are present initially. Even if they are not, minimization of internal interfaces is expected to lead to the agglomeration of small voids, vacancies, or incorporated gases, which can lead to hole nucleation, as reported in Au films by Kwon *et al*. [184]. Thus, the high temperature stability of different thin

films should be compared for similar continuous microstructures, but this is rarely the case. Many authors do not clearly demonstrate that their un-doped Ag films are continuous prior to annealing [49], or display outright that they are not [32], [84], [89]. Those that ensure appropriate comparability in the starting morphologies show that while dopants can greatly improve stability, they are not necessarily the panacea that some reports claim, nor are they all made equal [50], [92], [93], [165]. For example $Ag_{(Cu)}$ shows higher temperature stability than $Ag_{(Zn)}$ layers, despite the former having a slightly discontinuous structure [93]. Similarly, Ni-doped Ag films were found to be more stable than pure Ag films at certain concentrations, but these did not systematically improve upon their pure-Ag counterparts [92]. Thus, while dopants can significantly improve high temperature stability, one must be careful to not overestimate their stabilizing effect due to improved wetting.

2.3.3 Interdiffusion of film species and contaminants

While the core issues resulting from annealing low-E coatings occur in the plane of the Ag layer, it is essential to consider what happens when other elements intrude upon it.

Indeed, just as minimization of free energy will drive structural reorganization, it will drive compositional reorganization; this is straightforwardly encapsulated by Fick's law of diffusion, shown below [170].

$$F_D = -D\frac{\mathrm{d}C}{\mathrm{d}x} \tag{2.13}$$

Where F_D is the atomic flux resulting from diffusion, C is the concentration of the diffusing species being considered, and x is some linear spatial coordinate [170]; in practice, this will represent a thickness gradient, under the assumption that the various layers deposited in a low-E stack are uniform along the surface plane. The diffusivity D has already been discussed to some extent, but mostly in the context of Ag diffusion on the substrate surface or at Ag interfaces, at least so far. Here it will be important to keep in mind that D varies both with the diffusing species, and the surface or matrix it is diffusing in [170].

Effect of external contaminants notwithstanding, interdiffusion of Ag into adjoining dielectrics is the primary mechanism with which to concern ourselves [185], [186], [187], [188]. It is intuitive

to see that the empty space resulting from Ag diffusion out-of-layer can contribute to the generation of voids or holes inside the Ag layer; in addition to this, out-diffused Ag will, under the same thermodynamic constraints as previously, form Ag nanoparticles inside the dielectrics, generating characteristic optical features [185], [187]. Section 2.2.4 established ZnO and TiO_2 seed layers as important, if not necessary features of low-E coating architectures; thus the reported optical and electrical performance changes related to interdiffusion into these materials will need to be managed without undermining their beneficial properties [186], [188]. Moreover, this can occur even during deposition: Ag interdiffusion with encapsulating layers due to their energetic deposition conditions has been reported [185].

The other stack materials being oxides and nitrides, with much lower diffusivity, these tend to be matrices in which Ag or contaminants diffuse. This can nevertheless occur, as highlighted for SiO_2 interdiffusion with soda-lime glass [189]. Similarly, changes in the concentration of Al in $ZnO_{(Al)}$ films has been shown to effect their optical bandgap [190], [191], [192]. That being said, as the dielectrics commonly used in low-E coatings have similar optical properties, their intermixing is mainly expected to result in subtle changes following effective media approximations [186]. An over-stoichiometric oxide may allow oxygen desorption and diffusion [193], and ostensibly the same could be true for a highly sub-stoichiometric layer and a metal, but at that point, the unwanted incorporation of diffusing species is tantamount to contamination rather than an inherent issue with diffusion from dielectrics.

Let us then turn our attention towards contaminants. Here we will focus on some key categories, broadly addressing contaminants present on the surface of substrates, diffusion of sodium (Na) from glass substrates at high temperatures, oxygen, corrosive species, and humidity present in the atmosphere.

Regardless of their chemistry, contaminants present at the substrate surface are specific in that, regardless of whether they diffuse through the stack at high temperatures, they will affect the surface quality during the initial coating phases, leading to low adhesion, pinhole formation, or otherwise poor film quality [194], [195]. Given that much of the previous discussion concerning the mitigation of intrinsic Ag changes at high temperatures was predicated on ensuring the high quality of the Ag film and its adjoining layers, and that the formation of holes in the encapsulating layers will allow contaminant diffusion, these cause very serious issues. Surface contaminants are

typically understood to be small particles that cause shadowing or low-surface energy organic contaminants, resulting in low adhesion or formation of discontinuous films [194], [195]. No specific techniques to deal with these will be discussed in the following section. Indeed, the most effective way to do so is simply to remove them entirely, by minimizing sources of contamination with proper system maintenance and appropriate sample cleaning, which will be discussed in Section 3.1.1.

A challenging contaminant to control during glass tempering is the Na diffusion from the SLG substrate. Alkali and alkali-earth elements, e.g. sodium, calcium, magnesium (Na, Ca, Mg), must be added to silica glasses in order to decrease the processing temperature required to work them, [196], [197]. However, this can result in the diffusion of their respective cations at high temperatures; being particularly mobile, Na is typically the focus when considering the diffusion of these elements, and the same will be true here [196], [198], [199], [200], [201], [202]. Interestingly, the effect of Na diffusion on low-E coatings is not broadly understood; it is frequently cited as a problem to be managed, with no explanation of why [6], [203], [204]. Moreover, the measurement of Na diffusion is complicated by its high mobility; it has been reported to diffuse as a result of X-ray radiation and, more importantly so, electron irradiation, due to its diffusion as a Na^+ cation [205], [206]. Furthermore, Li *et al*. found that sodium diffused from SLG substrates at high temperature partially returned to the substrate during cooling [201]. This can be attributed, once again, to Na diffusion as a cation; residual negative charge remains in the glass following its diffusion, promoting the diffusion of positively charged ions back into the glass.

This can also promote the diffusion of other ions into the glass to replace Na, referred to as the ion-exchange mechanism [39], [199], [207], [208], [209]. This has been shown to enable Ag diffusion to depths of multiple hundreds of microns from the glass surface in certain conditions, as well as leading to the generation of Ag nanoparticles within the glass [199], [207]. Kulczyk-Malecka *et al*. observed that, following long annealing durations, that Ag could no longer be detected in their coatings, and thus proposed that Ag-Na ion exchange may drive depletion of Ag films during tempering [39], [208]. While Na-Ag ion exchanged glasses are typically produced in molten salt baths, field-assisted solid-state ion exchange has been demonstrated at temperatures of 400 °C, suggesting that, in the presence of higher temperatures, such as during tempering, this could occur without field-assistance [209]. On the other hand, Hummel *et al*. observed that alkali doping of Au films promoted their hole formation and dewetting [202], [210]. Given that Na diffusion is used in

copper alloy solar cells to promote grain growth [201], [211], it is plausible for it to facilitate grain growth for Ag films as well, leading to GB grooving and subsequent dewetting.

The effects of oxygen on Ag are rather contextual: for example, at room temperature, exposed to molecular oxygen, Ag does not readily form an oxide, although oxygen adsorption at the surface occurs [212]. Moreover, while it is susceptible to forming an oxide when exposed to atomic oxygen, e.g. as present in oxygen plasmas, these oxides are unstable at high temperatures: above ≈ 400 °C, thermal dissociation begins to outcompete oxidation [149], [213]. As a result, the issues pertaining to Ag's exposure to oxygen at high temperatures are not equivalent to the oxidation processes which may occur during deposition. Jacquet *et al*. demonstrate that the presence of oxygen in the annealing atmosphere vastly changes the dewetting behavior of Ag; they suggest that oxygen will decrease Ag surface energy while maintaining fixed GB surface energy, resulting in accentuated thermal grooving (per equation 2.11) and greater hole nucleation [34]. This is shown in **Figure 2.10**. Moreover, dewetting is shown to occur via Ag transport to, and grain growth of, select grain orientations, albeit the mechanism behind this is as-of-yet unclear [34]. Birnbaum *et al*. observed Ag deposited with oxygen exposure developed a (100) preferred orientation; these developed extremely large grains during annealing, attributed to the return to a preferred (111) orientation as well as stress-relief considerations [214]. In both cases, the relative isolation of the grains of the newly preferred orientation may be instrumental, as these could then "monopolize" the mass transfer to preferential grains. Both papers also consider Ag annealed at similar temperatures, on Si (100) substrates, suggesting stress relaxation is contributing in both cases [34], [214].

In addition to this, O adsorption on Ag surfaces is known to increase Ag diffusion on said surfaces, and speculated to limit Ag nucleation on certain facets [34]; combined with the observations that O diffusion on Ag is facet dependant and that Ag diffusion on oxygen saturated surfaces occurs through O-mediated Ag cluster diffusion (albeit the latter was simulated on ZnO surfaces), anisotropic changes in mobility may also play a role [131], [215]. The mobility changes induced by oxygen are indeed an important consideration, resulting in important mass transport when sufficient diffusion paths are available [40], [216].

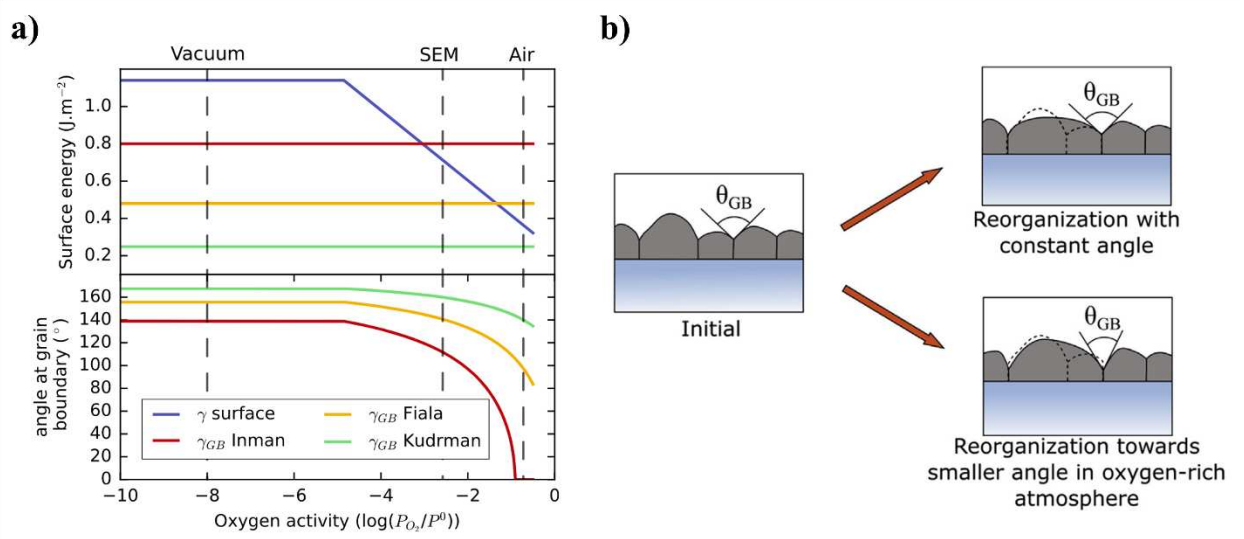


Figure 2.10: a) Surface and grain boundary energies, as well as the resulting angle at the grain boundary, for different concentrations of oxygen. **b)** Schematic representation of the effect of oxygen exposure on the Ag grain structure. Reprinted from [34], Copyright (2018), with permission from Elsevier.

Corrosion of Ag by more reactive species, namely sulfur- and chlorine-based contaminants (S, Cl) is known to cause important degradation, even at ambient temperatures, especially when facilitated by humid environments [20], [36], [37], [212], [217]. In this work, we will not make any particular distinctions between these: the degradation features caused by different contaminants of this category are similar, and similar techniques are effective to protect Ag from them [20], [217]. In protected Ag coatings, these typically result in the formation of large, agglomerated Ag corrosion products at points where contaminants can access the Ag layer, with depletion of the Ag layer around them [20], [37]. Koike *et al*. demonstrate that Cl reactions with Ag result in the formation of dense, agglomerated corrosion products consisting largely of Ag [36]; the generation of vacancies around the cluster could then facilitate Ag diffusion towards the corrosion site, consistent with the suggestions of Hafezian *et al*. [149]. As such, Ag degradation would directly enable diffusion towards the degradation center, leading to the observations of Ag-depleted areas around small egress points where contaminants have reached Ag.

Finally, the presence of humidity (H_2O) can affect Ag via a variety of effects; Ross outlines these well [38]. However, the exacerbation of other degradation mechanisms via its presence can make

it difficult to directly isolate its effect. For example, in regard to Ag corrosion, it can allow the dissolution and removal of soluble corrosion products, or facilitate the interaction of corrosive species present as airborne particles by forming a solution with them [38], [212]. The presence of humidity, even at low temperatures, increases Ag mobility [38]; this facilitates Ag reorganization in and of itself, but also further enhances the effect of oxygen [218]. At high temperatures, this leads to significantly enhanced degradation of the Ag film [219], [220]. While the combination of Na and H_2O exposure also enhances degradation, even in Cu-alloy solar cells where Na is usually beneficial [221], [222], the exact reason is unclear. The lack of a definitive mechanism for Na's effect on Ag, as well as the multitude of ways H_2O can interact with it, e.g. facilitating Ag diffusion in response to Na, leaching out additional Na^+ via ion exchange with hydrogen ions [196], or participating in chemical or electrochemical reactions with it [38]. This is not to say that other contaminants will not interact together. For example, subsequent oxidation and reduction reactions have shown to enable accelerated metal diffusion, ostensibly enabling diffusion in oxidizing atmospheres, with thermal or Na-assisted reduction increasing diffusion [223], [224]. More generally, disruptions to the Ag morphology may make it susceptible to further degradation by other mechanisms [21].

Finally, the effect of humidity on dielectric film layers bears mentioning. Absorption of water in film pores has been shown to induce stress changes which, in addition to previously discussed effects, can lead to formation of cracking and delamination in the dielectric layers [109], [225], [226].

2.3.4 Mitigating the effects and the diffusion of contaminants

The previous section demonstrates that contaminants mainly alter or facilitate degradation modes already occurring in Ag rather than generating new ones: they change surface energies, mobilities, grain grooving and dewetting dynamics, perhaps create new low-energy states for Ag to move to, but the equilibrium seeking mechanisms discussed in Section 2.3.1 are overall the same. Thus, the means to mitigate these, addressed in Section 2.3.2 remain relevant.

As previously, starting from a metastable, fully continuous morphology can greatly improve durability, as demonstrated by Fryauf *et al*. [21]. Likewise, abnormal grain growth, thermal

grooving and diffusion towards corrosion sites will be mitigated by strong adhesion at the interfaces limiting Ag mobility [76], [149], [227], [228].

One point in which previously described techniques qualitatively differ is the usage of dopants. While their effects on the previous points remains (solute drag slowing grain growth, reduced surface diffusion impeding grooving and dewetting), the addition of distinct atomic species with different reactivity than Ag can greatly improve durability when exposed to contaminants [32], [36], [49], [50], [90], [91]. Koike *et al*. elegantly demonstrate this by showing how different alloying agents with lower or higher reactivities to Cl, e.g. Cu or Au, will respectively limit Ag degradation by preferentially and sacrificially reacting with Cl on one hand, and by restricting the availability of reactive species on the other [36].

Nonetheless, the most preferable approach to mitigating the effect of contaminants is to simply stop them from ever interacting with the Ag layer. As discussed previously, this can be accomplished by removing sources of contamination with proper substrate cleaning and system maintenance. Arguably, control of atmospheric particles and humidity during coating storage and processing could also be achieved. However, Na is an intrinsic component of the SLG substrate, and annealing hundreds of square meters of glass under oxygen-free atmosphere is not a feasible approach. Thus, low-E coatings must be designed such as to impede the diffusion of environmental contaminants towards the Ag layer.

In the context of mitigating GB grooving, it was mentioned that diffusion at GBs was much faster than through the bulk of the lattice, particularly given the high density of grain boundaries in polycrystalline thin films [170], [171]; controlling the density of grain boundaries therefore offers significant control over diffusivity. Indeed, even the microstructure of Ag must be considered in these terms; Ag alloys have been found to be extremely permeable to oxygen given rapid diffusion at its grain boundaries [229]. Conversely, (nearly) mono-crystalline Ag has been shown to be much more environmentally stable than standard films [143], [230].

When considering dielectric barrier layers, it is often more practical to remove GBs via the deposition of amorphous layers. Given that typical metal oxides and nitrides interact much more strongly with conventional substrates, these form amorphous layers readily, as long as the deposition rate is sufficiently high [26]. These may nonetheless generate defects, nucleate crystal phases, transition between phases, or undergo grain growth at high temperatures in order to relieve

strain or decrease their free energy [109], [155], [170], which may result in film structures with higher diffusivity. For example, Liu *et al*. and Kulczyk-Malecka *et al*. both find that their as-coated titania films are without any pronounced crystallinity, but form anatase phases when annealed [39], [208], [231]. While there may be disordered crystalline domains in the samples prior to annealing, this transition nevertheless results in higher Ag diffusivity [208]. This may seem to be in contradiction with the previous statement: if there are minuscule grains in the as-coated sample, there ought to be a high density of GBs, and plentiful diffusion paths. However, small equiaxed grains may generate rather meandering diffusion paths, as opposed to relatively straight channels in a columnar structure, or present less pores or defects which facilitate diffusion [232]. This is shown schematically in **Figure 2.11**. The interfaces between different materials may also have different binding potentials specifically affecting diffusion [171]; this explains the observation of Na accumulation at interfaces following annealing and cooling, and the usage of dielectric nanolaminates to improve chemical stability [201], [204].

Mitigating the formation of large-scale diffusion paths is also important: scratches, buckles, cracks and pinholes likewise enable large-scale mass transport, and important degradation around these [20], [37], [38], [40], [216]. As mentioned previously, conformal deposition and control of contaminants is important to limit pinhole formation. Beyond this, controlling the formation of cracks or buckles and increasing the coating's resistance to external solicitation largely depends on film stress [41], [109], [233]. In this case as well, chemical changes and stress relaxation during annealing have been shown to reduce coating durability [41], [233]. Given the limited processing and gentle environments in which low-E coatings operate following annealing, limited degradation risks remain if coating durability is ensured up to that point. Thus, it is especially the formation of such defects before and during annealing, as a result of stress relaxation or mechanical loading, which must be mitigated.

Finally, selection of appropriate materials is required to reduce diffusivity. A review of the vast array of materials available to encapsulate Ag, especially in a complex multilayer format, is beyond the scope of this work. However, some insight can be given into the main requirements. Blocking Na and O diffusion at the lower and upper coating extremities is essential. Moreover, usage of layers with comparable mechanical properties on either side of the Ag layer appears to improve

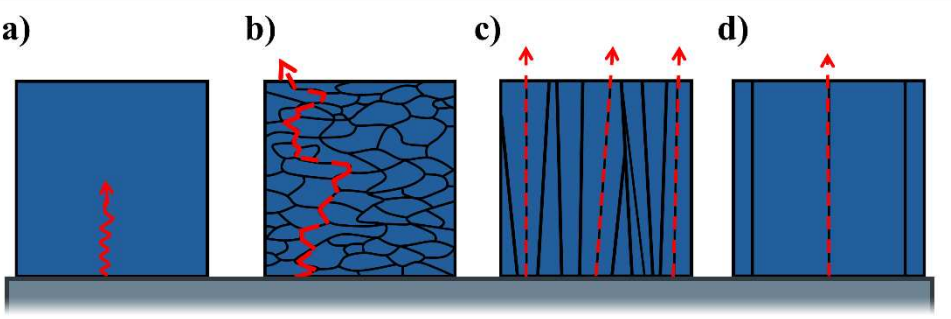


Figure 2.11: Schematic showcasing the effect of different grain structures on through-coating diffusion. **a)** Amorphous coating allowing much slower bulk diffusion. **b)** Small, equiaxed grains allowing GB diffusion along meandering paths. **c)** Fine columnar grains with a high density of straight diffusion paths along the GBs. **d)** Large-grained columnar structure with few diffusion paths.

durability [234]. Thus, hard diffusion barriers may be employed as the outermost coating layers. SiN has been shown to be a good barrier layer against O and Na [22], [39], [235], [236], in addition to providing mechanical durability [41], [237]. In addition to this however, layers ensuring coating performance and mitigation of other degradation mechanisms are required, i.e. a crystalline seed layer. We must therefore balance the performance differences discussed in Section 2.2.4 with diffusion resistance. Ag diffusivity is particularly important here, given that these films will be adjacent to the Ag layer. Whereas zinc-tin oxide and crystallized TiO_2 coatings were found to be poor diffusion barriers, $ZnO_{(Al)}$ is found to have low Ag diffusion regardless of annealing; in some cases, Ag diffusivity in $ZnO_{(Al)}$ even decreases following HT [39], [208], [238]. Usage of doped ZnO, specifically, may be preferable: addition of aluminum has been shown to improve humidity resistance of these films [220]. Moreover, dielectrics doped with small concentrations of complementary gases (i.e. nitrogen doping in oxides and vice-versa) has been shown to improve stability [239], [240], [241], and metallic dopants are expected to do the same, as discussed in the context of grain growth. With two such materials, and a coating allowing to protect the upper Ag interface during deposition of the encapsulating layers [237], the main performance and durability requirements can be met.

CHAPTER 3 METHODOLOGY

The previous chapter ought to have provided a suitable understanding of the key processes and properties guiding the evolution of Ag films throughout their deposition and subsequent exposure to environmental hazards. Prior to describing experiments and their results, however, it is important to present the tools and techniques used to fabricate and investigate coatings.

This section will start by addressing coating fabrication, a foundational requirement for further study. Means to evaluate coating performance will then be discussed, allowing one to track its degradation during chemical and high-temperature stability testing. Finally, more advanced characterization methods will be discussed, which will allow to investigate specific film properties and relate them to various tested functionalities.

3.1 Sample fabrication

3.1.1 Substrate cleaning and preparation

Different experiments in this work needed different sample cleaning procedures; specifically, coatings destined to high temperature stability testing were found to require more rigorous cleaning in order to achieve acceptable stability. It is this procedure that this section describes; it will be taken as the default where not specified. In the following chapters, different approaches may be presented, in which case a lower standard of cleaning was not found to have significant impact.

Glass substrates were first cut to their desired size and identified by scratching them with a diamond-tip stylus. Cutting and marking was performed on the tin side of float glass samples, which was identified using a UV lamp, leaving the air side pristine for deposition. Particles resulting from this process and general dirtiness remaining on samples following shipping were cleaned by hand, while wearing gloves, using a soft wipe and a 1% solution of Cole Parmer Micro-90 soap.

Subsequently, samples were cleaned in an ultrasonic bath [195], first in the 1% Micro-90 solution, then deionized (DI) water, acetone, and isopropanol, for 10, 5 10, and 10 minutes, respectively. Between each cleaning step, samples were rinsed using the next solvent in the sequence (e.g. after cleaning in acetone, rinsing in isopropanol). An EXAIR compressed air knife was used to dry the samples. This was particularly important for substrates larger than 2 in. by 2 in., as this allows

uniform removal of any liquid residue. Once transferred under vacuum for film deposition, a 25 W, -235 V radiofrequency (RF) bias plasma discharge was applied to the substrate holder to provide a final cleaning step, using an 8 mTorr argon/oxygen mixture (100/35 sccm) in order to volatilize any organic residue [195].

Float glass surfaces, as used in this work, are highly smooth [242]; thus, substrate cleaning plays a central role in achieving high coating stability, as discussed previously. This is demonstrated in additional detail in Appendix A.

3.1.2 Coating deposition via magnetron sputtering

Coatings were deposited via magnetron sputtering, in which a plasma is magnetically confined against a target of the material to be deposited, and energetic collisions of the plasma ions eject atoms from the target through momentum transfer. This technique allows suitable deposition rates of a wide variety of materials, to deposit films which generally retain the composition of the target, or to tune their stoichiometry by depositing films using a plasma containing reactive gas species, making it widely used in industrial applications [170], as well as the technique of choice for deposition of low-E coatings [5], [45], [54].

Film deposition was performed using a Kurt J. Lesker CMS-18 magnetron sputtering system; it includes four 3-in. (75 mm) diameter magnetrons, which can be powered in either direct current (DC) or RF modes. A fifth 2-in. (50 mm) diameter magnetron was added to enable usage of more materials in early experiments, but its usage was eventually discontinued as simpler architectures were found to perform well, and low deposition rates were obtained with it. In addition, a RF power source connected to the substrate holder allows substrate biasing, as described in the previous subsection, and quartz heating lamps, positioned behind it, allow to increase the substrate temperature. Given its fixed pumping speed, the pressure and composition of the working gas used to generate the plasma are controlled by changing the flow rate of inserted gases; process control software allows to set a fixed ratio between select gases, then automatically adjusts the total flow to maintain the desired pressure.

Together with the power applied to the target, these allow one to control the film composition and adatom kinetics, as described in Section 2.2.2, enabling control of the microstructure and resulting

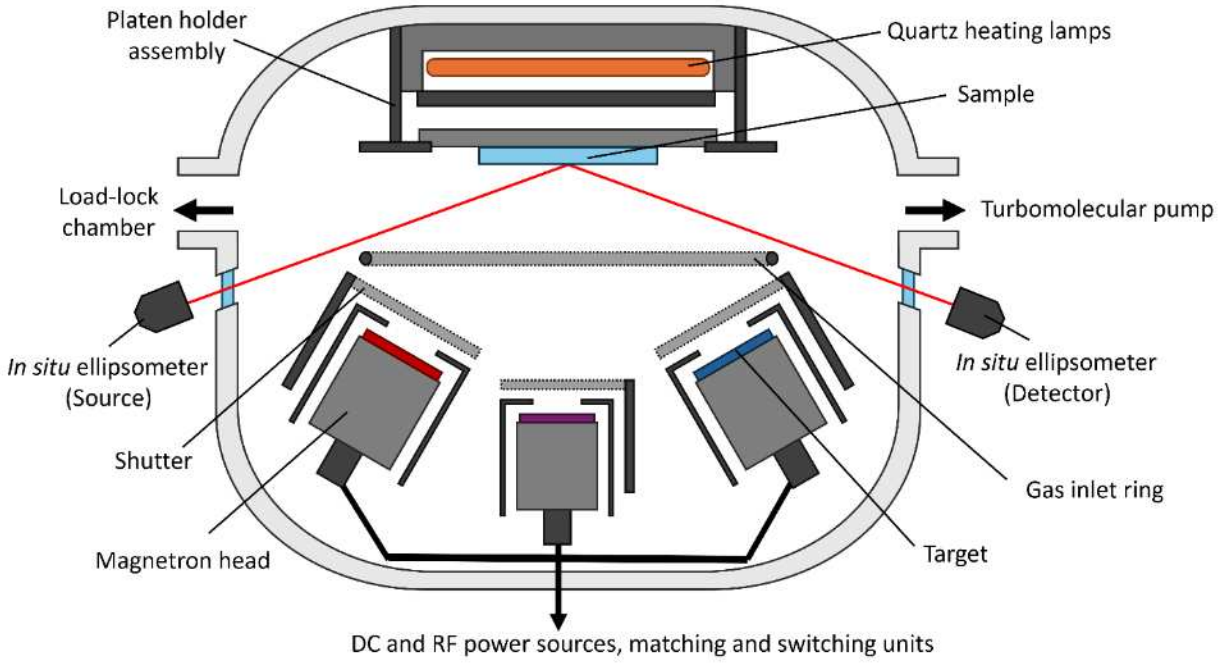


Figure 3.1: Schematic representation of the magnetron sputtering system used in this work. Only two of the four 3 in. magnetrons are shown, for the sake of readability.

properties of the deposited coatings. Moreover, the substrate holder bias plasma helps to re-sputter film material for post-deposition etching, as described in Section 2.2.3.

Industrial deposition conditions must be adapted to optimize not only performance and durability, but also the deposition rate, and the cost of operation per unit of glass produced. Thus, guided by these considerations, film deposition conditions were selected to maximize compatibility with reference properties provided by the industrial partner, to improve transferability of results as well as to limit the scope of material properties to explore. An overview of these steps is provided in Appendix A. As deposition parameters were adjusted over time to keep up with gradual changes induced by target erosion, system modifications, and more, tables of the deposition conditions used will not be listed here; rather, the deposition conditions used in different sets of experiments will be given in their respective chapters, in Sections 5.3 and 6.3

Finally, it should be noted that *in situ* deposition monitoring was performed via ellipsometry, as will be described in Section 3.4.1.

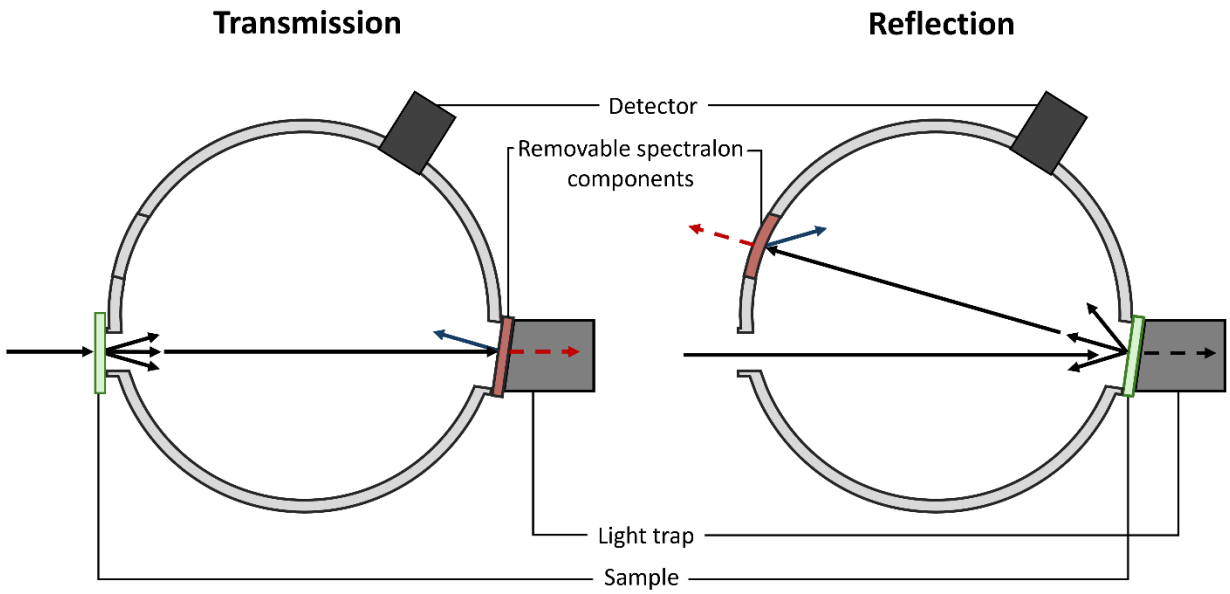


Figure 3.2: Schematic representation of integrating sphere of the Lambda 1050 spectrophotometer. In transmission, the sample is placed at the opening of the sphere: when the spectralon reference in removed, the specularly transmitted beam is absorbed in the light trap. In reflection, the sample is placed at the opening of the light trap: when a portion of the integrating sphere is removed, the specularly reflected beam exits the integrating sphere. In both cases, the diffuse components are collected by the integrating sphere regardless of the removal of spectralon components.

3.2 Film performance characterization methods

3.2.1 Spectrophotometry

Given the main low-E functionalities and properties metrics outlined in Section 2.1.1, i.e. maximizing transmission in the visible, and minimizing it in IR, spectrophotometry is used as one of the main tools to evaluate low-E performance.

The measurements were primarily performed using a Perkin Elmer Lambda 1050 spectrophotometer, with an effective wavelength range of 250 nm to 2500, allowing to effectively probe the UV, visible, and NIR regions. Furthermore, it is equipped with a 150-mm-diameter integrating sphere: this module allows to collect the entirety of the transmitted or reflected intensity, regardless of the presence of diffusivity. A light trap can be opened at the back of the sphere to capture light in specular transmission, allowing to isolate the scattered transmission, and thus quantify sample haze [243]. Similarly, one of sphere's inner panels can be taken out such that

the specular component of the reflection is removed, allowing to measure the scattered reflection. This is shown schematically in **Figure 3.2**. Its primary caveat is that transmission measurements are performed at normal incidence, whereas reflection measurements are made at 8° incidence: as a result, while sample absorption can still be estimated via conservation of energy, i.e. $R + T + A = 1$, the greater the angular sensitivity of R, the greater the resulting error in A. Thus, monitoring transmission losses will frequently be preferred over monitoring increases in absorption.

In some cases, an Agilent Technologies Cary 7000 spectrophotometer, equipped with a universal measurement accessory, was used. This allows specular transmission and reflection measurements to be obtained at the same angle (which can be adjusted over a wide range), effectively resolving the previous issue: however, as these are strictly specular measurements, any scattered light will be lost, artificially increasing the value of A. Thus, this device was only used in cases where scattering was considered negligible, or angular sensitivity was expected or observed to be important, i.e. the antireflective coatings presented in Chapter 5.

3.2.2 Contactless sheet resistance monitoring

The wavelength range of the spectrophotometers used in this work being limited to the NIR, the film conductivity was used as a stand-in to replace MIR reflectance or emissivity measurements.

Indeed, equation 2.1 highlights the relation between conductivity and IR reflectance at higher wavelengths; moreover, Szczyrbowski *et al*. show that for thin Ag films, in the range of 5 to 20 nm, the emissivity, ε, is proportional to the sheet resistance, R_{Sh} [10]. The latter is a measurement of resistance adapted for 2D systems, and is equivalent to the resistivity of a film, ρ, divided by its thickness, t, such that $R_{Sh} = \rho/t$. As the sheet resistance will remain constant for a square of material with fixed thickness for any given size, it is typically expressed in ohms per square, written either Ω/□ or Ω/sq.

Sheet resistance was primarily assessed using non-contact eddy-current measurements, in which a varying magnetic flux is applied to the sample, inducing an electrical current in the plane of any conductive layers and generating an induced magnetic field proportional to the in-plane conductivity, which is then converted into sheet resistance. This was performed using first a Delcom 737 contactless sheet resistance monitor; however, this system both requires that samples

be at least 2 in. in diameter, while being thinner than 3 mm. As float glass substrates with thickness of 3, 4 or 6 mm were primarily used in this work, as is conventional for low-E windows, sheet resistance measurements could not be performed regularly. Later acquisition of a Delcom RD200 model, with minimal sample diameter of 1 in. and maximum thickness of 6 mm, allowed these measurements to be made more broadly. Finally, it should be noted that some measurements were made using four-point probe measurements in a Van-der-Pauw geometry, as described in Chapter 6. While this allowed *in situ* sheet resistance monitoring, it rendered sample transfer in-and-out of vacuum difficult and required breaking vacuum to deposit metallic contacts and install the multimeter probes, making it unsuitable for general use.

3.3 Stability characterization methods

Sample stability was in large part performed by comparing the sample performance prior to and following exposure to environmental degradation. Thus, for the different environments used to test stability, a recurring metric is the change in transmission, e.g. $\Delta T = T^{HT}\text{-}T^{AC}$, comparing the heat-treated (HT) and as-coated (AC) transmission of a sample. Given the enormous spectral variation in the transmission of a low-E coating, going from ≈ 90% in the visible to ≈ 5% in the upper ranges of the NIR, this allows to easily visualize changes of a few percentage points across the entire spectrum.

This was particularly useful for comparing samples in situations where sheet resistance measurements could not be obtained, such as in *in situ* measurements, or, prior to obtaining the RD200 sheet resistance monitor, when using samples with sizes which were not compatible with the 737 model. Indeed, while this does not allow a rigorous evaluation of the emissivity per se, comparing the optical changes of a coating with constant film thicknesses and minor changes in the optical properties of the dielectric layers, particularly in the NIR (as shown in Appendix A), evolution of a given sample allows a general evaluation of the changes of the Ag film's electrical properties.

With this in mind, we may now discuss the different tools and conditions in which coating stability were tested.

3.3.1 High temperature stability

High temperature stability testing in this work consisted of a heat treatment at 650 °C, with duration adjusted based on the size and thickness of the substrates. Both of the ovens used in this work allow to directly insert or remove samples during operation, improving the comparability to industrial processes [47]. Samples were typically 2 in. by 2 in. (50 mm by 50 mm) in size for 3- or 4-mm thick substrates. By default, these were annealed for 8 or 10 minutes, respectively. In preliminary work, aiming to adjust cleaning processes and calibrate deposition conditions to obtain an optical performance and HT stability comparable to those of coatings produced by the industrial partner, 4 in. by 4 in. (100 mm by 100 mm), 6-mm-thick substrates were used, and annealed for 12 minutes. In some specified cases, these durations were purposefully shortened or extended to draw greater contrast between samples which, respectively, degraded faster than expected or displayed comparable changes following standard HT durations.

In order to isolate the effects of high temperatures on Ag diffusivity from those of atmospheric contaminants, as in Chapter 4, a Carbolyte Gero tube furnace was used. Each end of the tube was plugged, with one end incorporating a gas inlet; select gasses were then pumped into the chamber at 7 scfh, using a source pressure of 30 psi in order to drive out ambient atmospheric gases. The plug at the opposite end had a small hole open to keep the overall annealing pressure at atmosphere; it is shown schematically in **Figure 3.3**. The tube was purged at least 10 minutes prior to sample loading, and temperatures inside the furnace were verified manually with a separate thermocouple. Samples were placed flat on a small ceramic boat keeping samples at the center of the tube, such that they would rest on the boat edges rather than the tube walls. Given the tube size, sample sizes were limited to 2 in. across and below for this furnace.

Experiments that did not require annealing in controlled atmospheres were performed using a Barnstead/Thermolyne 48000 Furnace provided by the industrial partner. Samples were placed on a raised, ceramic substrate holder, perforated at its center, such as to be held at center height of the furnace chamber, and benefit from convective heating at the sample backside. Furthermore, holes in the top and bottom of the furnace chamber enabled *in situ* transmission spectrophotometry. This was performed using a Zeiss MCS621 VIS II spectrophotometer with a wavelength range of 380 to 1050 nm, acquiring data at 10 s intervals and a reference beam ensuring the stability of the incident intensity and thus the long-term accuracy of the baseline. A ceramic guide placed on the

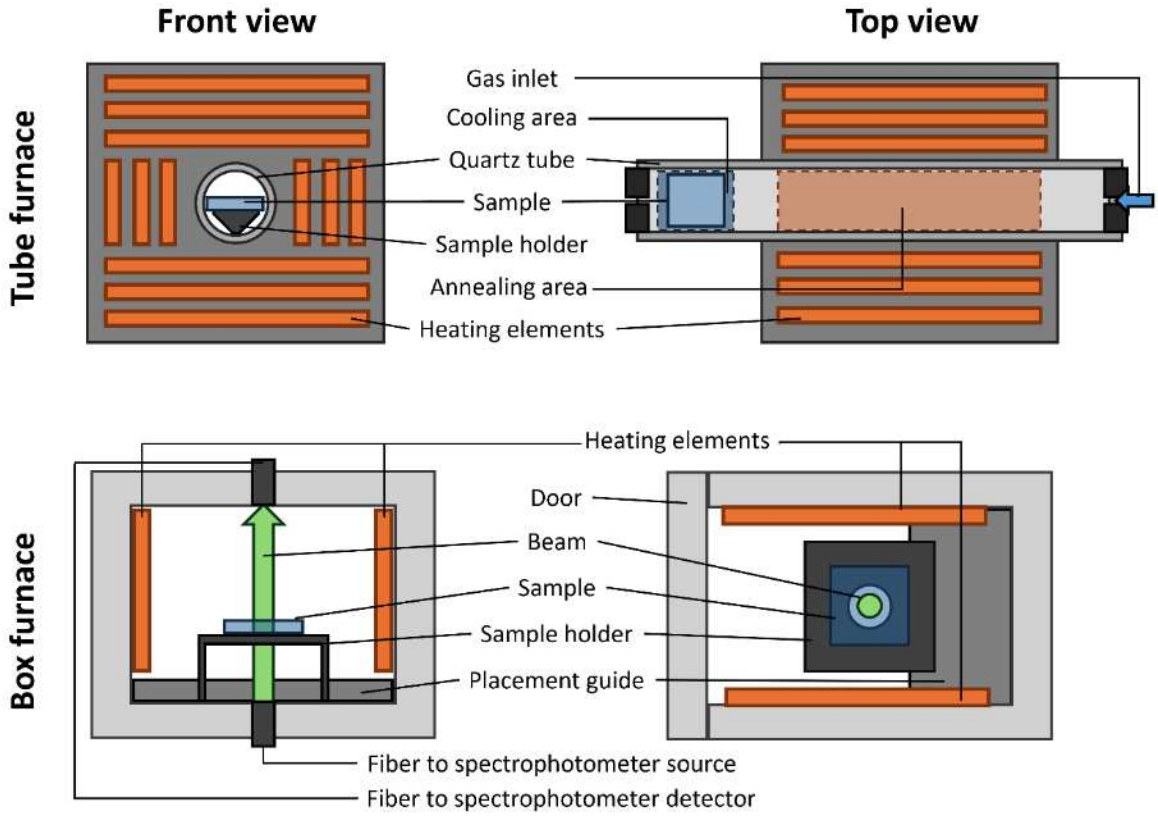


Figure 3.3: Schematic representation of the tube furnace and box furnace used in this work, respectively enabling annealing in controlled atmospheres and with *in situ* spectrophotometry monitoring.

bottom of the furnace chamber ensured repeatable positioning of the samples relative to the spectrophotometer's beam path. Likewise, its layout is shown schematically in **Figure 3.3**. It should be noted that SLG was found to have temperature-dependant optical properties: corrections accounting for this in *in situ* measurements are presented in Appendix E.

3.3.2 Stability of scratch defects

While this work will not address the approaches to improve the mechanical durability of low-E coatings, it does take interest in the stability of mechanical defects, i.e. scratches, during heat treatment. To produce consistent and comparable scratch morphologies, a CMS+ Instruments Micro Scratch Tester was employed; scratches were made with a 20-µm-radius diamond indenter

tip (Rockwell-C type) applied to the sample surface with a constant load (between 0.3 and 0.9 N) and displacement speed (10 mm/min.). Proper cleaning of the indenter tip with a cotton swab and acetone, as well as drying the tip and removing any stray particles with compressed air, was found to improve scratch repeatability. Scratches were systematically observed via optical microscopy to evaluate the types of formed defects. Their morphologies were compared to those of scratches generated on commercial low-E glass provided by the industrial partner and found to be qualitatively similar.

Scratch stability at high temperatures was evaluated by comparing the scratch visibility before and after HT. Visibility was quantified using a custom darkfield imaging set-up and subsequent analysis of the images using a *Python* image treatment script. The former allows one to obtain images in which light scattered by defects is in clear contrast to the background, with consistent lighting and photo acquisition parameters. An image treatment script then removes background intensity, extracts the remaining average pixel brightness and the width of each scratch, allowing to compare the impact of various features on the visible intensity and size of the defects before and after HT.

Additional details regarding the visibility set-up and image analysis can be found in Section 4.3.

3.3.3 Corrosion stability

As mentioned in Section 2.3.3, while there are multiple species that may result in Ag corrosion these have been found to result in similar degradation features and to be mitigatable by similar means [20], [217]. As a result, Cl exposure was used as a stand-in for exposure to corrosive species in general.

Corrosion stability testing was performed by submerging samples in an aqueous NaCl solution, using a temperature-controlled cell allowing *in situ* spectrophotometry. A concentration and temperature of 0.1 mol/L and 30 °C was used to test low-durability samples; to increase the harshness of the testing conditions, the concentration was increased to 200 g/L (≈ 3.4 mol/L), and the temperature increased to 50 °C. This drives higher Fick's diffusion (see equation 2.13) via the concentration, and the increased temperature will increase diffusivity for most diffusion processes (following the general form in equation 2.5). The latter will thus affect the mobility of Cl as it

diffuses towards the Ag layer, but also the Ag mobility as the film reorganizes in response to interactions with Cl.

Degradation was quantified by the time required for loss of visible transmission to begin and complete degrading; samples that showed no obvious degradation *in situ* were compared to their as-coated properties by *ex situ* spectrophotometry, as described above.

Additional details regarding this method are presented in Section 5.3.3.

3.4 Materials characterization

3.4.1 Ellipsometry

Ellipsometry is a versatile optical characterization technique, allowing to non-destructively obtain the thickness, interfacial roughness and optical properties of thin films in single or multilayer architectures. To do so, the sample is probed with a beam of light of known polarization; when compared to that of the reflected (or transmitted) beam, one can establish what changes resulted from interaction with the sample. The polarization of the reflected beam can be expressed as:

$$-\frac{r_p}{r_s} = \tan(\Psi)e^{i\Delta} \qquad 3.1$$

Where r_p and r_s are the reflected amplitudes in the *p* and *s* polarization, and Ψ and Δ are, respectively, the ratio of the amplitudes and the dephasing between them. In and of itself, this information does not contain explicit information about the sample. Rather, a model of the optical properties, thicknesses, roughnesses, etc., of the layers is used to predict the expected polarization changes for a given sample and compared to the measured data. Then, by adjusting the model to improve the agreement between predicted and measured values of Ψ and Δ, more precise sample properties can be inferred. In this work, modelling was performed using the *CompleteEASE* software by J.A. Woollam; in this software, minimization of the mean-square error (MSE) between predicted and measured ellipsometric values is used to evaluate the validity of the model.

As a result, ellipsometry measurements are indirect, and the quality of the used model will greatly impact them. Thus, a good understanding of the physical properties of a given material and of the optical features which result from them is required; [244] and [245] are good references in this regard. Additionally, the initial parameters used in the model must be as accurate as possible:

otherwise, when fitting the model to measured data, the regression algorithm can converge at a local minimum of the MSE, yielding inaccurate results. Preliminary measurement of specific film properties can improve this, e.g. by ellipsometric measurements of individual layers prior to modelling them in a multilayer stack, or by measuring of the film thickness via stylus profilometry (discussed in the following subsection).

In addition to the previous points, there must be sufficient experimental data to identify unique solutions during fitting. Indeed, one cannot determine all three of its main parameters, i.e., the thickness and both refractive index components (t, n, k), from only two ellipsometric parameters (Ψ, Δ); as even for a non-absorbing material ($k = 0$), there will exist multiple combinations of parameters which yield identical Ψ and Δ. Assuming these solutions are sufficiently distinct, and that the initial model values are reasonably accurate, this needn't cause issues, but especially when considering rough layers, absorbing layers, multilayer architectures, and so on, approaches alleviating this will be gain in importance. A variety of such methods are reviewed in Hilfiker *et al*. [246]; namely, the benefits of spectroscopic ellipsometry (ellipsometry performed at multiple wavelengths, as used throughout this work) is described. Below, the two types of ellipsometers used in this work will be presented, as well as the techniques used to increase the amount of data points relative to the number of modeled parameters associated to each of them.

Ex situ ellipsometry was performed using a J.A. Woollam RC2-XI variable angle spectroscopic ellipsometer with dual rotating compensators, with a wavelength range extending from 210 nm to 2500 nm. By enabling acquisitions at multiple angles (45°, 55°, 65° and 75°, by default) it can obtain data from reflections above and below a given material's Brewster angle, adding meaningful additional data for dielectric layers and multilayer stacks in particular. Transmission spectrophotometry data can also be acquired directly using this instrument or imported from the spectrophotometers described in Section 3.2.1; this is particularly useful for the analysis of absorbing films. As the total transmission lost to absorption will vary with the thickness as well as with k, this allows to restrain the value-pairs these parameters can assume.

In situ ellipsometry (ISE) was performed primarily using a J.A. Woollam iSE spectroscopic ellipsometer (400-1000 nm), mounted on the CMS-18's deposition chamber; some of the data in the Chapter 7 used a M-2000 model from the same manufacturer (245-1650 nm). Both are qualitatively similar, albeit the M-2000 includes a rotating compensator, notably allowing

improvements in terms of data accuracy and sample alignment. Naturally, being restricted to a fixed position at the chamber viewports, variable angle measurements and addition of transmission data are not possible. Preliminary calibration of dielectric optical properties via *ex situ* ellipsometry greatly facilitates their analysis, and the ability to acquire data throughout the fabrication allows the fitting of one layer at a time, simplifying analysis of multilayers. To deconvolute thickness and absorption, interference enhanced (IE)-ISE can be used [246], [247]. This technique relies on using substrates with pronounced interference features, such as silicon with a thick thermal oxide; as these features are sensitive to the intensity of the light transmitted through an absorbing layer and to the substrate, they allow much greater sensitivity. Whereas the original technique proposed by Arwin and Aspnes proceeds by fitting film properties and evaluating the presence of interference artefacts within them [247], in this work we shall rather proceed by modelling the film material properties with smooth parametrizations (i.e. modelling the film with a limited amount of broad physical oscillator functions), so that such artefacts cannot be formed. Thus, using optical parametrizations that restrict the ability of n and k to vary independently, the thickness and optical properties of Ag can be measured throughout deposition. This allows to identify the continuous film formation threshold thickness, t_c, as presented by Colin *et al.* [85].

An example illustrative of these two approaches is shown in **Figure 3.4**, where *in situ* ellipsometry measurements of a Ag film deposited on a silicon wafer with 1 μm of thermal oxide are compared are compared to the results obtained with different modelling parameters. The Ag optical properties were modelled using a b-spline function with an energy resolution of 0.05 eV or parametrized with a Drude oscillator, and the modelled layer thickness was fixed at either 15 or 22.5 nm. As can be seen in the top two subplots, the b-spline model allows a very close fit to the experimental data and yields low values of MSE for both thicknesses. However, for a layer thickness of 15 nm, large spikes appear in the resulting refractive index values; this is an example of substrate artifacts, which are minimized for an appropriate fit. On the other hand, the smooth Drude parametrization does not allow such features in the optical properties, resulting in important mismatch in Ψ and Δ for the 15 nm thick layer, with much higher values of MSE. Fitting the Drude model at a thickness of 22.5 nm, the mismatch is minimized, yielding low MSE, and realistic optical properties from which one can infer physical properties of the Ag layer, namely its resistivity.

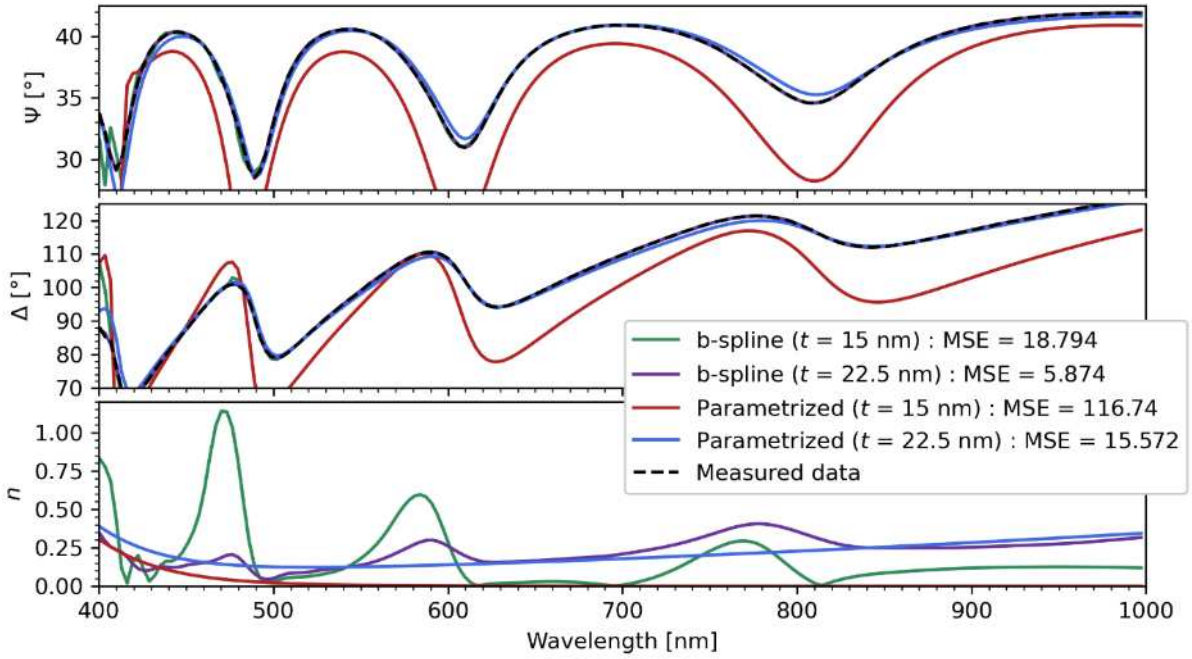


Figure 3.4: a), b) *In situ* ellipsometric measurements (Ψ, Δ, respectively) of a Ag film deposited on a silicon substrate with 1 µm of thermal oxide. These are compared to simulated results obtained by modelling the Ag layer with a b-spline function or Drude oscillator, as well as with different film thicknesses. **c)** Refractive indices (n) of the Ag film, as obtained with each of the models used in **(a)** and **(b)**.

More details regarding this approach, as well as the description of a novel method allowing to measure the percolation threshold thickness, t_p, regardless of the chosen substrate, are presented in Sections 6.3 and 6.4.1.

3.4.2 Stylus profilometry and atomic force microscopy

In order to measure the thickness and the roughness of films independently of their optical properties, stylus profilometry and atomic force microscopy (AFM) were respectively used.

Stylus profilometry consists of applying a cantilever with a fine pointed tip (radius 12.5 µm) to a sample with extremely low force (< 0.0001 N) such as to not disrupt or deform the sample. Moving the tip across the sample and measuring its vertical displacement, surface topography can be measured. In the case of the samples in this work, the scale of roughness encountered is far too low

to be measured by this method, however by masking areas of a given sample such as to produce a neat edge between coated and uncoated regions, this approach could be used to measure the thickness of films during calibration of films with as-of-yet unknown optical properties, in addition to measuring the size of larger structural defects, such as the scratches discussed in Section 3.3.2. Stylus profilometry was performed using a Bruker DektakXT instrument.

AFM, while more advanced, follows the same principle of using a cantilever with a sharp tip to map out the sample topography. In this case however, minute deflections of the cantilever, induced by atomic forces working between it and the sample, are monitored by a laser reflected off its back surface. Rastering the cantilever over the sample surface then allows to reconstruct a topographical map of the surface with sub-nanometer-scale vertical and nanometer-scale lateral resolution, measuring roughness and small morphological features such as discontinuous Ag islands. All AFM results were obtained with a Bruker Dimension ICON AFM; controllers and other parameters used are specified in a case-by-case basis in Sections 5.3.4 and 6.3.

3.4.3 X-ray diffraction

X-ray diffraction (XRD) relies on constructive interference of X-rays reflected at atomic planes; if light reflected at two atomic planes spaced apart by a distance d have an optical path difference equal to the wavelength multiplied by an integer n, they will undergo constructive interference. By changing the angle of the incident X-rays, the difference in path length changes, and for a known wavelength λ, the angle at which constructive interference occurs allows to measure the spacing between atomic planes, following Bragg's law, shown in the following equation:

$$n\lambda = 2d\sin(\theta) \tag{3.2}$$

where θ is the angle between the incident beam and the reflecting plane. XRD can be used in different geometries to tailor the gathered information. Often this is performed in Bragg-Brentano, or θ-2θ, geometry, in which the sample and detector are rotated such that the reflecting (detected) crystalline planes are parallel to the sample surface; this allows to identify the crystal orientation relative to the surface of the material. Alternatively, grazing incidence can be used, with the incident beam arriving at a constant, shallow angle from the surface ($\approx 1°$), and the detector is swept across a wide range. While this doesn't explicitly inform us how crystallites within a layer

are oriented relative to the surface, it creates a much larger volume of interaction, which is particularly useful to obtain meaningful signal from thin layers. Thus, this can be help identify if any crystalline phases are present in samples where no obvious diffractions peaks are observed in Bragg-Brentano geometry.

In principle, the Scherrer equation can be used to estimate crystallite sizes by measuring the full width at half-maximum of diffraction peaks; however, particularly for thin samples with low signal (and thus, weak maxima), other contributions broadening the signal can gain in importance, and such measurements need to be taken with appropriate reserve [248].

Given these caveats, XRD was used to a limited extent in the following chapters. However, this technique was important in identifying which phases were present in deposited layers, or emerged following heat treatment, as well as their crystalline orientation. This allowed to identify the main crystallinity changes taking place during annealing; some preliminary results are shown in Appendix A. All XRD measurements were performed using a Bruker Discover D8 instrument, utilising Cu Kα radiation (λ = 0.15406 nm).

3.4.4 Wafer curvature stress measurements

Wafer curvature is a non-destructive technique allowing one to assess the total stress state of thin films. To do so, films are deposited on a thin substrate with known mechanical properties (typically a Si wafer), and its curvature is measured by the deflection of a laser at the sample surface before and after deposition, allowing to obtain the chang in curvature induced by the film stress. Knowing the thickness of the film, which can be easily obtained using *ex situ* ellipsometry for films with known optical properties, its average stress can be obtained from the Stoney equation. Further reading on the measurement and mechanisms of stress in thin films can be found in [109].

While stress measurements are scarcely referred to in the following chapters, it was notably used to investigate the effect of different process parameters on amorphous $SiN_{(Al)}$ layers. Indeed, significant changes in their performance as diffusion barriers was found, but these could not be correlated to changes in the optical properties, nor did they display diffraction features to be studied by XRD. These results are discussed in Appendix A and highlight the importance of film stress on barrier layer functionality and low-E temperature stability. All stress measurements were

performed with a Tencor Flexus FLX 2900 instrument, allowing *in situ* heating under a N_2 purged environment for measurements of high temperature stress changes.

3.4.5 Scanning electron microscopy

Scanning electron microscopy (SEM) was used to investigate the planar microstructure of various samples in this work, particularly that of the Ag films. True to its name, this technique measures the electrons emitted or reflected from the sample while scanning an electron beam across its surface, using the much smaller wavelength of electrons to overcome traditional optical diffraction limits. Controlling the accelerating voltage of the probing electrons, as well as selecting specific subsets of emitted electrons allows further information to be extracted.

Secondary electron imaging collects low-energy, inelastically scattered electrons; given their low energies (resulting in low escape depths) and the angular dependence of the scattering cross-section, this allows high sensitivity to the surface topography. This method is typically used at lower accelerating voltages to ensure that electrons are emitted from a shallow interaction volume.

Backscattered electron imaging collects high-energy electrons which are elastically scattered from the sample. As the cross section for elastic scattering increases with the size of the atomic nucleus, this method allows contrast in atomic number; this is particularly useful to identify Ag, as all of the other film materials used in this work are oxides or nitrides (which decreases the average atomic number of the materials) of elements with significantly lower atomic number than Ag. Conversely, this method can be used at higher accelerating voltages to increase the depth probed and investigate the morphology of encapsulated Ag films.

Finally, energy dispersive X-ray spectroscopy (EDS) enables more precise elemental identification. Inelastic scattering of electrons can eject core electrons, resulting in the emission of characteristic X-rays as higher level electrons relax to occupy the empty core state. While this technique is highly useful in the identification of specific elements, the accelerating voltage must be sufficiently high to eject said core electrons, and overlapping X-ray peaks can result in difficulties in deconvoluting certain elements [249].

In this work a number of different SEM systems were used for different experiments; these are described in Sections 4.3 and 6.3.

3.4.6 Transmission electron microscopy

Transmission electron microscopy (TEM) uses higher accelerating voltages to both achieve higher resolution as well as transmit electrons through thin samples (≈ 100 nm or below); this allows electromagnetic lenses to reconstitute the transmitted electrons into an image without rastering the beam across the sample surface. Given the high energy of the incident electrons, the interactions highlighted for secondary electrons do not play an important role. Instead, signal losses due to backscattered electrons create contrast according to the density and thickness of the studied samples; however, as here me measure the transmitted rather than backscattered electrons, high-density areas result in dark areas rather than bright ones, at least in brightfield TEM. In addition to this, diffraction effects can take place given the extremely short wavelength of the high energy electrons, adding contrast due to diffracting crystalline planes. To isolate the contribution of diffracted electrons to contrast, darkfield TEM, imaging subsets of scattered electrons, can be used.

In this work, TEM is used to image thin coating cross-sections extracted by focused ion beam (FIB) milling and investigate their structure as a function of the depth from the surface. In this case, distinguishing layers, their interdiffusion, and their uniformity being the main objective, TEM was primarily performed in brightfield mode. Further elemental analysis is performed using EDS. Different TEM and FIB systems were used in this work and are described in Section 4.3.

3.4.7 X-ray photoelectron spectroscopy

X-ray photoelectron spectroscopy (XPS) is a chemical analysis technique that functions by probing the core electrons of elements similarly to EDS, but using opposite mechanisms; here, the sample is irradiated with X-rays, stimulating emission of photoelectrons; these are ejected with kinetic energy (KE) equal to that of the incident X-ray energy ($h\nu$) minus the electron's binding energy (BE). Measuring relative to the Fermi level, this must be offset to the detector's work function (Φ_{detector}), which is constant. Together, this yields equation 3.3, shown below. Rearranging to isolate BE, we find that for an X-ray source with a well-defined energy, measuring the kinetic energy of ejected electrons provides the binding energy of the state they were ejected from.

$$\text{KE}_{measured} = h\nu - \text{BE} - \Phi_{detector} \qquad 3.3$$

XPS has the advantage of probing the sample with photons, rather than electrons, as in EDS; the limited charging induced by ejection of photoelectrons is minimal compared to the effect of electron irradiation, which has proven essential to monitoring Na diffusion. Indeed, Na^+ ions readily migrate under electron irradiation, complicating their identification in EDS [205], [250].

In principle, small variations in the binding energy of different electrons allows to access information about the chemical state in addition to elemental identification. However, in this work XPS will exclusively be used for atomic composition depth profiles. Given its surface sensitivity, which results from the low escape depth of the produced photoelectrons, depth profiling requires periodic high-energy etching steps to be carried out between each acquisition. This was found to gradually shift the measured peak energies, despite charge compensation; as a result, binding energy corrections could not be applied with sufficient precision to perform high resolution XPS measurements in which the different chemical states are resolved.

All XPS experiments presented in this work used a Thermo Fisher Scientific ESCALAB Xi+ system with an Al Kα X-ray source. Depth profiling and acquisition parameters are detailed in Appendix B.

CHAPTER 4 ARTICLE 1 : ROLE OF ATMOSPHERIC AND SUBSTRATE CONTAMINANTS ON THE DEGRADATION AND DEFECT VISIBILITY IN AG-BASED LOW-EMISSIVITY COATINGS

4.1 Foreword

Having established the mechanisms that determine the formation and degradation of Ag films, as well as the techniques with which we can analyze these processes, the scientific context of this work is now in place; its results can now be presented.

This chapter thus presents the first of three articles written as part of this thesis. While not chronologically the first to be written, this article demonstrates well the scope of the degradation that can occur when coatings are subjected to contaminant diffusion or structural changes, and thus contextualizes the rest of this work well.

Here, the first objective of the thesis is addressed, investigating the role of contaminants in the degradation of low-E coatings at high temperatures, in pristine ‘as-coated’ stacks and at scratch defect sites, where their diffusion is facilitated and their impact is amplified. To do so, contaminant diffusion is selectively enabled to isolate the effect of a given species, decoupling the multitude of factors affecting HT stability, and allowing to quantify their impact on coating performance and defect stability. Microstructural analysis of the coating morphologies resulting from each contaminant then allows to pinpoint the mechanisms driving degradation and inform the design of improved low-E coatings.

It should be noted that this article begins from a point where low-E coatings with performance and stability comparable to those of commercial coatings has already been achieved. While this doesn’t expand the state of the art, and thus isn’t of great interest for a publication, neither is it a trivial result. Consequently, there is a lack of literature explicitly discussing the methods to reach this point, which can make replicating this starting point unnecessarily challenging. To remedy this, Appendix A offers a brief overview of the steps taken to obtain low-E coatings with decent high temperature stability, which ought to allow others to reproduce and improve upon this work more easily.

Finally, in addition to the integral text of the article presented in this chapter, the supporting information associated to it is included in Appendix B; references in this chapter have been adjusted to appropriately refer the reader there.

ROLE OF ATMOSPHERIC AND SUBSTRATE CONTAMINANTS ON THE DEGRADATION AND DEFECT VISIBILITY IN AG-BASED LOW-EMISSIVITY COATINGS

Phillip Rumsby, Bill Baloukas, Etienne Bousser, Oleg Zabeida, Ludvik Martinu*

Department of Engineering Physics, Polytechnique Montréal, Montréal, QC H3T 1J4, Canada

Submitted to *Acta Materialia* on 2026-01-15.

Abstract

Ag-based low-emissivity (low-E) window coatings allow for important energy savings. However, in architectural applications, it is required that the coating be deposited prior to tempering the glass. During this process, several mechanisms can lead to coating degradation: amongst these, Ag interaction with contaminants, which present increased diffusivity at high temperatures, is particularly important. Even when appropriate barrier layers are present, any defects can become highly visible following tempering.

This work aims to isolate the effect of different contaminants, to evaluate their impact on Ag degradation alone, in combination with other contaminants, and at defect sites. To do so, partial stacks with various barrier layer configurations are deposited on substrates with different contaminant concentrations and tempered in controlled atmospheres in order to selectively enable contaminant diffusion in otherwise identical coatings. Subsequent scanning electron microscopy measurements allow to identify the distinct effects of Na and O_2 on Ag dewetting and correlate these to electrical and optical changes.

Defects are then generated in a controlled fashion using a microscratch tester. Quantitative analysis of defect visibility is extracted from dark-field photographs of the scratched samples. Controlling for the presence of different defect types within the scratches and the availability of atmospheric and substrate contaminants, their effects on scratch visibility accentuation are evaluated. Scanning and transmission electron microscopy observations reveal that buckling defects, whose formation during tempering is facilitated by Ag dewetting, lead to the highest visibility due to formation of small, highly scattering Ag nanoparticles within the buckled areas.

4.2 Introduction

Silver (Ag)-based coatings are growing increasingly important for optical applications, including transparent conductive electrodes [24], [27], [251], telescope mirrors [21], [37], [252] and low-emissivity (low-E) windows [5], [8], [253]. However, the Ag layer is susceptible to a number of agents which can be present as part of typical usage environments [37], [38], [252] and is prone to further forms of degradation when exposed to high temperatures [34], [40], [160], [254].

To stabilize Ag-based coatings, various protective strategies (such as encapsulating layers [156], [255], [256], metallic barrier layers [20], [22], [178] and dopants [32], [92], etc.) are put in place. However, in the occurrence of small defects disrupting these, exposure to damaging environments can lead to significant localized degradation, which can impede the overall functionality of the coating [37], [38], [40], [252], [254].

Scratch visibility accentuation during tempering of low-E glass is one such case: coating scratching, occurring as part of handling and preparation of the glass prior to tempering [6], may result in the generation of minor defects which are difficult to screen initially but which become highly visible following tempering. As glass cannot be cut with conventional methods following tempering [47], these small initial defects can lead to coated glass being rejected from usage at the very end of its production. The implementation of effective strategies to understand and counter high-temperature defect accentuation is complicated by the vast number of processes can take place during tempering. Namely, high temperatures may enable contaminants from the atmosphere (H_2O, O_2, S, Cl) [34], [37], [38], [252] or the substrate (Na) [201], [208], [257] to more easily diffuse to the Ag layer, enable Ag thermal grooving or dewetting [34], [35], [258], as well as generate phase and stress changes [41], [109], [208] in the adjacent layers which may prompt

further degradation [35], [259], [260]. Moreover, not all of these are well understood: namely, the importance of mitigating sodium diffusion is frequently discussed, even though an accounting of its specific effects on the Ag layer is, to this day, absent [6], [203], [204].

This work, therefore, first aims to investigate the effect of given contaminants, combined and in isolation, as well as determine their degree of contribution to high-temperature defect accentuation in low-E glass. To this end, various partial stacks allowing selective contaminant diffusion are produced and annealed in controlled environments and on substrates with different compositions, allowing one to decouple the effect of the coating architecture from the effect of different combinations of contaminants. Performance changes are evaluated by their impact on the coating optical and electrical properties. Additionally, scanning electron microscopy (SEM) imaging of the sample surfaces and transmission electron microscopy (TEM) analysis of coating cross-sections are used to observe the morphological changes occurring in these samples and are correlated with the resulting performance changes.

Controlled defects are then generated in standard low-E samples with a micro-scratch tester. The morphology and visibility of these scratches, prior to and following heat treatment, are measured and correlated. Using the same controlled annealing atmospheres and substrate compositions as previously, scratch visibility accentuation is compared as a function of the initial scratch morphologies as well as the presence of atmospheric and substrate contaminants. Finally, investigation of the morphological changes at scratched sites are performed with SEM and TEM analysis of cross-sections extracted from the scratches. In conclusion, a discussion of the relative importance of the observed mechanisms is proposed, and modifications to reduce scratch visibility accentuation are suggested.

4.3 Methods

Substrates used in this work were 3-mm-thick soda-lime glass (SLG) or borosilicate glass (BSG), typically 50 mm × 50 mm in size. Their chemical composition was analyzed by X-ray photoelectron spectroscopy, as shown in **Table B.1** of Appendix B. Their mechanical and thermal properties are given in **Table B.2** of Appendix B.

Substrate cleaning consisted of manual wiping with a Cole-Parmer Micro-90 cleaning solution, diluted to 1% in deionized water, followed by subsequent ultra-sound baths in a Micro-90 solution, deionized water, acetone, and isopropanol. Following removal from the isopropanol bath, samples were dried using a compressed air knife to uniformly remove any remaining solvent. Finally, all substrates were pretreated by RF plasma cleaning using an Ar/O_2 gas mixture (100/35 sccm) at a pressure of 8 mTorr, with a -235 V (25 W) bias for 5 minutes.

Film fabrication was performed by magnetron sputtering using a Kurt J. Lesker CMS-18 deposition system with four 3-inch magnetrons, allowing to deposit all layers without breaking vacuum. All layers were deposited from high purity compound targets (purity of 99.9% or higher), to ensure the absence of contaminants in the as-coated stacks, with the exception of Ag, deposited from a 99.99% pure Ag target. Target compositions and deposition parameters were selected to emulate industrial reference coatings.

Annealing was performed in a Carbolyte Gero tube furnace. Samples were heat-treated for 8 minutes at 650 °C, confirmed using a thermocouple. Plugs with a feed tube for controlled gas insertion and a small opening to maintain pressure while feeding in gas were used to anneal samples in controlled atmospheres, using a flow of approximately 7 scfh (140 slm), with an inlet pressure of approximately 30 psi (200 kPa). In addition to ambient air, dry air (N_2 with 20-22% O_2, < 3 ppm H_2O) and argon (99.999% pure) were used. Samples are referred to as as-coated (AC) or heat-treated (HT) depending on whether or not they have been annealed.

Optical and electrical characterization were performed using a Perkin-Elmer Lambda 1050 spectrophotometer equipped with a 150-mm-diameter integrating sphere allowing to obtain total and diffuse transmittance and reflectance measurements. Characterization of the optical properties of individual layers was performed using a J.A. Woollam RC2-XI variable angle spectroscopic ellipsometer. Film thickness during deposition was monitored using an iSE fixed-angle ellipsometer from the same manufacturer in order to ensure comparability between samples. Sheet resistance measurements were obtained with a Delcom RD200 non-contact sheet resistance monitor.

Scanning electron microscopy (SEM) was performed with various systems as a function of the investigated features. Initial sample overviews at low magnification were performed using a Thermo Fisher Scientific Helios 5 UC FIB-SEM. Following observations on partial stacks were

performed using a JEOL JSM-IT800 with energy dispersive X-ray spectroscopy (EDS) capabilities. Select scratched samples were also imaged using a Thermo Fisher Scientific Helios 5 UX FIB-SEM, prior to extraction of thin lamellae by focused ion beam (FIB) milling.

Transmission electron microscopy (TEM) was performed on un-scratched partial stacks using a Thermo Fisher Scientific Talos F200. TEM measurements of scratched samples were performed using a JEOL JEM-F200. TEM cross-sections were extracted with the respective FIB-SEM systems listed above. Prior to FIB extraction, scratched samples were overcoated with a ≈ 50 nm carbon layer by arc evaporation in order to protect the sample during deposition of an additional tungsten layer within the FIB system.

Controlled scratch generation was performed using a CSM Instruments Micro Combi Tester, equipped with a Rockwell-C sphero-conical diamond indenter with a 20 μm tip radius. Scratches were generated using constant loads ranging between 0.3 N and 0.9 N, with 10 mm scratch lengths and a tip displacement speed of 10 mm/min. The indenter tip was cleaned before each scratch using an acetone-soaked swab and dried with compressed air. Scratch sets were placed at the center of each sample, with 2 mm spacing between them. Optical microscopy was performed on scratched samples prior to heat-treatment to qualitatively evaluate the types of occurring defects.

Quantification of scratch visibility was performed using a custom darkfield imaging camera set-up and a custom-made *Python* image treatment script. The imaging set-up is largely the same as used by Rocha *et al.* [261], with adjustments accounting for the usage of transparent samples. It consists, in first part, of a Nikon D7000 camera with a Sigma 105 mm F2.8 macro lens, circular polarizer filter, and extension tubes, attached to a support rail such as to point down through an opening in a hemispherical dome, in which the sample is placed flat below the camera. A strip of LED lights is set along the circumference of the dome, at an angle of approximately 30° from the sample normal. The dome is painted in a highly absorbing black paint (Musou black) to remove specular reflections from the sample and other internal light reflection. The sample is held in a 3D-printed holder inside which a custom absorbing filter (88 nm SiO_2 /9 nm Cr/60 nm SiO_2) is placed at an angle, trapping light transmitted by the sample. As a result, only the light scattered in reflection from the sample, i.e. by defects, reaches the camera. Photos are then taken with fixed conditions: an aperture of f/16, ISO 100, and exposure time of 2 s. The setup is shown schematically in **Figure B.1** of Appendix B.

The overall visibility of the scratches was quantified following two metrics: their intensity (i.e., their brightness) and their width. Each sample was photographed in two orientations (rotated by 180° from its initial position) in order to account for experimental errors, such as sample placement affecting the lighting conditions. Samples were imaged before and after annealing such that defect visibility accentuation could be quantified by the increase in intensity and in width for each individual scratch.

To obtain quantified values, the images captured with the darkfield imaging set-up were first converted to grayscale images, then the average pixel intensity was calculated for each row of pixels; the average intensity along the axis perpendicular to the scratch can then be presented as a curve in which the scratches form neat peaks, as shown in **Figure 4.1**. Once peaks are identified from the resulting curve, a background curve is fit to the data between the peaks, allowing one to fit the background intensity of the image.

The scratch widths are extracted from the raw signal using the *SciPy* "peak_widths" function [262]. In order to avoid over-evaluation of the scratch widths due to noise (caused by dust particles, sample haze, or unwanted defects resulting from handling) widening the peak base, the intensity at which the width measurement is performed is increased for samples with a high background to peak intensity ratio. While this allows consistent measurements without introducing user bias, it can lead to lower width measurements for peaks with low raw intensity relative to the background. This is exemplified in **Figure 4.1**, where the addition of a background filter, which increases the overall background intensity, but not the raw peak intensity, results in measuring the width at a higher point on the peak, yielding a lower scratch width. Scratches with peak intensities which are comparable to the background are assigned a width of 0. Finally, when measuring multiple scratches, the distance between peaks (which is fixed at 2 mm, as described above) is used to calibrate the pixel size, allowing to convert scratch width into microns.

Following this, the background is subtracted from the curve and the resulting peak values are tallied as the intensity of each scratch. The average value of the background intensity (i.e., the dashed orange curve in **Figure 4.1**) is also recorded. Scratches with peak intensities which are comparable to the background intensity are similarly assigned an intensity of 0. The rightmost column of **Figure 4.1** reveals that a higher background value will thus result in a lower scratch intensity, accounting for any variations due to sample lighting. Moreover, it shows that a

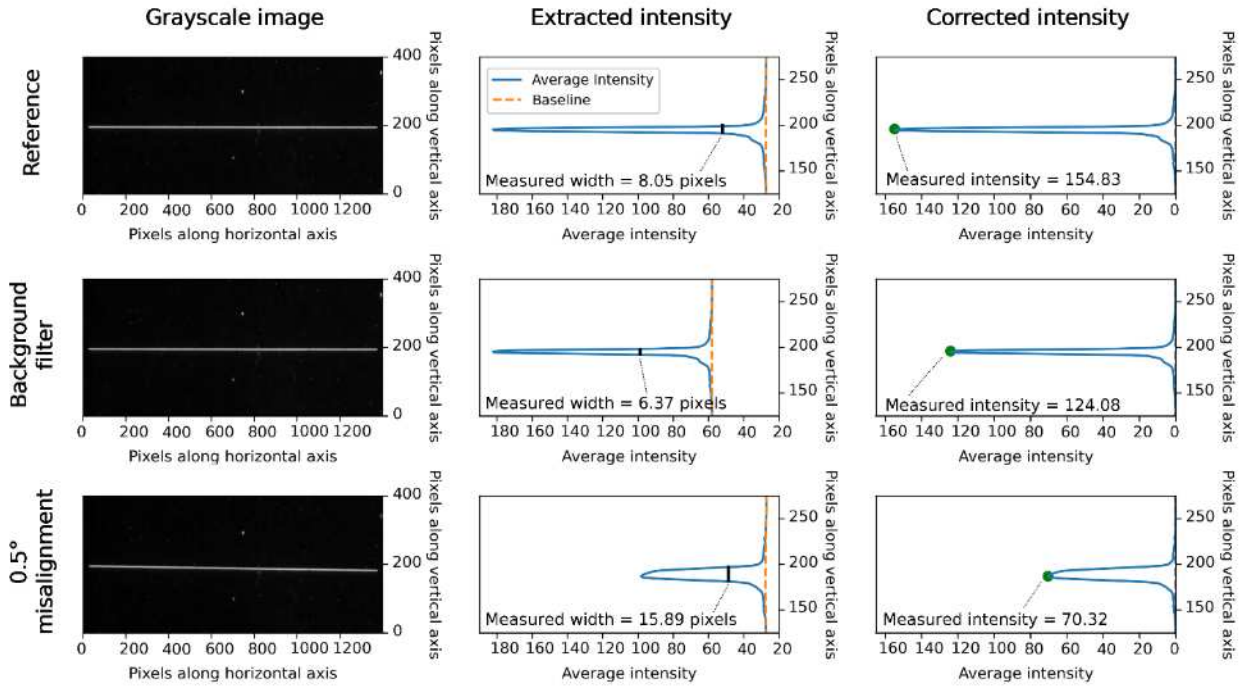


Figure 4.1: Example of the image treatment process used to quantify scratch visibility. From left to right: conversion to grayscale images, conversion to intensity curves and width measurement, and background correction and intensity measurement. Additional examples (middle and bottom rows) show how the measured scratch width and scratch intensity vary for a higher background intensity and for misalignment between the scratch direction and measurement axis.

misalignment of only 0.5° between the scratch direction and the measurement axis can result in much lower scratch intensity, as well as much higher widths. Thus, each image was automatically rotated in a range of -0.5° to 0.5°, in increments of 0.1° to find optimal alignment of the averaging axis and the scratch direction.

4.4 Results & discussion

4.4.1 Effects of contaminants and structural changes in the absence of defects

4.4.1.1 Heat treatment of partial stacks

In the first set of experiments, the effect of contaminants on coatings, irrespective of defects, was investigated. This is complicated by the fact that the type of coatings relevant to this work, which undergo defect accentuation during annealing, are specifically those are stable at high

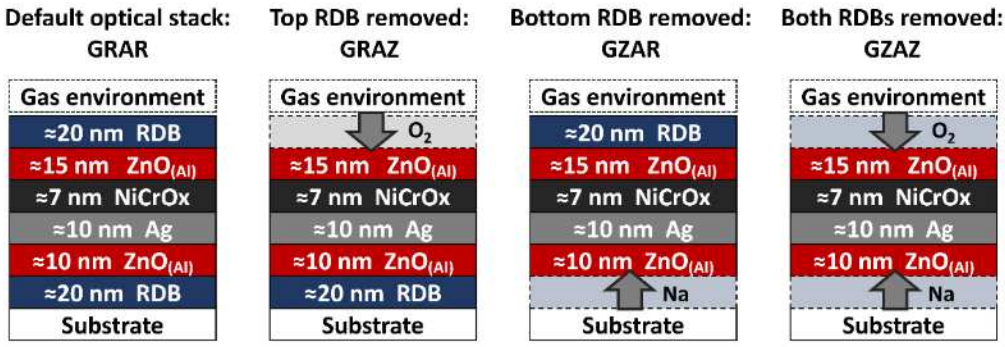


Figure 4.2: Schematic overview of model stack architectures used in Chapter 4.

temperatures, and which mitigate contaminant diffusion. To address this, various stack designs selectively enabling the diffusion of contaminants from the substrate (i.e., Na) and atmosphere (i.e., O_2) were produced, shown schematically in **Figure 4.2**. While, in principle, there are other potential atmospheric and substrate contaminants, given the high concentration of O_2 and high mobility of Na [196], [198], these are assumed to be the most important during tempering.

The stacks used in this work follow intentionally generic designs in order to highlight the qualitative roles of the different coating layers. The default stack type thus consists of rigid diffusion barrier (RDB) layers (such as SiO_2 [257], Al_2O_3 [263], [264], SiN [236], [265], TiN [266], and variations thereof [183], [267], [268]) deposited at the substrate and atmosphere interfaces, offering protection against contaminant diffusion. $ZnO_{(Al)}$ layers are deposited on either side of the Ag film to act as a seed layer and as an optical space layer, keeping the Ag layer encapsulated, even when RDB layers are absent. $NiCrO_x$ layers are deposited over the Ag film to protect the layer from oxidation during deposition of the subsequent $ZnO_{(Al)}$ layer. Thus, the selective removal of the RDB layers allows for controlled contaminant diffusion while keeping the core stack layers the same. Each of the partial stack designs is named after the materials used at the atmosphere and substrate interfaces (Z for $ZnO_{(Al)}$, R for RDB), indicated relative to the glass substrate and Ag layer (G and A, respectively), such that a sample with a glass/$ZnO_{(Al)}$/Ag/$NiCrO_x$/$ZnO_{(Al)}$/RDB architecture would be named GZAR, as shown in **Figure 4.2**.

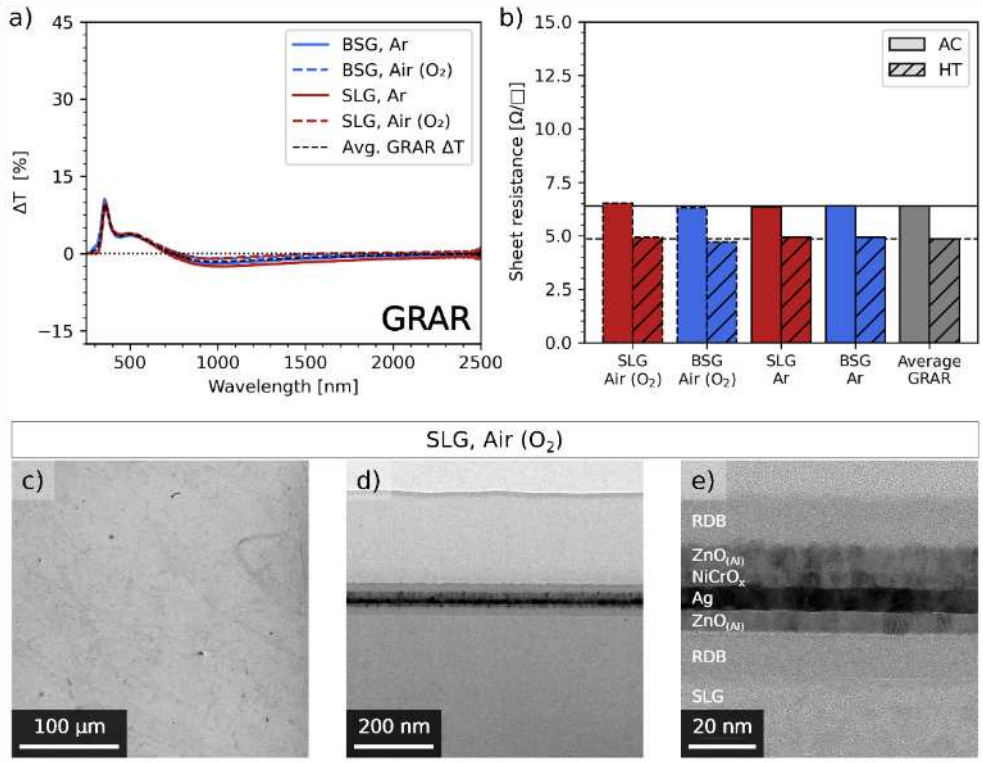


Figure 4.3: Optical, electrical and microstructural observations of annealed GRAR-type stacks. All samples were heat-treated for 8 minutes at 650 °C. **a)** Transmission change ($\Delta T = T^{HT} - T^{AC}$) and **b)** sheet resistance measurements for various annealing conditions. Full and dashed lines in **(b)** correspond to the average sheet resistance of all GRAR samples, for their AC and HT states, respectively. **c)** SEM (3 kV accelerating voltage, secondary electron mode; contrast enhanced for visibility) and **d)**, **e)** TEM imaging of a GRAR-type stack deposited on SLG and annealed in air.

To properly isolate the effect of contaminant diffusion, however, the effect of removing these layers (changing the effective deposition surface for subsequent layers, enabling recrystallization [269], modifying the stresses applied at various interfaces, etc.) must be taken into account.

To do so, each low-E architecture was deposited on soda-lime glass (SLG) as well as borosilicate glass (BSG) substrates with low Na content, as shown in **Table B.1** of Appendix B. For each substrate, one copy of each architecture was annealed in ambient air (allowing for O_2 diffusion) and another in Ar gas. **Figure B.2** and **Table B.3** of Appendix B, respectively, summarize the resulting optical and electrical changes of all samples.

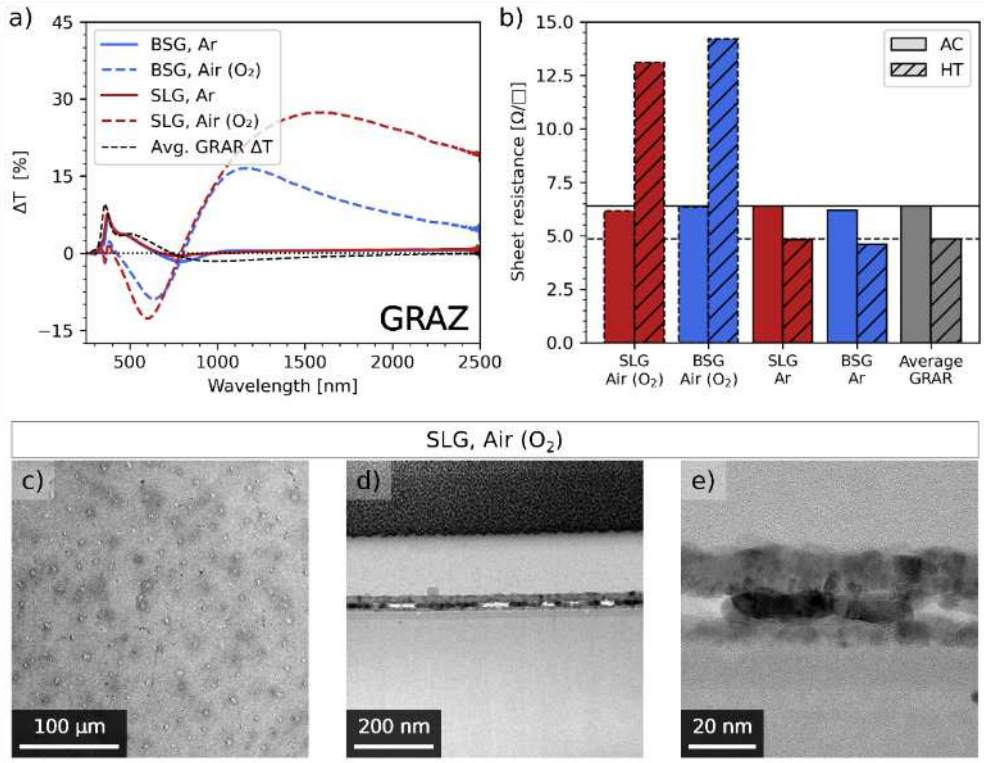


Figure 4.4: Optical, electrical and microstructural observations of annealed GRAZ-type stacks. All samples were heat-treated for 8 minutes at 650 °C. **a)** Transmission change ($\Delta T = T^{HT} - T^{AC}$) and **b)** sheet resistance measurements for various annealing conditions. Full and dashed lines in **(b)** correspond to the average sheet resistance of all GRAR samples, for their AC and HT states, respectively. **c)** SEM (3 kV accelerating voltage, secondary electron mode; contrast enhanced for visibility) and **d)**, **e)** TEM imaging of a GRAZ-type stack deposited on SLG and annealed in air.

For the default GRAR stacks, with both top and bottom protective layers, high stability is found. While there are minor optical and electrical changes consistent with grain growth in the Ag film, as shown in **Figure 4.3a-b**, these changes remain consistent regardless of annealing atmosphere or substrate, and result in a better overall performance, with higher visible transmission, lower transmission in the near IR, and decreased sheet resistance. Accordingly, electron microscopy imaging of the sample on SLG annealed in air (**Figure 4.3c**) shows only minor surface defects consistent with sample handling, and the TEM cross-section (see **Figure 4.3**, images **(d)** and **(e)**), shows the expected structure for the low-E coating, with neatly aligned interfaces, and a uniform, dense Ag layer.

Results for GRAZ stacks, in which the top barrier layer is removed, are shown in **Figure 4.4**. In **(a)** and **(b)**, a sharp decrease in visible transmission is found for samples annealed in air, accompanied by an increase in sheet resistance; this is typical of dewetting, an expected result of O_2 diffusion [34]. Annealing in Ar shows no significant deviation when compared to GRAR stacks, suggesting that no other significant changes occur due to the removal of the top barrier layer. No sensitivity to the substrate type is observed either; thus the sample deposited on SLG and annealed in air was selected for microstructural investigations. SEM images in **Figure 4.4c** show large agglomerations, spaced apart by multiple microns or tens of microns. Around these, gradual changes in signal intensity can be observed; this indicates a decrease in Ag coverage around the agglomerations, in turn suggesting that the film is partially dewet in these areas. It should be noted that the image contrast was enhanced to highlight the changes; as the raw format shows much smaller differences in intensity, the gradient in dewetting around these points is taken to be relatively small. Accordingly, the TEM cross-section shown in **Figure 4.4d-e** is taken to be representative of the overall sample: here, consistent dewetting at the sub-micron scale is found, as well as roughening of the $ZnO_{(Al)}$ layers.

GZAR stacks, where the bottom RDB layer is removed instead of the top one, show similar sensitivity to the substrate's composition instead of to the atmosphere's (see **Figure 4.5a-b**). These samples undergo a visible transmission decrease and sheet resistance increase, not unlike the GRAZ samples, albeit the increase in sheet resistance is smaller. The aforementioned changes are inhibited for samples deposited on the low-Na BSG substrates, indicating that the impact of the bottom RDB layer's removal also mostly derives from contaminant diffusion. Although there are other differences between these substrates, namely in terms of thermal expansion coefficient, and changes in mechanical properties at high temperature, as highlighted in **Table B.2** of Appendix B, these are in large part governed by the concentration of alkali metals in the glass and their effect on the glass networks [196]. Therefore, while changes in applied stress from the RDB interfaces could also influence coating evolution, this appears unlikely for a few reasons. Namely, removing the top RDB layer does not result in important changes when annealing in inert atmosphere, and substituting the bottom RDB layer with a stress-relaxed SiO_2 layer, as shown in **Figure B.3a** of Appendix B, similarly maintains stability, indicating that the different behaviors for each substrate are not due to stress applied by the barrier layer. Rather, it appears that as long as a thick enough barrier is present to mitigate Na diffusion, the optical and electronic changes are suppressed.

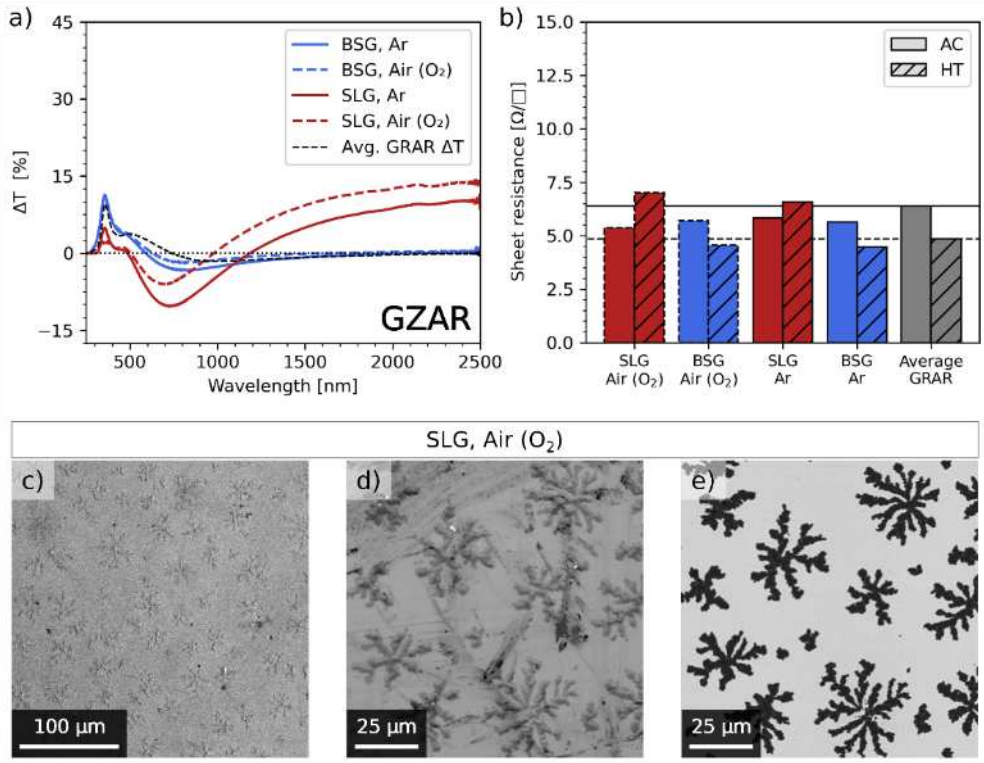


Figure 4.5: Optical, electrical and microstructural observations of annealed GZAR-type stacks. All samples were heat-treated for 8 minutes at 650 °C. **a)** Transmission change ($\Delta T = T^{HT} - T^{AC}$) and **b)** sheet resistance measurements for various annealing conditions. Full and dashed lines in **(b)** correspond to the average sheet resistance of all GRAR samples, for their AC and HT states respectively. **c)** Large-scale SEM (3 kV accelerating voltage, secondary electron mode; contrast enhanced for visibility) image. **d)** High magnification SEM image in secondary electron mode (3 kV accelerating voltage) for enhanced topographical contrast and higher surface sensitivity, and **e)** in backscattered electron mode (10 kV accelerating voltage) for enhanced atomic number contrast and lower surface sensitivity. All SEM images were taken for a GZAR-type stack deposited on SLG and annealed in air.

Further decoupling of Na diffusion from mechanical changes could be performed using field-assisted Na diffusion [209], substitution of Na with a less diffusive alkali network modifier (e.g., K) [198], or usage of an alkali glass with lower levels of alkali earth metals (e.g., Ca or Mg), which decrease Na diffusion [196].

The effect of Na diffusion on the microstructure is investigated on GZAR samples deposited on SLG substrates and annealed in air. Indeed, as the top RDB layer blocks the diffusion of atmospheric contaminants, samples annealed in air or Ar show no meaningful differences. The

large-scale SEM image shown in **Figure 4.5c** reveals widespread coverage of large branching structures: **Figure 4.5e** shows that these correspond to areas have been depleted of Ag (as confirmed by **Figure B.4** of Appendix B) whereas **Figure 4.5d** reveals curvature of the dielectric layers above the Ag-depleted areas. These patterns are indicative of dewetting of a polycrystalline film undergoing fingering instability, in accordance with the low number of sites at which dewetting has initiated [35]. Before addressing this in more depth, however, the changes observed in GZAZ stacks will be presented: these enable Na diffusion in different conditions, and their comparison to GZAR stacks will allow for a more nuanced and complete discussion.

Indeed, GZAZ stacks, with both barrier layers removed, enable diffusion of both O_2 and Na; from the results in **Figure 4.4** and **Figure 4.5**, it would be expected that samples deposited on BSG and annealed in Ar would yield optical changes similar to those found for GRAR stacks. However, **Figure 4.6a-b** reveal optical and electrical degradation in all samples, although not in equal magnitude. Annealing in air results in vastly different behavior for each substrate: on BSG, results are consistent with GRAZ samples annealed in air, where the impact of Na was restricted, whereas the sample on SLG undergoes catastrophic degradation with a much higher sheet resistance increase than any other sample. Annealing in Ar yields similar results for both SLG and BSG substrates, with sheet resistance increases which are higher than those obtained for GZAR stacks on SLG. This highlights the impact of the stack structure; if the top RDB layer was only responsible for suppressing the diffusion of atmospheric contaminants, one would expect GZAZ samples annealed in Ar to show the same changes as GZAR samples. The degradation observed in GZAZ-type stacks was found not to be inherent to the stack structure either, however. Additional results, shown in **Figure B.3b** of Appendix B, reveal that GZAZ stacks deposited on Na-free fused silica substrates do not show characteristic degradation patterns when annealed in Ar. Thus, it would appear that the GZAZ partial stack design increases susceptibility to certain degradation mechanisms, without necessarily generating new ones. Specifically, the rigid upper layer (as in the case of the GZAR stack) may restrict the formation of thick dewetting rims or other deformations allowing Ag surface diffusion, and inhibit the small amounts of Na diffusing out of BSG from initiating Ag dewetting [35].

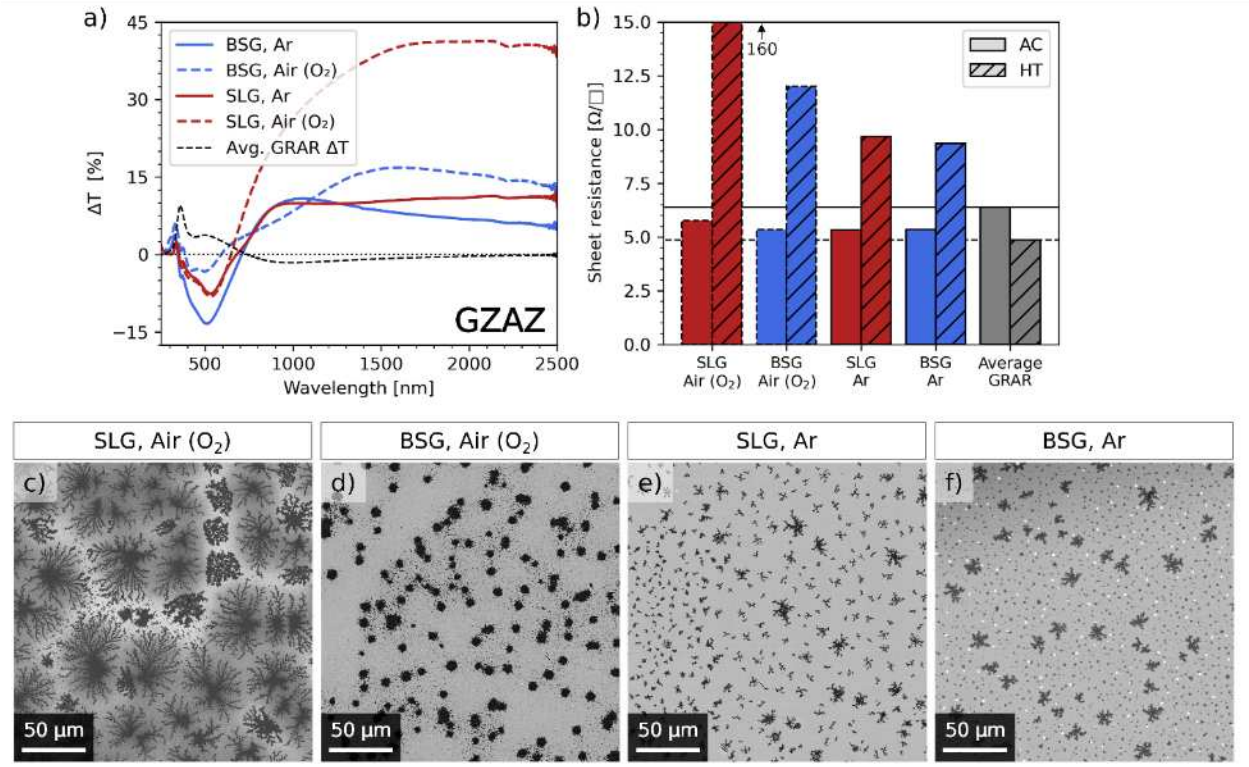


Figure 4.6: Optical, electrical and microstructural observations of annealed GZAZ-type stacks. All samples were heat-treated for 8 minutes at 650 °C. **a)** Transmission change ($\Delta T = T^{HT} - T^{AC}$) and **b)** sheet resistance measurements for various annealing conditions. Full and dashed lines in **(b)** correspond to the average sheet resistance of all GRAR samples, for their AC and HT states respectively. SEM images of GZAZ samples deposited on **c)**, **e)** SLG and **d)**, **f)** BSG, annealed in **c)**, **d)** air, and **e)**, **f)** argon. All SEM images were acquired in backscattered electron mode (10 kV accelerating voltage) to obtain enhanced contrast in atomic number and lower sensitivity to the surface topography.

SEM imaging of the morphological changes arising for each substrate in each of the annealing environments is shown in **Figure 4.6c-f**, allowing one to draw further conclusions. Images **(e)** and **(f)** reveal a much higher density of holes than for GZAR stacks, confirming that the top RDB layer mitigates formation of dewetting fronts. While the formation of a higher density of smaller dewetting pattern results in a larger increase in sheet resistance (see **Figure 4.5b** and **Figure 4.6b**), these result in less optical scattering, as shown in **Figure B.5** of Appendix B. Moreover, image **(e)**, on SLG, shows holes which are almost exclusively undergoing fingering instability, exhibiting wiry, branching shapes. On the other hand, image **(f)**, on BSG, shows only a few such structures, but with thicker channels. This confirms that Na diffusion to the Ag layer promotes dewetting,

consistent with reports for Na-doped Au [202], [210], and fingering instabilities, more specifically. This is in agreement with the observation that annealing Au in hydrogen (which may dissociatively adsorb onto Au [270]) results in formation of more fingering instabilities and faster dewetting [184]. While Na diffusion from the BSG substrate also occurs, albeit at a lower level, it seems insufficient to provoke significant dewetting when restricted by an upper RDB layer, accounting for the discrepancy between GZAZ and GZAR samples on BSG. Moreover, this is consistent with results shown in **Figure 4.5d**-**e**: the precise overlap of the areas where the top dielectrics are deformed and where the Ag layer is dewet supports the conclusion that disruption of the top RDB layer allows for greater dewetting.

Comparing images **(c)** and **(e)** of **Figure 4.6** allows one to evaluate the effect of O_2 diffusion on the fingering instabilities induced by Na diffusion from GZAZ samples on SLG. Elongation of the branches in the fingering instabilities is observed; this is consistent with increased surface diffusion for Ag films exposed to oxygen at high temperatures [34], as the speed of the dewetting front in fingering instabilities has been shown to vary mainly with the film atoms' surface diffusivity and the film thickness [35]. Moreover, intensity gradients suggest uneven Ag dewetting at a sub-micron scale, as observed for the GRAZ stack annealed in air shown in **Figure 4.4**. Modelling, presented in **Figure B.6** of Appendix B, allows to resolve the distinct optical effects of large-scale Ag depletion and dewetting at the sub-micron scale, supporting that both are taking place in this case.

The holes formed in the GZAZ samples on BSG annealed in air are notably different: **Figure 4.6d** reveals approximately circular holes with rough edges. A closer view of these holes, shown in **Figure B.7** of Appendix B, reveals some branch-like structures at the edges, and small islands remaining within them, suggesting that these are in fact due to fingering instability structures which have stagnated in radius and whose channels have widened enough to connect into a more circular defect. Indeed, some of the holes in **Figure 4.6c** appear to be converging towards a similar morphology, and are also highlighted in **Figure B.7**.

4.4.1.2 Coating degradation mechanisms under exposure to contaminants

We attribute the observed behaviors to the following model. On one hand, oxygen can be assumed to easily diffuse through the $ZnO_{(Al)}$ seed layer at grain boundaries. The decrease in Ag interfacial

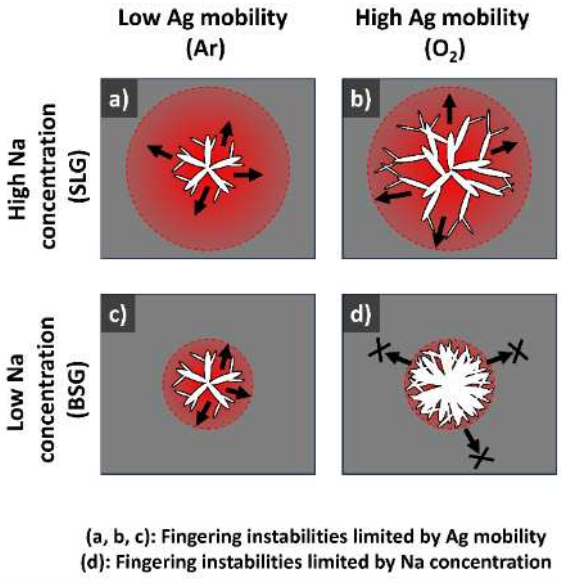


Figure 4.7: Schematic representation of the proposed model of fingering instability dewetting patterns caused by Na diffusion into Ag. Dewetting patterns (white shapes) initiate in areas where there is sufficient Na concentration (red areas) and propagate outward. **a)**, **b)** For high Na concentrations, large Na-rich areas are formed, and regardless of the Ag mobility, there is sufficient Na in the adjacent area to allow the fingering instabilities to continue to expand. **c)** For low Na concentrations, smaller Na-rich areas are formed; this does not have a significant impact for low mobilities. **d)** For high Ag mobilities, however, the fingering instabilities reach the edge of smaller Na-rich areas, and dewetting continues within their radius rather than continuing to expand outward.

energies and Ag mobility resulting from O_2 exposure are known to promote dewetting at the sub-micron scale, in agreement with the observations of Section 4.4.1.1 [34].

On the other hand, we suggest that sodium first diffuses vertically through the $ZnO_{(Al)}$ seed layer at certain egress sites, where the Na concentration in the glass is higher or via specific features such as defects, triple boundaries or pinholes. Following this, Na diffuses laterally through the Ag layer following Fick's diffusion law [170], leading to radial Na concentration gradients surrounding said egress sites. Although we do not advance a mechanism here, increased Na concentration at these points is shown to lead to hole formation and develop into fingering instabilities in agreement with previous reports [202], [210].

For GZAZ samples annealed in Ar, the rate of dewetting, limited by the Ag diffusivity [35], would limit the size of the fingering instabilities. However, with the addition of O_2, increasing Ag

diffusivity [34], different behaviors would emerge from different Na concentrations. For substrates with high Na concentration, i.e. SLG, this would simply lead to larger fingering instabilities, as is observed in **Figure 4.6c**. For substrates with low Na concentration, i.e. BSG, the advance of the dewetting front would then be limited by the size of the area with Na concentration high enough to generate dewetting [210], leading to stagnation of the size of the dewetting features following the radial Na diffusion, also in agreement with the above observations. This is shown schematically in **Figure 4.7**.

As Na typically diffuses out of glass as a Na^+ ion [196], and given the difficulties associated with monitoring Na migration [201], [205], [249], [250], using field-assisted Na diffusion may be of interest to confirm this hypothesis: quantitative control of Na diffusion would allow one to straightforwardly evaluate its ensuing impact on Ag films. In this case, other works studying field-assisted diffusion may offer additional insight [209], [271].

4.4.2 Defects and their evolution at high temperature

4.4.2.1 Defects in as-deposited stacks

Having demonstrated the impact of each contaminant on morphological and optical changes, we now aim to isolate their effect from those of mechanical damage on scratch visibility accentuation at high temperatures. To do so, the presence of contaminants must be controlled during HT; however, the stack structure must be kept consistent to ensure repeatable scratch morphologies. Thus, in this section, only the GRAR stack type, shown in **Figure 4.2**, will be used. Thus, contaminant availability will be regulated using controlled atmospheres and substrates, as performed in Section 4.4.1. However, SLG and BSG substrates are known to have notably different mechanical properties [272], confirmed by nanoindentation results shown in **Table B.2** of Appendix B; this gives rise to different morphologies for equivalent scratch loads. Scratch morphology must, therefore, be tracked differently than via the applied load to evaluate its effect on scratch visibility and its accentuation following annealing at high temperatures. Consequently, to assess the effect of different defect types on scratch visibility before and after heat treatment, all produced scratches are individually evaluated by optical microscopy.

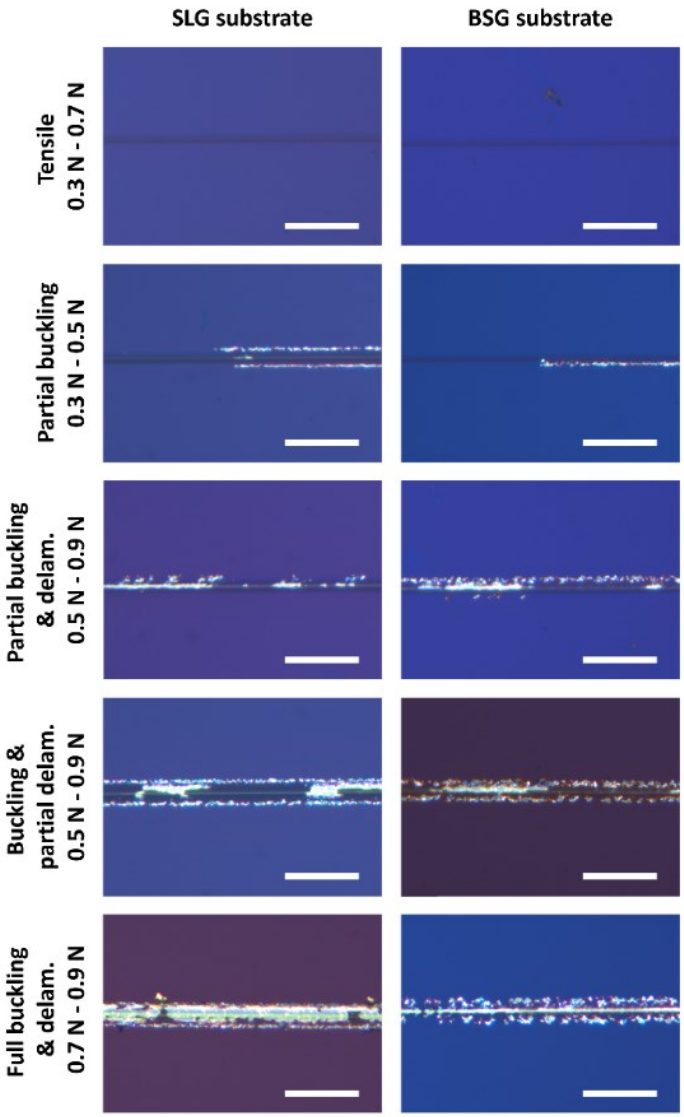


Figure 4.8: Optical microscope images of the main scratch morphologies. These are annotated with the scratch loads at which these have been recorded, as obtained on GRAR-type stacks deposited on each of the substrate types. All scale bars correspond to 50 μm. Higher magnification images showing the tensile cracks are presented in **Figure B.9** of Appendix B. All scratches were generated with tip movement going from left to right.

Three general defect types were found to occur and are shown in **Figure 4.8**. Tensile cracking is mostly observed at low loads, resulting in scratch tracks which are practically invisible; indeed, these can be seen faintly by eye if the sample is held at a very specific angle, under appropriate lighting, and the individual searching for the scratch knows where to search for it. These are mainly

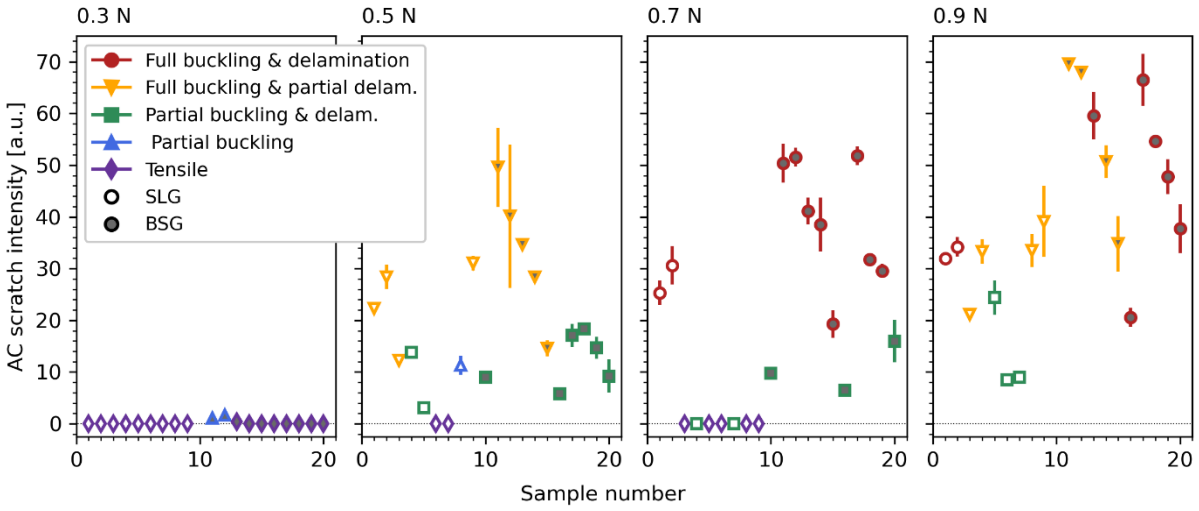


Figure 4.9: As-coated (AC) visibility and defect types of scratches obtained for different scratch loads. All scratches were performed at constant load on GRAR-type stacks (see **Figure 4.2**). Each sample was arbitrarily numbered from 1 to 20. Optical microscope images representative of each defect type are shown in **Figure 4.8**.

visible in optical microscopy due the to the plastic deformation of the glass substrate, but the cracks can

be seen at higher magnifications, as exemplified in **Figure B.9** of Appendix B. They are typically not registered by the darkfield visibility set-up: even when visible in imaging, their average intensity typically falls below that of noise caused by dust particles or random defects, and these are thus assigned a width and intensity of 0. At intermediate loads, conformal cracks appear, accompanied by coating buckling along the edges of the scratch track; these appear to result from recovery spallation [273]. The coating buckles are easily visible by eye, by optical microscope and with the visibility set-up. Removing all but the bottom RDB layer via chemical etching, the coating buckles are no longer observed, indicating that the delamination occurs above the SLG-RDB interface; this is shown in **Figure B.9** of Appendix B. Finally, at higher loads, coating buckling at the scratch edges continues, but in addition adhesive failure occurs within the scratch track; these delaminations are assumed to originate from buckling defects, possibly initiated by the conformal cracking [273]. The addition of coating delamination does not significantly increase scratch visibility.

For easier comparison, **Figure 4.9** shows the as-coated intensity and defect type for each scratch load, as obtained on each scratched sample. It should be noted that as scratches can present multiple different defect types along a given scratch track, the presence of buckling and delamination are distinguished as being present over most of the scratch length (full) or only intermittently (partial); indeed, as the scratch intensity is averaged over the full 10 mm scratch length, the proportion of defect types with a different intensity will affect the final value. Additionally, no scratches were found with widespread buckling that did not show at least partial delamination. Error bars are obtained by analysing two images of the same sample in different positions, as described in Section 4.3.

While there is a correlation between the scratch load and resulting defect type, this relation is neither systematic, nor monotonic: a given defect type may occur more or less based on imperfections in the coating or glass, and for each substrate there appears to be loads at which the main defects observed are less severe than at a lower load (e.g.: on SLG, scratches at 0.7 N are frequently tensile, and on BSG less delamination is found at 0.9 N than at 0.7 N).

While a detailed accounting of the morphological differences occurring as a function of the chosen substrate and applied load are beyond the scope of this work, some additional details are worth highlighting. **Figure B.10** of Appendix B shows that the measured scratch width does not vary substantially between substrates. However, it can be seen in the bottom row of **Figure 4.8**, which shows optical microscope images of each of the observed defect types, that for a comparable overall width, scratches on BSG may display much thinner delaminated areas with much wider buckling compared to SLG. Although defect types do not evolve monotonically with scratch load, residual depth, intuitively, does, as also shown in **Figure B.8** of Appendix B. The lower residual depths observed for BSG are consistent with the higher hardness found for these substrates (8.1 ± 0.3 GPa for BSG vs 7.3 ± 0.3 GPa for SLG).

4.4.2.2 Defect visibility accentuation as a function of contaminants

With the previous assessment of scratch morphologies in place, their enhancement can be evaluated as a function of substrate and atmospheric contaminants. **Figure 4.10** shows the intensity and width of scratches following HT as a function of their as-coated values. Defect types are not identified here, contrarily to **Figure 4.9**, as the scratch visibility changes were not found to vary with the type

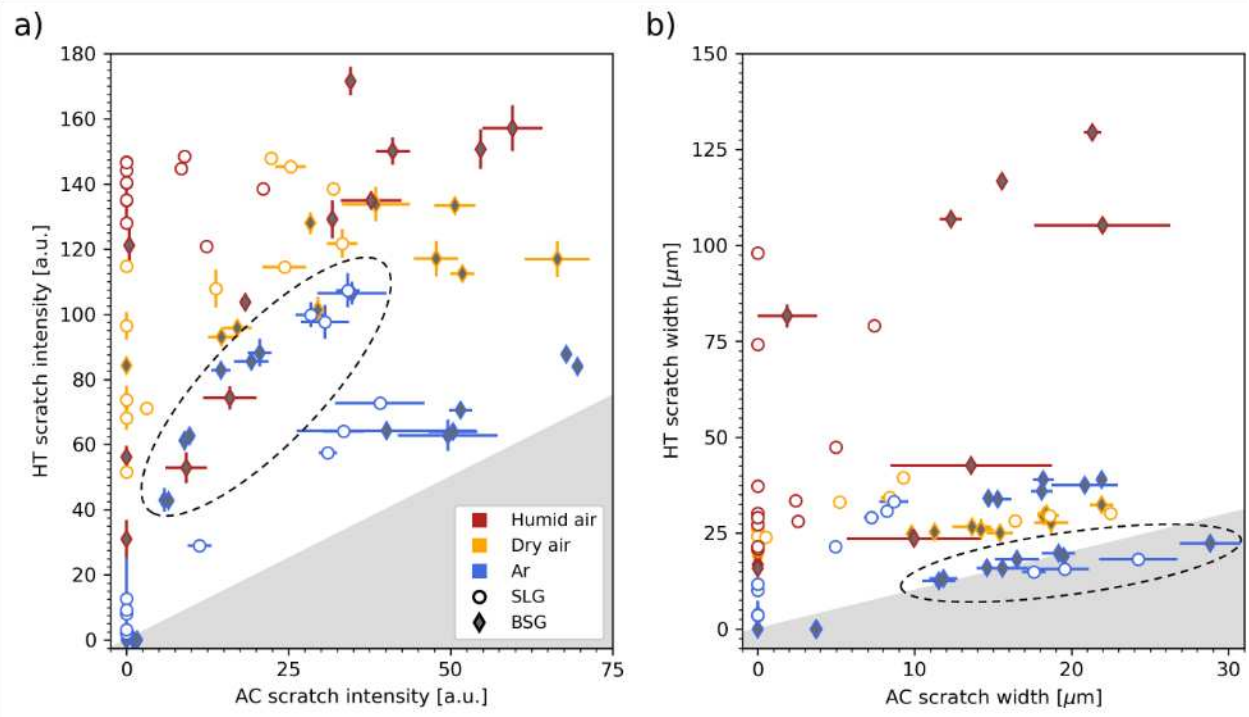


Figure 4.10: Scratch intensities and widths before and after annealing in different conditions. **a)** Scratch intensity and **b)** scratch width of heat-treated (HT) samples as a function of their as-coated (AC) values, for low-E coatings deposited on SLG or BSG substrates and annealed at 650 °C for 8 minutes in different gas environments. Shaded areas represent where heat-treated values are equal or lower than as-coated ones. Dashed ellipses highlight different clusters of datapoints of interest, discussed in the text.

of initial defect, except for tensile cracking which can easily be assessed from AC scratch intensity. Rather, scratch visibility changes following heat treatment reveal high sensitivity to the annealing atmosphere; ambient humidity was found to have a notable effect on scratch visibility accentuation, and thus tests were performed under ambient (humid) air, as well as in controlled dry air and argon atmospheres.

Coatings annealed in humid air (red) yield similar or slightly higher intensity than those annealed in dry air (yellow); both show substantially higher intensity than those annealed in Ar (blue) however, highlighting the pivotal role of oxygen in scratch visibility enhancement, consistent with previous reporting on Ag outflow from Ag-based nanolaminates [40], [254]. From this, we may assume that the mechanisms lead to increased intensity are not fundamentally different for humid or dry air and are primarily linked to O_2 in the atmosphere. On the other hand, the width increase

of the scratches does not vary substantially with a change from Ar to dry air, while annealing in humid air causes the width to increase dramatically. Thus, humidity appears to mainly impact defect propagation; the observed increases in scratch intensity may be due to propagation of defects along the scratch axis, increasing the average intensity of scratches with intermittent levels of damage.

Samples annealed in Ar are not without scratch visibility accentuation, however. A subset of samples with distinct behavior are circled with a dashed line in each subplot of **Figure 4.10**. In **(a)**, while most samples closely follow the edge of the shaded area (representing scratches which are scarcely more intense than prior to heat-treatment), the samples in the circled area display markedly higher intensities, similar to samples annealed in air. On the other hand, in **(b)** most samples display widths comparable to scratches annealed in air, whereas samples in the circled subset show extremely low scratch widths.

The samples associated with the circled scratches are found to have higher background intensity in the initial images than other samples annealed in Ar, with two of the four samples showing very high values, as shown in **Figure B.11** of Appendix B. As demonstrated in **Figure 4.1**, higher background intensity in the initial image shifts the intensity at which the scratch width is measured, leading to lower measured widths for otherwise similar scratches. Thus, the low width obtained for these scratches can be attributed to the higher background intensity.

The higher background intensity in the images of these samples is the result of haze in the unscratched coating areas. Optical haze, in turn, has been shown to result from coating degradation, namely Na diffusion, as evidenced in **Figure B.5** of Appendix B. Thus, it appears that the coating's susceptibility to degradation outside of scratches facilitates scratch visibility accentuation during HT, regardless of the annealing atmosphere. Additionally, it should be noted that the only scratches which show this accentuation present some amount of buckling; scratches with strictly tensile cracking (i.e., with low AC intensity) annealed in Ar consistently display low HT intensity as well. This is in agreement with the previous optical and electrical analysis of the GZAZ partial stacks in Section 4.4.1.1, showing that removal of dielectric layers can reduce the threshold for Ag disruption during HT.

Interestingly, while the substrate composition has shown an important effect on coating stability in un-scratched partial stacks (4.4.1) , almost no difference is found in terms of scratch visibility

accentuation for samples deposited on BSG or SLG. Indeed, except for tensile-type scratches, annealed in Ar, which result in higher HT scratch intensity for SLG (7 ± 4 a.u.) than BSG (0.5 ± 1.0 a.u.), no clear change in defect accentuation is observed for SLG versus BSG substrates. As a result, Na only appears to have a small impact on scratch visibility accentuation, which is overshadowed by parameters with greater impact such as the presence of O_2, H_2O, or buckling defects. Given the important role of Na diffusion in the degradation of un-scratched coatings, it was considered that scratches may not create Na diffusion paths (i.e. cracks) in the bottom RDB barriers. However, their presence was verified by etching away all but the bottom barrier layer, as shown in **Figure B.9** of Appendix B. Thus, further investigation of the morphological features causing scratch visibility accentuation following heat treatment and their dependence on different contaminants is required.

To complete the interpretation of these results, the morphological changes causing scratch visibility accentuation were investigated via SEM imaging of tensile-type scratch surfaces, annealed under dry air or Ar, as shown in **Figure 4.11**, as well as TEM imaging of thin cross-section lamellae extracted from them by FIB, shown in **Figure 4.12**.

Heat-treated scratched stacks exhibit notable differences when compared to as-coated scratches (imaged by SEM in **Figure B.12** of Appendix B); following annealing in dry air (**Figure 4.11**, images **(a)** and **(b)**), buckling appears along the scratch edges where it was previously absent, and large Ag particles (radii > 250 nm) are found at the surface above the cracked area. Backscattered electron images show Ag depletion around the scratch track and buckled areas, and reveal the presence of smaller, irregularly shaped Ag particles inside the buckles (short axes ≈ 100-150 nm). Annealing in Ar, shown in images **(c)** and **(d)**, results in the formation of smaller Ag-depleted areas and only a few very large Ag particles at the scratch surface (radii > 500 nm). Moreover, no buckle formation is observed and, accordingly, no formation of smaller Ag nanoparticles either. The increased mass transport of Ag to the surface of nanolaminates in an oxygen-containing atmosphere has been well described [40], [216]. The smaller size of the particles observed at the surface when annealing in air is attributed to decreased Ag surface energy resulting from oxygen exposure [34], [216].

We thus attribute the observed increases in scratch intensity mainly to the presence of small Ag agglomerations within the buckled areas. In addition to being consistent with the fact that, when

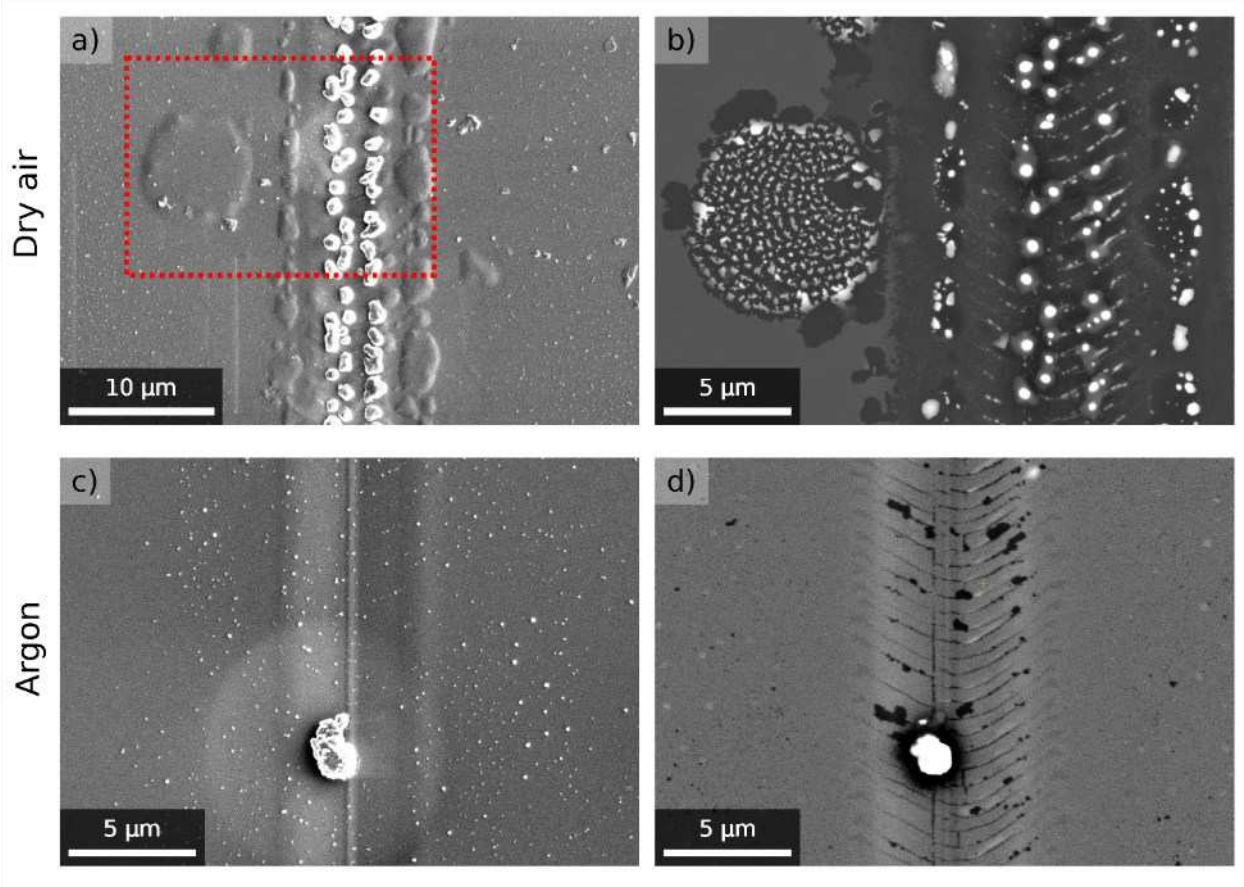


Figure 4.11: SEM images of tensile-type scratch defects annealed in different atmospheres. Samples were deposited on SLG and annealed at 650 °C for 8 minutes in **a)**, **b)** dry air and **c)**, **d)** argon, overcoated with ≈ 50 nm of carbon, prior to lamella extraction. Images **(a)** and **(c)** were captured at low accelerating voltage (2 kV) in secondary electron mode to emphasize coating topography; **(b)** and **(d)** were taken with a higher acceleration voltage (15 kV) in backscattered electron mode to increase sensitivity to Ag in a wider range of depths. The dashed red outline in **(a)** corresponds to the approximate zone imaged in **(b)**. Scratches were generated with the tip movement going from bottom to top.

annealing in Ar, large scratch intensities are exclusively achieved for scratches with buckling defects prior to annealing, Mie theory predicts that the total visible light scattering which can be obtained by dewetting into spherical Ag particles will peak for sizes between 50 and 200 nm, as demonstrated in **Figure B.13** of Appendix B [274].

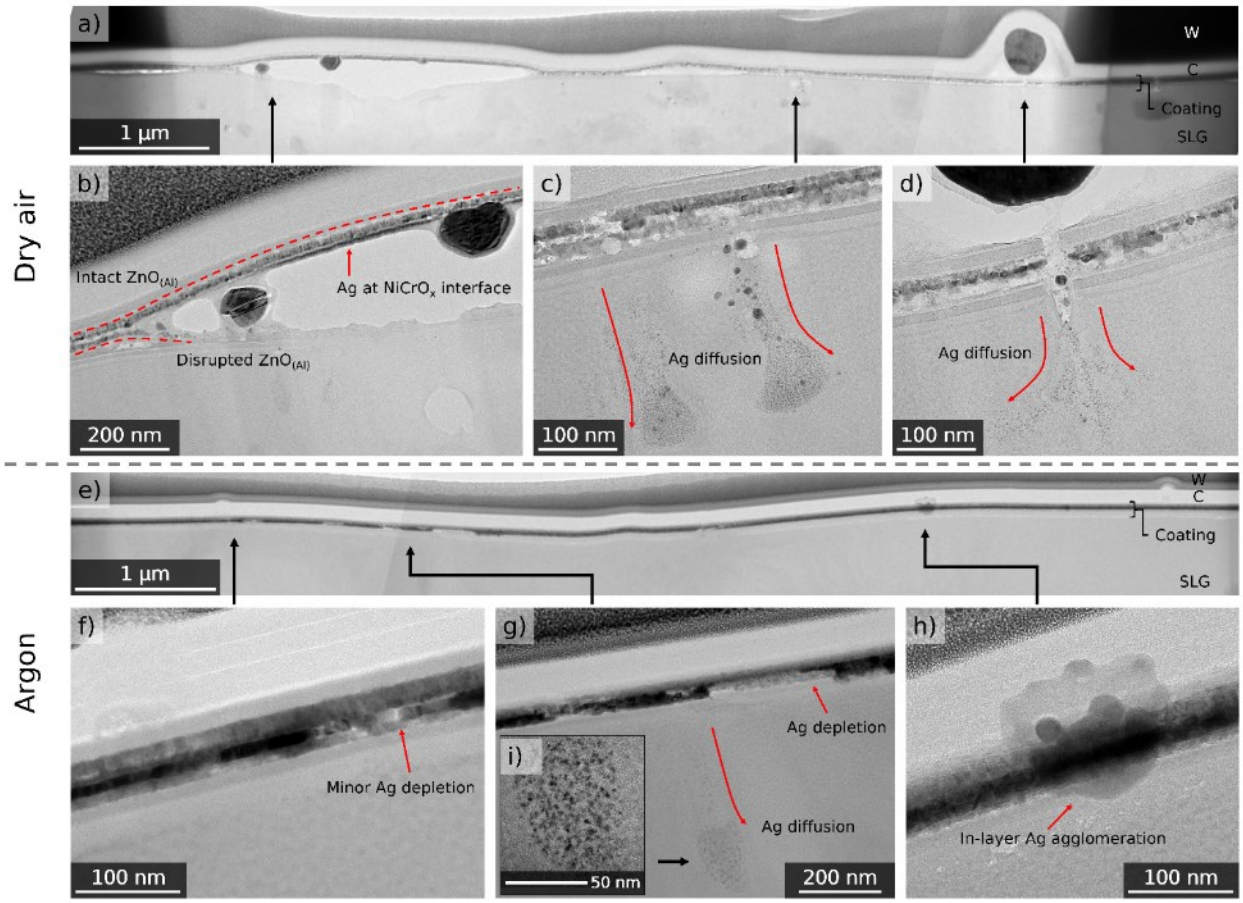


Figure 4.12: Bright-field TEM cross-section imaging of tensile-type scratches annealed in different atmospheres. Images **(a)-(d)** correspond to annealing in dry air; the cross-section was extracted from the sample shown in **Figure 4.11a-b**. Images **(e)-(i)** correspond to annealing in argon; the cross-section was extracted from the sample shown in **Figure 4.11c-d**. **a)**, **e)** Panoramic overviews composed of multiple stitched images, identifying the main areas associated to the substrate and coating, as well as the carbon and tungsten layers deposited as part of the cross-section preparation. **b)-d)**, **f)-i)** Magnified images of the zones identified by arrows in **(a)** and **(e)**, respectively.

This is further supported by SEM imaging of a tensile scratch annealed in humid air, shown in **Figure B.12** of Appendix B, which reveals practically no large Ag particle formation in these conditions: rather, there is widespread formation of small Ag clusters (radii of ≈ 50-150 nm). It is difficult to identify buckling features in these images, as the degraded area is very wide and large non-Ag particles are present at the coating surface, impeding the assessment of height variations of the coating in secondary electron imaging. Humidity may thus lead to the formation of more

widespread buckling, as humidity is known to promote stress changes in dielectrics which may lead to formation of cracks or delaminations [109], [226]. It may also facilitate the formation of small Ag nanoparticles, as coating buckles were previously found to promote their formation, and as humidity can enhance Ag diffusivity [38], [275].

TEM measurements of scratched coatings annealed in dry air, presented in **Figure 4.12**, show that buckling initiates from delamination of the Ag layer; more specifically, image **(b)** shows residual Ag and Ag nanoparticles adhered to the $NiCrO_x$ layer, indicating that delamination was likely initiated at the Ag-$ZnO_{(Al)}$ interface. Moreover, degradation of the bottom $ZnO_{(Al)}$ layer is observed; as discussed in the context of GZAR samples in 4.4.1, this may allow Ag diffusion at its bottom interface, facilitating dewetting. The suggested hypothesis, by which sufficient disruption of the Ag layer would lead the top dielectrics to become essentially freestanding, and subsequently deform, is well supported by the correlation between O_2-induced dewetting and buckle formation. The sample annealed in Ar, presented in **Figure 4.12**, displays much less degradation: small holes and agglomerations, shown in **(b)** and **(d)**, are present but result in minimal impact to the adjoining coating areas. Despite that, no outstanding differences are observed in the degree of deformation of the substrate, as shown in images **(a)** and **(e)** of **Figure 4.12**, the coating remains well-adhered when annealing in argon, highlighting the role of oxygen in delamination.

In both cases, Ag diffusion into the glass, ostensibly resulting from ion exchange, is observed at multiple sites, highlighted in **Figure 4.12**, images **(c)**, **(d)**, **(g)** and **(i)**. In the case of the coating annealed in Ar, Ag interdiffusion appears next to the largest Ag-depleted areas, implying that it plays a central role in their formation; the extent to which Ag mass transport into the glass contributes to Ag depletion, as opposed to merely generating holes which propagate into larger dewetting fronts, is unclear. The sample annealed in dry air shows denser, more numerous areas of Ag interdiffusion with larger Ag clusters, albeit at shallower depth. While **Figure 4.12a** shows some darker regions deeper in the glass, which may be associated with Ag interdiffusion, given the high damage incurred by milling in these areas and less defined structures, these cannot be reliably identified as Ag diffused into the glass during annealing. Nevertheless, this suggests that exposure to O_2 not only facilitates Ag surface diffusion, but its diffusion into the substrate, consistent with previous work which reports that tin diffusion into glass is accelerated by subsequent redox reactions [224]. Moreover, **Figure 4.12d** shows a clear break in all dielectric layers, and despite massive Ag outflow to the surface, interdiffusion with the substrate remains non-negligible: thus,

in the case of GZAZ samples, without such damage allowing competition with rapid mass transport to the sample surface, it is plausible that Ag diffusion into the glass contributes to the vast depleted areas observed in **Figure 4.6c**.

Together, all of the above observations not only highlight the role of O_2, Na, and barrier layer damage in the scratch visibility accentuation process, they offer insight into the limited effect of the substrate type on the scratch intensity, as discussed in the context of **Figure 4.10a**. Indeed, the small size of the Ag particles formed by interdiffusion into the glass will greatly decrease their scattering efficiency, as shown in **Figure B.13** of Appendix B, leading to small changes, if any. While this process is facilitated by the presence of oxygen, O_2 exposure will also lead to mass transport towards the surface, competing with substrate interdiffusion, as well as facilitating formation of buckled areas filled with high scattering-efficiency nanoparticles. Thus, the effect of Na diffusion on scratch visibility accentuation is overshadowed in the presence of O_2, and weakened in its absence. This explains the previous observation that no meaningful scratch visibility changes result from annealing samples on either SLG or BSG substrates, unless there are no initial buckling defects and annealing takes place in Ar.

4.4.2.3 Scratch accentuation mechanisms and potential coating improvements

In the following, we present an overview of the main mechanisms leading to scratch accentuation; this is presented schematically in **Figure 4.13**, along with an overview of the main effects of contaminants on undamaged partial stacks. In a first step, applied loads lead to the formation of cracks and elastic recovery leads to the formation of residual compressive stresses at the scratch edges, if not outright formation of buckles due to delamination at the Ag-$ZnO_{(Al)}$ interface. During annealing, diffusion of oxygen to the Ag layer through cracks in the diffusion barriers, grain boundaries in the Ag or $ZnO_{(Al)}$ layers, or through open interfaces (as in the case of delamination) leads to accelerated dewetting of the Ag layer, facilitating formation of buckling, if not already present. As opposed to particles formed at the coating surface, buckled areas allow the formation of rounded nanoparticles while restricting their size, leading to the formation of a particle size distribution with a higher density of particles which efficiently scatter visible light. It was found previously that the formation of small nanoparticles and the propagation of these buckled areas may be promoted by the presence of humidity during annealing, leading to the formation of wider

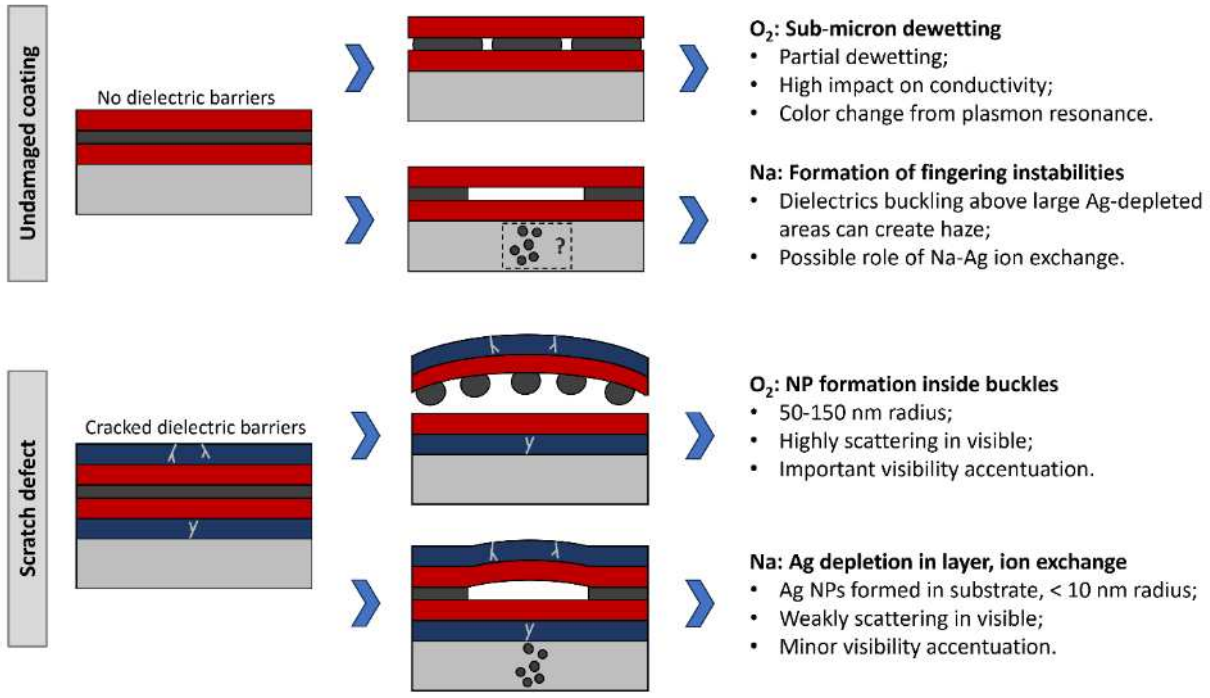


Figure 4.13: Schematic overview of the main effects of O_2 and Na diffusion on undamaged coatings and coatings presenting scratch defects.

visible scratches, although it does not show an obvious impact on the size of Ag particles formed. Diffusion of Na to the Ag layer may generate Ag depletion to some extent, either by ion-exchange or by nucleating holes which expand into dewetting fronts, but susceptibility to dewetting generated by oxygen diffusion or buckling defects in the as-coated state dominate in the majority of tested conditions, indicating a limited role in practice.

Following the above-described considerations, stack improvements can de suggested. Modifications to the coating architecture should be investigated as a means to mitigate crack propagation, e.g., via nanolaminated dielectrics [276], which may also mitigate Na diffusion [204]. This may indeed decrease accentuation even more than the usage of controlled atmospheres; while annealing in Ar suppresses diffusion of contaminants to the Ag layer and adjacent interfaces, it does not impede outward Ag diffusion, as mitigation of crack formation would. As the possibility of cracks propagating from the substrate has not been investigated, further modifications to the substrate properties or usage of a thick dielectric bottom layer to achieve different effective

substrate properties may also be relevant. Given that buckled coating areas enable high scratch intensity, even for samples annealed in Ar in some cases, limiting these defects is also highly important. Improved adhesion at dielectric interfaces, potentially achieved via intermixing [277], may mitigate delamination and buckle formation, both as a result of mechanical solicitation as well as during heat treatment.

Given the weakness of the Ag layer to delamination, improvements to the existing $NiCrO_X$ layer may improve stabilization of the Ag layer: diffusion of metallic Ni into the Ag layer is expected to mitigate surface diffusion at this interface [20], and may also improve adhesion. Nonetheless, Ag particles were found to remain adhered to this interface, but delaminated from the $ZnO_{(Al)}$ seed layer; usage of a metallic seed in addition to $ZnO_{(Al)}$ may improve stability while maintaining performance [151], [278]. Finally, decreasing the susceptibility of the Ag layer to atmospheric contaminants via doping may offer an additional redundancy: despite reduced as-coated performance, doped Ag layers have shown optical and electrical properties much closer to that of undoped Ag following annealing [32], [50], making them particularly suitable for improving stability in products destined to be annealed as part of their fabrication.

4.5 Conclusion

In this work, the effects of atmospheric and substrate contaminants on the optical, electrical and morphological evolution of low-emissivity coatings at high temperature were investigated. In the first part, these were studied in undamaged partial coatings, allowing one to assess the effect of stack architecture changes. In the second part, the evolution of scratch defects in full low-E stacks were studied, where the diffusivity of contaminants or the stack structure were locally modified.

In SEM imaging of non-scratched coatings, both oxygen and sodium are found to disrupt the Ag film if diffusion barriers are removed, allowing contaminant diffusion. Although Na diffusion has been identified as a contributor to low-E performance changes at high temperature, its effects are not often described in current literature; here we find that Na diffusion generates widely spaced dewetting features in the Ag film which develop into large fingering instabilities. Specifically, these are found to generate haze due to deformation of the dielectric layers where the Ag film is depleted, showcasing the range of impacts Na may have in the performance changes of low-E coatings. Moreover, the coating structure is found to impact film stability, as removal of both

barrier layers renders coatings more susceptible to degradation by even small contaminant concentrations. Oxygen, in addition to promoting sub-micron scale dewetting, as has been previously observed in the literature, is found to amplify the effect of sodium, both in terms of increasing Ag diffusion into the substrate, as well as increasing the scale of the resulting fingering instabilities. Finally, even when contaminant availability is reduced, the removal of layers is found to have a meaningful impact on coating stability, increasing susceptibility to Ag microstructural changes.

For the study of defect evolution, applied scratch loads were first correlated to the resulting defect morphologies and their visibility, the latter of which was quantified by a custom *Python* image analysis script. This allowed us to evaluate scratch visibility accentuation quantitatively, as a function of the contaminants and defect types. Oxygen was found to have the most impact on visibility accentuation, resulting in dewetting-facilitated buckling. While oxygen exposure leads to significant outwards mass transport, as has been reported in similar nanolaminate structures, we report that it is the formation of small Ag nanoparticles within the buckled areas which results in the largest changes in visibility. These nanoparticles, ranging between 50 and 150 nm in radius, lead to the highest levels of visible light scattering, as supported by Mie scattering calculations. The presence of buckling defects, whether formed as part of the scratch process, or resulting from heat treatment, was found to increase the coatings' susceptibility to forming highly visible defects following annealing, coherent with the susceptibility to degradation found in partial stacks. Thus, delamination and Ag dewetting achieved by any means appears to promote the formation of highly visible scratches following HT, with oxygen being the primary vehicle for it. Humidity was found to substantially increase the width of the defects, which may be attributed to a combination of higher rates of delamination and increased Ag diffusion. The presence of humidity also increases the scratch intensity, or brightness, to a small extent, which may be attributed to a larger amount of small Ag particles below the coating surface for scratches annealed in humid air. Na diffusion was not found to have a meaningful impact on the accentuation of scratch visibility, as Ag disruption by other means takes precedence in the majority of cases, despite crack formation in the bottom barrier layer during scratching.

Together, these results provide clear pathways towards improving the durability of low-E window coatings to defect accentuation during tempering, and various suggestions are made to improve these.

4.6 Acknowledgements

The authors wish to thank Covalent Metrology Corp. for obtaining the low-magnification SEM images and TEM images of unscratched partial stacks. All other electron microscopy was performed at the $(CM)^2$ laboratory of Polytechnique Montréal; we would like to thank Ms. Nicole MacDonald, Dr. Pavel Pleskunov, and, in particular, Mr. Jean-Philippe Masse for their assistance with SEM and TEM analyses. Finally, we would like to thank Mr. Oumar Touré and Mr. Michael Mayerhofer for their work developing the scratch formation and visibility quantification methodology, as well as Mr. Francis Boutet, Mr. Sylvain Fleury, and Mr. Francis Turcot for their assistance with the maintenance of the deposition and measurement systems.

The project was financially supported by the Natural Sciences and Engineering Research Council (NSERC) of Canada through the NSERC-Alliance grant (no. ALLRP 576758 - 22), by Prima Quebec (grant no. R24-13-003), and by Guardian Glass.

CHAPTER 5 ARTICLE 2 : ENHANCED DURABILITY AND ANTIREFLECTIVE PERFORMANCE OF AG-BASED TRANSPARENT CONDUCTORS ACHIEVED VIA CONTROLLED N-DOPING

5.1 Foreword

The work presented in this article aims to address the second and third objectives of this thesis, i.e. investigating methods to tailor the microstructure of Ag films, and applying these to increase the durability of Ag-based coatings, without the usage of metallic dopants. Here, the combination of $Ag_{(N)}$, to control wetting, and of $ZnO_{(Al)}$, to mitigate the former's impact on Ag grain size, is explored as a means to improve corrosion durability.

While not directly pertaining to high temperature stability, this allows a proof of concept, demonstrating the impact that the Ag microstructure can have on Ag stability. It was also found previously that the environmental conditions in which scratched low-E coatings were stored had a profound impact on scratch intensification; thus, the environmental stability of low-E coatings at ambient temperatures may have meaningful repercussions on this as well.

Moreover, in order to align the work in this chapter to more general applications, the coating structures used here are not typical of low-E coatings, with a low *n* top dielectric and a single extremely thin Ag film. However, these allow to demonstrate features of significant interest. By the very fact that the encapsulating dielectric is not optimized for durability, stability improvements resulting from structural differences in the Ag film are highlighted. Similarly, the low Ag thicknesses showcase the potential benefits of N doping on Ag wetting. Finally, while this work focuses on single-Ag coatings, low-E architectures using multiple Ag films to achieve a sharp cut-off between the visible and NIR spectra can benefit from thinner Ag films; this work demonstrates how these can be leveraged with reduced impact on film stability.

As previously, this chapter includes the integral text of the article, with the associated supporting information included in Appendix C.

ENHANCED DURABILITY AND ANTIREFLECTIVE PERFORMANCE OF AG-BASED TRANSPARENT CONDUCTORS ACHIEVED VIA CONTROLLED N-DOPING

Phillip Rumsby, Bill Baloukas, Oleg Zabeida, Ludvik Martinu*

Department of Engineering Physics, Polytechnique Montréal, Montréal, QC H3T 1J4, Canada

Published April 27th 2024 in *ACS Applied Materials and Interfaces*, vol. 16, no. 18, p. 2403.
doi: 10.1021/acsami.4c02255

Abstract

Ag-based transparent conductors (TCs) are often proposed as an alternative to ITO coatings. However, while their performance has been widely demonstrated, their environmental durability is frequently overlooked, or addressed with the use of highly specific encapsulating layers.

In this work, durability and antireflective performance of Ag-based TCs are simultaneously enhanced. To do so, a transfer matrix modelling approach is used to determine the general requirements for high performance antireflective properties as a function of Ag thickness and dielectric refractive indices, offering more widely applicable insight into stack optimization.

Coating durability is investigated as a function of the Ag microstructure, which is modified by altering the N_2 concentration used for doping of the Ag layer and the selection of the seed layer. Increasing N_2 concentration during Ag deposition was found to decrease grain size and durability of Ag coatings deposited on Si_3N_4 whereas all coatings on $ZnO_{(Al)}$ showed higher stability. Significantly higher durability is found when specifically combining intermediate N_2 concentrations in the sputtering gas mixture ($Ag_{(N):5\%}$, compared to 0% and 50%) and a $ZnO_{(Al)}$ seed layer, and a mechanism accounting for this increased durability is proposed. The addition of $NiCrN_x$ protective coatings increases system durability without altering these trends.

These findings are combined to fabricate a highly performant Ag-based TC (T_V = 89.2 %, R_V^{FS} = 0.23 %, 21.4 Ω/□), which shows minimal property changes following corrosion testing by immersion in a heated and highly concentrated aqueous NaCl solution (200 g/L, 50 °C).

5.2 Introduction

Transparent conductive (TC) layers are an essential component in a number of applications, including touchscreen displays, organic light-emitting diodes, solar cells, low-emissivity window glazings and others. While indium tin oxide (ITO) has been held in high regard for such applications, technical issues, such as its brittleness and annealing requirements which may be incompatible with temperature-sensitive substrates (e.g.: polymer substrates), as well as supply and pricing issues, have highlighted the need for alternative TCs [27], [279], [280], [281].

Silver (Ag)-based layers are one such alternative, and multiple layer morphologies have been investigated, including continuous Ag films [27], [279], [280], [281], Ag nanowire structures [179], [282], and patterned Ag grid layers [283], [284]. In this work, we fabricate Ag-based TC coatings with a dielectric-metal-dielectric (DMD) architecture, while specifically focusing on optimizing the antireflective (AR) properties via optical interference.

By minimizing reflection, transmission is increased, but perhaps more importantly, the real-life functionality of the coating is improved, as the contrast between reflected and transmitted light can be greatly increased, which is not guaranteed when optimizing transmission only. This has already accrued some interest for ITO-based architectures [285], [286]; however, there has been relatively little interest in Ag-based coatings specifically for AR purposes, despite the fact that this has been proposed since the late 1970's [16], [287], [288].

More recent work has demonstrated that this can lead to highly transparent coatings, although the approaches used to determine loss, e.g., subtracting the measured transmission of a coated sample from that of a non-absorbing uncoated substrate, place importance on optimizing transmission without making a distinction between decreasing absorption or reflection [24], [25], [44]. On the contrary, minimising the absolute value of the reflection is the aim of our present work.

To ensure that the optical and electrical properties of the Ag film are suitable for AR and TC applications, control of Ag coalescence must be considered. The Volmer-Weber growth mode ([94], [289]) of Ag on many commonly used transparent substrates (e.g., soda-lime glass) is a well-known issue in which the high surface energy of Ag causes the clustering of Ag into disconnected islands during early growth phases [290], leading to the formation of continuous films only at higher thicknesses. This is problematic as thicker films, although more conductive, will also be more absorbing. On the other hand, rough, discontinuous, or partially coalesced films will have

poor conduction and increased absorption due to localized surface plasmon resonance [17], [245]. Different methods can be used to supress this effect, namely the usage of an appropriate seed layer to decrease the surface energy mismatch of Ag and the substrate [27], [43], [291], different dopants or gas additives (Al, O_2, N_2) to modify the Ag's surface energy or mobility [18], [32], [92], [106], [292], [293]. As most dopants impact Ag's optical properties, often negatively [50], [92], [292], this work focuses on studying the use of aluminum-doped zinc oxide ($ZnO_{(Al)}$) and nitrogen-doped silver ($Ag_{(N)}$). ZnO, frequently doped with gallium or aluminum, is ubiquitous as a transparent seed layer for Ag, and nitrogen addition has garnered significant attention as it has been demonstrated that it can accelerate continuous film formation with negligible effect on Ag optical properties [18], [23], [294].

While Ag has attracted considerable attention due to its potential in TC applications, the chemical stability of these films (and that of most Ag-based TCs) has gone largely unaddressed. Whereas ITO is fairly stable when exposed to moisture [295], Ag-based coatings require particular encapsulation to achieve similar durability [25], [219], [296], [297], [298], [299]. In addition to encapsulation in dielectrics, Ag layers are frequently stabilised using $NiCrN_x$ or other transition metal barrier layers: while these are well known for their ability to protect Ag coatings from chemical degradation, as their thickness increases, transmission rapidly decreases, reducing the optical performance [139], [177], [178], [217], [300]. Although not discussed at length in this work, appropriate metallic dopants can enable improved durability with less severe impact on optical performance [36]. The specificity of encapsulation used to protect Ag films can be disadvantageous in that they may require specific techniques or equipment, such as solution processed layers or atomic layer deposition, and may limit the selection of materials that can be used to improve Ag durability. Alternatively, investigations into the durability of Ag-based coatings commonly consider changes in sheet resistance. However, despite that the Haacke figure of merit (FoM), which is commonly used for TC applications, is highly sensitive to minute changes in transmission, optical performance changes often aren't quantitatively studied [139], [282], [296]. It should be noted that the purpose of this work is not to optimize the Haacke FoM, but rather to present durability improvements simultaneously with high AR performance. The FoM is kept as a comparative tool to demonstrate that the durable AR TC coatings produced in this work are similarly performant to typical Ag-based TCs.

To address these problems, first the optical performance of DMD devices is modelled using a transfer matrix approach. Performance is mapped to the thickness and refractive indices of the encapsulating dielectrics, as well as the Ag layer thickness, allowing one to identify effective designs for any Ag thickness. TCs are fabricated following an optimized AR design, which uses an ultra thin (6 nm) Ag layer, and their optical and electrical performances are compared. Following this, the durability improvement of the Ag layer is addressed by optimizing its microstructure, which we control by implementing a $ZnO_{(Al)}$ seed layer and $Ag_{(N)}$ deposition parameters, minimizing the requirements placed on the top encapsulating layer. Using a combination of *in situ* and *ex situ* spectrophotometry, sample degradation in aqueous NaCl solution is studied in detail as a function of Ag microstructure. A mechanism explaining the observed durability improvements is proposed. Finally, the optical modelling and durability evaluation results are combined to produce conductive Ag-based devices which simultaneously exhibit high transparency, exceptional AR performance, and high stability following exposure to a severe corrosive environment.

5.3 Experimental details

5.3.1 Sample fabrication

Samples were prepared in a magnetron sputtering system (CMS-18, Kurt J. Lesker) equipped with four 3" magnetrons and an additional 2" magnetron. 5 cm x 5 cm B270 glass substrates, cleaned and rinsed with deionized water and isopropanol, were placed on a 15 cm diameter substrate holder-electrode and were pretreated with a 100 V bias RF plasma in an Ar/O_2 gas mixture (100/35 sccm) at a pressure of 8 mTorr. The individual films were deposited following the conditions shown in **Table 5.1**. A RF bias of -85 V was applied to the substrate holder during the deposition of the Si_3N_4 layer. All other films were deposited at a floating potential.

$NiCrN_x$ films were sputtered from a composite target (80 wt.% Ni, 20 wt.% Cr) which is commonly applied in industry and in research [20], [46], [178], [300], [301]. N_2 is used as a reactive gas, as purely metallic NiCr is less common, and reactive deposition of oxide-based layers may negatively impact Ag properties [149]. The N_2 concentration was chosen based on preliminary experiments (not shown here) performed with CrN_x layers exhibiting an acceptable trade-off between decreasing the Cr absorption and retaining durability improvements.

5.3.2 Modeling

Design of the antireflective filter architecture was performed by using a brute-force modelling approach. A custom-made code was designed in *Python* using the transfer matrix approach. Typically, modelling approaches utilizing the transfer matrix method consider a pre-defined DMD architecture with fixed dielectric materials and a fixed Ag thickness; performance can then be modelled and mapped as a function of the thickness of each dielectric [24], [302], [303], [304]. Alternatively, the open-source *OpenFilters* software can optimize stack designs by searching for the optimal thickness of additional layers and simultaneously adjusting their refractive indices with the step method, but ultimately returns a single optimized configuration [305].

In this work, the optical performance is mapped for multiple stack configurations and simultaneously models different silver thicknesses, different dielectric thicknesses and different dielectric optical properties. To do so, a custom refractive index (n) is obtained by taking linear combinations of the optical constants of TiO_2 and SiO_2 to emulate a range of materials, where the relative weight of each material's optical properties is adjusted to return specific values of n at a wavelength of 550 nm. This combines the best aspects of each of the other approaches, allowing the entirety of the enlarged data set to be viewed as a set of 2D maps, explored with a simple graphical user interface, as exemplified in **Figure 5.1**, or used to analyse trends within the whole parameter space that was modelled.

Table 5.1: Summary of the sputtering conditions used for the deposition of the various films used in Chapter 5.

Layer	**Target**	**Power density [W/cm^2]**	**Mode**	**Pressure [mTorr]**	**Gas flow ratio [sccm]**	**Power and substrate RF bias**
Ag	Ag	2.63	DC	4	Ar/N_2 (variable)	-
$NiCrN_x$	Ni/Cr (80/20 wt. %)	3.29	DC	4	Ar/N_2 (100/50)	-
Si_3N_4	Si	9.87	RF	5	Ar/N_2 (100/40)	5 W, -85 V
$ZnO_{(Al)}$	Zn/Al (98/2 wt. %)	6.56	RF	2	Ar/O_2 (100/35)	-
SiO_2	SiO_2	7.40	RF	2	Ar	-

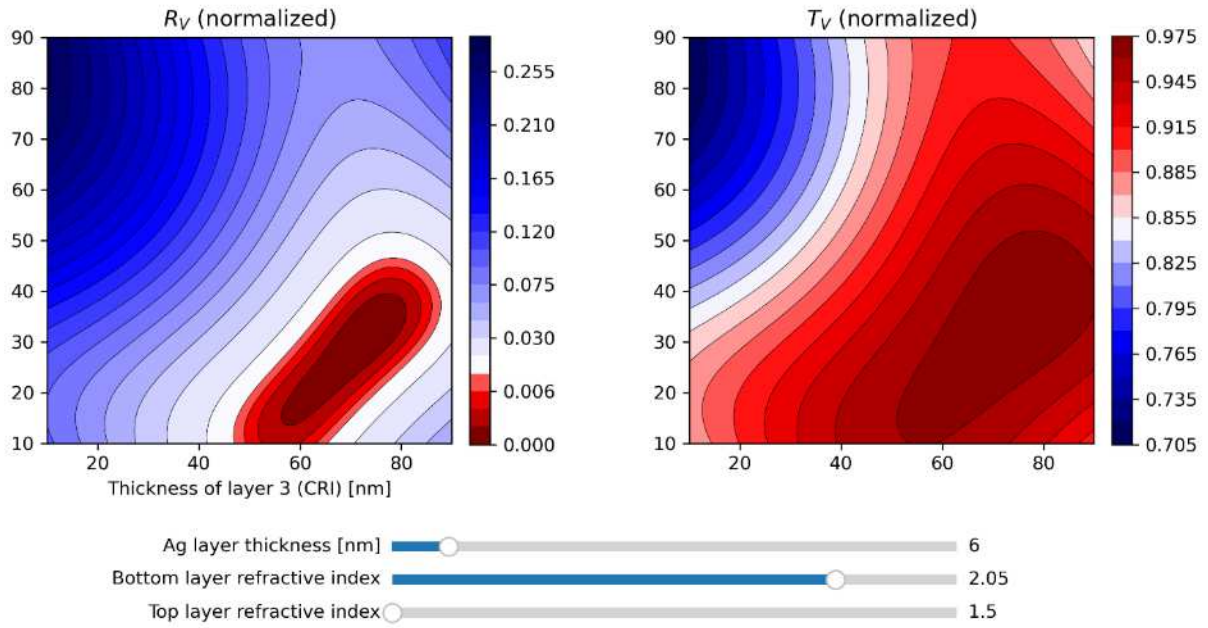


Figure 5.1: Example of the graphical user interface allowing one to plot R_V and T_V, (CIE standard illuminant D65, 1931 CIE observer), as a function of the thickness or refractive index of the mapped layers. The modelled filter architecture was B270 / dielectric (bottom) / Ag / dielectric (top), where each layer's thickness and each of the dielectric layers' refractive indices were varied. Mappings shown are displayed as a function of the dielectric layer thicknesses, for a Ag thickness of 6 nm, n (bottom) = 2.05, and n (top) = 1.50.

For modelling purposes, B270 glass is applied as the substrate, as it is used for experimental work, and its optical properties are an appropriate stand-in for most low-index glasses and polymers. Ag optical properties are taken from Palik [14].

To simplify the implementation of these features and limit the random-access memory required to run the code, the rest of the model is kept deliberately simple; propagation is considered strictly at normal incidence, all interfaces are considered perfectly smooth and flat, and the substrate is modelled as a semi-infinite medium. Thus, the reflection and transmission values returned by the code only take the coated interface into account.

Finally, it should be noted that, given the sheer amount of configurations which can be tested at a time, the transmission (T) and reflection (R) spectra are replaced with the visual transmittance and reflectance values, T_V and R_V. These scalar values are indicators of the perceived brightness in transmission and reflection for a given viewer in given lighting conditions; they are obtained by

averaging T and R weighted by the spectral power distribution of the lighting, or illuminant (Φ_S), and the spectral sensitivity of the observer, or spectral luminous efficiency ($\bar{y}$), as given by equation 4.1. In this work, the CIE (International Commission on Illumination) standard illuminant D65 and the 1931 CIE observer functions are used for all calculations of T_V and R_V, with the exception of the *in situ* monitoring of corrosion durability (see Section 5.3.3).

$$R_V = \frac{\int \Phi_S(\lambda)\bar{y}(\lambda)R(\lambda)\mathrm{d}\lambda}{\int \Phi_S(\lambda)\bar{y}(\lambda)\mathrm{d}\lambda} \tag{4.1a}$$

$$T_V = \frac{\int \Phi_S(\lambda)\bar{y}(\lambda)T(\lambda)\mathrm{d}\lambda}{\int \Phi_S(\lambda)\bar{y}(\lambda)\mathrm{d}\lambda} \tag{4.1b}$$

Modelling was performed using a simple 3-layer DMD architecture. Dielectric refractive indices at 550 nm were mapped from 1.50 to 2.20, with a step size of 0.05, using the aforementioned customizable refractive index model. Their thicknesses were mapped from 10 to 90 nm with a step size of 1 nm. The Ag thickness was mapped from 5 to 15 nm, with steps of 1 nm.

5.3.3 Corrosion durability and in situ optical monitoring

Corrosion durability was tested by immersing samples in an aqueous NaCl solution. Ag degradation in Cl-containing environments has been shown to be representative of other contaminants, as Cl fog exposure replicates the effects of mixed flowing gas and real-life aging [217], [300], and immersion in NaCl solution has been used with success to test the durability of Ag as well as dielectric materials [36], [139], [306]. To effectively compare the degradation rate of different Ag-containing film stacks, an *in situ* transmission spectrophotometry setup was implemented, as shown schematically in **Figure 5.2a**. Incident light was generated from a halogen source of a Mikropack DH-2000 unit and collected using a TEC5 MultiSpec Desktop spectrophotometer. Spectra were recorded over a wavelength range from 350 nm to 1025 nm, with 1 nm increments. Measurements were performed every 2 seconds and each measurement consisted of the average of 10 acquisitions. The solution temperature was controlled using a resistive heating element and thermocouple, connected via a PID controller. As different sample architectures display vastly different degrees of corrosion durability, two sets of testing conditions were used: (i) low-severity testing conditions using a 0.1 mol/L solution of NaCl heated to 30 °C; (ii) high-severity testing conditions using a 200 g/L solution of NaCl (approximately 3.4 mol/L) held at

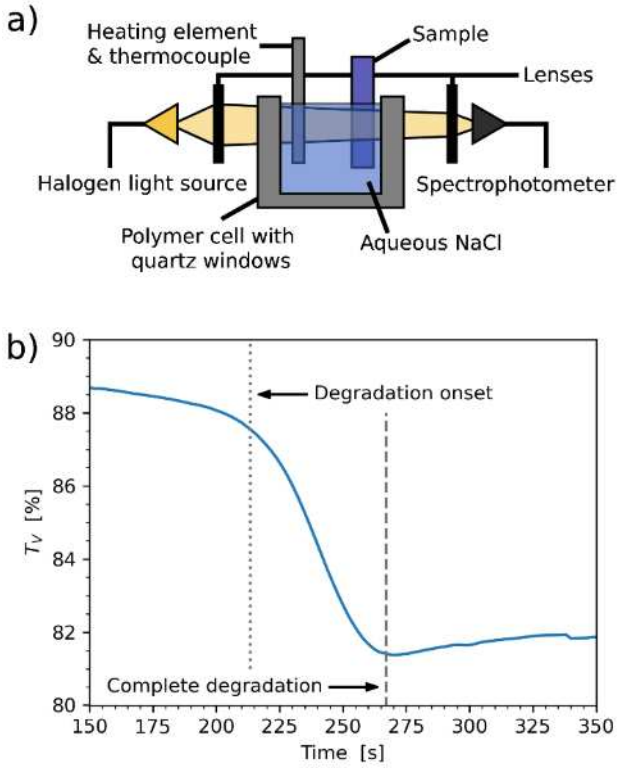


Figure 5.2: a) Schematic representation of the *in situ* corrosion monitoring setup. **b)** Example of the resulting in situ Tv showing the two main points used for inter-sample comparison: onset of visible degradation (dotted line) and completion of degradation (dashed line).

50 °C. For both conditions, samples were immersed for 20 minutes, or until visual confirmation of coating failure. The low-severity conditions correspond to those used by Koike *et al*., with a substantially shorter duration [36], [139]. The high severity conditions correspond to those used by Caron *et al*. for the evaluation of dielectric layer stability in ophthalmic applications [306]; these are, therefore, taken to be a suitable test to compare the durability of present Ag-based coatings to oxides, and thus conventional TC oxides .

Particularly, with the addition of solution heating, the *in situ* transmission signal is susceptible to noise and other fluctuations: to reduce noise sensitivity of the data, the measured spectra were converted to a scalar value by transforming them to T_V, taking again the 1931 CIE observer values, but using a constant illuminant (CIE illuminant E) with no spectral dependence, which effectively removes the effect of Φ_S in equation 4.1. The constant illuminant E is selected instead of D65 to reduce the weight of data in the blue and near-IR ranges, which have substantially higher noise due

to lower signal intensity. Plotting this value over time, sample degradation is then observed by a drop in visible transmission, corresponding to full failure and corrosion of the Ag layer. Samples measured with this setup will be compared based on the immersion time undergone before the onset of this rapid degradation, and on the immersion time before complete degradation is observed, as shown in **Figure 5.2b**. Given that the sensitivity of this setup is limited and that the spectral range does not extend into the IR, where changes in Ag conductivity would be more apparent, samples showing small variations of *in situ* measurements are studied in more detail *ex situ*, as described in the following section. It should be noted that illuminant E is only used for *in situ* durability monitoring (**Figure 5.2b**, **Figure 5.6a** and **Figure 5.6b**) and all other instances of T_V and R_V use illuminant D65.

5.3.4 Other characterization methods

In addition to the methods described above, sheet resistance (R_{Sh}) measurements were performed using a Delcom 737 contactless conductance monitor. It should be noted that the environmental cell used for *in situ* saline testing is limited to samples of 2.5 cm in width, whereas a minimum sample size of 5 cm by 5 cm is required for accurate sheet resistance measurements; therefore, no sheet resistance measurements were performed on samples following *in situ* durability testing.

Sample transmittance and reflectance were measured using an Agilent Cary 7000 spectrophotometer equipped with a universal measurement accessory (UMA). Measurements were performed at a beam incidence of 6°, enabling same-angle transmission and reflection assessment, while remaining close to normal incidence. Measurements were performed in *s* and *p* polarizations and averaged.

To evaluate the performance of the AR coated interfaces, relevant samples were measured using an adhesive tape backing to supress reflections from the backside of the substrate, as performed by Synowicki [307]. In such cases, the reflection of the front side of the sample, or its visual reflectance, are respectively referred to as R^{FS} and R_V^{FS}.

Moreover, the combination of spectrophotometry data and sheet resistance data enables us to quantify the performance of our samples using the Haacke figure of merit (FoM), which is a function of the TC's sheet resistance and normalized transmission at 550 nm [283]:

$$\mathrm{FoM} = \frac{T_{(550\ \mathrm{nm})}{}^{10}}{R_{Sh}} \qquad 4.2$$

Samples were imaged by atomic force microscopy (AFM) in ambient conditions using a Bruker Dimension ICON AFM and NanoscopeV controller. All AFM images were acquired using the PeakForce tapping mode using ScanAsyst-Air aluminium-coated silicon nitride probes with tip radius ranging between 2-12 nm and nominal spring constant of 0.4 N/m.

5.4 Results and discussion

5.4.1 AR design approach

As previously stated, this work aims to produce Ag-containing coatings that are antireflective as well as highly transparent and conductive: the previously described transfer-matrix modelling approach was employed to determine which are the key parameters to attain this objective.

Figure 5.3a shows the minimum values of R_V achieved within this mapping, as well as the dielectric refractive indices at which they are obtained, as a function of thickness of the Ag layer. Note that the dielectrics' indices may saturate at low and high thickness ranges; and it can be assumed that better results may be reached at certain thicknesses with a wider range of dielectric optical properties. For example, Macleod proposed an AR design in which a 1.36 nm thick Ag layer was placed between cryolite (n = 1.35) layers [16]. However, the bounds used in our work's modelling approach are chosen to be representative of conventionally used dielectrics to ensure that the produced designs are more widely implementable.

From **Figure 5.3a**, it can be concluded that effective AR devices, with R_V^{FS} below 1%, can be achieved with a wide range of Ag thicknesses when appropriate encapsulating materials are selected. This offers a straightforward approach to improve the optical properties of devices where the Ag thickness is selected on the basis of reaching specific sheet resistance targets. We also find that, to reach our objective of obtaining an optimal AR performance, an ultrathin Ag layer must be coupled with a low-index top dielectric, and high-index bottom dielectric.

Figure 5.3b shows that, for this configuration, the requirement for a low-index top dielectric is significantly more sensitive than that of the lower dielectric. To meet these requirements, SiO_2 was selected as a low-index dielectric for the top layer and Si_3N_4 and $ZnO_{(Al)}$ were selected as high-

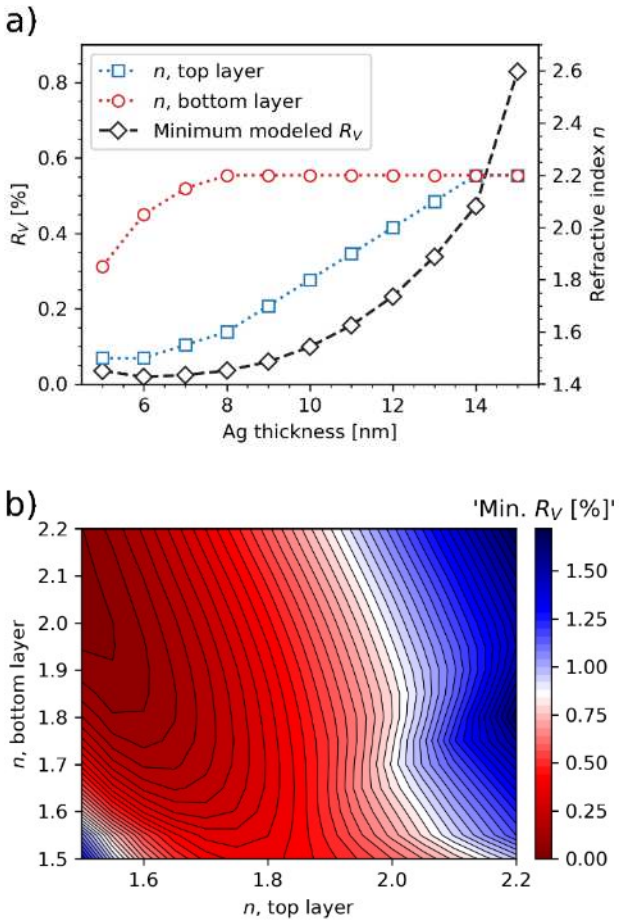


Figure 5.3: a) Minimum modelled R_V and refractive indices of dielectrics at which minimum R_V is achieved as a function of the Ag thickness in a modelled dielectric-Ag-dielectric architecture in which the thickness and refractive indices (at 550 nm) of the dielectric layers are free to vary, between 10 nm and 90 nm (steps of 1 nm) and between 1.50 and 2.20 (steps of 0.05). **b)** Mapping of the minimum modelled values of R_V as a function of the refractive indices of the dielectrics, using the same modelling as in **(a)**, for a Ag thickness of 6 nm with dielectric thickness free to vary. As the model does not take reflections from the backside of the substrate into account, modeled values of R_V are representative of R_V^{FS}.

index bottom layers. Although the latter two have lower n than the optimal value found in the modelling approach (n_{SiN} = 1.91, n_{ZnO} = 1.96, compared to n_{bottom} = 2.05), these are chosen as their refractive indices are sufficiently close to the target value n_{bottom} to yield high AR performance (given the much lower sensitivity to n of the bottom layer), they have comparable refractive indices to one another and are commonly used in Ag-containing stacks.

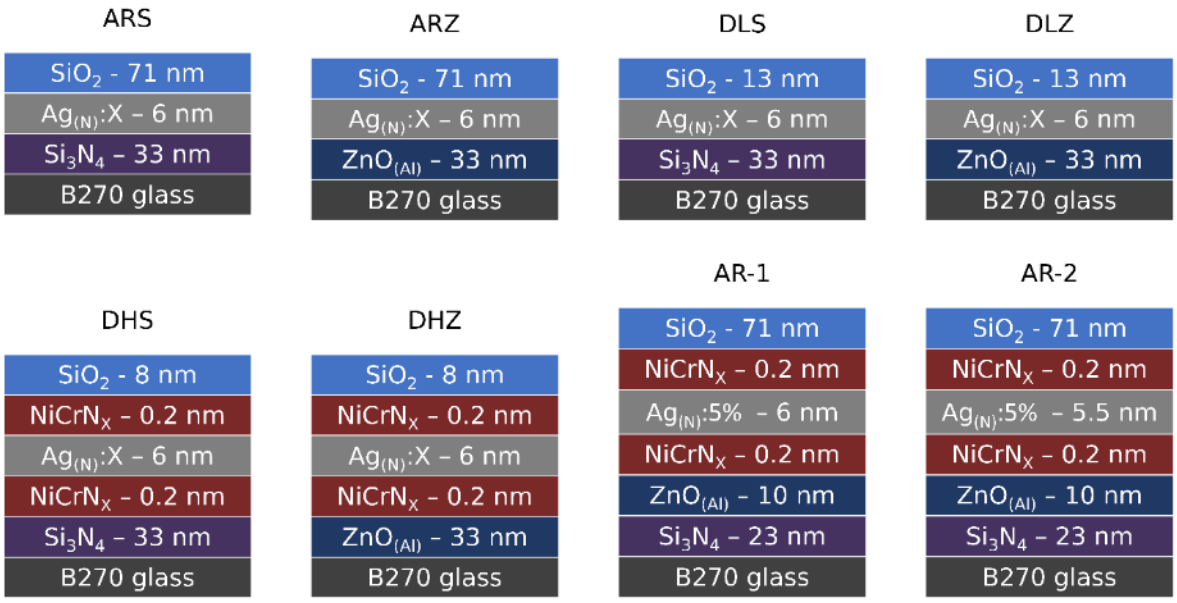


Figure 5.4: Schematic representation of the different filter architecture types used in Chapter 5, with their associated labels referred to throughout the text.

AR devices were fabricated following the optimized thicknesses obtained during modelling, replacing the custom refractive index layers with the materials selected above, resulting in a B270 / Si_3N_4 (33 nm) / $Ag_{(N)}$:X (6 nm) / SiO_2 (71 nm) architecture, referred to as ARS, and in an otherwise identical architecture substituting the Si_3N_4 for $ZnO_{(Al)}$, referred to as ARZ. Both architectures are shown in **Figure 5.4**. Thicknesses were not reoptimized for either of the materials, to compare these dielectrics at equal thickness. Modelling of each of these architectures, using dielectric refractive indices obtained via *ex situ* ellipsometry measurements, yield a predicted value of R_V^{FS} = 0.15% for ARS and R_V^{FS} = 0.12% for ARZ, confirming the low sensitivity to the bottom layer's refractive index. N_2 concentration in the Ar/N_2 sputtering gas was also varied, using 0%, 5% or 50% of N_2 in the sputtering gas mixture. The main performance metrics of these coatings are shown in **Figure 5.5**.

All ARS coatings are somewhat more reflective than the ARZ coatings. Given that the design was optimized using the Ag optical properties from Palik [14], this appears to be due to the $ZnO_{(Al)}$ seed layer promoting the growth of $Ag_{(N)}$ films with optical properties better matching those of Palik.

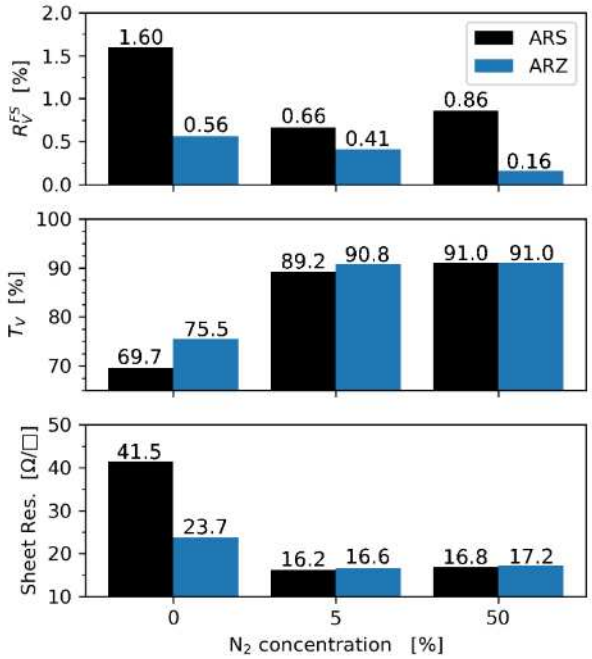


Figure 5.5: R_V^{FS}, T_V, and sheet resistance of samples deposited following ARS and ARZ architectures detailed in **Figure 5.4**, as a function of the N_2 concentration in the gas mixture during sputtering of $Ag_{(N)}$.

Despite this lower performance, all of the produced coatings display satisfying antireflective properties ($R_V^{FS} < 1\%$), with the exception of the ARS-$Ag_{(N)}$:0% coating. This is not unexpected, as N doping of the Ag layer has been shown to greatly improve film coalescence [18], [23], [294]. As a result, $Ag_{(N)}$:0% coatings deposited at a thickness of 6 nm display significantly lower performance, with high sheet resistance and low transmission attributable to a discontinuous morphology and plasmonic absorption. While the substitution of Si_3N_4 with $ZnO_{(Al)}$ offers significant improvement in both regards, these coatings still underperform when compared to those deposited with N_2 in the sputtering gas mixture.

The performance of $Ag_{(N)}$:5% and $Ag_{(N)}$:50% films show minor dependence either on the concentration of N_2 or the choice of the bottom layer. The $Ag_{(N)}$:5% shows a 1.6% increase in visual transmittance with the addition of the $ZnO_{(Al)}$ seed layer but is otherwise mostly unchanged. $Ag_{(N)}$:5% and $Ag_{(N)}$:50% coatings both show a marginal increase in sheet resistance with the addition of the $ZnO_{(Al)}$ seed layer, of 2.5% and 2.4% respectively, which is attributed to a higher

roughness of the $ZnO_{(Al)}$ seed layers as determined by *ex situ* ellipsometry and AFM measurements presented in **Figure C.2** of Appendix C. This is not unexpected, as non-negligible roughness of $ZnO_{(Al)}$ has also been reported elsewhere [308], [309]. For the final devices presented in Section 5.4.3, thinner $ZnO_{(Al)}$ layers are used to attempt to reduce their surface roughness.

The ARZ-$Ag_{(N)}$:50% sample displays the lowest reflectance (R_V^{FS} = 0.16%), which is remarkably close to the values modeled for reflection at normal incidence (R_V^{FS}= 0.12%), as well as high transmittance (T_V = 91.0%) almost equal to that of uncoated glass (T_V = 91.6%), and low sheet resistance (17.2 Ω/□). Its Haacke FoM is of 23.3 $k\Omega^{-1}$, whereas ARS-$Ag_{(N)}$:50% and ARZ-$Ag_{(N)}$:5% respectively yield FoMs of 23.7 $k\Omega^{-1}$ and 23.4 $k\Omega^{-1}$. These all outperform the values obtained for the continuous Ag coatings fabricated by Han *et al.* (16.2 $k\Omega^{-1}$), the Ag grids studied by He *et al.* (~17 $k\Omega^{-1}$), and the commercial ITO used as comparison by Maniyara *et al* (16.9 $k\Omega^{-1}$) [24], [283], [310].

There are numerous reports of Ag-based TCs with higher FoM [24], [280], [302], [303], [304], [311], [312]; therefore, it is worth reiterating that the present work is not focused on optimizing the Haacke FoM, which would be better pursued with optimization of the sheet resistance and transmission. Rather, the AR coatings presented here are merely meant to be comparable to conventional non-protected TCs, in order to demonstrate that these coatings can be made significantly more durable while enabling AR or other optical interference effects and maintaining conductivity and high transmission. Although N_2 doping was required to improve conductivity and reduce plasmonic absorption given the low Ag thickness, there were otherwise no specific requirements to achieve performance competitive with other TCs in our conductive AR coatings. As a result, the material choices and deposition conditions which will be found to yield the highest durability in the following section can be used as selection criteria to design durable and performant Ag-based TCs.

5.4.2 Evaluation of Ag durability

In order to identify the deposition conditions which promote the highest durability, a variety of coatings were evaluated, using both $ZnO_{(Al)}$ and Si_3N_4 seed layers, the three N_2 concentrations in $Ag_{(N)}$:X doping used in the previous subsection, and designs which include or do not include $NiCrN_x$ protective layers. It should be noted that samples with $NiCrN_x$ protective layers are used

exclusively with the high-severity testing conditions and vice-versa, as their addition or removal yields significantly different durability levels: samples without $NiCrN_x$ protection are completely degraded in only a few seconds in the high-severity conditions. Given that for certain applications durability requirements may be lower, it is of interest to optimize the durability in both regimes.

It has been demonstrated that increasing the thickness of dielectric layers generally reduces their permeability to water vapor [313]. Similarly, it has been shown that decreasing the thickness of an encapsulating dielectric can reduce the durability of the coating in hot water immersion [25]. As similar results are expected for immersion in a corrosive aqueous solution, to minimize the impact of the top encapsulating layer on durability, its thickness should also be minimized. However, the complete absence of a top encapsulating dielectric is known to drastically change coating durability [301]: this work focusing on DMD coatings, it would not be representative to test the durability of stacks without an encapsulating layer. As a result, 8 nm top layers were used to encapsulate samples with $NiCrN_x$ protective films. It was found in previous experiments (results not shown here) that for Ag layers with a 0.2 nm bottom $NiCrN_x$ layer continuous film formation was promoted, consistent with the observations of Fukuda *et al*. for Ni [151]. As a consequence, $Ag_{(N)}$:0% films used without $NiCrN_x$ were found to have substantially higher roughness. To compensate for this, the thickness of the encapsulating layers used for samples without $NiCrN_x$ was increased to 13 nm. Additionally, the top SiO_2 films used here are not optimized for conformality or density; as a result, the durability improvements reported in this work should be applicable to most encapsulated Ag films.

Finally, it should be noted that multiple other configurations were tested in addition to those reported here, using different types of bottom layers (ZrO_2, ZnO, B270 glass) and top layers (Si_3N_4), as well as different deposition methods (e-beam evaporation), deposition conditions (doping, reactive gases, substrate biasing, ion beam assistance), and deposited thicknesses, for both dielectric layers as well as the Ag layer. The results presented here are chosen as they are representative of the conclusions of the overall work.

Durability testing under low-severity conditions (0.1 mol/L NaCl, 30 °C) was performed with samples fabricated in a B270 / Si_3N_4 (33 nm) / $Ag_{(N)}$:X (7.5 nm) / SiO_2 (13 nm) architecture, referred to as DLS, and in an otherwise identical architecture substituting the Si_3N_4 for $ZnO_{(Al)}$, referred to as DLZ (see **Figure 5.4**). These architectures are highly comparable to ARS and ARZ

but use a higher $Ag_{(N)}$ layer thickness of 7.5 nm to ensure a more continuous $Ag_{(N)}$:0% layer, so that the significant difference in wetting for these samples at 6 nm does not affect durability, and a decreased SiO_2 layer thickness of 13 nm to simplify durability testing, as discussed above.

Durability testing under high-severity conditions (50 °C, 200 g/L) was performed with samples deposited in a B270 / Si_3N_4 (33 nm) / $NiCrN_x$ (0.2 nm) / $Ag_{(N)}$:X (6 nm) / $NiCrN_x$ (0.2 nm) / SiO_2 (8 nm), architecture, referred to as DHS, and in an otherwise identical architecture substituting the Si_3N_4 for $ZnO_{(Al)}$, referred to as DHZ (see **Figure 5.4)**. As mentioned previously, it was found that low thicknesses of $NiCrN_x$ (results not shown here), in the range of those suggested for optimal barrier layers by Xu *et al*. [178], were found to improve coalescence, particularly for undoped Ag films. At 0.2 nm mass-equivalent thickness, there should be less than a monolayer and thus the $NiCrN_x$ layer is expected to be highly discontinuous, leading to defect-driven continuous film formation [114], [151]. This results in continuous $Ag_{(N)}$ films at lower thicknesses, allowing the use of 6 nm $Ag_{(N)}$ films and thinner (8 nm) SiO_2 encapsulating layers.

Figure 5.6a and **Figure 5.6b** show the *in situ* spectrophotometry measurements of corrosion durability as a function of the concentration of N_2 used during the deposition of the $Ag_{(N)}$ films for the DLS and DHS filters, respectively. DLZ and DHZ films showed minimal variation following 1200 s of *in situ* corrosion testing, and were therefore compared using *ex situ* spectrophotometry measurements, as shown in **Figure 5.6c** and **Figure 5.6d**, respectively.

Figure 5.6a indicates that degradation occurs significantly faster for the DLS coatings when adding N_2 to the sputtering gas mixture, with sample stability decreasing as the N_2 concentration increases. The equivalent measurements for the DHS coatings, shown in **Figure 5.6b**, exhibit strong similarities to that of the DLS coatings. In both cases, $Ag_{(N)}$:50% displays rapid onset of degradation as well as a steep change in transmission. The observed change in transmission of DHS-$Ag_{(N)}$:5% is less steep than that of DHS-$Ag_{(N)}$:0%, and does not have a clear point of completion, possibly due to delamination. However, as both clearly indicate the onset of degradation, it can still be shown that the addition of even a relatively small concentration of N_2 during the deposition of the Ag layer can negatively impact durability.

The durability dependence on $Ag_{(N)}$:X concentration in the DLS and DHS samples, observed in **Figure 5.6a** and **Figure 5.6b**, can be attributed to a reduction in grain size with increasing N_2 concentration, as reported by Hu *et al*. [314]. The resulting increase in density of grain boundaries

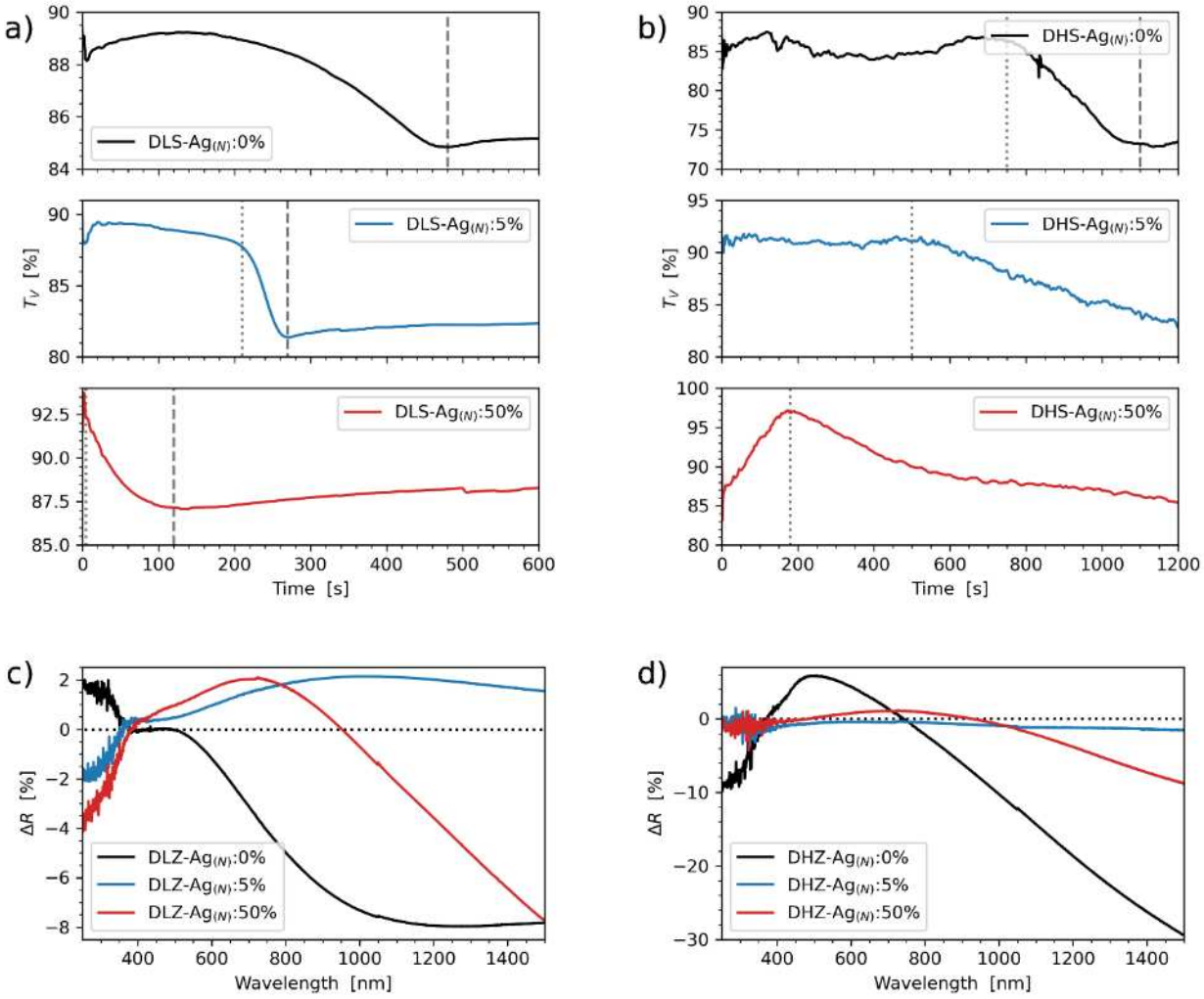


Figure 5.6: a), **b)** *In situ* transmission monitoring and **c)**, **d)** change in reflection ($\Delta R = R^{\text{Post}} - R^{\text{As-coated}}$) measured by *ex situ* spectrophotometry obtained in low-severity (**(a)**, **(c)**) and high-severity (**(b)**, **(d)**) corrosion tests of coatings deposited in various architectures for different N_2 concentrations in the gas mixture during sputtering of $Ag_{(N)}$. *In situ* measurements are annotated with approximative points of degradation onset (dotted lines) and complete degradation (dashed lines) where a clear transition can be observed. *Ex situ* measurements were only performed on samples which showed negligible change during *in situ* transmission monitoring. All architectures are detailed in **Figure 5.4**.

is then expected to accelerate degradation, as these are the main diffusion path for in-layer diffusion at low temperatures [170]. Grain size analysis of XRD measurements performed on 7.5 nm Ag layers, shown in **Figure C.1** of Appendix C, similarly supports this interpretation.

Figure 5.6c shows that DLZ-$Ag_{(N)}$:5% displays minor variation across the measured spectrum following corrosion testing, whereas other samples exhibit a significant decrease in near-IR reflectance. Presented in **Figure 5.6d**, DHZ samples show very similar behavior; despite quantitative differences, the main trends are repeated, with $Ag_{(N)}$:5% once again displaying extremely little change both in the visible and the near IR.

The improved durability observed for $ZnO_{(Al)}$ can be attributed in part to larger Ag grains, as reported in the literature [291], [315]. This is consistent with the observations found for DLS samples, and in agreement with XRD results shown in **Figure C.1** of Appendix C. Moreover, improved adhesion at the $ZnO_{(Al)}$-Ag interface, as opposed to most other transparent seed layers, is expected to reduce Ag diffusion towards corrosion sites, as demonstrated by Hafezian *et al.* [149]. However, the increased durability of samples with $Ag_{(N)}$:5% deposited on $ZnO_{(Al)}$ is not explained by these features.

Therefore, there appears to be a specific durability improvement when combining a $ZnO_{(Al)}$ seed layer with low (but not null) $Ag_{(N)}$:X concentrations. Yun *et al.*'s SIMS measurements revealed the presence of residual N_2 at the $ZnO_{(Al)}$ / $Ag_{(N)}$ interface and Hu *et al.* showed that thick $Ag_{(N)}$ films deposited with high N_2 content develop voids between grains: hence, it is suggested that at higher N_2 concentrations the formation of these voids, possibly near the lower interface, accelerate degradation by creating additional diffusion paths [18], [149], [314]. Given the qualitatively similar behavior of samples deposited with or without $NiCrN_x$, shown in **Figure 5.6a** and **Figure 5.6b** for Si_3N_4 seed layers and **Figure 5.6c** and **Figure 5.6d** for $ZnO_{(Al)}$ seed layers, the addition of $NiCrN_x$ appears to reinforce durability changes induced by the $Ag_{(N)}$:X deposition conditions and seed layer choice without changing the key mechanism. The bottom 0.2 nm $NiCrN_x$, therefore, appears to be sufficiently discontinuous to enable significant interaction between the $Ag_{(N)}$:X and $ZnO_{(Al)}$ layers, similarly to the observations of Fukuda *et al.* where it was found that certain sites showed heteroepitaxial growth of Ag on $ZnO_{(Al)}$ despite the presence of a discontinuous 0.5 nm titanium layer deposited between them [151]. As such, investigations of this improved durability can be simplified by studying $Ag_{(N)}$:0% and $Ag_{(N)}$:5% coatings on $ZnO_{(Al)}$ without the addition of $NiCrN_x$.

Figure 5.7 shows AFM images of 7.5 nm thick $Ag_{(N)}$:0% and $Ag_{(N)}$:5% films, deposited on 33 nm Si_3N_4 seed layers, which display high roughness, ($Ag_{(N)}$:0%: r_q = 4.36 nm, $Ag_{(N)}$:5%: r_q = 1.89 nm). The large elevated clusters are consistent with the TEM observations of Dannenberg *et al.*,

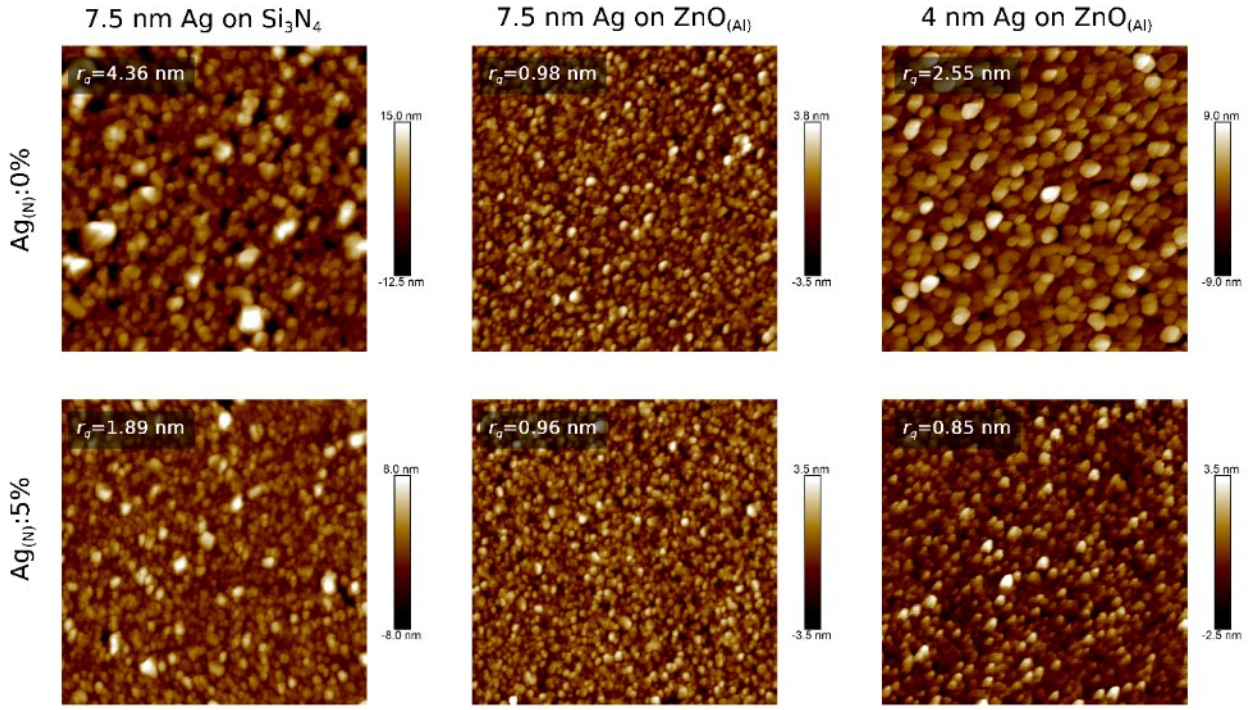


Figure 5.7: 1 µm × 1 µm AFM images of $Ag_{(N)}$:0% and $Ag_{(N)}$:5% films, with nominal thicknesses of 7.5 nm and 4 nm, deposited on 33 nm thick seed layers of Si_3N_4 or $ZnO_{(Al)}$, annotated with their root mean square roughness, r_q.

which showed large abnormal grains in Ag deposited on silicon nitride membranes [86]. These features are less pronounced for the sample using $Ag_{(N)}$:5%. Analysis of the AFM images, presented in **Figure C.3** of Appendix C, indicates that the 7.5 nm Ag layer deposited on Si_3N_4 has a relatively high density of large discontinuities for $Ag_{(N)}$:0%, whereas for $Ag_{(N)}$:5% there are only a few, substantially smaller discontinuities. The lower roughness and lower density and size of discontinuities in the $Ag_{(N)}$:5% film is in accordance with the literature and the optical and electrical performance measurements shown in **Figure 5.5** [18].

In comparison, the AFM images of 7.5 nm $Ag_{(N)}$:0% and $Ag_{(N)}$:5% films deposited on 33 nm $ZnO_{(Al)}$ shown in **Figure 5.7** display substantially lower roughness ($Ag_{(N)}$:0%: r_q = 0.98 nm, $Ag_{(N)}$:5%: r_q = 0.96 nm), as expected given its superior Ag wetting properties. Roughness of the uncoated Si_3N_4 (r_q = 0.24 nm) is lower than that of the $ZnO_{(Al)}$ (r_q = 0.76 nm) seed layers, as shown in **Figure C.2** of Appendix C, which confirms that there is not a substantial difference in the seed layer roughness. 7.5 nm $Ag_{(N)}$:0% and $Ag_{(N)}$:5% films deposited on $ZnO_{(Al)}$ do not have a

substantial difference in roughness, nor do they display an obvious difference in morphology at the upper surface which could explain the improved durability.

To evaluate morphological differences at the lower interface, $Ag_{(N)}$:0% and $Ag_{(N)}$:5% films in their early growth stages are investigated. AFM images of each $Ag_{(N)}$ type deposited on $ZnO_{(Al)}$, at a nominal thickness of 4 nm, are shown in **Figure 5.7**. It is found that despite the similar final morphology observed for continuous films, in this early stage of the $Ag_{(N)}$ film formation $Ag_{(N)}$:5% films show much lower roughness (r_q = 0.85 nm) than $Ag_{(N)}$:0% (r_q = 2.55 nm), with a higher density of smaller nucleation sites. This is consistent with the data in **Figure 5.5**, where 6 nm $Ag_{(N)}$:0% films on $ZnO_{(Al)}$ showed higher absorption and lower sheet resistance denoting a less continuous film morphology, and further supported by the observations of Zhao *et al*. which show distinct differences in initial wetting, including earlier coalescence with N_2 addition [23]. We propose that the enhanced durability observed for $Ag_{(N)}$:5% is a result of this improved wetting in the initial growth stages.

This hypothesis is consistent with reported mechanisms which could improve durability. Improved wetting may lead to higher Ag conformality at the lower interface; the reduction of voids within encapsulated structures has been shown to greatly impact durability [21], and improving the conformality is also expected to reduce surface diffusion at the Ag interfaces [156]. Improving the conformality of Ag encapsulation layers is a well accepted means to improve stability, but the lower interface is rarely considered [25], [179], [297], [298]. This lower interface should not be neglected: Ag films directly encapsulated with Al_2O_3 by atomic layer deposition were shown to be much more durable than Ag films which had evaporated dielectric coating between the Al_2O_3 and the Ag layer [297]. This supports the idea that conformal contact at the interfaces is required to optimize durability, and that simply generating a low permeability encapsulating layer is insufficient. As these improvements are not observed for $Ag_{(N)}$:5% deposited on Si_3N_4, it appears that the improved binding of Ag on $ZnO_{(Al)}$ plays a significant role as well. Therefore, improved contact leading to accentuation of the stabilizing effect of the seed layer previously demonstrated by Hafezian *et al.*, should be considered as well [149].

The suggested mechanisms are consistent with the decrease in durability encountered when switching from $Ag_{(N)}$:5% to $Ag_{(N)}$:50%: as discussed previously, existing literature has shown

elevated N_2 concentrations can produce features which could undermine the mechanisms proposed above.

5.4.3 Fabrication of Ag-based TCs with optimized AR performance and durability

Based on the results of the previous subsection, to fabricate a highly durable Ag-based coating, the design should include $NiCrN_x$ protection, N_2 doping at low concentration during Ag deposition and a $ZnO_{(Al)}$ seed layer. As higher roughness was observed for 33 nm $ZnO_{(Al)}$ seed layers than their Si_3N_4 counterparts (see **Figure C.2** of Appendix C), a Si_3N_4 underlayer is used below the $ZnO_{(Al)}$ seed layer to reduce the required thickness of $ZnO_{(Al)}$, with the aim of reducing its roughness. Finally, to optimize the AR performance, a thin (≈ 6 nm) Ag layer coupled with a low index top dielectric is required.

Therefore, an optimized AR filter was fabricated using the following architecture: B270 / Si_3N_4 (23 nm) / $ZnO_{(Al)}$ (10 nm) / $NiCrN_x$ (0.2 nm) / $Ag_{(N)}$:5% (6 nm) / $NiCrN_x$ (0.2 nm) / SiO_2 (71 nm), which shall be referred to as AR-1 (see **Figure 5.4**). Using experimental values of the dielectric refractive indices in lieu of the customizable refractive index previously used in the modelling approach, a second iteration of modelling was performed, and it was found that transmission and AR performance could be improved while retaining the current architecture, and simply reducing the $Ag_{(N)}$:5% thickness. A sample, referred to as AR-2, was made with a $Ag_{(N)}$:5% thickness of 5.5 nm based on this result. The optical performance of AR-1 and AR-2 are compared to that of uncoated B270 glass substrates in **Figure 5.8a** and **Figure 5.8b**.

These coatings, despite not having optical and electrical performance as high as their counterparts without $NiCrN_x$ presented in **Figure 5.5**, show both excellent performance in reflection and transmission. The decrease in reflection and increase in transmission from AR-1 to AR-2 (0.3% and 1.1%, respectively) follow the expected changes as predicted by the model (0.16% and 0.51%, respectively); the discrepancies may be due to the simplifications used in the model, discussed in Section 5.3.2, the omission of the $NiCrN_x$ layers from the model, or a combination of these. The improvements result in exceptional optical performance for AR-2, which has a R_V^{FS} nearly 20 times lower than that of uncoated glass and T_V less than 2.5% below that of uncoated glass. As such, it

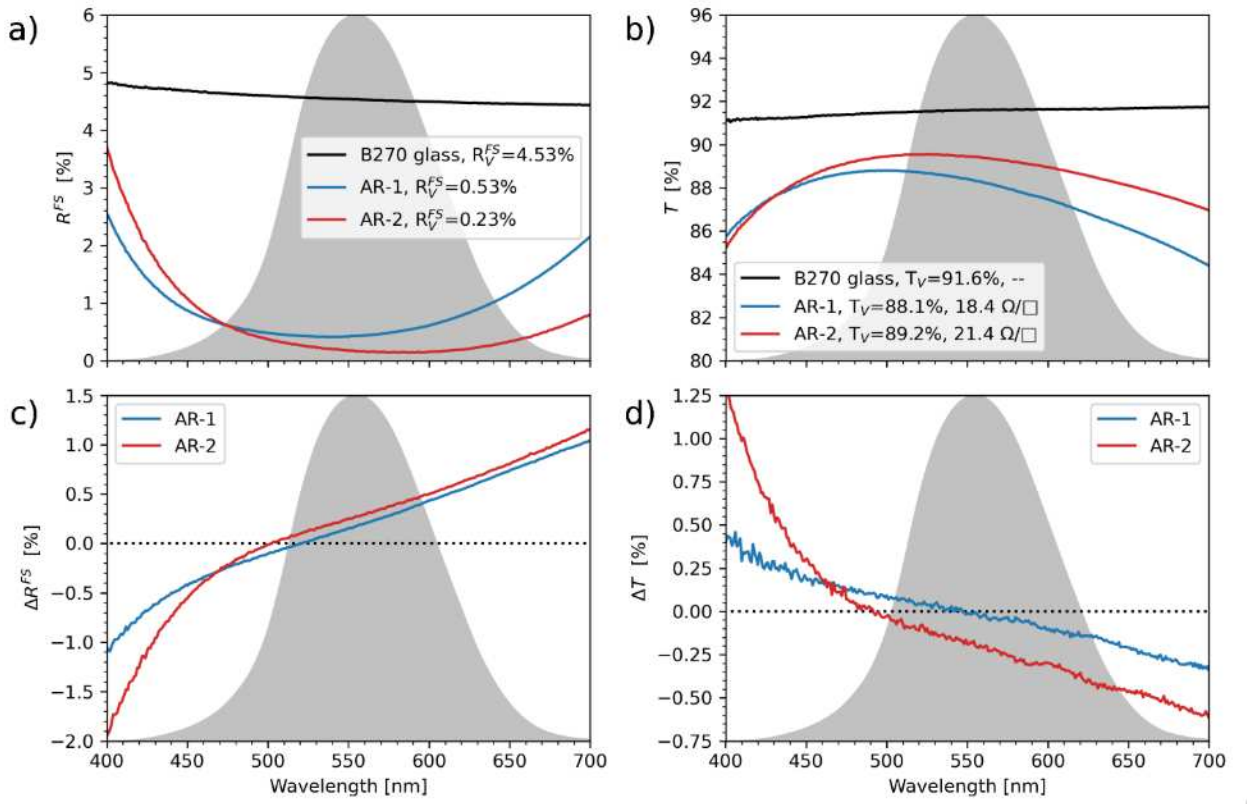


Figure 5.8: a) Front-side reflectance and **b)** transmittance of the AR-1 coated, AR-2 coated and uncoated B270 glass. R_V^{FS}, T_V, and sheet resistance are included in the graph legends. **c)** Change of front-side reflectance and **d)** of transmittance ($\Delta R^{FS} = R^{FS\text{-}Post} - R^{FS\text{-}As\ coated}$, $\Delta T = T^{Post} - T^{As\ coated}$) of the AR-1 and AR-2 samples following 20 minutes of sample immersion in high severity corrosion testing conditions (200 g/L of NaCl, 50 °C). Gray underfilled curves represent the luminous efficiency function of the CIE-1931 observer, normalized to the graph bounds. AR-1 and AR-2 architectures are detailed in **Figure 5.4**.

maintains performance in transmission just short of Maniyara *et al.*'s and displays AR performance which surpasses it by far (≈ 2% reflection at 525 nm) [24].

It should be noted that the addition of $NiCrN_x$ decreases both optical and electrical performance, which is associated to Ni interdiffusion with Ag [20]. AR-2 displays slightly higher sheet resistance than AR-1 as expected for a thinner Ag coating, though this increase does not appear to indicate a meaningful change in the Ag layer resistivity when accounting for the lower thickness. Although the sheet resistance obtained is higher than that of most designs employing thicker Ag layers, it remains well within the acceptable bounds of TC coatings for most applications. In terms of the

Haacke FoM, the high durability AR coatings, AR-1 and AR-2, show acceptable performance, respectively having values of 15.8 and 15.7 $k\Omega^{-1}$. Although this is substantially below the FoM of ARZ-$Ag_{(N)}$:50% at 23.3 $k\Omega^{-1}$, they remain competitive with other values in literature despite being optimized for AR performance (Continuous Ag, Han *et al.*: 16.2 $k\Omega^{-1}$, Ag grids, He *et al.*: ~17 $k\Omega^{-1}$, commercial ITO from Maniyara *et al*.: 16.9 $k\Omega^{-1}$) [24], [283], [310].

The particular novelty of the AR-1 and AR-2 coatings is not in their optical and electrical performance or in their antireflective performance, but in achieving all of these simultaneously with high environmental resistance. AR-1 and AR-2 coatings were submitted to saline corrosion testing under the high-severity testing conditions (200 g/L, 50 °C) for 20 minutes. Changes in front-side reflection and transmission in the visible range are shown in **Figure 5.8c** and **Figure 5.8d**, revealing minimal performance loss, mostly below 1%: this results in variation of R_V^{FS} and T_V of less than 0.5%. Furthermore, the near IR variation is below 1.5%, denoting that Ag conductivity is well maintained.

To support this, following successful results with sample AR-1 in the *in situ* corrosion monitoring cell, AR-2 was fabricated and submitted to corrosion testing as a 5 cm by 5 cm sample to enable sheet resistance measurements following corrosion testing. Tests were performed in the same conditions using a beaker and hot plate, where the solution temperature was monitored using the same thermocouple setup as for the *in situ* setup. To ensure that the larger volume of liquid was kept at even temperature and concentration, a magnetic stirrer was used. Following corrosion testing, AR-2's sheet resistance increases from 21.4 Ω/□ to 21.7 Ω/□, or less than a 2% change, demonstrating high stability of the sheet resistance as well as the optical stability (see **Figure 5.8**). In comparison, unprotected Ag-based TCs were found to degrade completely within a few seconds of high severity testing. The only device from literature known to the authors with comparable performance and durability (tested by water immersion at 100 °C, however, without NaCl addition) is that produced by Jeong *et al*.; it is worthwhile to note that it also makes use of $Ag_{(N)}$ deposited on a ZnO seed layer, rather than on $ZnO_{(Al)}$ [25].

Coating flexibility was not tested here, as the AR design makes use of relatively thick dielectric layers not designed for such implementation. However, as Kim *et al*. report on the fabrication of flexible TCs based on $Ag_{(N)}$ layers sandwiched between $ZnO_{(Al)}$ layers as thick as 30 nm, which show with minimal negative effects on flexion durability up to 4000 cycles, and prior experiments

found that $ZnO_{(Al)}$ seed layers of thicknesses as low as 5 nm maintain their wetting efficiency, the methods used to improve durability are expected to enable versatile designs compatible with flexible electronic device implementation.

5.5 Conclusions

In this work, we aimed to address and improve the environmental durability of Ag-based TCs, which is frequently overlooked in current literature. In order to allow versatile approaches which do not rely on specific Ag encapsulation strategies and enable the fabrication of high performance TCs and optical devices, we studied durability improvements obtained by modification of the Ag microstructure and redesign of the optical filter stacks. To achieve this goal without diminishing Ag's favorable optical and electrical properties, we first modified the microstructure by an appropriate choice of seed layer material and by adjusting the gas concentration used in N_2-doped Ag, or $Ag_{(N)}$.

In situ and *ex situ* spectrophotometry for assessing the effect of the Cl-containing environment were used to compare the durability of Ag-based devices. We demonstrated that increasing N_2 concentration during $Ag_{(N)}$ deposition on Si_3N_4 seed layers results in decreased $Ag_{(N)}$ durability due to a concurrent decrease in grain size. On the other hand, equivalent films deposited on $ZnO_{(Al)}$ were found to be substantially more durable, which was attributed to the improved crystal structure promoted by the seed layer and decreased Ag diffusion towards corrosion sites thanks to improved adhesion at the Ag-$ZnO_{(Al)}$ interface, as opposed to Ag and Si_3N_4.

Most importantly, it was found that when using intermediate N_2 concentrations in the sputtering gas mixture ($Ag_{(N)}$:5%, compared to 0% and 50%), $Ag_{(N)}$ films deposited on $ZnO_{(Al)}$ reached higher durability than with either other formulation, distinctly superior to that which could be obtained with Ag deposited in pure Ar. While the addition of $NiCrN_x$ protective coatings was found to greatly increase coating durability, all of the above trends were maintained, indicating a net benefit to the combination of a $ZnO_{(Al)}$ seed layer, $NiCrN_x$ protective layers, and $Ag_{(N)}$ with low, but non-zero N_2 concentrations. This enhanced durability is attributed to improved wetting of $Ag_{(N)}$:5% on $ZnO_{(Al)}$ in the early growth stages of the film, as shown by AFM measurements. Thus, the proposed mechanism relies on improved contact at the Ag-$ZnO_{(Al)}$ interface resulting in reduced voids in the encapsulated coating, and reduced diffusion at the lower Ag interface as a result of both the higher

conformality and the strong adhesion between Ag and $ZnO_{(Al)}$. Further analysis of the Ag microstructure and its relation to the observed durability improvements may lead to an improved understanding of this mechanism. Particularly, investigation of potential nanoscale defects, such as pinholes and voids, in otherwise continuous Ag films by high-resolution field emission scanning electron microscopy as well as direct observation of the crystallinity and interface quality of Ag and the various seed layers by cross-sectional TEM could bring additional insight into the behaviours reported here.

A transfer-matrix model was used to show that highly antireflective coatings could be produced at various Ag thicknesses by adjusting the refractive indices of the adjacent dielectrics, with optimal AR performance being obtained with an ultra-thin Ag (≈ 6 nm) coupled with a low-index top encapsulating dielectric. While having higher predicted reflectivity, such DMD stacks using other Ag thicknesses, which could enable lower sheet resistance, were also shown to be able to achieve low reflectance.

The combination of $ZnO_{(Al)}$, $NiCrN_x$, and $Ag_{(N)}$:5%, was implemented in the optimized AR design, resulting in a highly durable AR coating stack which exhibits high transmission (T_V = 89.2 %, less than 2.5% loss in visual transmission), ultra low reflection (R_V^{FS} = 0.23 %) and a sheet resistance of 21.4 Ω/□, all of which show minimal changes following saline corrosion testing by immersion in a 200 g/L aqueous NaCl solution at 50 °C, for a duration of 20 minutes. This demonstrated that the proposed modifications enable high versatility in terms of Ag thickness, optical performance, AR effectiveness, durability and material selection.

Given the commonplace usage of the materials and techniques required to achieve these improvements, and given the flexibility of material selection suggested by the modelling results, we believe that this approach enables one to benefit from high durability, optically performant Ag films in a variety of contexts, including but not limited to, touchable and flexible electrodes, single pane low-emissivity windows and filters, and antireflective antistatic ophthalmic and other filters.

5.6 Acknowledgements

The authors wish to thank Dr. Patricia Moraille for the AFM measurements, as well as Mr. Francis Turcot and Mr. Francis Boutet for their assistance with assembling the *in situ* corrosion testing set-up and maintenance of the deposition system. The project was financially supported by the Natural

Sciences and Engineering Research Council (NSERC) of Canada through the NSERC-Alliance grant (no. ALLRP 576758 - 22), by Prima Quebec (grant no. R24-13-003), and by EssilorLuxottica and Guardian Glass.

CHAPTER 6 ARTICLE 3: INVESTIGATING THE MORPHOLOGICAL EVOLUTION OF ION-THINNED AG FILMS VIA IN SITU ELLIPSOMETRY

6.1 Foreword

In Chapter 4, the stability of low-E coatings at high temperatures was investigated through the lens of contaminant diffusion; thus, coatings in which contaminant diffusion was successfully mitigated were lauded as stable. Indeed, the resulting changes led mainly to improved performance, with increased transmission in the visible and lower sheet resistance, highlighting the central role of Ag grain growth. For the purpose of achieving single-stock low-E glass, although, these changes remain an impediment.

As in Chapter 5, this work aims to mitigate these changes via microstructural control of the Ag layer, without modifying its composition. As outlined in Section 2.3.2, mitigation of grain growth without the usage of dopants requires improved interfacial adhesion, as well as larger and more uniform grain sizes. While the combination of $Ag_{(N)}$ and $ZnO_{(Al)}$, as used previously, should offer improvements on these points, particularly in regard to interfacial contact and grain uniformity, this was found to be insufficient to mitigate grain growth.

This leaves us with a difficult predicament; larger Ag grain sizes ought to improve optical stability, but this requires additional coalescence of Ag grains. In turn, greater coalescence of Ag grains will result in higher thresholds for continuous film formation, as discussed in Section 2.2.1. This calls for deposition methods that allow to break free from the interplay between the nucleation and coalescence of grains; we will turn to post-deposition etching.

Attempting to stabilize low-E optical performance during tempering, via microstructural control of the Ag film, will thus be broken down into two parts. This chapter will address the fabrication of Ag films via post-deposition etching, explicitly addressing the second objective of this thesis. As previously, this will include the integral text of an article in which the effect of post-deposition etching on the critical thicknesses achievable for Ag films for different deposition parameters; following this, additional results pertaining to the application of etched Ag films in antireflective coatings will be presented. Supporting information is included in Appendix D. The application of

post-deposition etching to optical stabilization of tempered low-E coatings will then be presented in Chapter 7, addressing the third objective of this thesis.

INVESTIGATING THE MORPHOLOGICAL EVOLUTION OF ION-THINNED AG FILMS VIA IN SITU ELLIPSOMETRY

Phillip Rumsby, Bill Baloukas, Oleg Zabeida, Ludvik Martinu*

Department of Engineering Physics, Polytechnique Montréal, Montréal, QC H3T 1J4, Canada

Submitted to the *Journal of Applied Physics* on 2025-11-18.

Abstract

Ion-etching of Ag films following their deposition presents an alternative method to improve wetting and obtain conductive Ag films at low thicknesses. Moreover, this approach does not rely on conventional wetting mechanisms, allowing one to obtain qualitatively different Ag morphologies at a given thickness. To evaluate how the Ag morphology evolves during etching, established interference-enhanced in situ ellipsometry monitoring methods are supplemented with a complementary comparative modelling approach, allowing one to monitor both the formation of fully continuous films and conductive Ag networks throughout deposition, as well as the breakdown of these morphologies during etching. This reveals that breakdown behaviors of continuous and percolated film structures are driven by distinct mechanisms, contrary to their formation during Ag deposition. The critical film thicknesses obtained via etching are studied as a function of various deposition conditions in relation to the resulting Ag properties. This particularly highlights the methods to improve the performance of etched films through control of the growth conditions, while revealing far less dependence on film-substrate surface energy mismatch than during Ag deposition. The observed film breakdown behaviors are explained in terms of conventional solid-state dewetting mechanisms, i.e. grain boundary grooving and hole expansion mechanism, adapted to the context of ion-etching.

6.2 Introduction

Thin silver (Ag) films are currently amassing interest as a flexible alternative to conventional transparent conductors (TC) such as indium-tin oxide; indeed, the latter's brittleness and high-temperature processing requirements complicate implementation into flexible devices, which typically use temperature-sensitive polymer substrates [316], [317]. Although metallic meshes and nanowires have proven to be performant flexible transparent conductors [69], [282], continuous Ag films allow for simple implementation in physical vapor deposition processes, and are preferrable for antireflective [44], [278], EMI shielding [24], [318], and energy-saving window applications [5], [52].

However, the deposition of highly conductive, thin, and continuous Ag films is inherently limited by its Volmer-Weber growth mode, wherein kinetic processes of cluster nucleation and agglomeration compete with reorganization into thermodynamic equilibrium structures [19]. Thus, conventional methods with which one may control the resulting morphology of Ag thin films, such as substrate temperature [99], [112], deposition rate [99], [111], energy and flux of incident particles [26], [113], diverse types of metallic seed layers [114], [115], as well as various dopants and surfactants [32], [48], [105], [108], lead to a correlation between low continuous film thickness (necessary for optical transparency) and fine grain structures (which increase film resistivity) [31]. Although usage of appropriate seed layers promoting Ag crystallinity may alleviate this issue [18], [23], [278], obtention of large grains in such layers may also require high temperature processing, introducing undesirable fabrication requirements.

In this work, we investigate a less common paradigm, which may circumvent these issues. Namely, ion etching is employed to reduce film thickness after achieving continuous film formation, resulting in a hysteresis of the Ag morphology as thickness is increased and subsequently decreased [82], [83], [127], [128], [319].

Early work surrounding this topic provides some useful observations and hypotheses. Netterfield and Martin showed that the use of different reactive species and ion bombardment energies can influence the thickness at which continuous gold films break down, which is attributed to a change in contact angle and surface coverage at the substrate-film interface. More specifically, they propose that the lowest achievable continuous film thickness is limited by the sum of the roughness at the upper and lower interfaces [127]. Moreover, Hodgkinson and Lemmon show that Au film

morphology (discontinuous islands, wormlike structures, continuous films), following deposition, strongly influences the morphology obtained during etching: for example, highly discontinuous droplets shrink individually while the island density remains more or less stable, and worm-like islands become narrower while maintaining their shape [128]. More recently, the work of Ma *et al*. leverages this approach to produce extremely thin continuous Ag films down to 4.5 nm; however, they attribute this effect to partial substrate implantation of their films, deposited by ion-beam-sputtering [82], at odds with similar results obtained by Ferrando *et al*. [83]. Thus, it would appear that the mechanisms controlling film breakdown during etching are not yet well understood.

Although optical monitoring was used in earlier investigations of the etching behavior of noble metal films, more recent work has not made use of such techniques, despite monitoring of Ag film morphologies via *in situ* ellipsometry (ISE) being well established [82], [127], [128], [319]. Namely, Colin *et al*. describe how changes in the film resistivity, obtained from Ag optical properties modeled to fit ISE data, can be used to identify the transition to a fully continuous Ag film [85]. However, to accurately model the Ag optical properties, which include both real and imaginary components, interference-enhanced (IE) ellipsometry is required to deconvolute the thickness from the film properties [246], [247]. In turn, this imposes a requirement for substrates which present resolved optical features (e.g.: interference fringes), limiting the choice of substrates.

In this work, we aim to obtain a more general understanding of the mechanisms controlling the morphology of thin Ag films during post-deposition etching in order to identify tunable parameters which allow its effective implementation in a broad range of fabrication techniques.

Tracking Ag resistivity with IE-ISE is well-suited for identifying the morphological transition to and from continuous film morphologies. However, the transition between isolated islands and percolated structures, which is shown to be significantly different during etching, is not clearly discernable with this approach. To remedy this, we propose a simple, substrate-agnostic ISE approach which uses comparative modelling, similarly to surface differential reflectance spectroscopy (SDRS) [153]. This method can identify the percolation threshold regardless of substrate interference features and without needing additional equipment, allowing it to be used simultaneously with conventional IE-ISE monitoring.

Using the comparative modelling approach and conventional IE-ISE monitoring of the film resistivity in concert, we evaluate the effect of a wide variety of film deposition conditions and

substrate properties on the morphological evolution of Ag films throughout deposition and etching. The trends observed within this work are explained on the basis of known solid-state dewetting mechanisms and recommendations are made to improve the range of thicknesses achievable via ion etching.

6.3 Experimental methodology

Sample fabrication was performed via magnetron sputtering in a Kurt J. Lesker CMS-18 deposition system equipped with 3-inch magnetrons and substrate heating. The deposition parameters of individual films are detailed in **Table 6.1**. SiO_2 layers, as well as select Ag layers, were deposited with a RF bias of -50 V applied to the substrate holder during deposition. All other films were deposited at floating potential. Ag layers were thinned post-deposition (etched) using a RF bias plasma, obtained by applying a power of 12 W to the substrate holder (15 cm diameter), with a working pressure of 8 mTorr of pure Ar, resulting in a -150 V bias.

To obtain IE-ISE compatible substrates, 1 μm SiO_2 layers were produced on Si(100) wafers, either by wet thermal oxidation or via RF sputtering (as described above). This thickness was chosen as it produces clear interference fringes throughout the wavelengths of interest, as shown by Hilfiker *et al*. [246], and wafers with this thickness of thermal oxide are readily commercially available. As each method results in characteristically different degrees of roughness, substrates using each type of SiO_2 are simply referred to as smooth or rough, respectively. SiO_2 surfaces are either left bare or overcoated with 10 nm of aluminum-doped zinc oxide ($ZnO_{(Al)}$). Note that the root-mean-square roughness, r_q, is not meaningfully attenuated by the addition of the $ZnO_{(Al)}$ films. The atomic force microscopy (AFM) scans used to obtain r_q are shown in **Figure D.1** of Appendix D.

Table 6.1: Summary of the deposition conditions used for the different films in Chapter 6.

Layer	Target	Power	Mode	Pressure	Gas flow ratio	RF bias voltage
-	-	[W]	-	[mTorr]	[sccm]	[V]
Ag	Ag	120	DC	4	Ar/N_2 (100/ 0, 5.26, 100)	0 / -50
$ZnO_{(Al)}$	Zn/Al (98/2 wt %)	300	RF	2	Ar/O_2 (100/35)	0
SiO_2	Si	450	RF	2	Ar/O_2 (100/30)	-50

For select samples, substrates were kept at elevated temperatures during Ag deposition using quartz heating lamps positioned behind the substrate holder; such samples were allowed to cool prior to ion etching. The various substrate conditions resulting from the combination of different SiO_2 types, overcoats, and substrate heating temperatures are summarized in **Table 6.2**. For experiments which did not make use of IE-ISE, standard Si(100) substrates were used. All substrates were precleaned with a -235 V (25 W) bias RF plasma in an Ar/O_2 gas mixture (100/35 sccm) at a working pressure of 8 mTorr, prior to the deposition of $ZnO_{(Al)}$ or Ag layers.

***In situ* ellipsometry** was performed using a J.A. Woollam iSE ellipsometer, with a wavelength range of 400 to 1000 nm, and analysed using the associated *CompleteEASE* software. Ag film properties were primarily modelled using a Drude oscillator allowing the fitting of the resistivity (ρ) and scattering time (τ). A scalar shift of the real part of the dielectric function and a Gaussian oscillator, both fixed, were sufficient to complete the model: as the used ellipsometer does not capture any UV data, most of Ag's additional optical dispersion features are outside its range. The model was initially fit to Palik's Ag to obtain starting values before fitting to experimental data [14].

When fitting the optical properties of a continuous Ag film after deposition, ρ and τ are fit independently, and their product is calculated. However, as this product should be constant for a given ideal metal, when fitting to *in situ* data obtained during the deposition or etching processes, the previously obtained product is kept fixed, with any change of ρ forcing an inverse change for τ [85], [320]. This allows both parameters to vary, albeit not independently, and to obtain appropriate optical properties while maintaining a robust parametrization.

Table 6.2: Summary of the different substrate conditions used for IE-ISE monitoring, where r_q is the root-mean-square roughness obtained by AFM over a 1 μm × 1 μm area.

Name	Added layers	SiO_2 type	r_q	Temperature
SiO_2	None	Wet thermal oxidation	0.18 nm	-
SiO_2 [60 °C]	None	Wet thermal oxidation	0.18 nm	60 °C
SiO_2 [rough]	None	RF sputtering	2.61 nm	-
$ZnO_{(Al)}$	10 nm $ZnO_{(Al)}$	Wet thermal oxidation	0.39 nm	-
$ZnO_{(Al)}$ [80 °C]	10 nm $ZnO_{(Al)}$	Wet thermal oxidation	0.39 nm	80 °C
$ZnO_{(Al)}$ [rough]	10 nm $ZnO_{(Al)}$	RF sputtering	2.57 nm	-

***In situ* sheet resistance** measurements were performed using a Keysight EDU34450A digital multimeter in a 4-wire configuration: to do so, 100-nm-thick Ag contacts were deposited at the corners of a 2 in. by 2 in. substrate and probes were connected to these contacts in a Van der Pauw geometry using copper tape [321]. For each sheet resistance measurement, wire connections to the multimeter were switched in order to obtain data for all probe configurations.

***Ex situ* ellipsometry** measurements were performed using a J.A. Woollam RC2-XI variable angle ellipsometer, in order to confirm ISE results and obtain more precise optical properties of deposited layers for use in modelling.

Scanning electron microscopy (SEM) imaging was carried out in a Thermo Fisher Scientific Helios 5 Hydra CX system. Measurements were performed in immersion mode, with an acceleration voltage of 2 kV and a working distance of 2.1 mm. All shown images have a horizontal full width of 1.18 μm.

Atomic force microscopy (AFM) images were captured using a Bruker Dimension ICON AFM with a NanoScope VI controller. All 1 μm × 1 μm AFM scans were acquired using PeakForce QNM Tapping mode and were performed at a scanning rate of 1 Hz. Scan Asyst Air probes, with a spring constant of 0.4 $N \times m^{-1}$ and a tip of 5-10 nm radius were used with applied imaging force setpoints ranging between 700-900 pN. Root-mean-square roughness (r_q) was obtained for each image using the Bruker Nanoscope Analysis software after applying 1st order plane fit and 1st order flatten operations.

X-ray diffraction (XRD) measurements were performed using a Bruker D8 Discovery diffractometer equipped with a Cu anode (Kα wavelength = 0.15406 nm) in Bragg-Brentano geometry.

6.4 Results & discussion

6.4.1 Monitoring the formation and breakdown of conductive networks via *in situ* ellipsometry

In order to investigate their morphological evolution, a series of Ag films were deposited on $ZnO_{(Al)}$-coated Si wafers and subsequently etched via a RF bias plasma; this process was interrupted at different points to obtain scanning electron microscopy (SEM) images of the films

obtained at various stages, as shown in **Figure 6.1a-h**. These reveal that conventionally deposited and etched films can present very different transitions between fully discontinuous and percolated film morphologies, even when transitioning to or from a fully continuous film at the same thickness. As a result, typical IE-ISE techniques monitoring the formation of continuous films are insufficient. However, *in situ* measurements of early stages of film formation following the Lorentz resonance with ISE are rather involved and do not lend themselves to easy quantification [108], while *in situ* sheet resistance or SDRS measurements of the percolation threshold require additional equipment [153], [322].

Therefore, as a complement to conventional IE-ISE monitoring of the film resistivity, we propose a comparative modelling approach which can be used with or without substrates presenting interference features and which allows one to monitor the formation and breakdown of conductive networks. In fact, the proposed approach only requires that ISE measurements be taken throughout deposition (and etching, when performed) and that deposition is long enough to ensure continuous film formation. Following deposition, the optical properties (ρ, τ) and thickness (t) of the continuous Ag coating are fitted to the experimental data, referring to known values and following the procedure in the experimental methodology section. This model is then fitted to each time increment of the remaining experimental data, while leaving only the Ag film thickness as an adjustable parameter (ρ and τ are fixed, t is fitted). This allows the model to accommodate small variations in optical properties without deviating from experimental data, and the obtained thickness values can be compared to known deposition rates to validate the fit. As a result, the modelled data only begins to deviate from the experimental data when the optical properties of the film significantly depart from those obtained for the continuous reference film. Thus, comparison between the modelled and experimental data allows one to evaluate the thicknesses at which there are qualitative changes of the optical properties which cannot be convoluted with thickness changes, i.e. during formation and breakdown of large-scale conductive Ag networks. Thus, the proposed comparative modelling method identifies the percolation transition in a manner highly comparable to SDRS, without requiring different equipment than is used for IE-ISE monitoring. As in the case of SDRS, to quantify the deviation from the reference film properties, the mean-square-error (MSE) between the experimental and the modelled data is used [153]. It should be noted that, in principle, this technique could be used for real-time growth monitoring, assuming the deposition rate and continuous film optical properties are well known. In such case, the thickness

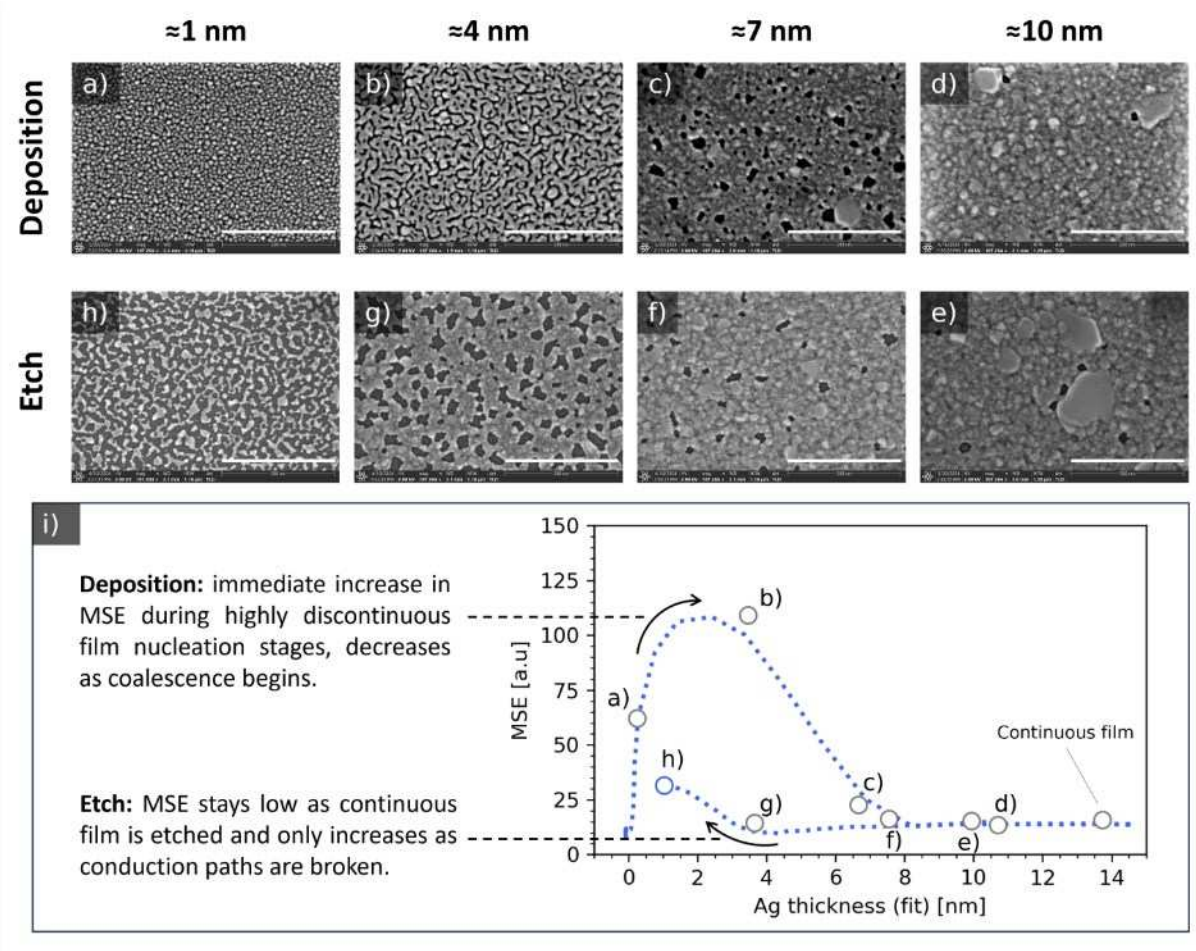


Figure 6.1: SEM images of Ag films produced by **a)-d)** deposition on $ZnO_{(Al)}$-coated Si substrates and **e)-h)** subsequent etching. All etched films were deposited at an equal nominal thickness of 15 nm before beginning the etching process. All scale bars correspond to 500 nm. **i)** MSE obtained via comparative modelling, as a function of the fitted Ag thickness for the films presented in **(a)-(h)**. The blue curve shows the monitoring results of a full deposition and etching cycle, obtained for sample **(h)**. Gray circle markers represent the final MSE and fitted thickness of the other samples, which were interrupted at different stages of deposition or etching.

should be allowed to vary about the nominal thickness to allow it to accommodate small optical changes, as discussed above.

Figure 6.1i shows the MSE-thickness curve obtained during the deposition and etching of Ag deposited on $ZnO_{(Al)}$. The SEM images shown in **Figure 6.1a** to **Figure 6.1h** were monitored with the comparative modelling method, and the position of the final data point obtained for each sample is identified in **Figure 6.1i** with its respective letter. Samples **(a)-(d)** show the film morphology

obtained during various stages of deposition; similarly, samples **(e)-(h)** show the morphology obtained following the etching of such films. This demonstrates that even in cases where etching yields no obvious improvement in terms of minimum achievable continuous film thicknesses, clear enhancements can be obtained at lower thicknesses, highlighting the need to monitor the formation and breakdown of conductive networks. Indeed, samples in the image pair **(d)** and **(e)** show no appreciable differences in terms of continuous film formation, with holes respectively remaining and appearing in approximately equal quantity within the same thickness range. On the other hand, for the films shown in the image pair **(b)** and **(g)**, etched films show a dramatic improvement, retaining a well-percolated network with clear conduction paths, whereas standard deposition results in a barely percolated, highly discontinuous film with worm-like structures. The difference in structure is clearly identified with the comparative modelling approach, as shown by the stark difference in MSE obtained for these samples in **Figure 6.1i**.

Furthermore, these images confirm that the comparative modelling method is not sensitive to the formation or breakdown of continuous films as no significant changes in MSE are detected above 8 nm, despite passing to and from discontinuous morphologies (as seen for point **(c)** onwards to 15 nm, and from 15 nm down to point **(g)**). This is expected, as small changes in film resistivity can be convoluted with changes in film thickness: consequently, only the more distinctive changes occurring when transitioning from plasmonic Ag nanostructures to a conductive, percolated network are readily detectable. This is further demonstrated in **Figure 6.2**, which shows that for samples without interference enhancement, the change in MSE corresponds to large-scale changes in resistivity (ρ), measured via *in situ* sheet resistance measurements and converted to resistivity using nominal thickness values.

While this approach does not require interference enhancement, it can be used with it. However, some adjustments must be made to take into consideration the resulting increase in sensitivity which comes with changing to an IE-ISE compatible substrate; indeed, the comparative modelling approach relies on a lack of sensitivity to small changes in the film resistivity, rather than the opposite. To account for the increased sensitivity imparted by the oxide layer, two models are fit to IE-ISE data: one for which only the Ag thickness is allowed to vary (t-only), and one for which both the Ag thickness and the resistivity of the Drude oscillator (coupled to its scattering time) can vary (t-ρ). The latter will account for optical changes which are consistent with an ideal metal, and thus comparison between the two fits will once again highlight qualitative differences in the optical

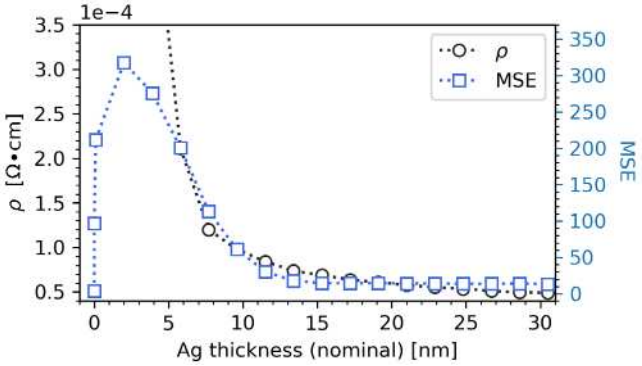


Figure 6.2: MSE obtained with interference agnostic ISE monitoring and associated Ag resistivity, obtained from *in situ* sheet resistance measurements and nominal Ag thickness values, as a function of the nominal Ag thickness. Ag deposition was performed in 5 s increments, between which sheet resistance and ISE measurements were performed; resistivity was obtained by converting the sheet resistance measurements with nominal thickness values.

properties. Therefore, the thickness at which we consider there to be a transition to a conductive percolated network, t_{perc}, is obtained by taking the thickness for which the slope of the MSE of the *t*-only model intersects with the MSE curve of the *t*-ρ model, as indicated by the dotted lines in subplots **(a)** and **(d)** of **Figure 6.3**.

This allows our proposed approach to be used alongside conventional IE-ISE approaches, where the thickness at which the transition to a continuous film morphology occurs, t_{cont}, can be identified by the point at which the film resistivity stops decreasing with increasing thickness, as performed elsewhere in the literature [48], [85], [99], [105], [108]. An example is shown in **Figure 6.3**, in **(b)** and **(e)**. The changes in resistivity obtained from the *t*-ρ model, which are shown in a broader range in **Figure 6.3**, in **(c)** and **(f)**, do not show any obvious features with which one could straightforwardly identify t_{perc}. Albeit that for both deposition and etching, t_{perc} is found within the onset of large-scale resistivity changes, it does not allow one to identify a specific thickness in the same way as comparison to the *t*-only model.

6.4.2 Effect of process parameters on Ag stability during etching

To identify key parameters and potential mechanisms which guide the breakdown of continuous Ag films into percolated ones, and percolated films into discontinuous island, film behavior during

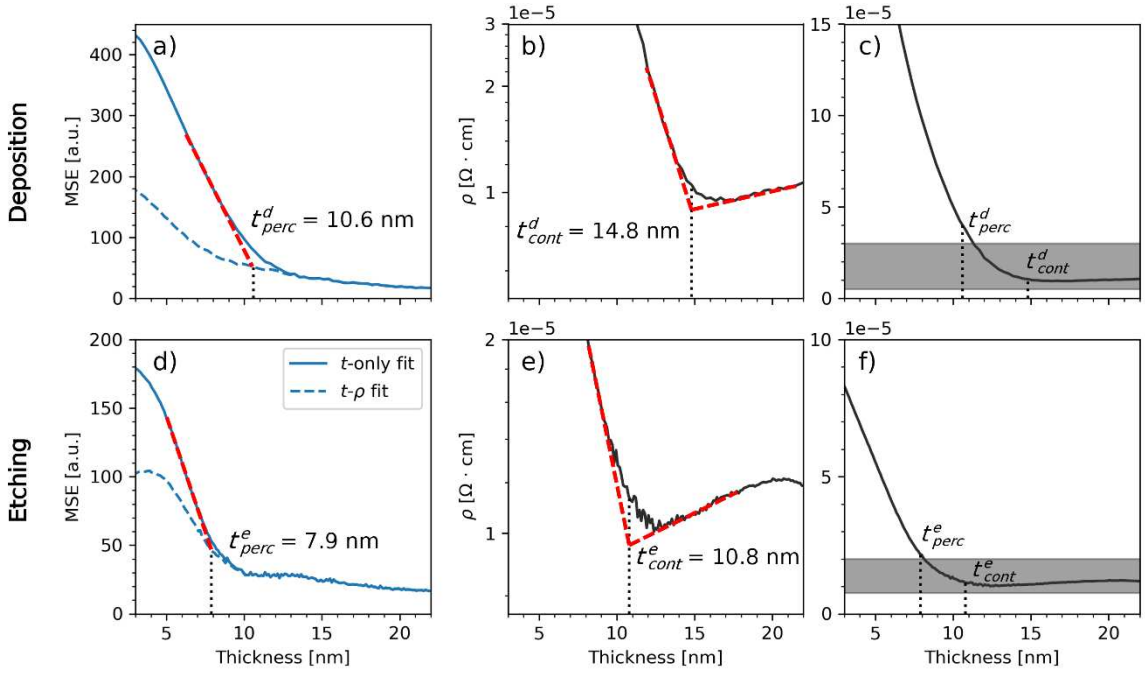


Figure 6.3: Example of critical thickness assessments by IE-ISE monitoring for Ag deposition on a Si|SiO_2 (1 µm) substrate. **a)**, **d)** MSE with and without fitting the optical properties of the Ag layer, and percolated film formation thickness, t_{perc}, obtained. **b)**, **e)** Resistivity values obtained from fitting the Ag optical properties (*t-ρ* model) and the derived continuous film formation thickness, t_{cont}. **c)**, **f)** Linear scale view of the resistivity values shown in the center subplots and comparison with the values obtained for t_{perc} and t_{cont}. Shadowed areas represent the resistivity ranges displayed in the center subplots. Each row presents data for either deposition (t_{perc}^{d}, t_{cont}^{d}) (**(a)**, **(b)**, **(c)**) or etching (t_{perc}^{e}, t_{cont}^{e}) (**(d)**, **(e)**, **(f)**).

etching was studied using the IE-ISE methods described in the previous subsection and shown in **Figure 6.3**. Ag deposition conditions (different concentrations of N_2 in the sputtering gas mixture, and application of a -50 V RF bias to the substrate holder), substrate materials (SiO_2 and $ZnO_{(Al)}$) and properties (substrate roughness and temperature) were varied in order to produce Ag films with different preferred grain orientation [18], [23], grain size [99], [108], stress [113], [153], etc., on IE-ISE compatible substrates. The used parameters are detailed in the experimental methodology section.

To reveal if the resulting film properties play an important role in the breakdown mechanisms of Ag films, both comparative modelling and conventional IE-ISE were employed, allowing the percolated film formation thickness and continuous film formation thickness during deposition

(t_{perc}^{d}, t_{cont}^{d}) and etching (t_{perc}^{e}, t_{cont}^{e}) to be obtained, and subsequently compared to the aforementioned film properties. To this end, **Figure 6.4** compiles all four of the critical thicknesses, sorted by the substrate conditions (*x*-axis position, marker color) and deposition conditions (marker shapes).

Critical thicknesses obtained during deposition, shown in the left half of **Figure 6.4**, follow expected trends. For example, alleviating the surface energy mismatch by using a $ZnO_{(Al)}$ substrate decreases both t_{perc}^{d} and t_{cont}^{d}, when compared to SiO_2 [27], [278]. The high roughness substrates (r_q^{Si} = 2.61 nm, r_q^{Zn} = 2.57 nm, as shown in **Figure D.1** of Appendix D) increase t_{cont}^{d} for both materials, but have relatively little impact on t_{perc}^{d}, consistent with the work of Zhou *et al*. [133]. Conversely, heating the substrate during deposition greatly increases both t_{perc}^{d} and t_{cont}^{d}, particularly for samples which are sputtered in Ar gas, as opposed to an Ar-N_2 mixture [19], [85], [99]. The addition of N_2 to the sputtering gas mixture decreases t_{perc}^{d} and t_{cont}^{d} in almost all cases [18], [23], [85], [108], [153], [278]. Exceptions are shown in **Figure D.2** and discussed in Appendix D. Finally, application of a -50 V RF bias during Ag deposition in pure Ar does not cause consistent changes in t_{perc}^{d} or t_{cont}^{d}. While not explicitly expected, Reck *et al*. have shown that the effect of adding substrate biasing to magnetron sputtering deposition can vary with the substrate, and the low proportion of ionized metal particles participating in the film growth during magnetron sputtering has been linked more broadly to introduction of defects and stresses rather than consistent changes in film coalescence [85], [121].

Critical thickness values obtained during etching, shown on the right side of **Figure 6.4**, present interesting differences. Namely, these are nearly always lower than those obtained during deposition: the dashed horizontal lines shown in **Figure 6.4** denote the lowest thicknesses achieved for both t_{perc} and t_{cont}, regardless of whether they are achieved during deposition or etching. These reveal that etching allows a net decrease of t_{perc} for both $ZnO_{(Al)}$ and SiO_2. Indeed, etching results in lower t_{perc} than the majority of conventionally deposited Ag films, regardless of the substrate. For t_{cont}, significant improvements are obtained when etching Ag deposited on SiO_2 substrates, or on rough $ZnO_{(Al)}$, although conventionally deposited films with a smooth $ZnO_{(Al)}$ seed layer still achieve lower t_{cont} than any etched film. It should be noted that some values of t_{cont}^{e} for Ag deposited in Ar on smooth SiO_2 (blue circle markers), and biased Ag deposited on rough $ZnO_{(Al)}$ (green diamond marker) stand out from this overall trend. Given the variance observed in t_{cont}^{d} for

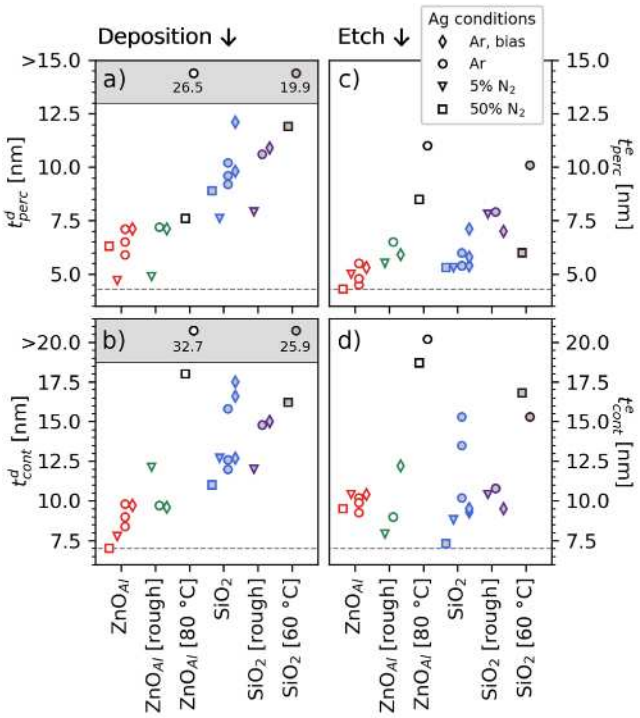


Figure 6.4: Critical thicknesses observed during deposition (**(a)**, **(b)**) and etching (**(c)**, **(d)**) for percolated film formation (**(a)**, **(c)**) and continuous film formation (**(b)**, **(d)**) as a function of the substrate conditions during deposition. Dashed lines correspond to the minimum value achieved for each critical thickness. Points outside of the normal scale are shown in the grayed areas and annotated with their corresponding values. Substrate conditions and Ag deposition parameters are detailed in **Table 6.1** and **Table 6.2**.

films deposited on smooth SiO_2, it may be that non-uniformity between depositions results in film features leading to earlier film breakdown during etching; thus, these are considered to be outliers.

More to the point, **Figure 6.4** also allows to better evaluate the effect of each deposition parameter on the critical thicknesses achieved during etching. As for deposition, decreasing film-substrate surface energy mismatch allows films to remain percolated at lower thicknesses, as evidenced by the lower values of t_{perc}^{e} observed for samples deposited on $ZnO_{(Al)}$ rather than on SiO_2. This is consistent with the reports of Netterfield and Martin, who suggested that improved Au wetting allowed films to be etched to lower thicknesses [127]. It should be noted, however, that the disparity between their percolation thresholds during etching, t_{perc}^{e}, ($ZnO_{(Al)} \approx 5$ nm, $SiO_2 \approx 6$ nm) are much lower than during deposition, t_{perc}^{d}, ($ZnO_{(Al)} \approx 7$ nm, $SiO_2 \approx 10$ nm).

The same is not observed for the breakdown of continuous films, highlighting the importance of monitoring both morphologies. Indeed, for films deposited without substrate heating, all t_{cont}^{e} values converge to a similar range, with Ag deposited on smooth $ZnO_{(Al)}$ seed layers showing no improvement over other substrates, despite showing much lower t_{cont}^{d} values. In fact, all samples deposited on smooth $ZnO_{(Al)}$ show higher t_{cont}^{e} than t_{cont}^{d}. **Figure D.1** of Appendix D shows that only the smooth $ZnO_{(Al)}$ substrates present clear (001)-oriented crystallinity. Differences between smooth SiO_2 and smooth $ZnO_{(Al)}$ substrates, as well as between smooth and rough $ZnO_{(Al)}$, are thus convoluted with differences due to the substrate's crystallinity and its impact on Ag microstructure. Comparing the t_{cont}^{e} values found for rough $ZnO_{(Al)}$ seed layers and rough SiO_2 layers, no important differences are found. Thus, for the breakdown of continuous films, surface energy mismatch appears to have minimal effect whereas substrate crystallinity may play a role.

It can also be seen from **Figure 6.4** that higher substrate roughness decreases film cohesion during etching, for both percolated and continuous films. Indeed, smooth SiO_2 films yield lower t_{cont}^{e} and t_{perc}^{e} than rough SiO_2 films, and rough $ZnO_{(Al)}$ substrates also result in higher t_{perc}^{e} than smooth $ZnO_{(Al)}$. While this is not observed for smooth $ZnO_{(Al)}$ films, this is attributed to the negative effect observed previously, attributed to the substrate crystallinity.

As depositing Ag on heated substrates is known to result in rougher, larger-grained Ag layers [99], [110], [112], [323], it is consistent with the previous observations for rough substrates that these samples result in lower stability during etching, with higher t_{perc}^{e} and t_{cont}^{e}. Given that substrates are cooled passively between deposition and etching, the impact of heating may be further exacerbated due to the continuation of grain growth and thermal grooving during cooling [258].

While it has been suggested that preferential etching at the grain boundaries (GBs) may be a key factor resulting in earlier breakdown during etching [82], this would be enhanced when increasing the total thickness of etched material (i.e., for longer etch durations with the same etching rate), yet no trend is found between the total thickness etched and earlier film breakdown, as shown in **Figure D.3** of Appendix D. From this, it can be assumed that the earlier breakdown of rough and large-grained films occurs through a different mechanism. Roughness, resulting in areas where the film is locally thinner, may facilitate the formation of holes earlier during etching, e.g. at grooved GBs [86], [87]. Hole formation and breakdown during etching could also be worsened by the growth of abnormal grains, similar to the observations of Jacquet *et al*., where grain growth at the

expense of the surrounding film is shown to play an important role in film dewetting [34]. This would be consistent with the SEM images in **Figure 6.1e**, showing initial hole formation adjacent to abnormal grains.

On the other hand, the addition of N_2 to the sputtering gas mixture is expected to decrease the grain size and roughness of Ag films, and accordingly seems to allow the fabrication of thinner etched films [23], [108], [153], [278]. With the exception of samples deposited on smooth $ZnO_{(Al)}$, addition of N_2 to the sputtering gas mixture systematically decreases the value of t_{cont}^{e}, as shown in **Figure 6.4** (triangle and square markers). This is consistent with previous work, in which Ag layers deposited on crystalline $ZnO_{(Al)}$ were shown to have much less variability in roughness and crystallite size as a result of changing N_2 concentration in the sputtering gas mixture than layers deposited on amorphous substrates [278]. Therefore, the decreased grain size induced by N_2 addition, supressed on the smooth $ZnO_{(Al)}$ substrates, may play a role in improving etchability. A similar effect is observed for percolated films; films deposited with N_2 addition consistently yield lower t_{perc}^{e} values than films deposited in Ar, albeit the discrepancy is smaller than for continuous films.

Finally, substrate biasing, which is expected to introduce compressive stress to the Ag film [26], [113], [123], results in systematically lower t_{cont}^{e} values for Ag films deposited on SiO_2 substrates, as shown in **Figure 6.4**, Additionally, biased films show much more repeatable t_{cont}^{e} values than unbiased ones; despite similar variability in t_{cont}^{d} values for smooth SiO_2 substrates, these all show very similar values in t_{cont}^{e}. Biased films deposited on SiO_2 also show marginally lower t_{perc}^{e} values, despite an increase in t_{perc}^{d}, suggesting an improvement for percolated films as well. As biasing Ag during DC magnetron sputtering can result in different effects as a function of the substrate material [121], we consider these results independently from those obtained on $ZnO_{(Al)}$. Biased Ag films deposited on $ZnO_{(Al)}$ do not show a consistent trend and given that crystallinity differences between the different $ZnO_{(Al)}$ types can interfere with result interpretation, more data would be required to discuss these appropriately.

Indeed, estimating the effect that stress might play on Ag etching without dedicated measurements, and instead relying on published literature, is difficult. On one hand, *in situ* stress monitoring of Ag deposited in an Ar-N_2 sputtering gas mixture has shown higher compressive stress values than films deposited in pure Ar [153], and Ag films deposited on heated substrates show more tensile

stress than on room temperature substrates [99], consistent with a correlation between tensile stress and earlier film breakdown. However, as the relaxation of these stresses following deposition scales inversely with the grain size, the true residual stress in films during etching cannot be easily estimated [324]. *In situ* stress monitoring should be included in future work to provide additional avenues to monitor Ag films during etching and investigate this hypothesis.

6.4.3 Proposed mechanisms and suggested changes for improved etching stability

Having observed the dependence of t_{cont}^{e} and t_{perc}^{e} on various deposition parameters, mechanisms explaining these dependencies may now be proposed. **Figure 6.5** shows the relation between the percolation threshold and continuous film formation thresholds for Ag films during deposition and etching, highlighting a characteristic change of behavior during etching. It has been shown that in typical deposition conditions t_{cont}^{d} and t_{perc}^{d} scale linearly with one another, both being defined by the interplay between the nucleation of new Ag clusters and their reorganization into larger, grain-free islands.[19] Thus, the linear trend observed in **Figure 6.5a** is expected. A few deviations to this were observed, which are discussed in Appendix D, following **Figure D.2**.

Figure 6.5b highlights the stark difference in etched films; while there is some loose alignment along the same diagonal (i.e. films with higher t_{cont}^{e} tend to have higher t_{perc}^{e}), distinct behaviors emerge. Certain films encounter an apparent thickness limit in t_{cont}^{e} but differ significantly in t_{perc}^{e}, and vice-versa, as denoted by the dotted lines. This demonstrates that the breakdown of continuous films, i.e. hole formation, and the breakdown of percolated films, i.e. dewetting, are driven by largely independent mechanisms. As this is also the case for high-temperature solid-state dewetting, we will argue here that the same mechanisms can be used to interpret film breakdown behaviors in post-deposition etching, with some additional nuances specific to ion etching.

For solid-state dewetting to occur, hole formation in a continuous film first requires initiation by some sort of defect [35]. Indeed, whereas surface energy minimization drives Ag to form clusters during its initial growth stages, forming a hole in a continuous layer requires the film to pass through an intermediate step where additional Ag interfaces are formed, causing a net increase in free energy. This intermediate state acts as a potential barrier, maintaining the deposited film

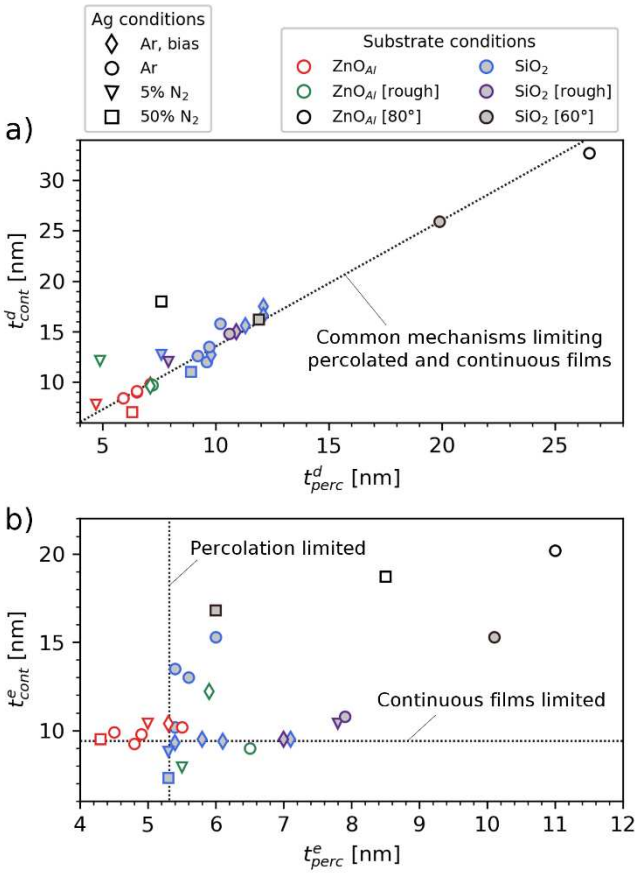


Figure 6.5: a) Continuous film formation thickness (t_{cont}^{d}) as a function of percolation threshold thickness (t_{perc}^{d}) during deposition. **b)** Continuous film breakdown thickness (t_{cont}^{e}) as a function of percolated network breakdown thickness (t_{perc}^{e}) during etching.

morphology. Hole formation is thus commonly attributed to grain boundary grooving, arising from thermodynamic equilibrium between the surface energies of the film's exposed surface and grain boundaries [35], [154]. This results in the formation of a groove of depth Δt_{GB}, as shown in **Figure 6.6a**; if it exceeds the film thickness, a hole is formed. As Δt_{GB} depends only on the film surface energy, grain boundary energy and the radius of the grains, hole formation ought to be independent of the film-substrate surface energy mismatch. This is in agreement with the observations in **Figure 6.4**, in which t_{cont}^{e} values were found to not to vary appreciably with the choice of substrate material. Thus, we attribute the continuous film limit in **Figure 6.5b** to hole formation by GB grooving in the affected coatings.

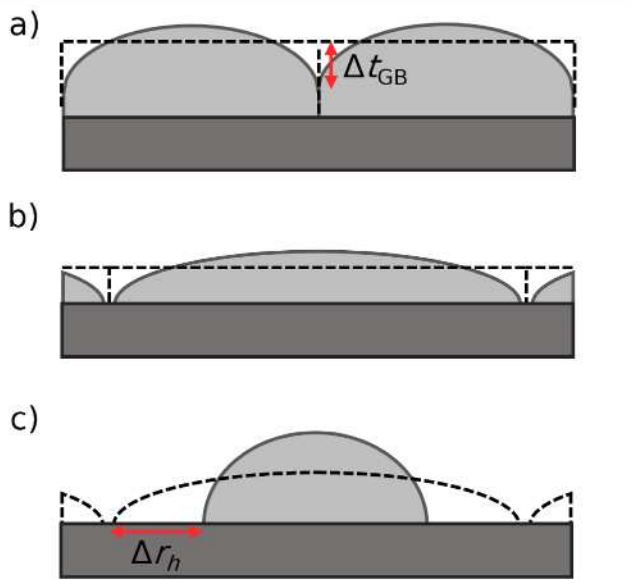


Figure 6.6: Schematic representation of hole formation and subsequent dewetting. **a)** Formation of grain boundary (GB) grooves of depth Δt_{GB}. **b)** Hole formation upon GB grooves reaching the substrate interface. **c)** Hole edge retraction by a length Δr_h and decrease of film coverage.

On the other hand, hole expansion, leading to decreased Ag coverage and dewetting, is driven by surface energy minimization in a way very similar to Ag clustering during deposition. Once holes are formed in the film, the hole edge will retract, decreasing the surface area of the film and film-substrate interface, while exposing the substrate [35], [154]. This is schematically shown in **Figure 6.6b-c**. Srolovitz and Safran show that as the $[(\gamma_i - \gamma_s) / \gamma_f]$ ratio increases, with γ_f, γ_s, γ_i being the surface energies of the film, substrate, and their interface, hole formation becomes more energetically advantageous and results in larger hole sizes [154]. Similarly, increasing this ratio promotes higher contact angles in the capillary model of wetting [19], [26]. Thus, for SiO_2 substrates, with low surface energy (low γ_s) and weak adhesion to Ag (high γ_i), films coalesce later during deposition and dewet earlier during etching, as can be seen by the higher values of $t_{perc}{}^d$ and $t_{perc}{}^e$ shown in **Figure 6.4**. The percolated film limit in **Figure 6.5b** is, therefore, believed to result from films which are susceptible to hole expansion during etching.

The above-mentioned processes, GB grooving and hole expansion, also explain a number of other dependencies observed in the previous section. Rough films present points where the film is locally

thinner, and less grooving is required to nucleate a hole. Substrate roughness has also been shown to promote dewetting, with film agglomerating in the "pits" of the substrate [35]. These are consistent with the lower critical thicknesses found for rough substrates.

Both GB grooving and hole expansion are also expected to be promoted for larger grain sizes: these result in deeper grooves and are assumed to increase inter-hole spacing, which also promotes larger hole sizes [35], [154]. Thus, the observation that large-grained films (deposited at high temperatures) break down at higher thicknesses than small-grained films (deposited with N_2) is also consistent with these mechanisms. Finally, both processes are exacerbated for lower Ag thicknesses: the groove depth required for hole formation is decreased, and both the equilibrium size and the retraction rate of the hole edges are increased [35], [154]. This accounts for critical thicknesses obtained during etching converging at low thicknesses, as shown in **Figure 6.4** and **Figure 6.5b**.

The breakdown of continuous films is not fully explained by the conventional model of GB grooving, however. Indeed, the groove depth, Δt_{GB}, should not significantly exceed one-tenth of the radius of the adjoining grains, assuming reasonable values of the grain boundary and Ag surface energies [35], [96], [126], [154]. However, despite displaying numerous holes, **Figure 6.1f** does not present any grains large enough to justify them; by this measure, for a 7 nm film, grain radii of 70 nm would be required to induce hole nucleation, but upon closer investigation no grains are found with a radius above 50 nm, as shown in **Figure D.4** of Appendix D. Thus, other factors appear to promote hole formation.

It should be noted that the films in the SEM images were all deposited on smooth polycrystalline $ZnO_{(Al)}$ substrates, which were shown in **Figure 6.4** to result in higher values of t_{cont}^{e} than other substrates, despite evidence that smooth substrates allowed later breakdown for SiO_2, and that rough $ZnO_{(Al)}$ with no preferred crystal orientation performed marginally better than SiO_2 of equal roughness. Hence, its crystallinity appears to negatively impact the ability to obtain thin films during etching, which may give some insight into what is driving hole formation. One hypothesis is that crystalline $ZnO_{(Al)}$ substrates facilitate the formation of GBs with high free energy, while simultaneously limiting their ability to relax, due to the stability of individual grains in alignment with the substrate. Alternatively, stress at the GBs may also be a contributor; Ag adatoms preferentially diffusing to and being incorporated into well-aligned grains may promote trench

closure via grain boundary zipping [30], [109], resulting in stress at the boundaries, which may spontaneously 'unzip' or facilitate grooving. Indeed, relaxation of tensile stress or addition of compressive stress is expected to stabilize grain boundaries, limiting thermal grooving and decreasing their embodied energy [30], [166]. *In situ* investigation of the stress changes associated to hole closure and reopening, during deposition and etching, may offer further insight on this point.

Additionally, hole formation may be facilitated by film vacancies agglomerating to nucleate voids, as proposed by Kwon *et al*. [184], or greater thermal grooving mediated by diffusion at the Ag/substrate interface, as demonstrated by Kumar *et al*. [169]. The latter is consistent with the modest improvements for rough $ZnO_{(Al)}$ substrates compared to rough SiO_2, as the higher adhesion would limit Ag diffusion at this interface [278].

The etching parameters may also play a significant role in hole formation. Indeed, Ag shows low and rapidly decreasing sputtering yield for ion energies at and below ≈100 eV [325], [326]; however, the reported activation energies for Ag diffusion processes (bulk Ag diffusion, interfacial Ag diffusion, grain boundary diffusion, vacancy formation and migration) are at most only a few eV [254], [327]. Thus, there is a wide range of intermediate ion energies which give low sputtering yield but carry more than enough energy to stimulate Ag diffusion processes. These ions may generate defects which facilitate hole nucleation or dewetting processes. In addition to this, reducing the amount of Ag diffusion stimulated by the etching process would limit GB grooving and hole expansion, given that these occur via surface diffusion.

However, film etching via an RF plasma, as in this work, is not well suited to precisely control the incident ion energy. These discharges generate a broad saddle-shaped ion energy distribution, and while increasing discharge power can increase the lower bound of the distribution, this also broadens the ion energy distribution, increases the discharge current, and increases the density of ions with energies below that of the main distribution [328]. Furthermore, high energy incident ions are more likely to introduce defects or cause thermal spikes allowing structural relaxation [26], [110]. Thus, simply increasing the discharge power is unlikely to improve things – as such, control of the incident ion energies is required to ensure these efficiently contribute to thin film etching without stimulating other processes. Etching via an ion beam or cluster ion beam with well-defined incident energy instead of a RF bias plasma could improve upon this. Indeed, etching via ion beam

has been demonstrated to be able to decrease the roughness of Ag films, which could help maintain smooth and uniform films throughout etching [82].

Finally, the electrical properties of the substrate appear to influence the critical thicknesses at which films break down during etching; for example, it can be seen that while etching Ag films deposited in Ar on a $ZnO_{(Al)}$ seed layer, with an otherwise bare Si substrate (as in **Figure 6.1**), a t_{perc}^{e} of approximately 4 nm can be achieved, lower than what is found for any of the samples deposited and etched on IE-ISE compatible substrates with thick oxide layers. Further results presented in **Figure D.5** of Appendix D support this, suggesting that the substrate properties affect the electrical field at the substrate surface or lead to substrate charging effects, in turn affecting the etching process. Consequently, the ability to more precisely control the etching parameters and substrate neutralization with ion-beam etching may present an advantage.

Thus, from a structural perspective, maintaining film morphologies during etching may be improved by ensuring a uniform Ag microstructure, decreasing film roughness, and creating dense films with weakly tensile or compressive residual stress. From a kinetic perspective, reducing the mobility of Ag atoms should be pursued. While this could be performed by minimizing the imparted energy, as discussed above, another method may be to reduce Ag diffusivity via doping [32], [48], [329]. Thus, we believe the most relevant changes to implement would be to change the energy of the incident Ag atoms (e.g. using biased HiPIMS) [85], [121], the addition of metallic dopants (due to their effect on Ag mobility) [32], [48], [329], and the modification of the etching conditions [82], [83].

Consequently, while the ion beam sputtering employed by Ma *et al*. is consistent with the mechanisms we propose [82], it represents only one of the many approaches admissible to improve the minimum thicknesses achieved during etching; the framework presented here suggests that there is a much wider selection of applicable methods with which to enable ultra thin Ag films via etching, allowing post-deposition etching to be implemented far more broadly than initially considered.

6.5 Conclusions

In this work, the morphologies of ultra-thin Ag films produced by post-deposition ion etching are investigated. To this end, *in situ* ellipsometry is employed, using both conventional monitoring of continuous film formation with IE-ISE, as well as with a complementary comparative modelling method, which allows one to monitor the formation and breakdown of percolated networks regardless of interference enhancement. These techniques are then used to monitor the critical thicknesses at which continuous and percolated morphologies break down during etching and identify which substrate properties and Ag deposition conditions affect them.

An etching thickness limit is found for both continuous and percolated films. These show less sensitivity to deposition parameters than critical thicknesses obtained during deposition, trends are identified and discussed. Moreover, breakdown of continuous films into percolated networks and of percolated networks into isolated islands is found to evolve following distinct mechanisms. This behavior is explained in the framework of known solid-state dewetting mechanisms; the distinct breakdown behavior of continuous and percolated films is thus attributed to the different parameters controlling grain boundary grooving and hole expansion criteria. In this context, various recommendations are made to decrease the critical thicknesses achieved during etching. Smooth, uniform and dense Ag films appear to be the most likely ones to allow maintaining continuous morphologies at lower thicknesses, whereas decreased surface energy mismatch should further improve resistance to percolated film breakdown. Doped Ag films may allow this as well, while also limiting Ag mobility; this is suggested to stabilize films during etching. Finally, the importance of the etching process parameters is highlighted, and it is recommended that future work be pursued using ion beam etching in order to more precisely control the etching conditions.

6.6 Acknowledgements

The authors wish to thank Dr. Patricia Moraille for the AFM measurements, Dr. Etienne Bousser for the SEM imaging, as well as Mr. Francis Turcot and Mr. Francis Boutet for their assistance with maintenance of the deposition system. The project was financially supported by the Natural Sciences and Engineering Research Council (NSERC) of Canada through the NSERC-Alliance grant (no. ALLRP 576758 - 22), by Prima Quebec (grant no. R24-13-003), and Guardian Glass.

6.7 Antireflective coatings produced with post-deposition etching

In addition to the work presented in the article above, the performance limitations of optical coatings making use of etched Ag films were investigated. This subsection presents the main findings of said investigation.

The previous results show that film thinning via etching must be implemented in appropriate conditions to yield performance improvements. Namely, with the conditions used in this work, etching Ag on smooth $ZnO_{(Al)}$ substrates results in no improvement in regard to t_{cont}, and the same could ostensibly be true for other substrates enabling early Ag wetting. This leaves two main avenues for implementation: it can be used for the improvement of devices implementing continuous Ag films on substrates with poor affinity to Ag, or it can be employed to improve percolated Ag networks below the continuous film threshold on high affinity substrates. The latter will be investigated in this section, using the same methodology as in the preceding article.

B270 glass substrates, overcoated with thin dielectric layers used for fabrication of conductive AR coatings in this work do not enable IE-ISE. Therefore, certain considerations were taken to select the total deposition thickness (prior to etching) and final thickness targets to obtain continuous films without t_{cont} monitoring. Indeed, given that the morphology of etched films greatly depends on their as-coated morphology, it is important to ensure formation of continuous films prior to etching [128]. Using the linear correlation found between previously measured values of $t_{perc}{}^{d}$ and $t_{cont}{}^{d}$, shown in **Figure 6.5** and **Figure D.2** of Appendix D, the continuous film formation threshold was estimated, and Ag films with thicknesses above it were deposited. While this requires appropriate calibration on IE-compatible substrates, this allows the estimation of $t_{cont}{}^{d}$ even on common transparent substrates, using the comparative modelling approach to acquire $t_{perc}{}^{d}$. Although the results shown in **Figure D.3** of Appendix D indicate that there is little to no impact associated with longer etching durations, suggesting that continuous film formation could be ensured by depositing arbitrarily thick films, it is nonetheless preferable to be able to estimate $t_{cont}{}^{d}$ with the comparative modelling approach in order to minimize processing time and Ag waste. Moreover, as ISE measurements on glass substrates performed prior to device production showed etching behavior similar to smooth ISE substrates, the results presented in **Figure 6.4** are taken to be representative of the critical thicknesses that can be achieved on B270 glass. Nonetheless, as different etching behaviors are found for $t_{perc}{}^{e}$ as a function of the substrate choice, changes to $t_{cont}{}^{d}$

and t_{cont}^{e}, which cannot be observed without IE-ISE, may occur due to the chosen substrate, and this should be noted as a potential source of error until verified with additional techniques.

As a result, performance improvements achievable for percolated films on high affinity substrates using post-deposition etching were tested by fabricating antireflective coatings in a B270/$SiN_{(Al)}$ (36 nm)/$ZnO_{(Al)}$ (10 nm)/Ag (5.5 nm)/$SiN_{(Al)}$ (10 nm)/SiO_2 (73 nm) architecture, designed following similar modelling approaches as described in Chapter 5. For these filters, Ag layers produced either by standard deposition to 5.5 nm, or deposition to 15 nm, and subsequent etching to 5.5 nm, were used. In both cases, deposition was performed both in pure Ar and in a sputtering gas mixture composed of 5% N_2. Absorption, reflection and transmission spectra of each of these samples, as well as their sheet resistance, are shown in the left side of **Figure 6.7**.

In order to associate the resulting spectra with different hole morphologies, finite-difference time-domain (FDTD) modelling of devices was performed. More specifically, images **(b)**, **(c)**, **(f)**, and **(g)** of **Figure 6.1** were converted to binary patterns to create realistic input geometries for the Ag layer, as shown in **Figure D.6** of Appendix D, and compared to a fully continuous film geometry. The geometry of the Ag layer is modelled with flat interfaces and vertical sidewalls. This has been shown to produce realistic optical properties, although focusing on a small set of microstructural features leads to the appearance of peaks in the optical spectra unless the optical response from multiple sites of a sample are averaged [330]. Periodic boundary conditions are placed on the images used in this work, and, therefore, this must be taken into consideration when interpreting modelling results.

The binarized Ag layers were modelled in the same antireflective architecture as experimental samples, i.e.: B270/$SiN_{(Al)}$ (36 nm)/$ZnO_{(Al)}$ (10 nm)/Ag (t)/$SiN_{(Al)}$ (10 nm)/SiO_2 (73 nm). For a given layer with Ag coverage ratio f, the Ag thickness t is fixed such that $f \cdot t = 5$ nm, meaning that all structures are modelled with equal mass-equivalent thickness of 5 nm. Holes in the Ag layer were modelled as being filled with $SiN_{(Al)}$. Other information regarding the applied modelling parameters are given in Appendix D. It should be noted that although the Ag layer was modelled as a single uniform layer, experimentally-derived optical properties were used rather than bulk properties, which should account for most of the discrepancies reported by Kossoy *et al*. [331]. The modelled spectra for these structures are shown in the right side of **Figure 6.7**.

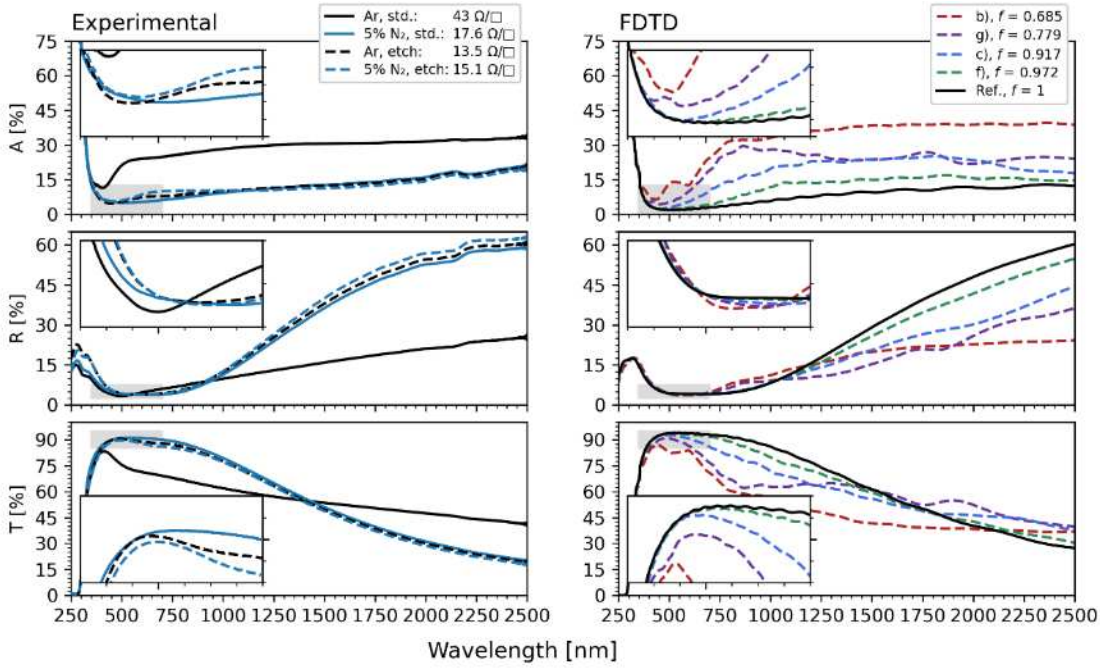


Figure 6.7: Absorption, reflection and transmission of optical devices deposited in a B270/$SiN_{(Al)}$ (36 nm)/$ZnO_{(Al)}$ (10 nm)/Ag (5.5 nm)/$SiN_{(Al)}$ (10 nm)/SiO_2 (73 nm) architecture, using Ag films deposited in pure Ar or in a 5% N_2 sputtering gas mixture, using standard deposition or post-deposition etching (left), compared to curves obtained from FDTD modelling using the same architecture, realistic Ag input geometries derived from SEM images (see **Figure D.6** in Appendix D) and a Ag thickness t such that $f \cdot t$ = 5 nm (right). All inserts have a horizontal scale of 350 to 750 nm. From top to bottom, inserts have vertical scales of 0 to 12.5%, 2.5 to 7.5%, and 85 to 95%.

The sample fabricated with standard deposition in Ar shows very strong broadband absorption, whereas no obvious absorption features are observed for standard deposition in N_2. Relatively broad absorption peaks are found in etched samples: for the etched sample deposited in Ar, it is centered around 600 nm, whereas the etched sample deposited with 5% N_2 shows a wider, red-shifted peak. No unexpected absorption peaks are observed for standard deposition with 5% N_2. Transmission losses closely follow the absorption increases, with highly comparable antireflective performance for all samples except for Ag with standard deposition in Ar. Etched films are found to have substantially lower sheet resistance regardless of the sputtering gas mixture used during deposition, showing a decrease of almost 25% between the most conductive standard and etched Ag films.

Experimental results match the behavior found in FDTD modelling to a limited extent. The low conductivity and broad absorption found for standard deposition in Ar is consistent with the type of structures found for the modelled sample **(b)** (see **Figure 6.7**): its highly asymmetrical worm-like holes, have wildly varying effective sizes depending on the electric field orientation relative to a given hole shape, leading to very broad absorption features [332]. The random orientation of the holes is expected to make this effect insensitive to the specific electric field orientation relative to the sample. These observations are consistent with the simulations of Mao *et al*., which show broader optical spectra for hole arrays with irregular hole shapes and sizes [333]. Beyond that, comparison to other samples is more difficult; simulations show overall higher absorption when the Ag coverage ratio decreases, although particularly in the IR, which consequently decreases visible transmission and IR reflection. Both etched samples show very high IR reflection, higher than the film produced with standard deposition in 5% N_2, suggesting high coverage, yet none of the simulated structures show visible absorption features similar to those of the etched samples. To leverage the high conductivity of etched films without introducing unwanted absorption at key wavelengths, a better understanding of the relationship between the hole morphologies and their resulting optical behavior is required.

In order to investigate the relationship between different hole morphologies and the plasmonic absorption induced by these, first the hole size distribution is quantified. Holes were fitted to ellipses using the software *ImageJ*, so that the major and minor axes can account for different effective sizes in a given hole [332]. Additional details are discussed in the context of **Figure D.6** of Appendix D. Second, the plasmonic portion of the holes' effect on the optical performance is isolated. To do so, the difference between the transmission spectra obtained for the $f = 1$ reference structure and the individual hole structures, ΔT, are calculated to obtain the change in transmission induced by a given hole morphology. This is repeated with the *CompleteEASE* (CE) software, which does not take any plasmonic effects into account. Finally, subtracting ΔT^{CE} from ΔT^{FDTD} isolates the transmission changes attributable to plasmonic effects. Additional details and a demonstration of this processing is shown in **Figure D.7** of Appendix D.

Figure 6.8 compares ΔT^{FDTD} - ΔT^{CE} with the hole size distribution obtained for each of the four hole morphologies considered in **Figure 6.7**; each morphology is simulated twice, with an Ag thickness t such that $f \cdot t$ = 5 nm and $f \cdot t$ = 10 nm. Thicker Ag films, for a given hole morphology, result in a blue-shift of the transmission losses. Hole patterns with lower coverage (thus higher

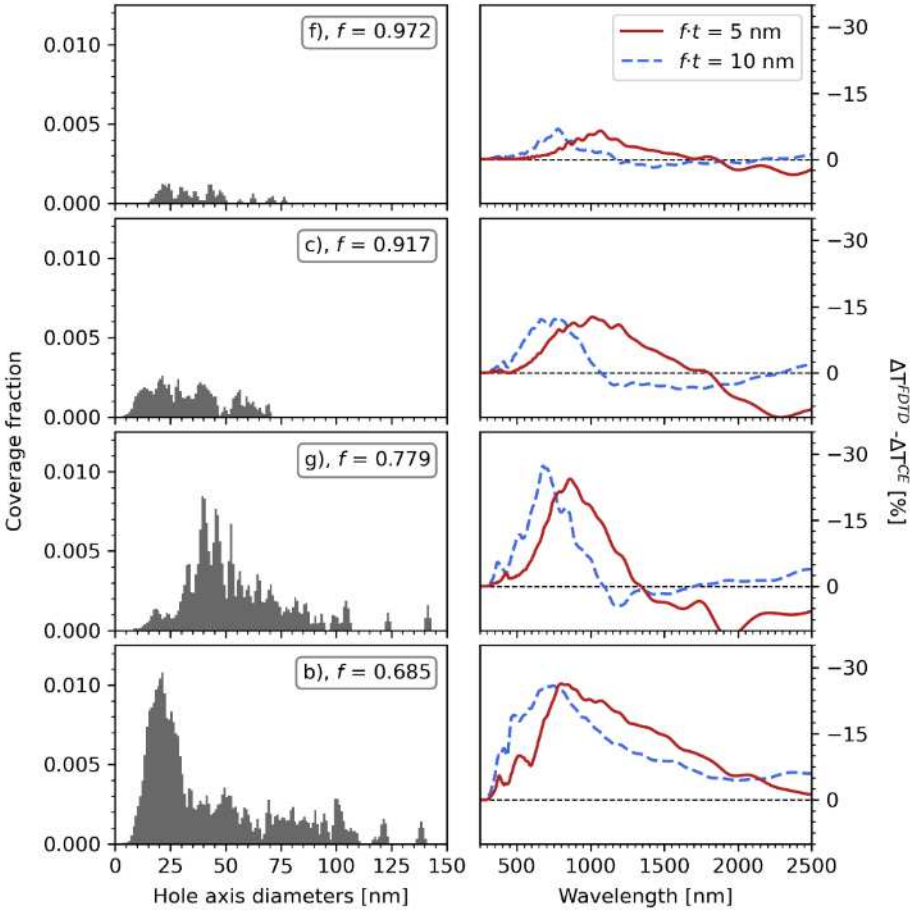


Figure 6.8: Hole size distributions (left) and change in transmission attributable to their plasmonic resonances, $\Delta T^{\mathrm{FDTD}} - \Delta T^{\mathrm{CE}}$ (right), for hole morphologies derived from SEM imaging and inserted into a simulated B270/$SiN_{(Al)}$ (36 nm)/$ZnO_{(Al)}$ (10 nm)/Ag (t nm)/$SiN_{(Al)}$ (10 nm)/SiO_2 (73 nm) architecture, with $f{\cdot}t$ = 5 nm. $\Delta T = T - T^{f=1}$, and CE and FDTD respectively refer to simulations in *CompleteEASE* (which do not account for plasmonic behavior) and in FDTD. Hole sizes were obtained by fitting ellipses to the holes in binarized SEM images used for FDTD simulations and characterized by major and minor axis diameters of these ellipses.

thickness for a constant value of $f{\cdot}t$) show smaller blue-shift for the same relative thickness change, which is consistent with the results of Kang *et al.*, showing blue-shift which saturates with increasing thickness in regularly spaced hole arrays [334].

Despite the irregularity of the hole shapes, spacings and orientations, a relatively clear correlation can be observed between the hole size distribution and the plasmonic transmission loss; the squat profiles of samples **(f)** and **(c)** result in similar transmission profiles. **(c)** displays a smaller average

hole size and higher hole coverage, yielding more blue-shifted, stronger transmission loss. Similarly, **(g)** shows narrow peaks in its hole size distribution, translating to transmission loss peaks or shoulders. Finally, **(b)** has higher coverage at the lower and higher ends of the size distribution and correspondingly shows higher transmission loss at both lower and higher wavelengths. This roughly linear relation between hole axis size and resonant wavelength, analogous to observations for metal nanorods, is consistent with existing literature; in circular hole arrays, localized surface plasmon resonances are expected to blue-shift when the hole size is decreased, with behavior highly comparable to nanoparticle arrays [28], [335].

While this relation is consistent for each of the simulated morphologies, and even within pairs with roughly similar *f*, **(f)** and **(c)** show substantially less transmission losses in the UV-vis spectra than **(g)**, despite higher coverage of small holes; this is attributed to higher average hole distances for higher Ag coverage, consistent with the literature. Periodic hole arrays with fixed hole sizes and decreasing hole spacing show blue-shifted transmission losses, while those with short periodicity and large variation in hole sizes, resulting in large changes the hole spacing, show that either parameter can become dominant, depending on the ratio of hole size to hole spacing [333], [336]. These results are consistent with simulations performed with fixed-diameter circular holes shown in **Figure D.8** of Appendix D.

The overall optical behavior of the irregular holes formed by ion etching, while not representative of regular hole arrays, therefore appears to follow the same overall trends, with broader features resulting from a variety of overlapping modes, resulting from wider hole size and hole-to-hole spacing distributions. As a general indication, transmission losses are increased by higher coverage of a given hole size, and are blue-shifted for thicker metal films, smaller hole sizes and shorter distances between holes. The low IR absorption and good overall comparability to AR coatings deposited with Ag deposited in 5% N_2 suggests that the etched AR samples produced in this work have high coverage and thickness close to the nominal values. Therefore, that the etched AR samples show blue-shifted absorption, when compared to simulated structures, suggests that they have smaller average hole sizes, or more closely spaced holes.

Multiple small holes forming around abnormal grains, as seen in **Figure 6.1e**, may be generating these optical features. **Figure D.5** (see Appendix D), suggests that Si substrates, as used for SEM observation of the Ag hole patterns, appear to have different etching behavior than insulating

substrates, such as the glass used for AR device fabrication; beyond that, exposure of the Ag films to atmosphere between deposition and observation in SEM, or differences in the film morphology resulting from the $SiN_{(Al)}$ underlayer modifying the $ZnO_{(Al)}$ surface may contribute to the formation of smaller holes for the AR samples.

These results highlight the importance of controlling the morphology of the holes produced during the etching process to improve the optical performance of etched films. Important transmission improvements are obtained at 500 nm when comparing films deposited in Ar to those prepared and subsequently etched in Ar ($T_{(500\ nm)}^{Ar}$ = 75.4% vs. $T_{(500\ nm)}^{Ar\text{-}etch}$ = 90.3%); these values are comparable with those of Ag films fabricated with standard deposition in an Ar-N_2 mixture ($T_{(500)}^{N}$ = 90.8%). However, the absorption peak observed in etched films quickly decreases their transmission at higher wavelengths. If the improved sheet resistance obtained via post-deposition etching (R_S^{Ar} = 43 Ω·sq^{-1}, R_S^{N} = 17.6 Ω·sq^{-1}, $R_S^{Ar\text{-}etch}$ = 13.5 Ω·sq^{-1}) could be accessed without this caveat, it would constitute a significant improvement.

While the results shown in **Figure 6.4** show that post-deposition etching could result in important thickness reductions for continuous films deposited on substrate materials with low affinity to Ag, such as the SiO_2 surfaces used with IE-ISE, a proper investigation of this paradigm is left for future experiments. In addition to other challenges discussed for percolated films, monitoring whether films remain continuous during etching would require either transparent IE-ISE substrates or a different monitoring approach. Nevertheless, some preliminary experiments were performed with deposition onto bare B270 substrates, with results presented in **Figure D.9** of Appendix D. These show similar issues as samples deposited on $ZnO_{(Al)}$, with localized absorption in the visible, but notable reductions of sheet resistance. This further supports that the substrate used, by charging effects or otherwise, influences the shape and size of the holes formed. It is worth noting that without the $ZnO_{(Al)}$ layer (which has high absorption at low wavelengths) one can observe a small absorption peak at ≈ 375 nm for films deposited with 5% N_2, suggesting the presence of holes with a smaller average size.

Moreover, this further supports that with improved control of the hole sizes produced during etching, visible transmission losses could be avoided. Usage of ion-beam irradiation may also be useful in this regard. The rapid decreases in film coverage observed by Simonot *et al*. during low-

energy ion-beam irradiation suggest that hole sizes could be increased with low sputtering yield, allowing to modify hole sizes without decreasing the film thickness [337].

Finally, it highlights the potential for post-deposition etching as a means to obtain transparent conductive noble metal films for a broader range of deposition conditions and substrates. Such an approach could allow deposition of Ag layers onto specific materials of interest with no interlayers, such as deposition onto low-surface energy flexible polymers, or enable wetting layers to be removed from current stack architectures, particularly when these present environmental or economic downsides [338], [339], [340]. It follows that appropriate Ag recovery techniques must be put in place to reduce waste, as substantially more Ag must be consumed to obtain the same given final thickness in post-deposition etching; however, implementing appropriate tools to reduce material loss during processing and improvements to Ag recovery may make this feasible [341], [342], [343].

CHAPTER 7 GENERAL DISCUSSION: PERSPECTIVES FOR HIGH TEMPERATURE OPTICAL STABILITY IN LOW-EMISSIVITY COATINGS

7.1 Foreword

In this chapter, we discuss general perspectives for improvement of the overall optical stability of low-E coatings, towards the goal of producing single-stock low-E coatings.

The previous chapter investigated the potential performance improvements that are obtainable by post-deposition etching, as well as outlining the limitations of this technique, but did not touch upon the durability of etched films. Thus, this chapter will begin by discussing presenting the application of post-deposition etching to increasing Ag stability at high temperatures. It is found that the addition of a separate annealing step between the deposition and etching steps is required to obtain optimized microstructures. Preliminary results obtained with this method and future improvements which could be added to it are discussed.

Following this, a short section dedicated to optical changes beyond those incurred from the Ag layer is presented. Here, the optical changes resulting from the dielectric stack layers, as well as potential improvements pertaining to these layers, are discussed.

7.2 Multi-step Ag deposition processes for high temperature stability

7.2.1 Preliminary results

We now come to the final objective of this work: using Ag microstructural control to improve the optical stability of tempered low-E coatings. As established in Section 2.3.2, without using dopants, the main path towards mitigating abnormal grain growth is to generate microstructures with large, uniform, preferentially aligned grains. $ZnO_{(Al)}$ seed layers promote uniformity and Ag (111) alignment, but this is still insufficient. Hence, to obtain optically stable low-E coatings, larger grains must be obtained in the as-coated state.

The post-deposition etching method presented in Chapter 6 allows to obtain continuous films at lower thicknesses than could normally be achieved during deposition. This is of interest given that the processes that create large-grained films during deposition (i.e. island growth and coalescence

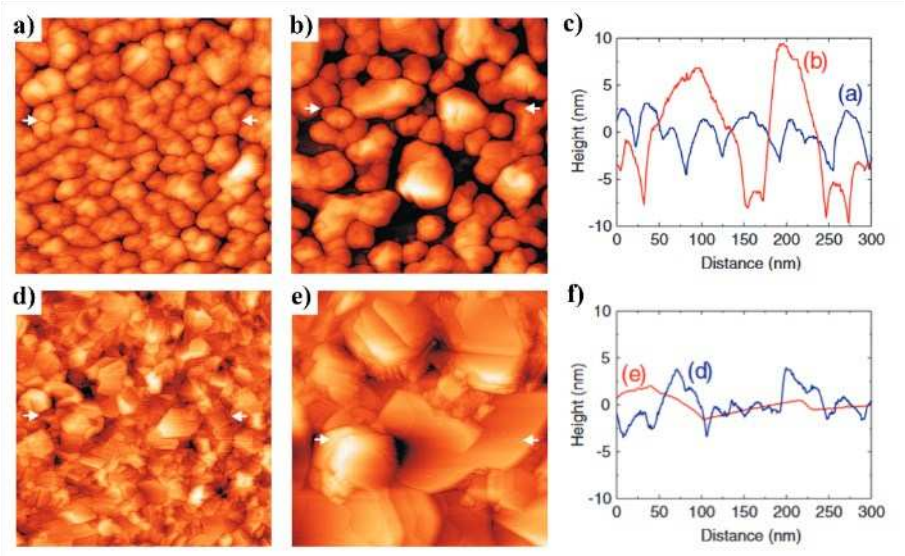


Figure 7.1: STM topography of Ag films deposited on amorphous Si before and after annealing: **a)**, **d)** 8.5 nm and 20 nm thick Ag films grown at ≈ 25 °C. **b)**, **e)** The same films, following annealing at ≈ 125 °C and ≈ 225 °C, respectively. **c)**, **f)** Graphs showing the height profiles between the white arrows shown in the topographs: **(c)** for the 8.5 nm thick film shown in **(a)** and **(b)**; **(f)** for the 20 nm thick film shown in **(d)** and **(e)**. Adapted from [30] with permission. © Deutsche Physikalische Gesellschaft. Reproduced by permission of IOP Publishing. All rights reserved.

of islands into grain-free shapes) also result in higher continuous film formation thicknesses. However, this is still not enough; the rough, large-grained films obtained when deposited at high temperatures still breakdown well above thicknesses of interest. Perhaps this could be improved with some of the methods proposed in Section 6.4.3 (e.g. ion beam etching, which may decrease surface roughness during etching), but it is better still to avoid this problem entirely. As a means to do so, post-deposition annealing of the Ag film can be used.

Indeed, as demonstrated by Polop *et al*., shown below in **Figure 7.1**, the morphological evolution of Ag films during heating depends greatly on the film morphology prior to heating [30]. This should come as no surprise: the importance of obtaining Ag films with continuous morphologies in the as-coated state to mitigate dewetting during HT has been discussed previously. To further decouple the range of achievable microstructures from the film thicknesses obtained during deposition or etching, a deposit-anneal-etch (DAE) multi-step process can be used. First, films are deposited to a stable thickness, annealed to obtain desired microstructures, and etched to obtain a desirable final thickness.

This is not a trivial endeavor, however. Namely, the annealing kinetics of the Ag layer must be well controlled, as grain growth has been shown to stagnate at different size thresholds limited by the annealing temperature [86], [163]. High maximum temperatures are therefore required to obtain large grains. In addition to this, the rate and duration of the annealing process must be considered: if grain growth is stagnant due to slow heating or cooling, thermal grooving can nevertheless take place. If this occurs during the heating, groove formation may mitigate grain growth [155], [162], [163], [164]. On the other hand, during the cooling process, large grains are likely to be present, which will exacerbate the depth of the GB grooves, potentially leading to hole formation and dewetting [35], [87].

In order to achieve higher annealing temperatures with faster heating and cooling rates, and thus test this approach, *ex situ* annealing was employed. Furthermore, Ag was substituted with Au, allowing one to anneal coatings in ambient air. Deposition conditions used in the production of these samples are given in **Table 7.1** below. Au thicknesses were monitored with the comparative modelling method, and using the same etching parameters as used in Chapter 6.

Figure 7.2 compares the performance and stability of Au-based low-E coatings produced with or without preliminary annealing of the metal layer. Two different variations of the Au layer were inserted into otherwise identical low-E architectures with the following design: SLG (3 mm)/Si_3N_4 (22 nm)/$ZnO_{(Al)}$ (14.9 nm)/Au (10 nm)/$NiCrO_x$ (2.5 nm)/$ZnO_{(Al)}$ (12.4 nm)/Si_3N_4 (22 nm). One sample incorporated a "standard" Au layer, deposited at a thickness of 10 nm; the other used a DAE Au film: deposited at a thickness of 25 nm, annealed at 550 °C for 5 minutes, and then etched

Table 7.1: Summary of the sputtering conditions used for the deposition of the various films used in Chapter 7.

Layer	Target	Power density [W/cm^2]	Mode	Pressure [mTorr]	Gas flow ratio [sccm]	Power and substrate RF bias
Au	Au	2.96	RF	2	Ar/N_2 (variable)	-
$NiCrO_x$	Ni/Cr (80/20 wt. %)	3.29	DC	4	Ar/O_2 (100/8)	-
Si_3N_4	Si	9.87	RF	2	Ar/N_2 (100/37)	3 W, -35 V
$ZnO_{(Al)}$	Zn/Al (98/2 wt. %)	6.56	RF	2	Ar/O_2 (100/35)	-

back down to 10 nm. The designs are resumed in **Figure 7.2a**. As shown in **Figure 7.2b**, this results in higher visible transmission and lower sheet resistance in the as-coated state. While these samples both showed significant degradation following a 7-minute HT in ambient air, the changes are slightly less pronounced for the DAE sample, as shown in **Figure 7.2c**. HT sheet resistance measurements are not shown, as one of the samples cracked following removal from the furnace, rendering it unmeasurable. Finally, *in situ* transmission measurements obtained during HT, shown in **Figure 7.2d** reveal that, for the DAE sample, much smaller transmission changes take place prior to the start of degradation. On the other hand, the standard sample displays optical changes bringing it closer to the AC transmission of the DAE sample. Thus, without introducing new vulnerabilities, this method could mitigate optical changes resulting from HT by leveraging already saturated grain sizes.

These results could not be successfully transferred to Ag films however, despite annealing them in inert atmospheres. The short exposure to ambient air occurring during transfer from the deposition system to the furnace was sufficient to degrade the Ag films: samples prepared in this way displayed dewetting, either directly during the annealing step or during the subsequent etching step. This was attributed to adsorption of oxygen and humidity at the Ag surface [38]. The addition of thin protective layers encapsulating films allows one to stabilize them during annealing, however, at least with the etching parameters available in the deposition system used, these could not be removed without damaging the Ag layer, as detailed in Appendix E.

Moreover, while the deposition system used in this work enables substrate heating, it does so via heating the substrate holder platen as shown in **Figure 3.1**, requiring that the entire thickness of the substrate be heated in order to heat the coated surface. Not only does this result in lower effective temperatures at the coated surface, it also results in a slow heating rate and even slower cooling, as the substrate and platen retain heat in the absence of active cooling. Thus, DAE samples produced using standard substrate heating procedures were found to yield performance no better than films deposited on heated substrates.

An approach for controlled Ag annealing has been patented by Saint Gobain Glass in recent years; specifically, they make use of absorbing layers (e.g., sub-stoichiometric oxides) deposited within the stack to efficiently transfer heat from high-power lasers to the coating, allowing rapid, targeted heating [344]. With this approach, improved as-coated performance and high colorimetric stability

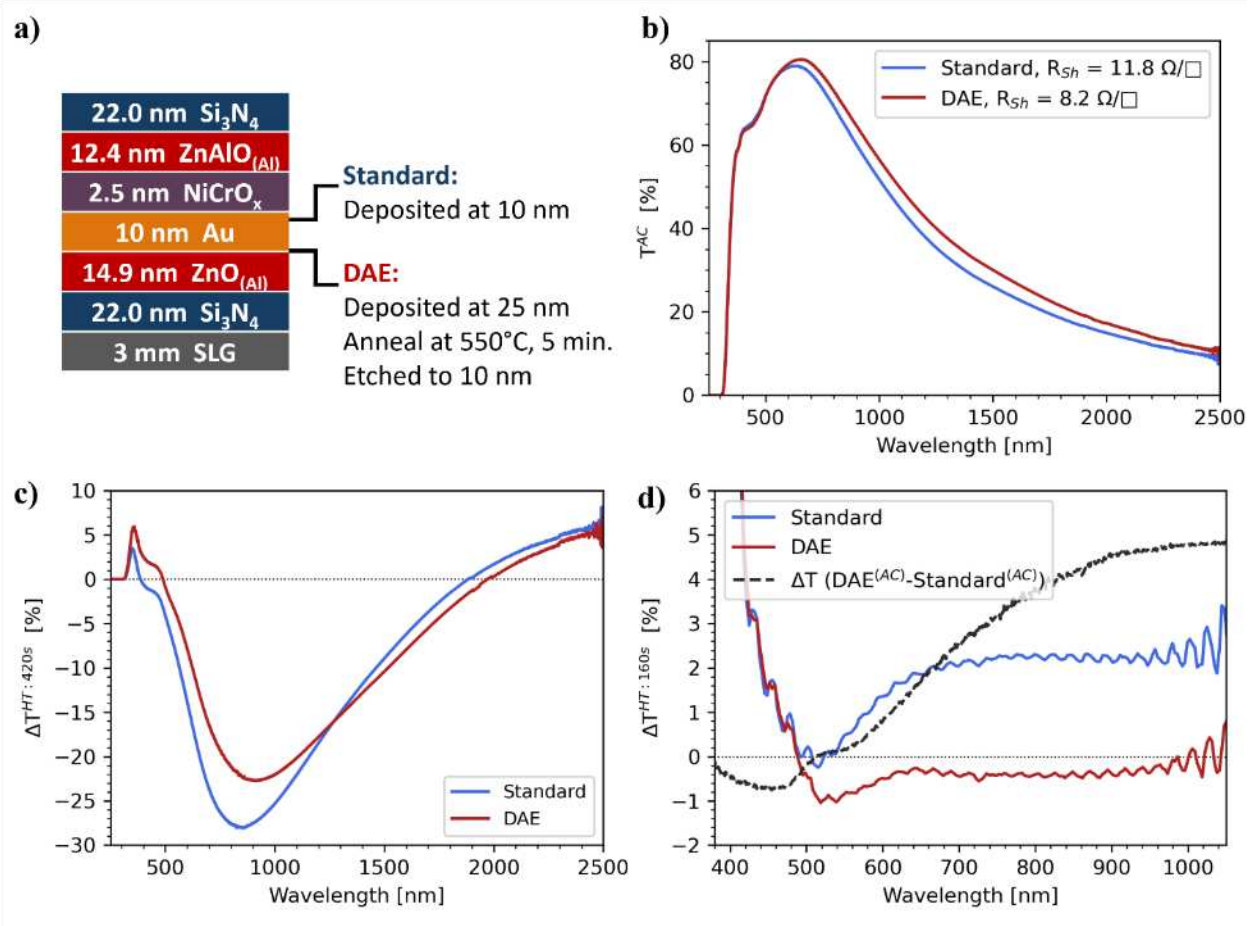


Figure 7.2: a) Schematic of a stack design used for the comparison of standard and DAE Au coatings. **b)** *Ex situ* transmission and sheet resistance measurements of the samples shown in **(a)**. **c)** ΔT of each sample, measured *ex situ* following a 7-minute HT in ambient air. **d)** ΔT of each sample, measured *in situ*, 160 s after the start of HT, compared to the difference in as-coated transmission between each sample. *In situ* data is corrected to account for high temperature optical changes of the SLG substrate, as described in **Figure E.1** of Appendix E.

during HT has been claimed for Ag-based low-E coatings, similar to the work reported here; however, in this case annealing may proceed once the whole coating is deposited, instead of immediately after the metal layer is deposited. Thus, it is worth considering the benefits that can be obtained specifically by combining annealing and etching.

This is exemplified in **Figure 7.3**, which shows sheet resistance measurements obtained after annealing (and etching, where applicable) for Au films produced on SLG substrates overcoated with 22 nm of Si_3N_4. As shown in **Figure 7.3a**, Au films were either deposited to a thickness of

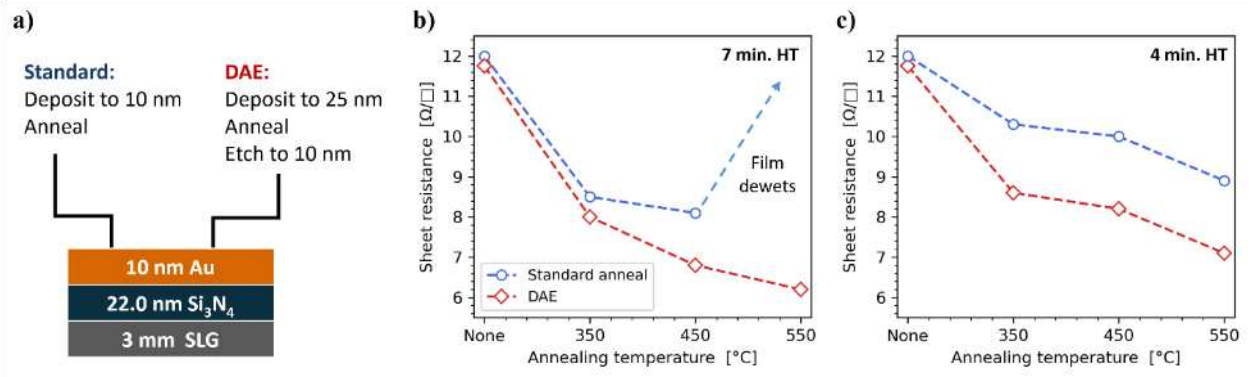


Figure 7.3: a) Schematic of the stack design used to evaluate the benefits achievable when annealing standard-deposited films, or thicker films, subsequently etched (following the DAE method). **b)**, **c)** Sheet resistance of the film stacks shown in **(a)** following annealing in ambient air, for different temperatures, for 7 or 4 minutes of annealing, respectively.

10 nm and immediately annealed, or deposited at a thickness of 25 nm, annealed, and then etched down to 10 nm. For an annealing duration of 7 minutes, as shown in **Figure 7.3b**, standard 10 nm films dewet at high temperatures; DAE films annealed at 25 nm, on the other hand, show lower sheet resistance than any of the other configurations tested, even after being etched back down to 10 nm. Even for a shorter annealing time of 4 minutes, as shown in **Figure 7.3c**, films annealed at high thicknesses show lower sheet resistance following etching; this may be an indicator of GB grooving or hole formation.

Indeed, it was discussed in Section 2.3.2 that thicker films were generally less susceptible to grain growth, GB grooving, and hole expansion than thinner ones. On the other hand, low thicknesses are required for high transparency. Thus, without etching to allow the modification of the Ag thickness between the annealing step and the completion of the coating, there will always exist a trade-off between the thickness required for stability and that which is required for performance.

This is particularly important for coatings which will undergo subsequent tempering, as repeated heating and cooling steps are known to destabilize thin metal films [35]; this may explain why laser annealing of Ag films to improve their performance is widely reported [345], [346], [347], but its usage to stabilize Ag films at high temperatures is not. While not strictly exclusive to the DAE method, annealing (and etching) the Ag layer prior to the deposition of encapsulating layers may provide another advantage in regard to successive heating steps. If the initial annealing step

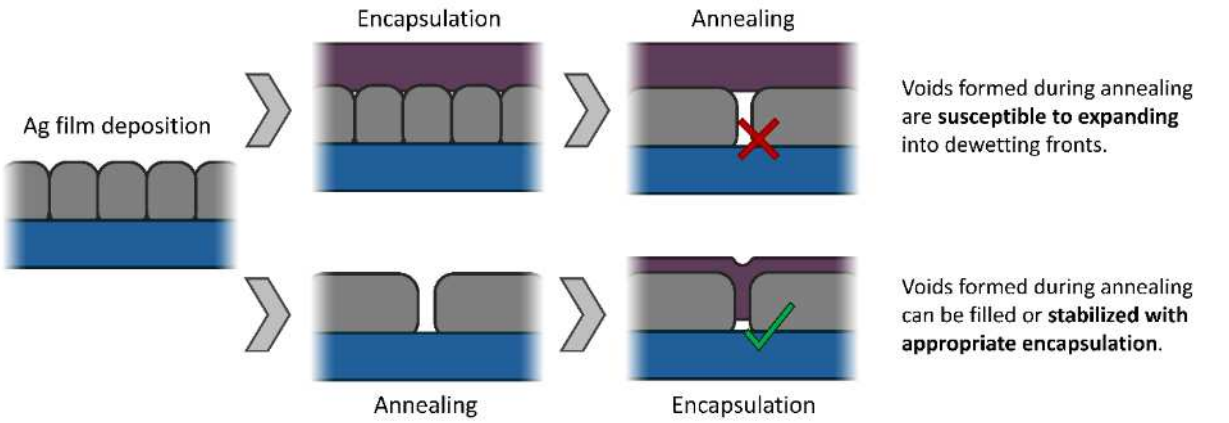


Figure 7.4: Schematic outlining the different morphologies which may be obtained when encapsulating an Ag film prior to annealing and vice-versa, and describing their consequences on film stability during subsequent tempering.

is performed on an encapsulated film, any holes that are formed will remain open during tempering, leaving the coating vulnerable to degradation [21]. On the other hand, holes formed prior to encapsulation could be filled and thus largely stabilized, as shown schematically in **Figure 7.4**.

These hypotheses are consistent with the thick metal films used in the Saint Gobain's patent claims (taking low-E coatings with thicknesses up to 17 nm to demonstrate stability improvements [344]). Moreover, their commercial single-stock coatings have lower visual transmittance than their other coatings produced with laser annealing [348], [349], [350], suggesting higher Ag thicknesses or additional protective layers are required to stabilize their coatings which undergo multiple annealing steps. Unfortunately, investigating and demonstrating these ideas would first require improving the overall stability of the Au films. In order to focus on Ag films this was not pursued, and thus this will be left for future experiments.

7.2.2 Improvements to the DAE approach

In addition to investigating the stability improvements described in the previous subsection, there remains a number of other aspects to continue improving upon multi-step Ag processes. Namely, there are a number of improvements to be made that are specific to the etching process, but as there are already outlined in Chapter 6, they will not be discussed here.

Different methods of heating the film would be worth investigating; this could enable more effective annealing, as well as make this technique more easily implementable. Moreover, exploring different etching methods, such as ion-beam etching, may be beneficial. In addition to the advantages already outlined in Chapter 6, this could help etch away encapsulating layers used during annealing as was attempted in Appendix E. Indeed, smoothing the surface during etching could stop the rapid formation of holes where the encapsulating film is thinner. Alternatively, simply changing the wavelength of the annealing laser may offer some flexibility; UV laser annealing may be of interest [345], if it can be employed without excessively heating the substrate. Assuming encapsulating layers can be successfully removed via etching, the combination of different annealing laser wavelengths and encapsulating layers, with different benefits in terms of laser absorption and Ag stabilization, could open a wide array of possibilities.

In addition to improvements to the etching process, further improvements to *in situ* monitoring should be pursued. IE-ISE monitoring of the film resistivity is sufficient to identify the continuous film formation threshold during deposition or etching; however, during annealing, resistivity changes resulting from the increased temperature, grain growth and hole formation may all take place at once, making morphological changes more difficult to identify. However, the plasmonic effect induced by hole formation in the Ag film, highlighted in Section 6.7, may allow to track this with greater confidence, particularly given the sensitivity to film absorption imparted by IE-ISE. Indeed, a method tracking the evolution of localized surface plasmon resonances (LSPR) could be used, similar to that used by Jamnig *et al*. [108].

Finally, the potential this method offers in regard to Ag dopants is particularly interesting. A self-imposed restriction in this work has been to not use any Ag dopants that would permanently alter the coating composition. This was done on the basis that increasing dopant concentrations would decrease the film's optical performance [48], [50], [89], [90]; however, these can significantly improve following annealing [49], [50], [79], [89], [92].

While this is an obstacle to the production of a single-stock coating when using traditional deposition methods, this could be completely overturned with the DAE approach. Selective deployment of dopants having been shown to greatly reduce their negative impact on Ag's optical properties while maintaining their benefits in regard to film coalescence [105], [108], subsequent annealing could very well result in films with optical properties indistinguishable to those of

undoped Ag. In fact, if we consider the thermal stability improvements that can result from doping, these films could be less susceptible to hole formation and dewetting, and may even show *better* properties than undoped Ag following annealing.

7.3 Stabilized dielectrics and improved stack architectures

In the foreword to Chapter 6, the optical changes encountered in the absence of contaminant diffusion were quickly attributed to grain growth in the Ag layer, and we moved on to explore various multi-step Ag deposition methods to try and manage this. Optical changes and stability improvements resulting from other layers should also be evaluated, however.

To this end, the effect of optical properties of different material changes, alone and in concert, was modelled. Referring back to the low-E stacks studied in **Figure 4.3**, TEM observations can be used to directly measure film thicknesses, allowing Ag resistivity before and after HT to be determined from sheet resistance measurements. Combining this with modelling of the optical changes observed in individual dielectrics and dielectric bilayers, presented in Appendix A, the relative impact of different optical variations incurred during tempering can be identified. **Figure 7.5** shows that HT performance changes can be qualitatively described with only a handful of changes.

First amongst these is grain growth of the Ag layer, justifying the previous focus on this layer. In addition to decreased Ag resistivity, this results in important increases in visible transmission, similar to those found for DAE samples in the AC state. Second, changes in UV absorption are observed, albeit the mechanism is not clear due to its dependence on adjacent layers, this is attributed to a shift in the bandgap of $ZnO_{(Al)}$ films. Third, stoichiometry changes (including oxidation) of the uppermost $SiN_{(Al)}$ layer, result in a decrease of its refractive index, shifting the transmission cutoff between the visible and NIR spectra.

These confirm the importance of Ag grain growth in visible transmission changes, as well in emissivity changes, but also that dielectric changes are not to be discounted, particularly as they pertain to modulating the optical changes induces by Ag. Intentional oxidation of the top $SiN_{(Al)}$

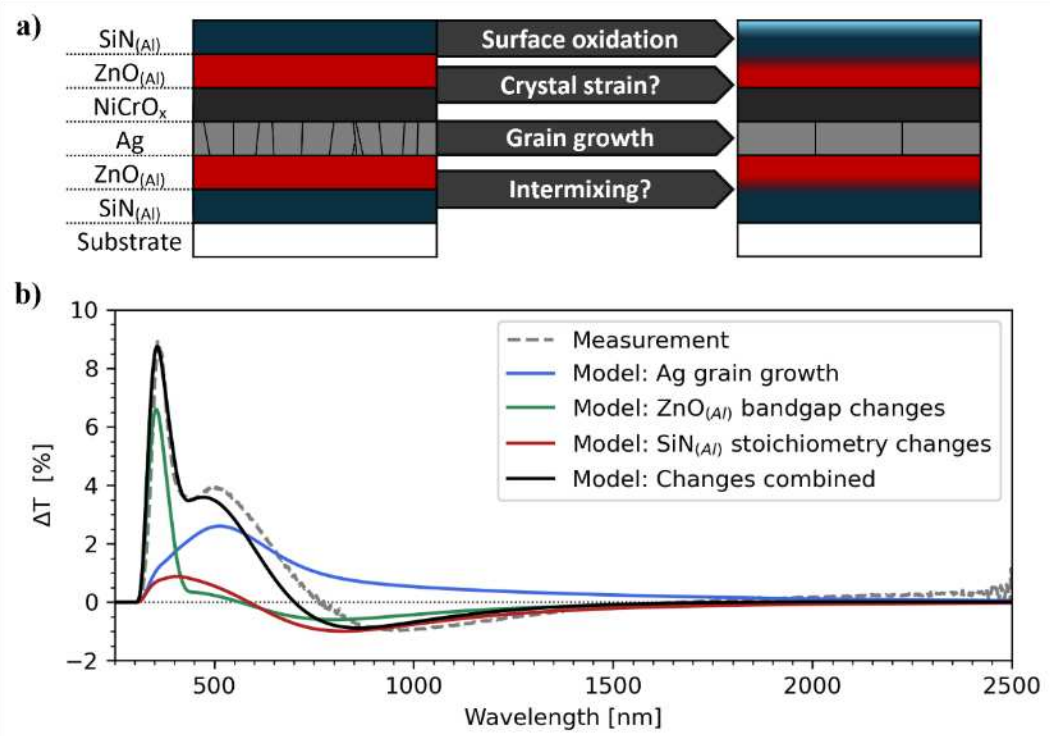


Figure 7.5: a) Schematic representation of the main changes resulting in optical changes during low-E tempering, excluding processes driven by Ag contamination. **b)** Measured values of ΔT following 8-minute HT of GRAR-type low-E glass samples (see **Figure 4.2**) produced on 3 mm SLG, compared to ΔT obtained via the modelling of specific material changes in *CompleteEASE*, as outlined in the text.

layer may offer a simple way to minimise its optical changes; this can also offer an opportunity to add an additional oxide layer with low coefficient of friction to improve mechanical durability.

Changes in the bandgap of $ZnO_{(Al)}$ films has been shown to result from different aluminum concentrations, albeit these may be at least partially due to effects of Al incorporation on crystallite strain or the concentration of oxygen vacancies in the resulting films [190], [191], [192]. Given the limited experiments dedicated to dielectric changes in this work, none of these mechanisms can be clearly attributed to optical changes observed. As these were found to be dependant on the stack configuration in Appendix A, showing distinctly different behavior in $ZnO_{(Al)}$-$SiN_{(Al)}$ bilayers than in single layers, changes in stoichiometry affected by the presence of the encapsulating $SiN_{(Al)}$ layer may play a role. Alternatively, stress applied by the $SiN_{(Al)}$ layer may be a factor. Similar to the investigations undertaken for low-E partial stacks in Chapter 4, a study of $ZnO_{(Al)}$ optical changes

on different substrates, in different annealing atmospheres, and adjacent to different layers, may help identify the root cause in order to find ways to mitigate these changes.

It should be noted that actual low-E stacks often include a larger number of layers, with a wider array of dielectric materials. In this case, one would need to investigate the optical changes taking place for different materials and their dependence on the adjacent materials, which could lead to the identification of several other changes. Indeed, while this will not be presented in this document, analysis of the electrical and optical changes following HT was conducted on more than twenty partial stacks, based on a commercial coating and produced by the industrial partner. These highlighted a number of different behaviors when different dielectric layers were inserted or removed, highlighting the nuance required to analyse more complex partial stack structures.

Finally, it must be kept in mind that beyond stabilizing their optical changes, dielectric films must continue to fulfill their roles in terms of protecting the Ag layer. Thus, the suggestions made to improve contaminant diffusion and mechanical durability in Chapter 4, for example the usage of nanolaminated dielectrics [276] and intermixing at the dielectric interfaces [277], should be pursued in tandem with the stabilization of the optical properties.

CHAPTER 8 CONCLUSION AND OUTLOOK

In conclusion, the various objectives set at the beginning of this work – to identify the role of contaminants and defects in low-E degradation, to achieve further control of the Ag microstructure, and to leverage it to improve coating durability – have been met.

Selectively controlling the presence of defects and the availability of contaminants, the under-reported effects of Na diffusion to the Ag layer were analyzed, the role of atmospheric oxygen in Ag dewetting was highlighted, and the latter's key role in scratch visibility accentuation was identified. Microstructural control of the Ag films was accomplished with more conventional, easily implementable methods (i.e. combining $Ag_{(N)}$ and a $ZnO_{(Al)}$ seed layer), as well as with novel multi-step processes. With the former, potent improvements in terms of corrosion durability were achieved. This approach fell short for the purpose of producing coatings with high optical stability following tempering: however, improvements to the etching, monitoring and annealing processes have been identified, laying a clear path ahead in this regard as well.

Indeed, this work has had the benefit of touching upon a wide range of topics: Ag deposition dynamics, *in situ* monitoring, film stability at defects, at high temperatures, under exposure to different contaminants, and many permutations thereof.

While any one of these topics could be the single object of its own thesis, it is my belief that the breadth of processes being investigated here is important, in and of itself. It is reflective of the inherent multifunctionality of low-E based coatings, and of the balance that needs to be met between fulfilling each of these functions, as well as practical fabrication concerns. The different aspects studied as part of this project and discussed with the industrial partner often came to inform one another, in ways a project with a narrower scope might miss. This also means that each of the topics studied in this work presents significant potential for future study.

While the work presented in Chapter 4 highlights the different degradation behavior underwent by low-E coatings when exposed to sodium, as compared to sulfur, chlorine or oxygen, there remains much more to be learned. Why does Na diffusion result in such widely spaced dewetting fronts, for example? It might pertain to its uniformity in the glass, its diffusion through the $ZnO_{(Al)}$ layer, or specific susceptibilities in the Ag film. Its promotion of fingering instabilities suggests it modifies the dynamics of edge retraction, but a mechanism cannot be clearly identified. Having

even shown to degrade the $ZnO_{(Al)}$ layer, if only in select instances, coating-glass interactions certainly warrant further study.

The nature of scratch defects, explored in the same chapter, are also worth investigating more closely. The mechanism by which humidity results in such intense defect propagation is of particular interest. While not shown in this work, preliminary experiments were performed using TEM with *in situ* heating to observe the evolution of scratch cross-section in real time, yielding promising results. With the addition of *in situ* control of the gas phase surrounding the sample, greater insight could be obtained. Moreover, while outside the scope of this work, a deeper investigation of how defects form and how different stack architectures can mitigate their formation would also be of great interest.

Potential improvements to post-deposition etching, particularly through the deposit-anneal-etch sequence, or DAE approach, discussed in Chapters 6 and 7, have potential to improve coating stability well beyond simply mitigating grain growth. Indeed, while the latter has been discussed at length in said chapters, the potential benefits this method could bring in terms of overall film stability are highly interesting. With the DAE approach alleviating the important optical changes associated with annealing doped films, the self-imposed restriction of not using doped Ag films could be abandoned, allowing to obtain a number of important stability benefits. For example, stabilization of the lower Ag interface via dopants or metallic seed layers (Ge, Ni, etc.) might prove essential in mitigating scratch intensification at high temperatures, whereas alloying Ag films to reduce their susceptibility to contaminants could yield improvements in a wide variety of circumstances.

Given the challenges in implementing this method, however, it may be worth it to first consider more straightforward endeavors. The chemical stability improvements presented in Chapter 5, obtained with relatively simple techniques to control the Ag microstructure, are highly encouraging. Exploring the benefits of other dopants, specifically when using selective deployment approaches, could pave the way for even greater stability. In the context of applications where tempering is not required, the usage of dopants is far less of an issue. One example that comes to mind is the fabrication of self-applicable low-E coatings on polymer substrates, adhered to glass or suspended in between windowpanes [5], [52]. Moreover, these present environmental stability challenges that doped Ag could significantly help with. On the one hand, application to a window

surface outside the sealed IGU environment creates a requirement for high chemical stability. On the other hand, these coatings being applied on a thin flexible polymer substrate, encapsulating layers may form cracks more easily, requiring highly stable Ag films. The stability improvements presented in Chapter 5, which were not particularly dependent on the encapsulating layers, are thus particularly well-suited.

Looking towards the general improvement of low-E coatings, the addition of a nitrogen surfactant explored in Chapter 5 is certainly the most easily actionable path found in this work, as it is rather straightforward to implement and can allow direct benefits to wetting and durability. However, while the results of Chapter 4 and Chapter 6 are more exploratory, it is interesting to note that the usage of metallic dopants could offer improvements in regard to film stability under contaminant exposure, when damaged by defects, and during etching. Metallic dopants were not studied in this work due to the potential degradation of the as-coated optical properties; however, recent work suggests that this could be managed with proper deployment of the dopants. Navigating the potential trade-offs and optimizing the performance and durability improvements achievable with metallic dopants, should be a priority in future work.

Finally, it is worth giving some thought to the practical implementation of low-E coatings. This work focuses strictly on the technical aspects of coating fabrication and durability. However, as stated in the introduction, low-E coatings are a crucial tool as we struggle to limit climate change: accessibility of this technology constitutes a distinct advantage in providing cooling or heating, without active consumption of electricity or fuel. While this requires coatings which are produced with great technical control, in order to achieve performance and stability, it also requires coatings that can be afforded by the people who need them the most. Alternative metals, simplified stack architectures, dopants enabling higher durability, self-applicable coatings, anything that enables easier, better or less expensive retrofitting will allow low-E coatings to have meaningful societal impact. Alternatively, perhaps one of the best changes that can be implemented to make low-E coatings more performant is appropriate evaluation of their overall impact on heating and cooling needs, something that is highly dependent on building architecture, window facing and local climate [351]. In other words, it is not sufficient to develop coatings, or any technology for that matter, with excellent technical performance: it is essential that we implement them with care and with consideration of their impact on our world.

REFERENCES

[1] "Transforming our world: the 2030 Agenda for Sustainable Development." UN, New York, 2015. [Online]. Available: https://digitallibrary.un.org/record/1654217

[2] Intergovernmental Panel on Climate Change (IPCC), Ed., *Climate Change 2022 - Mitigation of Climate Change: Working Group III Contribution to the Sixth Assessment Report of the Intergovernmental Panel on Climate Change*. Cambridge: Cambridge University Press, 2023. doi: 10.1017/9781009157926.

[3] A. Mastrucci, E. Byers, S. Pachauri, and N. D. Rao, "Improving the SDG energy poverty targets: Residential cooling needs in the Global South," *Energy Build.*, vol. 186, pp. 405–415, Mar. 2019, doi: 10.1016/j.enbuild.2019.01.015.

[4] V. Petra and K. Miloš, "Surface condensation on windows of non-insulated buildings and measures before their replacement," *Energy Build.*, vol. 328, p. 115165, Feb. 2025, doi: 10.1016/j.enbuild.2024.115165.

[5] K. Khaled and U. Berardi, "Current and future coating technologies for architectural glazing applications," *Energy Build.*, vol. 244, p. 111022, Aug. 2021, doi: 10.1016/j.enbuild.2021.111022.

[6] J. A. Ridealgh, "Large Area Coatings for Architectural Glass – Design, Manufacture, Processing Faults," *MRS Online Proc. Libr.*, vol. 890, no. 1, p. 110, Mar. 2006, doi: 10.1557/PROC-0890-Y01-10.

[7] International Energy Agency, "Technology Roadmap - Energy Efficient Building Envelopes," IEA, Paris, 2013. [Online]. Available: https://www.iea.org/reports/technology-roadmap-energy-efficient-building-envelopes

[8] C. Zhang, C. Ji, Y.-B. Park, and L. J. Guo, "Thin-Metal-Film-Based Transparent Conductors: Material Preparation, Optical Design, and Device Applications," *Adv. Opt. Mater.*, vol. 9, no. 3, p. 2001298, 2021, doi: https://doi.org/10.1002/adom.202001298.

[9] M. J. Riedl, *Optical Design Fundamentals for Infrared Systems*. SPIE Press, 2001.

[10] J. Szczyrbowski, A. Dietrich, and K. Hartig, "Bendable silver-based low emissivity coating on glass," *Sol. Energy Mater.*, vol. 19, no. 1, pp. 43–53, Sep. 1989, doi: 10.1016/0165-1633(89)90022-1.

[11] C. H. Stoessel, "20 - Optical coatings for automotive and building applications," in *Optical Thin Films and Coatings*, A. Piegari and F. Flory, Eds., in Woodhead Publishing Series in Electronic and Optical Materials. , Woodhead Publishing, 2013, pp. 718–740. doi: 10.1533/9780857097316.4.718.

[12] "Appendix 8: Electrical Conductivity of Selected Materials," in *An Introduction to Materials Engineering and Science*, John Wiley & Sons, Ltd, 2003. [Online]. Available: https://onlinelibrary.wiley.com/doi/abs/10.1002/0471473359.app8

[13] J. Bardeen, "Electrical Conductivity of Metals," *J. Appl. Phys.*, vol. 11, no. 2, pp. 88–111, Feb. 1940, doi: 10.1063/1.1712751.

[14] E. D. Palik, *Handbook of Optical Constants of Solids, Author and Subject Indices for Volumes I, II, and III*. Elsevier, 1998.

[15] P. B. Johnson and R. W. Christy, "Optical Constants of the Noble Metals," *Phys. Rev. B*, vol. 6, no. 12, pp. 4370–4379, Dec. 1972, doi: 10.1103/PhysRevB.6.4370.

[16] H. A. Macleod, "A New Approach to the Design of Metal-dielectric Thin-film Optical Coatings," *Opt. Acta Int. J. Opt.*, vol. 25, no. 2, pp. 93–106, Feb. 1978, doi: 10.1080/713819742.

[17] I. A. Rodionov *et al.*, "Quantum Engineering of Atomically Smooth Single-Crystalline Silver Films," *Sci. Rep.*, vol. 9, no. 1, pp. 1–9, Aug. 2019, doi: 10.1038/s41598-019-48508-3.

[18] J. Yun *et al.*, "An unexpected surfactant role of immiscible nitrogen in the structural development of silver nanoparticles: an experimental and numerical investigation," *Nanoscale*, vol. 12, no. 3, pp. 1749–1758, Jan. 2020, doi: 10.1039/C9NR08076G.

[19] K. Sarakinos, "A review on morphological evolution of thin metal films on weakly-interacting substrates," *Thin Solid Films*, vol. 688, p. 137312, Oct. 2019, doi: 10.1016/j.tsf.2019.05.031.

[20] K. A. Folgner, C.-T. Chu, Z. R. Lingley, H. I. Kim, J.-M. Yang, and J. D. Barrie, "Environmental durability of protected silver mirrors prepared by plasma beam sputtering," *Appl. Opt.*, vol. 56, no. 4, pp. C75–C86, Feb. 2017, doi: 10.1364/AO.56.000C75.

[21] D. M. Fryauf, A. C. Phillips, and N. P. Kobayashi, "Critical processing temperature for high performance protected silver thin film mirrors," *J. Astron. Telesc. Instrum. Syst.*, vol. 7, no. 03, Jul. 2021, doi: 10.1117/1.JATIS.7.3.034002.

[22] S. Gledhill, K. Steyer, C. Weiss, and C. Hildebrandt, "HiPIMS and DC Magnetron Sputter-Coated Silver Films for High-Temperature Durable Reflectors," *Coatings*, vol. 9, no. 10, Art. no. 10, Oct. 2019, doi: 10.3390/coatings9100593.

[23] G. Zhao *et al.*, "Nitrogen-Mediated Growth of Silver Nanocrystals to Form UltraThin, High-Purity Silver-Film Electrodes with Broad band Transparency for Solar Cells," *ACS Appl. Mater. Interfaces*, vol. 10, no. 47, pp. 40901–40910, Nov. 2018, doi: 10.1021/acsami.8b13377.

[24] R. A. Maniyara, V. K. Mkhitaryan, T. L. Chen, D. S. Ghosh, and V. Pruneri, "An antireflection transparent conductor with ultralow optical loss (<2 %) and electrical resistance (<6 Ω sq −1)," *Nat. Commun.*, vol. 7, no. 1, pp. 1–8, Dec. 2016, doi: 10.1038/ncomms13771.

[25] E. Jeong *et al.*, "Near-Zero Transmittance Loss, Highly Durable, Flexible, Transparent Electrode with an Ultrathin Ag Nanoporous Structure," *ACS Appl. Electron. Mater.*, vol. 4, no. 12, pp. 6164–6176, Dec. 2022, doi: 10.1021/acsaelm.2c01294.

[26] J. E. Greene, "Chapter 12 - Thin Film Nucleation, Growth, and Microstructural Evolution: An Atomic Scale View," in *Handbook of Deposition Technologies for Films and Coatings (Third Edition)*, P. M. Martin, Ed., Boston: William Andrew Publishing, 2010, pp. 554–620. doi: 10.1016/B978-0-8155-2031-3.00012-0.

[27] J. Yun, "Ultrathin Metal films for Transparent Electrodes of Flexible Optoelectronic Devices," *Adv. Funct. Mater.*, vol. 27, no. 18, p. 1606641, 2017, doi: 10.1002/adfm.201606641.

[28] E. A. Coronado, E. R. Encina, and F. D. Stefani, "Optical properties of metallic nanoparticles: manipulating light, heat and forces at the nanoscale," *Nanoscale*, vol. 3, no. 10, pp. 4042–4059, Oct. 2011, doi: 10.1039/C1NR10788G.

[29] A. Loiseau, V. Asila, G. Boitel-Aullen, M. Lam, M. Salmain, and S. Boujday, “Silver-Based Plasmonic Nanoparticles for and Their Use in Biosensing,” *Biosensors*, vol. 9, no. 2, p. 78, Jun. 2019, doi: 10.3390/bios9020078.

[30] C. Polop *et al.*, “The STM view of the initial stages of polycrystalline Ag film formation,” *New J. Phys.*, vol. 9, no. 3, pp. 74–74, Mar. 2007, doi: 10.1088/1367-2630/9/3/074.

[31] A. F. Mayadas and M. Shatzkes, “Electrical-Resistivity Model for Polycrystalline Films: the Case of Arbitrary Reflection at External Surfaces,” *Phys. Rev. B*, vol. 1, no. 4, pp. 1382–1389, Feb. 1970, doi: 10.1103/PhysRevB.1.1382.

[32] D. Gu, C. Zhang, Y.-K. Wu, and L. J. Guo, “Ultrasmooth and Thermally Stable Silver-Based Thin Films with Subnanometer Roughness by Aluminum Doping,” *ACS Nano*, vol. 8, no. 10, pp. 10343–10351, Oct. 2014, doi: 10.1021/nn503577c.

[33] M. Berni *et al.*, “Monitoring morphological and chemical properties during silver solid-state dewetting,” *Appl. Surf. Sci.*, vol. 498, p. 143890, Dec. 2019, doi: 10.1016/j.apsusc.2019.143890.

[34] P. Jacquet *et al.*, “On the solid-state dewetting of polycrystalline thin films: Capillary versus grain growth approach,” *Acta Mater.*, vol. 143, pp. 281–290, Jan. 2018, doi: 10.1016/j.actamat.2017.08.070.

[35] C. V. Thompson, “Solid-State Dewetting of Thin Films,” *Annu. Rev. Mater. Res.*, vol. 42, no. Volume 42, 2012, pp. 399–434, Aug. 2012, doi: 10.1146/annurev-matsci-070511-155048.

[36] K. Koike, K. Shimada, and S. Fukuda, “Aggregation in thin-film silver: Induced by chlorine and inhibited by alloying with two dopants,” *Corros. Sci.*, vol. 51, no. 11, pp. 2557–2564, Nov. 2009, doi: 10.1016/j.corsci.2009.06.044.

[37] E. Limam *et al.*, “Local Degradation Mechanisms by Tarnishing of Protected Silver Mirror Layers Studied by Combined Surface Analysis,” *J. Phys. Chem. B*, vol. 122, no. 2, pp. 578–586, Jan. 2018, doi: 10.1021/acs.jpcb.7b05015.

[38] R. C. Ross, “Observations on humidity-induced degradation of Ag-based low-emissivity films,” *Sol. Energy Mater.*, vol. 21, no. 1, pp. 25–42, Nov. 1990, doi: 10.1016/0165-1633(90)90040-8.

[39] J. Kulczyk-Malecka, “Diffusion Studies in Toughenable Low-E Coatings,” Manchester Metropolitan University, 2012.

[40] M. Chiodi, C. Cancellieri, F. Moszner, M. Andrzejczuk, J. Janczak-Rusch, and L. P. H. Jeurgens, “Massive Ag migration through metal/ceramic nano-multilayers: an interplay between temperature, stress-relaxation and oxygen-enhanced mass transport,” *J. Mater. Chem. C*, vol. 4, no. 22, pp. 4927–4938, Jun. 2016, doi: 10.1039/C6TC01098A.

[41] M. Sebastiani *et al.*, “Nano-Scale Residual Stress Profiling in Thin Multilayer Films with Non-Equibiaxial Stress State,” *Nanomaterials*, vol. 10, no. 5, Art. no. 5, May 2020, doi: 10.3390/nano10050853.

[42] Y. Tsuda, H. Omoto, K. Tanaka, and H. Ohsaki, “The underlayer effects on the electrical resistivity of Ag thin film,” *Thin Solid Films*, vol. 502, no. 1, pp. 223–227, Apr. 2006, doi: 10.1016/j.tsf.2005.07.279.

[43] D. Cornil, H. Wiame, B. Lecomte, J. Cornil, and D. Beljonne, "Which Oxide for Low-Emissivity Glasses? First-Principles Modeling of Silver Adhesion," *ACS Appl. Mater. Interfaces*, vol. 9, no. 21, pp. 18346–18354, May 2017, doi: 10.1021/acsami.7b03269.

[44] C. Ji, D. Liu, C. Zhang, and L. Jay Guo, "Ultrathin-metal-film-based transparent electrodes with relative transmittance surpassing 100%," *Nat. Commun.*, vol. 11, no. 1, p. 3367, Jul. 2020, doi: 10.1038/s41467-020-17107-6.

[45] W. N. S. Wan Shamsuddin, K. Zuber, P. J. Murphy, and M. L. Jane, "Environmental durability of soft low-e coatings: A review," *Sol. Energy Mater. Sol. Cells*, vol. 266, p. 112673, Mar. 2024, doi: 10.1016/j.solmat.2023.112673.

[46] J. D. Wolfe, "Durable low-emissivity thin film interference filter," CA2041038C, Jan. 02, 2001 [Online]. Available: https://patents.google.com/patent/CA2041038C/en

[47] J. Barr, *The Glass Tempering Handbook : Understanding the Glass Tempering Process*. 2016.

[48] A. Jamnig, N. Pliatsikas, G. Abadias, and K. Sarakinos, "On the effect of copper as wetting agent during growth of thin silver films on silicon dioxide substrates," *Appl. Surf. Sci.*, vol. 538, p. 148056, Feb. 2021, doi: 10.1016/j.apsusc.2020.148056.

[49] J. Xu *et al.*, "An Oxide-Dispersed Preparation Strategy for Silver Ultrathin Films with Low Percolation Threshold Thickness, Subnanometer Smoothness, and Prominent Durability," *Adv. Mater. Interfaces*, vol. 6, no. 16, p. 1900608, 2019, doi: 10.1002/admi.201900608.

[50] C. Zhang *et al.*, "High-Performance Doped Silver Films: Overcoming Fundamental Material Limits for Nanophotonic Applications," *Adv. Mater.*, vol. 29, no. 19, p. 1605177, May 2017, doi: 10.1002/adma.201605177.

[51] S. Yang, M. Liu, C. Zhao, S. Fan, and C.-W. Qiu, "Nonreciprocal thermal photonics," *Nat. Photonics*, vol. 18, no. 5, pp. 412–424, May 2024, doi: 10.1038/s41566-024-01409-y.

[52] B. P. Jelle, S. E. Kalnæs, and T. Gao, "Low-emissivity materials for building applications: A state-of-the-art review and future research perspectives," *Energy Build.*, vol. 96, pp. 329–356, Jun. 2015, doi: 10.1016/j.enbuild.2015.03.024.

[53] H. A. Macleod, *Thin-Film Optical Filters, Fifth Edition*. CRC Press, 2017.

[54] U. Berardi, "Light transmittance characterization and energy-saving analysis of a new selective coating for in situ window retrofit," *Sci. Technol. Built Environ.*, vol. 25, no. 9, pp. 1152–1163, Oct. 2019, doi: 10.1080/23744731.2019.1620546.

[55] "CIE standard photometric observer," e-ILV | CIE. [Online]. Available: http://eilv.cie.co.at/term/170

[56] "Standard Tables for Reference Solar Spectral Irradiances: Direct Normal and Hemispherical on 37° Tilted Surface." ASTM. [Online]. Available: https://www.astm.org/g0173-03r20.html

[57] N. Ohta and A. Robertson, *Colorimetry: Fundamentals and Applications*. John Wiley & Sons, 2006.

[58] D. L. Marinoski, S. Güths, and R. Lamberts, "Development of a calorimeter for determination of the solar factor of architectural glass and fenestrations," *Build. Environ.*, vol. 47, pp. 232–242, Jan. 2012, doi: 10.1016/j.buildenv.2011.07.017.

[59] N. Herguedas and E. Carretero, “Evaluation of low-emissivity coatings with single, double, and triple silver layers,” *Sol. Energy Mater. Sol. Cells*, vol. 263, p. 112592, Dec. 2023, doi: 10.1016/j.solmat.2023.112592.

[60] Q. Chen *et al.*, “Rapid annealing obtained ITO films with both extremely low infrared emissivity and high visible light transmission for energy-efficient window applications,” *Ceram. Int.*, vol. 51, no. 3, pp. 3163–3169, Jan. 2025, doi: 10.1016/j.ceramint.2024.11.291.

[61] Z. Huang and E. Yang, “Highly solar transparent and low-emissivity glass based on hydrogen-doped indium oxide,” *Mater. Sci. Eng. B*, vol. 312, p. 117818, Feb. 2025, doi: 10.1016/j.mseb.2024.117818.

[62] K. Sun, X. Tang, C. Yang, and D. Jin, “Preparation and performance of low-emissivity Al-doped ZnO films for energy-saving glass,” *Ceram. Int.*, vol. 44, no. 16, pp. 19597–19602, Nov. 2018, doi: 10.1016/j.ceramint.2018.07.207.

[63] J. Su, L. Yin, L. Qin, N. Ma, and J. Huang, “Preparation and performance of ZrAlN anti-reflective coatings for low-emissivity glasses,” *Ceram. Int.*, vol. 43, no. 17, pp. 14616–14622, Dec. 2017, doi: 10.1016/j.ceramint.2017.07.105.

[64] L. Liu *et al.*, “Achieving low-emissivity materials with high transmission for broadband radio-frequency signals,” *Sci. Rep.*, vol. 7, no. 1, p. 4840, Jul. 2017, doi: 10.1038/s41598-017-04988-9.

[65] F. Blanchard, “Bias-Enhanced Tungsten Oxide Films for Durable Electrochromic Devices,” masters, École Polytechnique de Montréal, 2018. [Online]. Available: https://publications.polymtl.ca/3115/

[66] B. Baloukas, S. Loquai, and L. Martinu, “VO2-based thermally active low emissivity coatings,” *Sol. Energy Mater. Sol. Cells*, vol. 183, pp. 25–33, Aug. 2018, doi: 10.1016/j.solmat.2018.03.048.

[67] E. Jeong *et al.*, “Strategy for Fabricating Ultrathin Au Film Electrodes with Ultralow Optoelectrical Losses and High Stability,” *ACS Appl. Mater. Interfaces*, vol. 14, no. 10, pp. 12797–12811, Mar. 2022, doi: 10.1021/acsami.1c22858.

[68] B. Hammer and J. K. Norskov, “Why gold is the noblest of all the metals,” *Nature*, vol. 376, no. 6537, pp. 238–240, Jul. 1995, doi: 10.1038/376238a0.

[69] M.-A. Dionne, B. Baloukas, O. Zabeida, J. Klemberg-Sapieha, and L. Martinu, “Fabrication and performance of randomly patterned tri-layer flexible and transparent electrodes,” *Opt. Mater.*, vol. 166, p. 117200, Sep. 2025, doi: 10.1016/j.optmat.2025.117200.

[70] K. Jenifer and S. Parthiban, “Highly stable, ultra-thin Au embedded zinc tin oxide multilayer transparent conductive thin films,” *Curr. Appl. Phys.*, vol. 53, pp. 94–103, Sep. 2023, doi: 10.1016/j.cap.2023.07.001.

[71] E. Jeong *et al.*, “Superstrong direct adhesion of Au, Ag, and Cu electrodes to oxide substrates via interfacial engineering,” *Acta Mater.*, vol. 291, p. 121008, Jun. 2025, doi: 10.1016/j.actamat.2025.121008.

[72] M. Todeschini, A. Bastos da Silva Fanta, F. Jensen, J. B. Wagner, and A. Han, “Influence of Ti and Cr Adhesion Layers on Ultrathin Au Films,” *ACS Appl. Mater. Interfaces*, vol. 9, no. 42, pp. 37374–37385, Oct. 2017, doi: 10.1021/acsami.7b10136.

[73] W. M. Abbott *et al.*, "Comparison of Metal Adhesion Layers for Au Films in Thermoplasmonic Applications," *ACS Appl. Mater. Interfaces*, vol. 12, no. 11, pp. 13503–13509, Mar. 2020, doi: 10.1021/acsami.9b22279.

[74] H. Yoshiki, V. Alexandruk, K. Hashimoto, and A. Fujishima, "Electroless Copper Plating Using ZnO Thin Film Coated on a Glass Substrate," *J. Electrochem. Soc.*, vol. 141, no. 5, p. L56, May 1994, doi: 10.1149/1.2054935.

[75] L. Yang, X. Yang, F. Gao, Y. Guan, R. Wan, and P. Wang, "Enhanced Adhesion of Copper Films on Fused Silica Glass Substrate by Plasma Pre-Treatment," *Materials*, vol. 16, no. 14, p. 5152, Jan. 2023, doi: 10.3390/ma16145152.

[76] E. Jeong *et al.*, "Cu-substrate interfacial adhesion: A key factor in controlling the oxidation of Cu thin films on oxide substrates," *Appl. Surf. Sci.*, vol. 640, p. 158319, Dec. 2023, doi: 10.1016/j.apsusc.2023.158319.

[77] P. Bellchambers, J. Lee, S. Varagnolo, H. Amari, M. Walker, and R. A. Hatton, "Elucidating the Exceptional Passivation Effect of 0.8 nm Evaporated Aluminium on Transparent Copper Films," *Front. Mater.*, vol. 5, 2018, doi: 10.3389/fmats.2018.00071.

[78] E. Jeong *et al.*, "A 3nm-thick, quasi-single crystalline Cu layer with ultralow optoelectrical losses and exceptional durability," *Acta Mater.*, vol. 223, p. 117484, Jan. 2022, doi: 10.1016/j.actamat.2021.117484.

[79] W. Chen, K. P. Chen, M. D. Thoreson, A. V. Kildishev, and V. M. Shalaev, "Ultrathin, ultrasmooth, and low-loss silver films via wetting and annealing," *Appl. Phys. Lett.*, vol. 97, no. 21, p. 211107, Nov. 2010, doi: 10.1063/1.3514257.

[80] E. Jeong *et al.*, "Minimizing optical loss in ultrathin Ag films based on Ge wetting layer: Insights on Ge-mediated Ag growth," *Appl. Surf. Sci.*, vol. 528, p. 146989, Oct. 2020, doi: 10.1016/j.apsusc.2020.146989.

[81] P. Liu, J. Zhang, S. Ma, Y. Huang, and Z. Wang, "Highly Thermal-Stable and Transparent Conductive Au-Based Thin Films through Al Doping," *Cryst. Growth Des.*, vol. 25, no. 10, pp. 3365–3373, May 2025, doi: 10.1021/acs.cgd.5c00168.

[82] D. Ma *et al.*, "Pushing the thinness limit of silver films for flexible optoelectronic devices via ion-beam thinning-back process," *Nat. Commun.*, vol. 15, no. 1, p. 2248, Mar. 2024, doi: 10.1038/s41467-024-46467-6.

[83] G. Ferrando, C. Mennucci, M. Barelli, M. C. Giordano, and F. Buatier de Mongeot, "Flexible and Transparent Ultrathin Gold Electrodes via Ion Beam Smoothing," *Small Sci.*, vol. 5, no. 1, p. 2400272, 2025, doi: 10.1002/smsc.202400272.

[84] E. Jeong *et al.*, "Thermal stability enhancement of ultrathin Ag film electrodes by incorporating atomic oxygen," *Appl. Surf. Sci.*, vol. 546, p. 149149, Apr. 2021, doi: 10.1016/j.apsusc.2021.149149.

[85] J. Colin *et al.*, "In Situ and Real-Time Nanoscale Monitoring of Ultra-Thin Metal Film Growth Using Optical and Electrical Diagnostic Tools," *Nanomaterials*, vol. 10, no. 11, Art. no. 11, Nov. 2020, doi: 10.3390/nano10112225.

[86] R. Dannenberg, E. A. Stach, J. R. Groza, and B. J. Dresser, “In-situ TEM observations of abnormal grain growth, coarsening, and substrate de-wetting in nanocrystalline Ag thin films,” *Thin Solid Films*, vol. 370, no. 1, pp. 54–62, Jul. 2000, doi: 10.1016/S0040-6090(99)00947-5.

[87] S. A. Jang, H. J. Lee, C. V. Thompson, C. A. Ross, and Y. J. Oh, “Crystallographic analysis of the solid-state dewetting of polycrystalline gold film using automated indexing in a transmission electron microscope,” *APL Mater.*, vol. 3, no. 12, p. 126103, Dec. 2015, doi: 10.1063/1.4937432.

[88] Z. Tian *et al.*, “Atomistic Insights into Aluminum Doping Effect on Surface Roughness of Deposited Ultra-Thin Silver Films,” *Nanomater. Basel Switz.*, vol. 11, no. 1, p. E158, Jan. 2021, doi: 10.3390/nano11010158.

[89] E.-T. Hu *et al.*, “Influence of thermal annealing on the optical and electrical properties of Ag-Al ultrathin film-based sandwich-like transparent conductor,” *Thin Solid Films*, vol. 759, p. 139484, Oct. 2022, doi: 10.1016/j.tsf.2022.139484.

[90] W. N. S. Wan Shamsuddin, A. Roccisano, K. Zuber, P. J. Murphy, and M. Llusca Jane, “Environmentally robust Ag–Cu based low-e coatings,” *Sol. Energy Mater. Sol. Cells*, vol. 248, p. 112033, Dec. 2022, doi: 10.1016/j.solmat.2022.112033.

[91] B. Ewald *et al.*, “How to Fix Silver for Plasmonics,” Jul. 13, 2025, *arXiv*: arXiv:2507.09569. doi: 10.48550/arXiv.2507.09569.

[92] J.-W. Jeong, H. Kong, and H.-Y. Lee, “Effect of Ni-doped Ag on the thermal stability of ZnO/Ag/ZnO multilayer thin films,” *Superlattices Microstruct.*, vol. 133, p. 106187, Sep. 2019, doi: 10.1016/j.spmi.2019.106187.

[93] G. Zhao *et al.*, “Comparison of the effect of gaseous and metallic additives on ultrathin Ag layer formation: An experimental and numerical investigation,” *Appl. Surf. Sci.*, vol. 682, p. 161774, Feb. 2025, doi: 10.1016/j.apsusc.2024.161774.

[94] H. Lüth, *Solid Surfaces, Interfaces and Thin Films*, 5th ed. in Graduate Texts in Physics. Berlin Heidelberg: Springer-Verlag, 2010. doi: 10.1007/978-3-642-13592-7.

[95] T. Young, “III. An essay on the cohesion of fluids,” *Philos. Trans. R. Soc. Lond.*, vol. 95, pp. 65–87, Jan. 1805, doi: 10.1098/rstl.1805.0005.

[96] R. Tran *et al.*, “Surface energies of elemental crystals,” *Sci. Data*, vol. 3, no. 1, p. 160080, Sep. 2016, doi: 10.1038/sdata.2016.80.

[97] B. Lü, G. A. Almyras, V. Gervilla, J. E. Greene, and K. Sarakinos, “Formation and morphological evolution of self-similar 3D nanostructures on weakly interacting substrates,” *Phys. Rev. Mater.*, vol. 2, no. 6, p. 063401, Jun. 2018, doi: 10.1103/PhysRevMaterials.2.063401.

[98] G. L. Kellogg, “Field ion microscope studies of single-atom surface diffusion and cluster nucleation on metal surfaces,” *Surf. Sci. Rep.*, vol. 21, no. 1, pp. 1–88, Dec. 1994, doi: 10.1016/0167-5729(94)90007-8.

[99] A. Jamnig, D. G. Sangiovanni, G. Abadias, and K. Sarakinos, “Atomic-scale diffusion rates during growth of thin metal films on weakly-interacting substrates,” *Sci. Rep.*, vol. 9, no. 1, p. 6640, Apr. 2019, doi: 10.1038/s41598-019-43107-8.

[100] Y. A. Kryukov and J. G. Amar, "Scaling of the island density and island-size distribution in irreversible submonolayer growth of three-dimensional islands," *Phys. Rev. B*, vol. 81, no. 16, p. 165435, Apr. 2010, doi: 10.1103/PhysRevB.81.165435.

[101] B. Lü, E. P. Münger, and K. Sarakinos, "Coalescence-controlled and coalescence-free growth regimes during deposition of pulsed metal vapor fluxes on insulating surfaces," *J. Appl. Phys.*, vol. 117, no. 13, Apr. 2015, doi: 10.1063/1.4916983.

[102] B. Lü, V. Elofsson, E. P. Münger, and K. Sarakinos, "Dynamic competition between island growth and coalescence in metal-on-insulator deposition," *Appl. Phys. Lett.*, vol. 105, no. 16, p. 163107, Oct. 2014, doi: 10.1063/1.4900575.

[103] F. A. Nichols, "Coalescence of Two Spheres by Surface Diffusion," *J. Appl. Phys.*, vol. 37, no. 7, pp. 2805–2808, Jun. 1966, doi: 10.1063/1.1782127.

[104] V. Elofsson, B. Lü, D. Magnfält, E. P. Münger, and K. Sarakinos, "Unravelling the physical mechanisms that determine microstructural evolution of ultrathin Volmer-Weber films," *J. Appl. Phys.*, vol. 116, no. 4, p. 044302, Jul. 2014, doi: 10.1063/1.4890522.

[105] A. Jamnig, N. Pliatsikas, G. Abadias, and K. Sarakinos, "Manipulation of thin metal film morphology on weakly interacting substrates via selective deployment of alloying species," *J. Vac. Sci. Technol. A*, vol. 40, no. 3, p. 033407, Apr. 2022, doi: 10.1116/6.0001700.

[106] G. Zhao *et al.*, "Strategy for improving Ag wetting on oxides: Coalescence dynamics versus nucleation density," *Appl. Surf. Sci.*, vol. 510, p. 145515, Apr. 2020, doi: 10.1016/j.apsusc.2020.145515.

[107] H. A. van der Vegt, H. M. van Pinxteren, M. Lohmeier, E. Vlieg, and J. M. C. Thornton, "Surfactant-induced layer-by-layer growth of Ag on Ag(111)," *Phys. Rev. Lett.*, vol. 68, no. 22, pp. 3335–3338, Jun. 1992, doi: 10.1103/PhysRevLett.68.3335.

[108] A. Jamnig *et al.*, "3D-to-2D Morphology Manipulation of Sputter-Deposited Nanoscale Silver Films on Weakly Interacting Substrates via Selective Nitrogen Deployment for Multifunctional Metal Contacts," *ACS Appl. Nano Mater.*, vol. 3, no. 5, pp. 4728–4738, May 2020, doi: 10.1021/acsanm.0c00736.

[109] G. Abadias *et al.*, "Review Article: Stress in thin films and coatings: Current status, challenges, and prospects," *J. Vac. Sci. Technol. A*, vol. 36, no. 2, p. 020801, Mar. 2018, doi: 10.1116/1.5011790.

[110] A. Anders, "A structure zone diagram including plasma-based deposition and ion etching," *Thin Solid Films*, vol. 518, no. 15, pp. 4087–4090, May 2010, doi: 10.1016/j.tsf.2009.10.145.

[111] M. Schwartzkopf *et al.*, "Role of Sputter Deposition Rate in Tailoring Nanogranular Gold Structures on Polymer Surfaces," *ACS Appl. Mater. Interfaces*, vol. 9, no. 6, pp. 5629–5637, Feb. 2017, doi: 10.1021/acsami.6b15172.

[112] E. Kusano, "Dependence of film structure on the film structure-independent equivalent film thickness in magnetron sputtering deposition of Ag thin films," *J. Vac. Sci. Technol. A*, vol. 40, no. 5, p. 053405, Sep. 2022, doi: 10.1116/6.0001989.

[113] T. C. Huang, G. Lim, F. Parmigiani, and E. Kay, "Effect of ion bombardment during deposition on the x-ray microstructure of thin silver films," *J. Vac. Sci. Technol. A*, vol. 3, no. 6, pp. 2161–2166, Nov. 1985, doi: 10.1116/1.573271.

[114] A. Anders, E. Byon, D.-H. Kim, K. Fukuda, and S. H. N. Lim, “Smoothing of ultrathin silver films by transition metal seeding,” *Solid State Commun.*, vol. 140, no. 5, pp. 225–229, Nov. 2006, doi: 10.1016/j.ssc.2006.08.027.

[115] G. Zhao *et al.*, “Underlying principles of Ge-induced early cluster-to-layer transition for ultrathin Ag layer formation on oxides,” *Surf. Interfaces*, vol. 54, p. 105208, Nov. 2024, doi: 10.1016/j.surfin.2024.105208.

[116] Logeeswaran VJ *et al.*, “Ultrasmooth Silver Thin Films Deposited with a Germanium Nucleation Layer,” *Nano Lett.*, vol. 9, no. 1, pp. 178–182, Jan. 2009, doi: 10.1021/nl8027476.

[117] H. Liu *et al.*, “Enhanced Surface Plasmon Resonance on a Smooth Silver Film with a Seed Growth Layer,” *ACS Nano*, vol. 4, no. 6, pp. 3139–3146, Jun. 2010, doi: 10.1021/nn100466p.

[118] S. Esch, M. Breeman, M. Morgenstern, T. Michely, and G. Comsa, “Nucleation and morphology of homoepitaxial Pt(111)-films grown with ion beam assisted deposition,” *Surf. Sci.*, vol. 365, no. 2, pp. 187–204, Sep. 1996, doi: 10.1016/0039-6028(96)00744-3.

[119] W. Ensinger, “Low energy ion assist during deposition — an effective tool for controlling thin film microstructure,” *Nucl. Instrum. Methods Phys. Res. Sect. B Beam Interact. Mater. At.*, vol. 127–128, pp. 796–808, May 1997, doi: 10.1016/S0168-583X(97)00010-4.

[120] M. Marinov, “Effect of ion bombardment on the initial stages of thin film growth,” *Thin Solid Films*, vol. 46, no. 3, pp. 267–274, Nov. 1977, doi: 10.1016/0040-6090(77)90182-1.

[121] K. A. Reck *et al.*, “Early-stage silver growth during sputter deposition on SiO2 and polystyrene – Comparison of biased DC magnetron sputtering, high-power impulse magnetron sputtering (HiPIMS) and bipolar HiPIMS,” *Appl. Surf. Sci.*, vol. 666, p. 160392, Sep. 2024, doi: 10.1016/j.apsusc.2024.160392.

[122] M. A. Makeev and A.-L. Barabási, “Ion-induced effective surface diffusion in ion sputtering,” *Appl. Phys. Lett.*, vol. 71, no. 19, pp. 2800–2802, Nov. 1997, doi: 10.1063/1.120140.

[123] H. Windischmann, “Intrinsic stress in sputter-deposited thin films,” *Crit. Rev. Solid State Mater. Sci.*, vol. 17, no. 6, pp. 547–596, Jan. 1992, doi: 10.1080/10408439208244586.

[124] M. Kawamura, R. Sagara, Y. Abe, T. Kiba, and K. H. Kim, “Large-grained Ag thin films with low electrical resistivity produced by sputtering in Kr gas,” *Jpn. J. Appl. Phys.*, vol. 59, no. 4, p. 048001, Mar. 2020, doi: 10.35848/1347-4065/ab8027.

[125] J. H. Park *et al.*, “Single-crystalline silver films for plasmonics,” *Adv. Mater. Deerfield Beach Fla*, vol. 24, no. 29, pp. 3988–3992, Aug. 2012, doi: 10.1002/adma.201200812.

[126] H. Zheng *et al.*, “Grain Boundary Properties of Elemental Metals,” Jul. 21, 2019, *arXiv*: arXiv:1907.08905. doi: 10.48550/arXiv.1907.08905.

[127] R. P. Netterfield and P. J. Martin, “Nucleation and growth studies of gold films prepared by evaporation and ion-assisted deposition,” *Appl. Surf. Sci.*, vol. 25, no. 3, pp. 265–278, Apr. 1986, doi: 10.1016/0169-4332(86)90059-0.

[128] I. J. Hodgkinson and J. Lemmon, “Morphology of gold films thinned by argon ion sputter etching,” *J. Appl. Phys.*, vol. 67, no. 11, pp. 6876–6881, Jun. 1990, doi: 10.1063/1.345078.

[129] E. Müller, “Electron-beam broadening in electron microscopy by solving the electron transport equation,” *Phys. Rev. Res.*, vol. 2, no. 4, 2020, doi: 10.1103/PhysRevResearch.2.043313.

[130] N. Jedrecy, G. Renaud, R. Lazzari, and J. Jupille, "Unstrained islands with interface coincidence sites versus strained islands: X-ray measurements on Ag/ZnO," *Phys. Rev. B*, vol. 72, no. 19, p. 195404, Nov. 2005, doi: 10.1103/PhysRevB.72.195404.

[131] T. Lee *et al.*, "Regulating Ag Wettability via Modulating Surface Stoichiometry of ZnO Substrates for Flexible Electronics," *Adv. Funct. Mater.*, vol. 31, no. 36, p. 2104372, 2021, doi: 10.1002/adfm.202104372.

[132] D. Cornil, N. Rivolta, V. Mercier, H. Wiame, D. Beljonne, and J. Cornil, "Enhanced Adhesion Energy at Oxide/Ag Interfaces for Low-Emissivity Glasses: Theoretical Insight into Doping and Vacancy Effects," *ACS Appl. Mater. Interfaces*, vol. 12, no. 36, pp. 40838–40849, Sep. 2020, doi: 10.1021/acsami.0c07579.

[133] H. Zhou, S.-J. Yu, Y.-J. Zhang, M.-G. Chen, Z.-W. Jiao, and P.-Z. Si, "In situ electric properties of Ag films deposited on rough substrates," *Philos. Mag. Lett.*, vol. 93, no. 1, pp. 18–26, Jan. 2013, doi: 10.1080/09500839.2012.728297.

[134] K. Tominaga, S. Iwamura, I. Fujita, Y. Shintani, and O. Tada, "Influence of Bombardment by Energetic Atoms on c-Axis Orientation of ZnO Films," *Jpn. J. Appl. Phys.*, vol. 21, no. 7R, p. 999, Jul. 1982, doi: 10.1143/JJAP.21.999.

[135] L. Kinner, T. Dimopoulos, G. Ligorio, E. J. W. List-Kratochvil, and F. Hermerschmidt, "High performance organic light-emitting diodes employing ITO-free and flexible TiOx/Ag/Al:ZnO electrodes," *RSC Adv.*, vol. 11, no. 28, pp. 17324–17331, May 2021, doi: 10.1039/D1RA02214H.

[136] S. Brossard, "Glazing comprising a substrate coated with a stack comprising a functional layer made from silver and a thick blocking underlayer made from TiOx," EP3068741A1, Sep. 21, 2016 [Online]. Available: https://patents.google.com/patent/EP3068741A1/en

[137] M. R. Soares, P. H. Dionísio, I. J. R. Baumvol, and W. H. Schreiner, "Influence of sputtering parameters on the composition and crystallinity of tin oxide," *Thin Solid Films*, vol. 214, no. 1, pp. 6–16, Jun. 1992, doi: 10.1016/0040-6090(92)90449-L.

[138] H. Lu *et al.*, "Preparation and investigation of ITO/metal/ITO electrodes for electrochromic application," *Opt. Mater.*, vol. 133, p. 112848, Nov. 2022, doi: 10.1016/j.optmat.2022.112848.

[139] K. Koike, F. Yamazaki, T. Okamura, and S. Fukuda, "Improvement of corrosion resistance of transparent conductive multilayer coating consisting of silver layers and transparent metal oxide layers," *J. Vac. Sci. Technol. A*, vol. 25, no. 3, pp. 527–531, Apr. 2007, doi: 10.1116/1.2722758.

[140] K. Tominaga, T. Yuasa, M. Kume, and O. Tada, "Influence of Energetic Oxygen Bombardment on Conductive ZnO Films," *Jpn. J. Appl. Phys.*, vol. 24, no. 8R, p. 944, Aug. 1985, doi: 10.1143/JJAP.24.944.

[141] I. Manzen, Y. Yoshimura, K. Matsubara, and A. Nitta, "Improvement of characteristics of flexible Al-doped ZnO/Ag/Al-doped ZnO transparent conductive film using silver," *J. Vac. Sci. Technol. B*, vol. 38, no. 2, p. 022205, Feb. 2020, doi: 10.1116/1.5137796.

[142] Y. Xu, B. Boyce, S. Boussaad, P. J. Lingle, J. Lao, and R. Vernhes, "Low-e matchable coated articles having doped seed layer under silver, and corresponding methods,"

US20200017402A1, Jan. 16, 2020 [Online]. Available: https://patents.google.com/patent/US20200017402A1/en

[143] B.-G. Jung *et al.*, "Wafer-scale high-quality Ag thin film using a ZnO buffer layer for plasmonic applications," *Appl. Surf. Sci.*, vol. 512, p. 145705, May 2020, doi: 10.1016/j.apsusc.2020.145705.

[144] K. Mizukoshi, T. Yamamura, Y. Tomioka, and M. Kawamura, "Effect of TiO2 lowermost layer on crystal orientation and electrical resistivity of glass/TiO2/ZnO/Ag structure in Low-E glass," *Jpn. J. Appl. Phys.*, vol. 60, no. 2, p. 025501, Feb. 2021, doi: 10.35848/1347-4065/abdabd.

[145] L. Xu, L. Shi, and X. Li, "Effect of TiO2 buffer layer on the structural and optical properties of ZnO thin films deposited by E-beam evaporation and sol–gel method," *Appl. Surf. Sci.*, vol. 255, no. 5, Part 2, pp. 3230–3234, Dec. 2008, doi: 10.1016/j.apsusc.2008.09.026.

[146] P. Li *et al.*, "Structural Optimization of Oxide/Metal/Oxide Transparent Conductors for High-Performance Low-Emissivity Heaters," *Adv. Mater. Interfaces*, vol. 5, no. 24, p. 1801287, Dec. 2018, doi: 10.1002/admi.201801287.

[147] G. E. Hallani, M. Khuili, N. Fazouan, A. Liba, H. A. E. Makarim, and E. H. Atmani, "Experimental and DFT investigations of Al-doped ZnO nanostructured thin films," *Chem. Phys. Impact*, vol. 8, p. 100648, Jun. 2024, doi: 10.1016/j.chphi.2024.100648.

[148] S. Hafezian, K. Maloney, J. Lefebvre, L. Martinu, and S. Kéna-Cohen, "Continuous ultrathin silver films deposited on SiO2 and SiNx using a self-assembled monolayer," *Appl. Phys. Lett.*, vol. 109, no. 12, p. 121603, Sep. 2016, doi: 10.1063/1.4963262.

[149] S. Hafezian, R. Beaini, L. Martinu, and S. Kéna-Cohen, "Degradation mechanism of protected ultrathin silver films and the effect of the seed layer," *Appl. Surf. Sci.*, vol. 484, pp. 335–340, Aug. 2019, doi: 10.1016/j.apsusc.2019.04.043.

[150] J. Zou, C.-Z. Li, C.-Y. Chang, H.-L. Yip, and A. K.-Y. Jen, "Interfacial Engineering of Ultrathin Metal Film Transparent Electrode for Flexible Organic Photovoltaic Cells," *Adv. Mater.*, vol. 26, no. 22, pp. 3618–3623, 2014, doi: 10.1002/adma.201306212.

[151] K. Fukuda, S. H. N. Lim, and A. Anders, "Coalescence of magnetron-sputtered silver islands affected by transition metal seeding (Ni, Cr, Nb, Zr, Mo, W, Ta) and other parameters," *Thin Solid Films*, vol. 516, no. 14, pp. 4546–4552, May 2008, doi: 10.1016/j.tsf.2007.05.080.

[152] C. Zhang *et al.*, "An Ultrathin, Smooth, and Low-Loss Al-Doped Ag Film and Its Application as a Transparent Electrode in Organic Photovoltaics," *Adv. Mater.*, vol. 26, no. 32, pp. 5696–5701, Aug. 2014, doi: 10.1002/adma.201306091.

[153] K. Sarakinos *et al.*, "Unravelling the effect of nitrogen on the morphological evolution of thin silver films on weakly-interacting substrates," *Appl. Surf. Sci.*, vol. 649, p. 159209, Mar. 2024, doi: 10.1016/j.apsusc.2023.159209.

[154] D. J. Srolovitz and S. A. Safran, "Capillary instabilities in thin films. I. Energetics," *J. Appl. Phys.*, vol. 60, no. 1, pp. 247–254, Jul. 1986, doi: 10.1063/1.337689.

[155] C. V. Thompson, "Grain Growth in Thin Films," *Annu. Rev. Mater. Sci.*, vol. 20, no. 1, pp. 245–268, 1990, doi: 10.1146/annurev.ms.20.080190.001333.

[156] P. H. Smith and H. Gurev, “Silicon dioxide as a high temperature stabilizer for silver films,” *Thin Solid Films*, vol. 45, no. 1, pp. 159–168, Aug. 1977, doi: 10.1016/0040-6090(77)90221-8.

[157] T. P. Nolan, R. Sinclair, and R. Beyers, “Modeling of agglomeration in polycrystalline thin films: Application to TiSi2 on a silicon substrate,” *J. Appl. Phys.*, vol. 71, no. 2, pp. 720–724, Jan. 1992, doi: 10.1063/1.351333.

[158] J.-H. Cho, T. James, and D. H. Gracias, “Curving Nanostructures Using Extrinsic Stress,” *Adv. Mater.*, vol. 22, no. 21, pp. 2320–2324, 2010, doi: 10.1002/adma.200904410.

[159] H.-J. Lee, P. Zhang, and J. C. Bravman, “Tensile failure by grain thinning in micromachined aluminum thin films,” *J. Appl. Phys.*, vol. 93, no. 3, pp. 1443–1451, Feb. 2003, doi: 10.1063/1.1532933.

[160] D. Lee and D. Choi, “Highly thermostable ultrathin planar Ag transparent heaters,” *Microelectron. Eng.*, vol. 251, p. 111658, Jan. 2022, doi: 10.1016/j.mee.2021.111658.

[161] A. J. Krisko and G. Pfaff, “Temperable high shading performance coatings,” US7138182B2, Nov. 21, 2006 [Online]. Available: https://patents.google.com/patent/US7138182B2/en

[162] D. Zöllner and W. Pantleon, “Effect of boundary grooving on grain growth by Potts model simulations,” *J. Phys. Conf. Ser.*, vol. 2635, no. 1, p. 012033, Nov. 2023, doi: 10.1088/1742-6596/2635/1/012033.

[163] E. A. Holm and S. M. Foiles, “How Grain Growth Stops: A Mechanism for Grain-Growth Stagnation in Pure Materials,” *Science*, vol. 328, no. 5982, pp. 1138–1141, May 2010, doi: 10.1126/science.1187833.

[164] W. W. Mullins, “The effect of thermal grooving on grain boundary motion,” *Acta Metall.*, vol. 6, no. 6, pp. 414–427, Jun. 1958, doi: 10.1016/0001-6160(58)90020-8.

[165] L. Chi and N. Bassim, “Ag Thin Film Dewetting Prevention by Ion Implantation,” *Adv. Mater. Interfaces*, vol. 6, no. 11, p. 1900108, 2019, doi: 10.1002/admi.201900108.

[166] M. D. Thouless, “Effect of surface diffusion on the creep of thin films and sintered arrays of particles,” *Acta Metall. Mater.*, vol. 41, no. 4, pp. 1057–1064, Apr. 1993, doi: 10.1016/0956-7151(93)90155-L.

[167] B. F. L. Almeida, “Structuration par laser de couches métalliques encapsulées par des diélectriques,” phdthesis, Ecole Centrale Marseille, 2022. [Online]. Available: https://theses.hal.science/tel-04050819

[168] D. Weygand, Y. Bréchet, and J. Lépinoux, “Influence of a reduced mobility of triple points on grain growth in two dimensions,” *Acta Mater.*, vol. 46, no. 18, pp. 6559–6564, Nov. 1998, doi: 10.1016/S1359-6454(98)00318-8.

[169] A. Kumar *et al.*, “Anomalous diffusion along metal/ceramic interfaces,” *Nat. Commun.*, vol. 9, no. 1, p. 5251, Dec. 2018, doi: 10.1038/s41467-018-07724-7.

[170] M. Ohring, *The Materials Science of Thin Films*. Academic Press, 1992.

[171] R. W. Balluffi and J. M. Blakely, “Special aspects of diffusion in thin films,” *Thin Solid Films*, vol. 25, no. 2, pp. 363–392, Feb. 1975, doi: 10.1016/0040-6090(75)90056-5.

[172] J. Yang *et al.*, “Improvement of high-temperature resistance of the Ag-based multilayer films deposited by magnetron sputtering,” *Mater. Lett.*, vol. 118, pp. 62–65, Mar. 2014, doi: 10.1016/j.matlet.2013.12.033.

[173] D.-C. Tsai *et al.*, “Thermal stability and optical properties of low emissivity multilayer coatings for energy-saving applications,” *Ceram. Int.*, vol. 46, no. 6, pp. 7991–7997, Apr. 2020, doi: 10.1016/j.ceramint.2019.12.021.

[174] Y. Lu *et al.*, “Coated article with low-e coating having protective doped silver layer for protecting silver based ir reflecting layer(s), and method of making same,” US20190203340A1, Jul. 04, 2019 [Online]. Available: https://patents.google.com/patent/US20190203340A1/en

[175] R. Huffer, “Temperable low emissivity and reflective windows,” US4790922A, Dec. 13, 1988 [Online]. Available: https://patents.google.com/patent/US4790922A/en?assignee=viracon&oq=viracon

[176] K. W. Hartig and P. J. Lingle, “High performance, durable, low-E glass,” US5344718A, Sep. 06, 1994 [Online]. Available: https://patents.google.com/patent/US5344718A/en

[177] C.-T. Chu, P. D. Fuqua, and J. D. Barrie, “Corrosion characterization of durable silver coatings by electrochemical impedance spectroscopy and accelerated environmental testing,” *Appl. Opt.*, vol. 45, no. 7, pp. 1583–1593, Mar. 2006, doi: 10.1364/AO.45.001583.

[178] X. Xu, B. Li, W. He, C. Wang, and M. Wei, “NiCrNx interlayer thickness dependence of spectral performance and environmental durability of protected-silver mirrors,” *Opt. Eng.*, vol. 57, no. 4, p. 045101, Apr. 2018, doi: 10.1117/1.OE.57.4.045101.

[179] A. Khan *et al.*, “Stability Enhancement of Silver Nanowire Networks with Conformal ZnO Coatings Deposited by Atmospheric Pressure Spatial Atomic Layer Deposition,” *ACS Appl. Mater. Interfaces*, vol. 10, no. 22, pp. 19208–19217, Jun. 2018, doi: 10.1021/acsami.8b03079.

[180] M. Fedel, C. Zanella, S. Rossi, and F. Deflorian, “Corrosion protection of silver coated reflectors by atomic layer deposited Al2O3,” *Sol. Energy*, vol. 101, pp. 167–175, Mar. 2014, doi: 10.1016/j.solener.2013.11.038.

[181] S. Aghazadehchors *et al.*, “Versatility of bilayer metal oxide coatings on silver nanowire networks for enhanced stability with minimal transparency loss,” *Nanoscale*, vol. 11, no. 42, pp. 19969–19979, Nov. 2019, doi: 10.1039/C9NR05658K.

[182] M. Higashino, S. Murai, and K. Tanaka, “Improving the Plasmonic Response of Silver Nanoparticle Arrays via Atomic Layer Deposition Coating and Annealing above the Melting Point,” *J. Phys. Chem. C*, Dec. 2020, doi: 10.1021/acs.jpcc.0c09112.

[183] Y.-P. Wang, X. Wu, W.-J. Liu, D. W. Zhang, and S.-J. Ding, “Plasma-Enhanced Atomic Layer Deposition of Low Resistivity and Ultrathin Manganese Oxynitride Films with Excellent Resistance to Copper Diffusion,” *ACS Appl. Electron. Mater.*, vol. 2, no. 6, pp. 1653–1660, Jun. 2020, doi: 10.1021/acsaelm.0c00224.

[184] J.-Y. Kwon, T.-S. Yoon, K.-B. Kim, and S.-H. Min, “Comparison of the agglomeration behavior of Au and Cu films sputter deposited on silicon dioxide,” *J. Appl. Phys.*, vol. 93, no. 6, pp. 3270–3278, Mar. 2003, doi: 10.1063/1.1556178.

[185] J. Y. Y. Loh and N. P. Kherani, “Silver diffusion effects in aluminum nitride/silver films on polydimethylsiloxane gratings via nitrogen–argon sputtering,” *J. Mater. Sci. Mater. Electron.*, vol. 31, no. 9, pp. 6861–6865, May 2020, doi: 10.1007/s10854-020-03246-5.

[186] S. Jena *et al.*, “Transfer matrix based reverse engineering approach to analyse annealing induced changes in optical transmission of TiO2/Ag/TiO2/Ag multilayer,” *Opt. Laser Technol.*, vol. 144, p. 107392, Dec. 2021, doi: 10.1016/j.optlastec.2021.107392.

[187] Y. Ye *et al.*, “Plasmonics of Diffused Silver Nanoparticles in Silver/Nitride Optical Thin Films,” *Sci. Rep.*, vol. 9, Dec. 2019, doi: 10.1038/s41598-019-56719-x.

[188] T. Wang and P. D. Bristowe, “Controlling Ag diffusion in ZnO by donor doping: A first principles study,” *Acta Mater.*, vol. 137, pp. 115–122, Sep. 2017, doi: 10.1016/j.actamat.2017.07.024.

[189] J.-T. Fonné, E. Burov, E. Gouillart, S. Grachev, H. Montigaud, and D. Vandembroucq, “Interdiffusion between silica thin films and soda-lime glass substrate during annealing at high temperature,” *J. Am. Ceram. Soc.*, Oct. 2018, doi: 10.1111/jace.16154.

[190] F. Maldonado and A. Stashans, “Al-doped ZnO: Electronic, electrical and structural properties,” *J. Phys. Chem. Solids*, vol. 71, no. 5, pp. 784–787, May 2010, doi: 10.1016/j.jpcs.2010.02.001.

[191] M. Xin, “Growth temperature on ZnO:Al thin films morphology and optical properties,” *Surf. Eng.*, vol. 0, no. 0, pp. 1–8, Sep. 2021, doi: 10.1080/02670844.2021.1976021.

[192] A. C. Aragonès, A. Palacios-Padrós, F. Caballero-Briones, and F. Sanz, “Study and improvement of aluminium doped ZnO thin films: Limits and advantages,” *Electrochimica Acta*, vol. 109, pp. 117–124, Oct. 2013, doi: 10.1016/j.electacta.2013.07.053.

[193] M. Zhu, H. Huang, J. Gong, C. Sun, and X. Jiang, “Role of oxygen desorption during vacuum annealing in the improvement of electrical properties of aluminum doped zinc oxide films synthesized by sol gel method,” *J. Appl. Phys.*, vol. 102, no. 4, p. 043106, Aug. 2007, doi: 10.1063/1.2772591.

[194] D. L. Williams and T. M. O’Bryon, “Chapter 5 - Cleanliness Verification on Large Surfaces: Instilling Confidence in Contact Angle Techniques,” in *Developments in Surface Contamination and Cleaning*, R. Kohli and K. L. Mittal, Eds., Oxford: William Andrew Publishing, 2013, pp. 163–181. doi: 10.1016/B978-1-4377-7879-3.00005-4.

[195] P. M. Martin, Ed., “Chapter 3 - Surface Preparation for Film and Coating Deposition Processes,” in *Handbook of Deposition Technologies for Films and Coatings (Third Edition)*, Boston: William Andrew Publishing, 2010, pp. 93–134. doi: 10.1016/B978-0-8155-2031-3.00003-X.

[196] G. Pintori and E. Cattaruzza, “XPS/ESCA on glass surfaces: A useful tool for ancient and modern materials,” *Opt. Mater. X*, vol. 13, p. 100108, Jan. 2022, doi: 10.1016/j.omx.2021.100108.

[197] M. Achintha, “5 - Sustainability of glass in construction,” in *Sustainability of Construction Materials (Second Edition)*, J. M. Khatib, Ed., in Woodhead Publishing Series in Civil and Structural Engineering. , Woodhead Publishing, 2016, pp. 79–104. doi: 10.1016/B978-0-08-100370-1.00005-6.

[198] N. Takamure, A. Kondyurin, and D. R. McKenzie, “Electric field assisted ion exchange of silver in soda-lime glass: A study of ion depletion layers and interactions with potassium,” *J. Appl. Phys.*, vol. 125, no. 17, p. 175104, May 2019, doi: 10.1063/1.5092545.

[199] J. Sheng, J. Li, and J. Yu, “The development of silver nanoclusters in ion-exchanged soda-lime silicate glasses,” *Int. J. Hydrog. Energy*, vol. 32, no. 13, pp. 2598–2601, Sep. 2007, doi: 10.1016/j.ijhydene.2006.11.009.

[200] W. Li, X. Yan, A. G. Aberle, and S. Venkataraj, “Effect of sodium diffusion on the properties of CIGS solar absorbers prepared using elemental Se in a two-step process,” *Sci. Rep.*, vol. 9, no. 1, p. 2637, Feb. 2019, doi: 10.1038/s41598-019-39283-2.

[201] S. Li *et al.*, “Unveiling Sodium Diffusion Kinetics and Locking Mechanisms for High-Performance CZTSSe Photovoltaics,” *Adv. Sci.*, vol. 12, no. 30, p. e04087, 2025, doi: 10.1002/advs.202504087.

[202] R. E. Hummel, R. T. DeHoff, S. Matts-Goho, and W. M. Goho, “Thermal grooving, thermotransport and electrotransport in doped and undoped thin gold films,” *Thin Solid Films*, vol. 78, no. 1, pp. 1–14, Mar. 1981, doi: 10.1016/0040-6090(81)90412-0.

[203] R. G. Gordon, “Criteria for Choosing Transparent Conductors,” *MRS Bull.*, vol. 25, no. 8, pp. 52–57, Aug. 2000, doi: 10.1557/mrs2000.151.

[204] H. Lage, J. Ferreira, and P. Pallotta, “Coated article with low-E coating having barrier layer system(s) including multiple dielectric layers, and/or methods of making the same,” US10125266B2, Nov. 13, 2018 [Online]. Available: https://patents.google.com/patent/US10125266B2/en

[205] O. Jbara, J. Cazaux, and P. Trebbia, “Sodium diffusion in glasses during electron irradiation,” *J. Appl. Phys.*, vol. 78, no. 2, pp. 868–875, Jul. 1995, doi: 10.1063/1.360277.

[206] O. Puglisi, G. Marletta, and A. Torrisi, “Radiation-enhanced diffusion of Na in alkaline glasses,” *J. Non-Cryst. Solids*, vol. 83, no. 3, pp. 344–352, Jul. 1986, doi: 10.1016/0022-3093(86)90247-4.

[207] A. Simo, J. Polte, N. Pfänder, U. Vainio, F. Emmerling, and K. Rademann, “Formation Mechanism of Silver Nanoparticles Stabilized in Glassy Matrices,” *J. Am. Chem. Soc.*, vol. 134, no. 45, pp. 18824–18833, Nov. 2012, doi: 10.1021/ja309034n.

[208] J. Kulczyk-Malecka *et al.*, “Investigation of silver diffusion in TiO2/Ag/TiO2 coatings,” *Acta Mater.*, vol. 66, pp. 396–404, Mar. 2014, doi: 10.1016/j.actamat.2013.11.030.

[209] M. Biesuz *et al.*, “Solid-State Field-Assisted Ion Exchange (Ag → Na) in Soda–Lime Float Glass: Tin Versus Air Side,” *Adv. Eng. Mater.*, p. 2201572, doi: 10.1002/adem.202201572.

[210] R. E. Hummel, S. Matts-Goho, and R. T. DeHoff, “New insights on the reversal of the site of electromigration failure in gold films doped with alkali,” *J. Appl. Phys.*, vol. 54, no. 5, pp. 2855–2856, May 1983, doi: 10.1063/1.332278.

[211] T. Prabhakar and N. Jampana, “Effect of sodium diffusion on the structural and electrical properties of Cu2ZnSnS4 thin films,” *Sol. Energy Mater. Sol. Cells*, vol. 95, no. 3, pp. 1001–1004, Mar. 2011, doi: 10.1016/j.solmat.2010.12.012.

[212] T. E. Graedel, “Corrosion Mechanisms for Silver Exposed to the Atmosphere,” *J. Electrochem. Soc.*, vol. 139, no. 7, pp. 1963–1970, Jan. 1992, doi: 10.1149/1.2221162.

[213] M. L. Zheludkevich, A. G. Gusakov, A. G. Voropaev, A. A. Vecher, E. N. Kozyrski, and S. A. Raspopov, "Oxidation of Silver by Atomic Oxygen," *Oxid. Met.*, vol. 61, no. 1, pp. 39–48, Feb. 2004, doi: 10.1023/B:OXID.0000016275.96500.24.

[214] A. J. Birnbaum, C. V. Thompson, J. C. Steuben, A. P. Iliopoulos, and J. G. Michopoulos, "Oxygen-induced giant grain growth in Ag films," *Appl. Phys. Lett.*, vol. 111, no. 16, p. 163107, Oct. 2017, doi: 10.1063/1.4998741.

[215] L. Zhu, H. Xu, Y. Nan, J. Zhu, and D. Cheng, "Facet-dependent diffusion of atomic oxygen on Ag surfaces," *Comput. Mater. Sci.*, vol. 155, pp. 17–27, Dec. 2018, doi: 10.1016/j.commatsci.2018.08.032.

[216] A. V. Druzhinin *et al.*, "Thermally-induced microstructure evolution of Ag/AlN nano-multilayers: The role of annealing atmosphere on the Ag outflow driving force," *Surf. Coat. Technol.*, vol. 471, p. 129880, Oct. 2023, doi: 10.1016/j.surfcoat.2023.129880.

[217] M. Boccas, T. Vucina, C. Araya, E. Vera, and C. Ahhee, "Coating the 8-m Gemini telescopes with protected silver," presented at the SPIE Astronomical Telescopes + Instrumentation, E. Atad-Ettedgui and P. Dierickx, Eds., USA, Sep. 2004, p. 239. doi: 10.1117/12.548809.

[218] H. Ohara, M. Kawamura, Y. Abe, and T. Kiba, "Surface morphology of silver thin films exposed to water vapour and/or oxygen in vacuum," *Trans. IMF*, vol. 100, no. 4, pp. 208–212, Jul. 2022, doi: 10.1080/00202967.2022.2062922.

[219] M. Theelen, C. Hagedoorn, M. Götz-Köhler, A. Weeber, and N. Neugebohrn, "Damp heat induced degradation mechanisms occurring in coloured oxide/metal/oxide films for thin-film solar cells," *Thin Solid Films*, vol. 730, p. 138711, Jul. 2021, doi: 10.1016/j.tsf.2021.138711.

[220] E. Ando and M. Miyazaki, "Moisture resistance of the low-emissivity coatings with a layer structure of Al-doped ZnO/Ag/Al-doped ZnO," *Thin Solid Films*, vol. 392, no. 2, pp. 289–293, Jul. 2001, doi: 10.1016/S0040-6090(01)01045-8.

[221] H. S. Park and D. E. Day, "Corrosion of evaporated Ag films on glass by saturated water vapor," *Sol. Energy Mater.*, vol. 13, no. 5, pp. 351–365, Jun. 1986, doi: 10.1016/0165-1633(86)90083-3.

[222] F. Daume *et al.*, "Damp Heat Treatment of Cu(In,Ga)Se2 Solar Cells with Different Sodium Content," *Materials*, vol. 6, no. 12, pp. 5478–5489, Nov. 2013, doi: 10.3390/ma6125478.

[223] W. M. Sears and D. A. Love, "Rapid migration of silver on roughened glass surfaces in a methanol/air mixture near 500 °C," *J. Appl. Phys.*, vol. 77, no. 6, pp. 2407–2414, Mar. 1995, doi: 10.1063/1.358766.

[224] Y. Hayashi, K. Matsumoto, and M. Kudo, "The diffusion mechanism of tin into glass governed by redox reactions during the float process," *J. Non-Cryst. Solids*, vol. 282, no. 2, pp. 188–196, Apr. 2001, doi: 10.1016/S0022-3093(01)00319-2.

[225] N. Tadokoro *et al.*, "Investigation of shrinkage and cracking of ophthalmic lens coating by a cycle test of UV radiation and high humidity," *Thin Solid Films*, vol. 520, no. 12, pp. 4169–4173, Apr. 2012, doi: 10.1016/j.tsf.2011.04.097.

[226] E. H. Hirsch, "Stress in porous thin films through absorption of polar molecules (and relevance to optical coatings)," *J. Phys. Appl. Phys.*, vol. 13, no. 11, pp. 2081–2094, Nov. 1980, doi: 10.1088/0022-3727/13/11/018.

[227] G.-S. Liu *et al.*, “Self-assembled monolayer modulated Plateau-Rayleigh instability and enhanced chemical stability of silver nanowire for invisibly patterned, stable transparent electrodes,” *Nano Res.*, Jan. 2022, doi: 10.1007/s12274-021-4042-3.

[228] D. Jung, S. Hwang, H.-J. Kim, S. Yun, J.-H. Han, and H.-N. Lee, “Environment-controlled agglomeration in nanoporous Ag films with ultrathin silicon oxide,” *Thin Solid Films*, vol. 821, p. 140683, Jul. 2025, doi: 10.1016/j.tsf.2025.140683.

[229] Y. Ueshima *et al.*, “Morphological Stability Limits of Ag–Cu–Al Nanocrystalline Thin Films Prepared via Reactive Sputtering in Ar–O2 Mixed Gas,” *Metall. Mater. Trans. A*, vol. 55, no. 9, pp. 3235–3248, Sep. 2024, doi: 10.1007/s11661-024-07462-0.

[230] A. S. Baburin *et al.*, “Epitaxial Silver Films Morphology and Optical Properties Evolution over Two Years,” *Coatings*, vol. 10, no. 10, Art. no. 10, Oct. 2020, doi: 10.3390/coatings10100911.

[231] Y. Liu, W. Zhang, Y. Sun, and W. Liang, “Diffusion behavior of Ag in TiO2 nanofilms,” *Mater. Res. Bull.*, vol. 98, pp. 240–249, Feb. 2018, doi: 10.1016/j.materresbull.2017.10.027.

[232] D. J. Ramesh *et al.*, “Comparative oxidation behavior of columnar and equiaxed Cr2AlC coatings,” *Corros. Sci.*, vol. 253, p. 112992, Aug. 2025, doi: 10.1016/j.corsci.2025.112992.

[233] R. Meszaros, B. Merle, M. Wild, K. Durst, M. Göken, and L. Wondraczek, “Effect of thermal annealing on the mechanical properties of low-emissivity physical vapor deposited multilayer-coatings for architectural applications,” *Thin Solid Films*, vol. 520, no. 24, pp. 7130–7135, Oct. 2012, doi: 10.1016/j.tsf.2012.07.086.

[234] T. Chommaux, P. Godard, D. Thiaudière, and P. O. Renault, “Impact of the brittle layers on the electrical and mechanical behaviours of 18 nm Ag layers in indium tin oxide-silver stackings,” *Thin Solid Films*, vol. 826, p. 140765, Sep. 2025, doi: 10.1016/j.tsf.2025.140765.

[235] C. Yuanru *et al.*, “Protective behaviour against high temperature oxidation of silicon nitride films synthesized by ion-beam-assisted deposition,” *Surf. Coat. Technol.*, vol. 51, no. 1, pp. 227–231, Apr. 1992, doi: 10.1016/0257-8972(92)90243-4.

[236] J. Kulczyk-Malecka, P. J. Kelly, G. West, C. G.c.b., and J. A. Ridealgh, “Diffusion studies in magnetron sputter deposited silicon nitride films,” *Surf. Coat. Technol.*, vol. 255, pp. 37–42, Sep. 2014, doi: 10.1016/j.surfcoat.2013.11.027.

[237] M. Vila, D. Cáceres, and C. Prieto, “Mechanical properties of sputtered silicon nitride thin films,” *J. Appl. Phys.*, vol. 94, no. 12, pp. 7868–7873, Dec. 2003, doi: 10.1063/1.1626799.

[238] J. Kulczyk-Malecka, P. J. Kelly, G. West, G. C. B. Clarke, and J. A. Ridealgh, “Investigations of diffusion behaviour in Al-doped zinc oxide and zinc stannate coatings,” *Thin Solid Films*, vol. 520, no. 5, pp. 1368–1374, Dec. 2011, doi: 10.1016/j.tsf.2011.08.076.

[239] D. M. Holzapfel *et al.*, “Enhanced thermal stability of (Ti,Al)N coatings by oxygen incorporation,” *Acta Mater.*, vol. 218, p. 117204, Oct. 2021, doi: 10.1016/j.actamat.2021.117204.

[240] Y. Wei *et al.*, “Enhanced Thermal Stability of Elevated-Metal Metal-Oxide Thin-Film Transistors via Low-Temperature Nitrogen Post-Annealing,” *IEEE Trans. Electron Devices*, vol. 68, no. 4, pp. 1649–1653, Apr. 2021, doi: 10.1109/TED.2021.3056635.

[241] J. Jang, N. S. Parmar, W.-K. Choi, and J.-W. Choi, “Rapid Defrost Transparent Thin-Film Heater with Flexibility and Chemical Stability,” *ACS Appl. Mater. Interfaces*, vol. 12, no. 34, pp. 38406–38414, Aug. 2020, doi: 10.1021/acsami.0c10852.

[242] D. Walter and J. Houghton, “The roughness parameters of glass films,” *Vacuum*, vol. 27, no. 1, pp. 7–10, Jan. 1977, doi: 10.1016/S0042-207X(77)80281-9.

[243] ASTM International, “Standard Test Method for Haze and Luminous Transmittance of Transparent Plastics,” *Book of standards*, vol. 08.01, doi: 10.1520/D1003-21.

[244] N. W. Ashcroft and N. D. Mermin, *Solid State Physics*. Holt, Rinehart and Winston, 1976.

[245] S. A. Maier, *Plasmonics: Fundamentals and Applications*. Springer Science & Business Media, 2007.

[246] J. N. Hilfiker *et al.*, “Survey of methods to characterize thin absorbing films with Spectroscopic Ellipsometry,” *Thin Solid Films*, vol. 516, no. 22, pp. 7979–7989, Sep. 2008, doi: 10.1016/j.tsf.2008.04.060.

[247] H. Arwin and D. E. Aspnes, “Unambiguous determination of thickness and dielectric function of thin films by spectroscopic ellipsometry,” *Thin Solid Films*, vol. 113, no. 2, pp. 101–113, Mar. 1984, doi: 10.1016/0040-6090(84)90019-1.

[248] D.-M. Smilgies, “Scherrer grain-size analysis adapted to grazing-incidence scattering with area detectors,” *J. Appl. Crystallogr.*, vol. 42, no. 6, pp. 1030–1034, Dec. 2009, doi: 10.1107/S0021889809040126.

[249] D. E. Newbury, “Mistakes encountered during automatic peak identification of minor and trace constituents in electron-excited energy dispersive X-ray microanalysis,” *Scanning*, vol. 31, no. 3, pp. 91–101, 2009, doi: 10.1002/sca.20151.

[250] A. Miotello and P. Mazzoldi, “Numerical analysis of field-assisted sodium migration in electron-irradiated glasses,” *J. Phys. C Solid State Phys.*, vol. 15, no. 27, p. 5615, Sep. 1982, doi: 10.1088/0022-3719/15/27/017.

[251] Y.-B. Park, S. Lee, M. Tobah, T. Ma, and L. J. Guo, “Optimized optical/electrical/mechanical properties of ultrathin metal films for flexible transparent conductor applications: review [Invited],” *Opt. Mater. Express*, vol. 13, no. 2, pp. 304–347, Feb. 2023, doi: 10.1364/OME.473277.

[252] K. A. Folgner, K. J. Nelms, C.-T. Chu, D. R. Alaan, C. J. Panetta, and J. D. Barrie, “Effects of stress, defects, and layer composition on the development of corrosion features on protected silver mirrors,” *Appl. Opt.*, vol. 62, no. 7, pp. B222–B230, Mar. 2023, doi: 10.1364/AO.477232.

[253] J. Wurm, S. T. Fujisawa-Phillips, and I. L. Rasskazov, “Optimal design of low-emissivity coatings,” *Sol. Energy Mater. Sol. Cells*, vol. 280, p. 113267, Jan. 2025, doi: 10.1016/j.solmat.2024.113267.

[254] A. V. Druzhinin, J. Janczak-Rusch, and C. Cancellieri, “Ag Surface Outflow Kinetics in Ag/AlN Nanomultilayers,” *Phys. Status Solidi A*, vol. 221, no. 7, p. 2300876, 2024, doi: 10.1002/pssa.202300876.

[255] S. Schwinde *et al.*, “Protected silver coatings for reflectors,” *CEAS Space J.*, vol. 11, no. 4, pp. 579–587, Dec. 2019, doi: 10.1007/s12567-019-00257-9.

[256] J. Huang, X. Yu, P. W. Shum, Z. Zhou, and Y. Ma, “Influence of ALD-Al2O3 film on anti-scratch and anti-tarnish of silver,” *Surf. Eng.*, vol. 0, no. 0, pp. 1–7, Jun. 2020, doi: 10.1080/02670844.2020.1773148.

[257] Y. Yan *et al.*, “SiO2 as barrier layer for Na out-diffusion from soda-lime glass,” in *2010 35th IEEE Photovoltaic Specialists Conference*, Jun. 2010, pp. 002519–002521. doi: 10.1109/PVSC.2010.5614657.

[258] O. Akyildiz and T. O. Ogurtani, “Thermal Grooving by Surface Diffusion: a Review of Classical Thermo-Kinetics Approach,” *Hittite J. Sci. Eng.*, vol. 4, no. 1, Art. no. 1, Jun. 2017, doi: 10.17350/HJSE19030000042.

[259] F. Boccardo, F. Rovaris, A. Tripathi, F. Montalenti, and O. Pierre-Louis, “Stress-Induced Acceleration and Ordering in Solid-State Dewetting,” *Phys. Rev. Lett.*, vol. 128, no. 2, p. 026101, Jan. 2022, doi: 10.1103/PhysRevLett.128.026101.

[260] L. Romano Brandt, E. Salvati, D. Wermeille, C. Papadaki, E. Le Bourhis, and A. M. Korsunsky, “Stress-Assisted Thermal Diffusion Barrier Breakdown in Ion Beam Deposited Cu/W Nano-Multilayers on Si Substrate Observed by in Situ GISAXS and Transmission EDX,” *ACS Appl. Mater. Interfaces*, vol. 13, no. 5, pp. 6795–6804, Feb. 2021, doi: 10.1021/acsami.0c19173.

[261] F. S. Rocha *et al.*, “Enhanced heavy oil fouling resistance of cobalt-based spray-deposited coatings by alloy design and heat treatment,” *Surf. Coat. Technol.*, vol. 495, p. 131528, Jan. 2025, doi: 10.1016/j.surfcoat.2024.131528.

[262] “peak_widths — SciPy v1.16.2 Manual,” SciPy. [Online]. Available: https://docs.scipy.org/doc/scipy/reference/generated/scipy.signal.peak_widths.html

[263] J. Chen *et al.*, “Ultrathin Aluminum Oxide Films Induced by Rapid Thermal Annealing for Effective Silicon Surface Passivation,” *Phys. Status Solidi RRL – Rapid Res. Lett.*, vol. 15, no. 10, p. 2100267, 2021, doi: 10.1002/pssr.202100267.

[264] L. Helmich, D. C. Walter, D. Bredemeier, and J. Schmidt, “Atomic-Layer-Deposited Al2O3 as Effective Barrier against the Diffusion of Hydrogen from SiNx:H Layers into Crystalline Silicon during Rapid Thermal Annealing,” *Phys. Status Solidi RRL – Rapid Res. Lett.*, vol. 14, no. 12, p. 2000367, 2020, doi: 10.1002/pssr.202000367.

[265] G. von Gastrow *et al.*, “Quantification of Sodium-Ion Migration in Silicon Nitride by Flatband-Potential Monitoring at Device-Operating Temperatures,” *Phys. Status Solidi A*, vol. 217, no. 16, p. 2000212, 2020, doi: 10.1002/pssa.202000212.

[266] B. Sun *et al.*, “Enhanced thermal stability of Mo film with low infrared emissivity by a TiN barrier layer,” *Appl. Surf. Sci.*, vol. 571, p. 151368, Jan. 2022, doi: 10.1016/j.apsusc.2021.151368.

[267] Ph. V. Kiryukhantsev-Korneev *et al.*, “Studying the Diffusion-barrier Properties, Thermal Stability and Oxidation Resistance of TiAlSiCN, TiAlSiCN/AlOx, and TiAlSiCN/SiBCN Coatings,” *Prot. Met. Phys. Chem. Surf.*, vol. 57, no. 5, pp. 1008–1024, Sep. 2021, doi: 10.1134/S2070205121050130.

[268] C. Cancellieri *et al.*, "Interface and layer periodicity effects on the thermal conductivity of copper-based nanomultilayers with tungsten, tantalum, and tantalum nitride diffusion barriers," *J. Appl. Phys.*, vol. 128, no. 19, p. 195302, Nov. 2020, doi: 10.1063/5.0019907.

[269] K. Hartig and A. Krisko, "Haze-resistant transparent film stacks," US Patent application 2002/0102352 A1, Aug. 01, 2002

[270] E. Bus, J. T. Miller, and J. A. van Bokhoven, "Hydrogen Chemisorption on Al2O3-Supported Gold Catalysts," *J. Phys. Chem. B*, vol. 109, no. 30, pp. 14581–14587, Aug. 2005, doi: 10.1021/jp051660z.

[271] E. Babich, D. Raskhodchikov, A. Redkov, A. Hmima, A. Nashchekin, and A. Lipovskii, "Dendritic structures by glass electrolysis: Studies and SERS capability," *Curr. Appl. Phys.*, vol. 24, pp. 54–59, Apr. 2021, doi: 10.1016/j.cap.2021.02.002.

[272] A. A. Wereszczak *et al.*, "Strength and Contact Damage Responses in a Soda-Lime-Silicate and a Borosilicate Glass," Oak Ridge National Lab TN, ADA481685, 2006. [Online]. Available: https://apps.dtic.mil/sti/citations/tr/ADA481685

[273] S. J. Bull, "Failure mode maps in the thin film scratch adhesion test," *Tribol. Int.*, vol. 30, no. 7, pp. 491–498, Jul. 1997, doi: 10.1016/S0301-679X(97)00012-1.

[274] S. J. Oldenburg, "Light scattering from gold nanoshells," Rice University, 2000. [Online]. Available: https://hdl.handle.net/1911/19543

[275] H. Jaeger, P. D. Mercer, and R. G. Sherwood, "The effect of exposure to air on silver and gold films deposited in ultra-high vacuum," *Surf. Sci.*, vol. 13, no. 2, pp. 349–360, Feb. 1969, doi: 10.1016/0039-6028(69)90196-4.

[276] L. W. Yang, C. R. Mayer, N. Chawla, J. LLorca, and J. M. Molina-Aldareguía, "Nanomechanical characterization of the fracture toughness of Al/SiC nanolaminates," *Extreme Mech. Lett.*, vol. 40, p. 100945, Oct. 2020, doi: 10.1016/j.eml.2020.100945.

[277] D. Rats, D. Poitras, J. M. Soro, L. Martinu, and J. von Stebut, "Mechanical properties of plasma-deposited silicon-based inhomogeneous optical coatings," *Surf. Coat. Technol.*, vol. 111, no. 2, pp. 220–228, Jan. 1999, doi: 10.1016/S0257-8972(98)00812-3.

[278] P. Rumsby, B. Baloukas, O. Zabeida, and L. Martinu, "Enhanced Durability and Antireflective Performance of Ag-Based Transparent Conductors Achieved via Controlled N-Doping," *ACS Appl. Mater. Interfaces*, vol. 16, no. 18, pp. 24039–24051, Apr. 2024, doi: 10.1021/acsami.4c02255.

[279] Z. Xue *et al.*, "High-Performance NiO/Ag/NiO Transparent Electrodes for Flexible Organic Photovoltaic Cells," *ACS Appl. Mater. Interfaces*, vol. 6, no. 18, pp. 16403–16408, Sep. 2014, doi: 10.1021/am504806k.

[280] A. K. Akhmedov, A. K. Abduev, V. M. Kanevsky, A. E. Muslimov, and A. S. Asvarov, "Low-Temperature Fabrication of High-Performance and Stable GZO/Ag/GZO Multilayer Structures for Transparent Electrode Applications," *Coatings*, vol. 10, no. 3, Art. no. 3, Mar. 2020, doi: 10.3390/coatings10030269.

[281] M. Ekmekcioglu *et al.*, "High transparent, low surface resistance ZTO/Ag/ZTO multilayer thin film electrodes on glass and polymer substrates," *Vacuum*, vol. 187, p. 110100, May 2021, doi: 10.1016/j.vacuum.2021.110100.

[282] S. Yu, X. Liu, M. Wu, H. Dong, X. Wang, and L. Li, "All-Solution-Processed Molybdenum Oxide-Encapsulated Silver Nanowire Flexible Transparent Conductors with Improved Conductivity and Adhesion," *ACS Appl. Mater. Interfaces*, vol. 13, no. 12, pp. 14470–14478, Mar. 2021, doi: 10.1021/acsami.0c22324.

[283] X. He, Q. Cao, J. Pan, L. Yang, and S. He, "Patterned few nanometer-thick silver films with high optical transparency and high electrical conductivity," *RSC Adv.*, vol. 11, no. 19, pp. 11481–11489, 2021, doi: 10.1039/D1RA00549A.

[284] H.-J. Lee *et al.*, "Optical and Electrical Properties of Multilayer Grid Electrodes for Highly Durable Transparent Conductive Electrodes," *Int. J. Precis. Eng. Manuf.-Green Technol.*, vol. 8, no. 2, pp. 501–508, Mar. 2021, doi: 10.1007/s40684-020-00205-7.

[285] Y. Sung *et al.*, "Anti-reflective coating with a conductive indium tin oxide layer on flexible glass substrates," *Appl. Opt.*, vol. 57, no. 9, pp. 2202–2207, Mar. 2018, doi: 10.1364/AO.57.002202.

[286] K. Choi, J. Jung, J. Kim, J. Lee, H. S. Lee, and I.-S. Kang, "Antireflective Transparent Conductive Oxide Film Based on a Tapered Porous Nanostructure," *Micromachines*, vol. 11, no. 2, Art. no. 2, Feb. 2020, doi: 10.3390/mi11020206.

[287] C. Garlisi *et al.*, "Multilayer thin film structures for multifunctional glass: Self-cleaning, antireflective and energy-saving properties," *Appl. Energy*, vol. 264, p. 114697, Apr. 2020, doi: 10.1016/j.apenergy.2020.114697.

[288] M. Keshavarz Hedayati and M. Elbahri, "Antireflective Coatings: Conventional Stacking Layers and Ultrathin Plasmonic Metasurfaces, A Mini-Review," *Materials*, vol. 9, no. 6, Art. no. 6, Jun. 2016, doi: 10.3390/ma9060497.

[289] J. E. Greene, "Chapter 13 - Nucleation, Film Growth, and Microstructural Evolution," in *Handbook of Deposition Technologies for Films and Coatings*, 2nd ed., R. F. Bunshah, Ed., Boston: William Andrew Publishing, 1994, pp. 707–765. doi: 10.1016/B978-0-8155-2031-3.00012-0.

[290] L. Vitos, A. V. Ruban, H. L. Skriver, and J. Kollár, "The surface energy of metals," *Surf. Sci.*, vol. 411, no. 1, pp. 186–202, Aug. 1998, doi: 10.1016/S0039-6028(98)00363-X.

[291] P. J. Ries, "Silver thin films : improving the efficiency of low-E coatings by employing different seed layers," Ph.D., RWTH Aachen University, Aachen, Germany, 2015.

[292] W. Wang *et al.*, "Transparent Ultrathin Oxygen-Doped Silver Electrodes for Flexible Organic Solar Cells," *Adv. Funct. Mater.*, vol. 24, no. 11, pp. 1551–1561, Mar. 2014, doi: 10.1002/adfm.201301359.

[293] X. Wang, H. Shen, K. Gao, Q. Zhao, and C. Du, "The effect of Cu doping into Ag in ZnO/Ag/ZnO/SiO2 on reduction of the thermal effect of solar cells," *Appl. Phys. A*, vol. 128, no. 3, p. 181, Feb. 2022, doi: 10.1007/s00339-022-05319-0.

[294] G. Kim, J. W. Lim, J. Lee, and S. J. Heo, "Flexible multilayered transparent electrodes with less than 50 nm thickness using nitrogen-doped silver layers for flexible heaters," *Mater. Res. Bull.*, vol. 149, p. 111703, May 2022, doi: 10.1016/j.materresbull.2021.111703.

[295] H. M. Lemire, K. A. Peterson, S. Sprawls, K. Singer, I. T. Martin, and R. H. French, "Degradation of transparent conductive oxides: mechanistic insights across configurations and exposures," vol. 8825, p. 882502, Sep. 2013, doi: 10.1117/12.2024691.

[296] H.-G. Im *et al.*, "Flexible Transparent Crystalline-ITO/Ag Nanowire Hybrid Electrode with High Stability for Organic Optoelectronics," *ACS Appl. Mater. Interfaces*, vol. 12, no. 50, pp. 56462–56469, Dec. 2020, doi: 10.1021/acsami.0c17130.

[297] A. C. Phillips *et al.*, "Progress and new techniques for protected-silver coatings," in *Advances in Optical and Mechanical Technologies for Telescopes and Instrumentation*, International Society for Optics and Photonics, Jul. 2014, p. 91511B. doi: 10.1117/12.2055706.

[298] A. C. Phillips *et al.*, "Update on UCO's advanced coating lab development of silver-based mirror coatings," in *Advances in Optical and Mechanical Technologies for Telescopes and Instrumentation II*, International Society for Optics and Photonics, Aug. 2016, p. 99122G. doi: 10.1117/12.2233009.

[299] A. Behrendt *et al.*, "Highly Robust Transparent and Conductive Gas Diffusion Barriers Based on Tin Oxide," *Adv. Mater.*, vol. 27, no. 39, pp. 5961–5967, 2015, doi: 10.1002/adma.201502973.

[300] K. A. Folgner, "Towards Understanding the Environmental Durability and Corrosion Behavior of Protected Silver Mirrors," Ph.D., University of California, Los Angeles, United States -- California, 2019. Accessed: Apr. 07, 2020. [Online]. Available: https://search.proquest.com/docview/2323127621/abstract/9F4351EF0F94996PQ/1

[301] J. D. Wolfe, R. E. Laird, C. K. Carniglia, J. P. Lehan, and O. S. of America, "Durable silver-based antireflection coatings and enhanced mirrors," in *Optical interference coatings: summaries of the papers presented at the topical meeting: June 5-9, 1995, Tuscon, Arizona*, Postconference ed., in 1995 technical digest series, no. v. 17. , Washington, DC: Optical Society of America, 1995, pp. 115–117.

[302] Y. Zhang *et al.*, "Low-Temperature Oxide/Metal/Oxide Multilayer Films as Highly Transparent Conductive Electrodes for Optoelectronic Devices," *ACS Appl. Energy Mater.*, vol. 4, no. 7, pp. 6553–6561, Jul. 2021, doi: 10.1021/acsaem.1c00586.

[303] X. Yang, P. Gao, Z. Yang, J. Zhu, F. Huang, and J. Ye, "Optimizing ultrathin Ag films for high performance oxide-metal-oxide flexible transparent electrodes through surface energy modulation and template-stripping procedures," *Sci. Rep.*, vol. 7, no. 1, Art. no. 1, Mar. 2017, doi: 10.1038/srep44576.

[304] A. Kumar, S. Rani, and D. Sundar Ghosh, "Thermally stable indium-free transparent electrode using ultrathin Ag film," *Mater. Today Proc.*, vol. 66, pp. 3265–3268, Jan. 2022, doi: 10.1016/j.matpr.2022.06.312.

[305] S. Larouche and L. Martinu, "OpenFilters: open-source software for the design, optimization, and synthesis of optical filters," *Appl. Opt.*, vol. 47, no. 13, pp. C219–C230, May 2008, doi: 10.1364/AO.47.00C219.

[306] M. Caron, O. Zabeida, J. E. Klemberg-Sapieha, and L. Martinu, "Stability and performance of organic-inorganic thin films on polymer substrates," *Surf. Coat. Technol.*, vol. 314, pp. 131–138, Mar. 2017, doi: 10.1016/j.surfcoat.2016.10.069.

[307] R. A. Synowicki, “Suppression of backside reflections from transparent substrates,” *Phys. Status Solidi C*, vol. 5, no. 5, pp. 1085–1088, May 2008, doi: 10.1002/pssc.200777873.

[308] P. da S. Erica *et al.*, “Al-Doping Effect on the Surface Morphology of ZnO Films Grown by Reactive RF Magnetron Sputtering,” *Mater. Sci. Appl.*, vol. 2013, Dec. 2013, doi: 10.4236/msa.2013.412096.

[309] C.-A. Tseng, J.-C. Lin, Y.-F. Chang, S.-D. Chyou, and K.-C. Peng, “Microstructure and characterization of Al-doped ZnO films prepared by RF power sputtering on Al and ZnO targets,” *Appl. Surf. Sci.*, vol. 258, no. 16, pp. 5996–6002, Jun. 2012, doi: 10.1016/j.apsusc.2012.02.061.

[310] Y. C. Han, M. S. Lim, J. H. Park, and K. C. Choi, “ITO-free flexible organic light-emitting diode using ZnS/Ag/MoO3 anode incorporating a quasi-perfect Ag thin film,” *Org. Electron.*, vol. 14, no. 12, pp. 3437–3443, Dec. 2013, doi: 10.1016/j.orgel.2013.09.014.

[311] D. S. Ghosh *et al.*, “Highly Flexible Transparent Electrodes Containing Ultrathin Silver for Efficient Polymer Solar Cells,” *Adv. Funct. Mater.*, vol. 25, no. 47, pp. 7309–7316, 2015, doi: 10.1002/adfm.201503739.

[312] H. Kang, S. Jung, S. Jeong, G. Kim, and K. Lee, “Polymer-metal hybrid transparent electrodes for flexible electronics,” *Nat. Commun.*, vol. 6, no. 1, Art. no. 1, Mar. 2015, doi: 10.1038/ncomms7503.

[313] J. Fahlteich, M. Fahland, W. Schönberger, and N. Schiller, “Permeation barrier properties of thin oxide films on flexible polymer substrates,” *Thin Solid Films*, vol. 517, no. 10, pp. 3075–3080, Mar. 2009, doi: 10.1016/j.tsf.2008.11.089.

[314] Y. Hu *et al.*, “Understanding the Preferred Crystal Orientation of Sputtered Silver in Ar/N2 Atmosphere: A Microstructure Investigation,” *Adv. Mater. Sci. Eng.*, vol. 2019, p. e3079393, 2019, doi: https://doi.org/10.1155/2019/3079393.

[315] M. Arbab, “The base layer effect on the d.c. conductivity and structure of direct current magnetron sputtered thin films of silver,” *Thin Solid Films*, vol. 381, no. 1, pp. 15–21, Jan. 2001, doi: 10.1016/S0040-6090(00)01341-9.

[316] Z. Chen, B. Cotterell, W. Wang, E. Guenther, and S.-J. Chua, “A mechanical assessment of flexible optoelectronic devices,” *Thin Solid Films*, vol. 394, no. 1, pp. 201–205, Aug. 2001, doi: 10.1016/S0040-6090(01)01138-5.

[317] M. Nisha, S. Anusha, A. Antony, R. Manoj, and M. K. Jayaraj, “Effect of substrate temperature on the growth of ITO thin films,” *Appl. Surf. Sci.*, vol. 252, no. 5, pp. 1430–1435, Dec. 2005, doi: 10.1016/j.apsusc.2005.02.115.

[318] Q.-D. Nguyen and C.-G. Choi, “Recent advances in multifunctional electromagnetic interference shielding materials,” *Heliyon*, vol. 10, no. 10, p. e31118, May 2024, doi: 10.1016/j.heliyon.2024.e31118.

[319] S. V. Nedelin *et al.*, “Ion Etching as a Method to Optimize the Optoelectric Parameters of Transparent Conductive Structures In2O3/Ag/In2O3,” *Bull. Russ. Acad. Sci. Phys.*, vol. 88, no. 2, pp. S192–S196, Dec. 2024, doi: 10.1134/S1062873824709000.

[320] D. Gall, “Electron mean free path in elemental metals,” *J. Appl. Phys.*, vol. 119, no. 8, p. 085101, Feb. 2016, doi: 10.1063/1.4942216.

[321] G. Rietveld *et al.*, "DC conductivity measurements in the Van der Pauw geometry," *IEEE Trans. Instrum. Meas.*, vol. 52, no. 2, pp. 449–453, Apr. 2003, doi: 10.1109/TIM.2003.809917.

[322] J. J. Colin *et al.*, "A load-lock compatible system for in situ electrical resistivity measurements during thin film growth," *Rev. Sci. Instrum.*, vol. 87, no. 2, p. 023902, Feb. 2016, doi: 10.1063/1.4940933.

[323] R. Koch, "The intrinsic stress of polycrystalline and epitaxial thin metal films," *J. Phys. Condens. Matter*, vol. 6, no. 45, p. 9519, Nov. 1994, doi: 10.1088/0953-8984/6/45/005.

[324] J. Leib, R. Mönig, and C. V. Thompson, "Direct Evidence for Effects of Grain Structure on Reversible Compressive Deposition Stresses in Polycrystalline Gold Films," *Phys. Rev. Lett.*, vol. 102, no. 25, p. 256101, Jun. 2009, doi: 10.1103/PhysRevLett.102.256101.

[325] N. Laegreid and G. K. Wehner, "Sputtering Yields of Metals for Ar+ and Ne+ Ions with Energies from 50 to 600 ev," *J. Appl. Phys.*, vol. 32, no. 3, pp. 365–369, Mar. 1961, doi: 10.1063/1.1736012.

[326] Kh. I. Grais, A. A. Shaltout, S. S. Ali, R. M. Boutros, K. M. El-behery, and Z. A. El-Sayed, "A new formula for sputtering yield as function of ion energies at normal incidence," *Phys. B Condens. Matter*, vol. 405, no. 7, pp. 1775–1781, Apr. 2010, doi: 10.1016/j.physb.2010.01.038.

[327] W. K. Rilling, C. M. Gilmore, T. D. Andreadis, and J. A. Sprague, "An embedded-atom-method study of diffusion of an Ag adatom on (111) Ag," *Can. J. Phys.*, vol. 68, no. 9, pp. 1035–1040, Sep. 1990, doi: 10.1139/p90-146.

[328] A. Hallil, O. Zabeida, M. R. Wertheimer, and L. Martinu, "Mass-resolved ion energy distributions in continuous dual mode microwave/radio frequency plasmas in argon and nitrogen," *J. Vac. Sci. Technol. A*, vol. 18, no. 3, pp. 882–890, May 2000, doi: 10.1116/1.582271.

[329] C. Loka and K.-S. Lee, "Preparation of TiO2/Ag/TiO2 (TAT) multilayer films with optical and electrical properties enhanced by using Cr-added Ag film," *Appl. Surf. Sci.*, vol. 415, pp. 35–42, Sep. 2017, doi: 10.1016/j.apsusc.2016.11.082.

[330] U. K. Chettiar, P. Nyga, M. D. Thoreson, A. V. Kildishev, V. P. Drachev, and V. M. Shalaev, "FDTD modeling of realistic semicontinuous metal films," *Appl. Phys. B*, vol. 100, no. 1, pp. 159–168, Jul. 2010, doi: 10.1007/s00340-010-3985-y.

[331] A. Kossoy, V. Merk, D. Simakov, K. Leosson, S. Kéna-Cohen, and S. A. Maier, "Optical and Structural Properties of Ultra-thin Gold Films," *Adv. Opt. Mater.*, vol. 3, no. 1, pp. 71–77, 2015, doi: 10.1002/adom.201400345.

[332] S. A. Maier and H. A. Atwater, "Plasmonics: Localization and guiding of electromagnetic energy in metal/dielectric structures," *J. Appl. Phys.*, vol. 98, no. 1, p. 011101, Jul. 2005, doi: 10.1063/1.1951057.

[333] F. Mao, G. L. Ngo, C. T. Nguyen, I. Ledoux-Rak, and N. D. Lai, "Direct fabrication and characterization of gold nanohole arrays," *Opt. Express*, vol. 29, no. 19, pp. 29841–29856, Sep. 2021, doi: 10.1364/OE.437510.

[334] E. S. H. Kang, H. Ekinge, and M. P. Jonsson, "Plasmonic fanoholes: on the gradual transition from suppressed to enhanced optical transmission through nanohole arrays in metal films of

increasing film thickness," *Opt. Mater. Express*, vol. 9, no. 3, pp. 1404–1415, Mar. 2019, doi: 10.1364/OME.9.001404.

[335] M. Schwind, B. Kasemo, and I. Zorić, "Localized and Propagating Plasmons in Metal Films with Nanoholes," *Nano Lett.*, vol. 13, no. 4, pp. 1743–1750, Apr. 2013, doi: 10.1021/nl400328x.

[336] T. Ohno *et al.*, "Hole-size tuning and sensing performance of hexagonal plasmonic nanohole arrays," *Opt. Mater. Express*, vol. 6, no. 5, pp. 1594–1603, May 2016, doi: 10.1364/OME.6.001594.

[337] L. Simonot, F. Chabanais, S. Rousselet, F. Pailloux, S. Camelio, and D. Babonneau, "Evolution of plasmonic nanostructures under ultra-low-energy ion bombardment," *Appl. Surf. Sci.*, vol. 544, p. 148672, Apr. 2021, doi: 10.1016/j.apsusc.2020.148672.

[338] P. Sanpradit, E. Byeon, J.-S. Lee, and S. Peerakietkhajorn, "Ecotoxicological, ecophysiological, and mechanistic studies on zinc oxide (ZnO) toxicity in freshwater environment," *Comp. Biochem. Physiol. Part C Toxicol. Pharmacol.*, vol. 273, p. 109720, Nov. 2023, doi: 10.1016/j.cbpc.2023.109720.

[339] Y. Dai *et al.*, "Life cycle environmental impact assessment of titanium dioxide production in China," *Environ. Impact Assess. Rev.*, vol. 105, p. 107412, Mar. 2024, doi: 10.1016/j.eiar.2023.107412.

[340] B. G. Lewis and D. C. Paine, "Applications and Processing of Transparent Conducting Oxides," *MRS Bull.*, vol. 25, no. 8, pp. 22–27, Aug. 2000, doi: 10.1557/mrs2000.147.

[341] S. Syed, "Silver recovery aqueous techniques from diverse sources: Hydrometallurgy in recycling," *Waste Manag.*, vol. 50, pp. 234–256, Apr. 2016, doi: 10.1016/j.wasman.2016.02.006.

[342] I. Teknetzi, S. Holgersson, and B. Ebin, "Valuable metal recycling from thin film CIGS solar cells by leaching under mild conditions," *Sol. Energy Mater. Sol. Cells*, vol. 252, p. 112178, Apr. 2023, doi: 10.1016/j.solmat.2022.112178.

[343] A. Kotliarenko, O. Azzolini, G. Keppel, C. Pira, and J. Esposito, "Investigation of a Possible Material-Saving Approach of Sputtering Techniques for Radiopharmaceutical Target Production," *Appl. Sci.*, vol. 11, no. 19, Art. no. 19, Jan. 2021, doi: 10.3390/app11199219.

[344] V. Reymond, A. Kharchenko, and N. Nadaud, "Thin film deposition method and resulting product," EP2440503B1, Jan. 06, 2021 [Online]. Available: https://patents.google.com/patent/EP2440503B1/

[345] M. Rajendran, K.-M. Lin, and W.-T. Hsiao, "Optoelectronic and structural properties of ITO/Ag/ITO transparent electrodes using ultraviolet laser annealing," *Mod. Phys. Lett. B*, vol. 37, no. 19, p. 2340036, Jul. 2023, doi: 10.1142/S0217984923400365.

[346] W. W. Lee *et al.*, "Development of transparent AZO-Ag-AZO electrodes using Xenon flash lamp annealing and application of transparent OLED," *Appl. Surf. Sci.*, vol. 684, p. 161861, Mar. 2025, doi: 10.1016/j.apsusc.2024.161861.

[347] A. Hacini, A. H. Ali, N. N. Adnan, N. Nayan, and L. Harkat, "High-performance of laser annealed ITO/Cr-Ag/ITO multilayered thin film for transparent conducting application.," *Surf. Interfaces*, vol. 42, p. 103449, Nov. 2023, doi: 10.1016/j.surfin.2023.103449.

[348] Saint Gobain Glass, “Planitherm Total+.” 2023. [Online]. Available: https://www.saint-gobain-glass.co.uk/wp-content/uploads/2024/05/PLANITHERM-TOTAL.pdf

[349] Saint Gobain Glass, “Gamme ECLAZ®.” 2024. [Online]. Available: https://www.saint-gobain-glass.fr/fr/documents/brochure/saint-gobain-brochure-eclaz-maj-05-2024-vf-web.pdf

[350] Saint Gobain, “Universal Registration Document 2020.” 2020. [Online]. Available: https://www.saint-gobain.com/sites/saint-gobain.com/files/sgo2020_urd_en_mel_210326_def.pdf

[351] J. Karlsson and A. Roos, “Annual energy window performance vs. glazing thermal emittance — the relevance of very low emittance values,” *Thin Solid Films*, vol. 392, no. 2, pp. 345–348, Jul. 2001, doi: 10.1016/S0040-6090(01)01055-0.

[352] “Cleaning Mechanisms,” co2clean. [Online]. Available: https://www.co2clean.com/cleaning-mechanisms

[353] SCHOTT, “BOROFLOAT® 33 – Thermal Properties.”

[354] Guardian Glass, “Guardian GlassTime - Technical Manual.” Guardian Europe S.à r.l., 2022.

[355] X. Zhang, K.-S. Chen, R. Ghodssi, A. A. Ayón, and S. M. Spearing, “Residual stress and fracture in thick tetraethylorthosilicate (TEOS) and silane-based PECVD oxide films,” *Sens. Actuators Phys.*, vol. 91, no. 3, pp. 373–380, Jul. 2001, doi: 10.1016/S0924-4247(01)00610-0.

[356] “Mie Theory Calculator,” nanoComposix. Accessed: Oct. 17, 2025. [Online]. Available: https://nanocomposix.com/pages/mie-theory-calculator

APPENDIX A OBTAINING BASIC OPTICAL PERFORMANCE AND HIGH TEMPERATURE STABILITY

In the main text, the effect of contaminant diffusion is studied by the removal of barrier layers, and the optical changes that remain when they are included are then discussed. However, how to reach this initial level of durability is not addressed. This is unfortunately common in scientific publishing: the work of achieving a certain established standard of coating properties is not an exciting publication. However, entirely omitting to describe this work leaves others to retread the steps of this unexciting task.

Thus, in this appendix, a brief outline of the main steps taken to obtain low-E coatings with sensible performance and stability will be presented, in the hope that it will help others spend their time advancing the state of the art rather than simply replicating it.

A.1 Initial calibration of the dielectric deposition conditions

As touched upon in Chapter 3, the practical and economic constraints of industrial fabrication of low-E coatings places significant importance on the deposition rate; maximizing this parameter can therefore help significantly in finding deposition parameters which result in comparable coating properties.

Applied power was set to the maximum values usable for a given target; this will vary according to the material deposited as well as the system specifications. Indeed, whereas $SiN_{(Al)}$ could be deposited from a 2 in. diameter magnetron with an applied power density of ≈ 9.9 W/cm^2 (200 W RF), switching to a 3 in. diameter magnetron required the power density to be reduced by a factor 2 (≈ 4.9 W/cm^2, 225 W RF) in order not to melt the indium bonding layer at the target base. Thus, a simple difference in the water-cooling flow per target area can affect the range of parameters. This being said, no great discrepancy was found in the properties of the $SiN_{(Al)}$ films produced with either magnetron, once other parameters were adjusted; hence, while this is a useful starting point, the capabilities of a typical laboratory coater ought to be enough to reach a satisfying baseline.

Working gas pressure must be high enough such that there is a high density of ions contributing to sputtering; simultaneously it must be low enough to allow a long mean free path for sputtering ions to efficiently eject film forming atoms, and for the latter to reach the sample without undergoing

too many collisions [170]. A good compromise was found at 2 mTorr for the dielectrics deposited in this work. This was later adjusted to control film properties, as the pressure influences the energy of film-forming species through collisions with the working gas, as discussed in section 2.2.2. Note that this is also system-dependant, as the number of collisions occurring will depend on the mean free path relative to the target-substrate distance.

Finally, composition of the working gas was adjusted. Formation of oxides and nitrides at the target surfaces will greatly reduce the deposition rate, whereas absorption and other undesirable optical behaviors will result from sub-stoichiometric coatings, once again requiring that an appropriate balance be found.

Figure A.1 shows the increasing deposition rate for deposition of $ZnO_{(Al)}$ and $SiN_{(Al)}$ with decreasing reactive gas concentration, as well as the resulting changes in optical properties. At low oxygen concentrations, $ZnO_{(Al)}$ exhibits metallic character which decreases *n* and leads to non-negligible *k* in the NIR. For $SiN_{(Al)}$, *n* can be tuned by making it more or less stoichiometric, although UV and low-wavelength visible absorption increase. Following this, reactive gas content can be chosen to maximize the deposition rate while maintaining desirable optical properties; at this preliminary stage, $Ar:O_2$ and $Ar:N_2$ ratios of 100:35 sccm and 100:30 sccm were taken for $ZnO_{(Al)}$ and $SiN_{(Al)}$, respectively; while a lower nitrogen content could have still been appropriate, this matched reference data supplied by the industrial partner for closely.

This approach is not quite appropriate for calibration of $NiCrO_x$, as its stoichiometry impacts its effect on durability more directly. On one hand, depending on how metallic it is, it can significantly decrease visible transmission. On the other, its been suggested that durability improvements result from metallic Ni diffusing into the top portion of Ag layer [20], or that sacrificial oxidation of the $NiCrO_x$ layer may protect Ag. Thus, $NiCrO_x$ needs to be as metallic as durability requires, and no more; in practice, this was a work of trial and error.

Finally, Ag deposition conditions should be selected in order to ensure that continuous films are formed at the desired film thickness, following the methodology for interference enhanced ellipsometry presented in Chapter 6. Lacking the means to do so, stress-based methods can be used [109]. Otherwise, film percolation can be monitored using SDRS, sheet resistance measurements, or the interference-agnostic method presented in Chapter 6, in which case the percolation threshold

should be comfortably below the desired film thickness. Section 2.2 offers insight into how different parameters can be used to adjust film wetting.

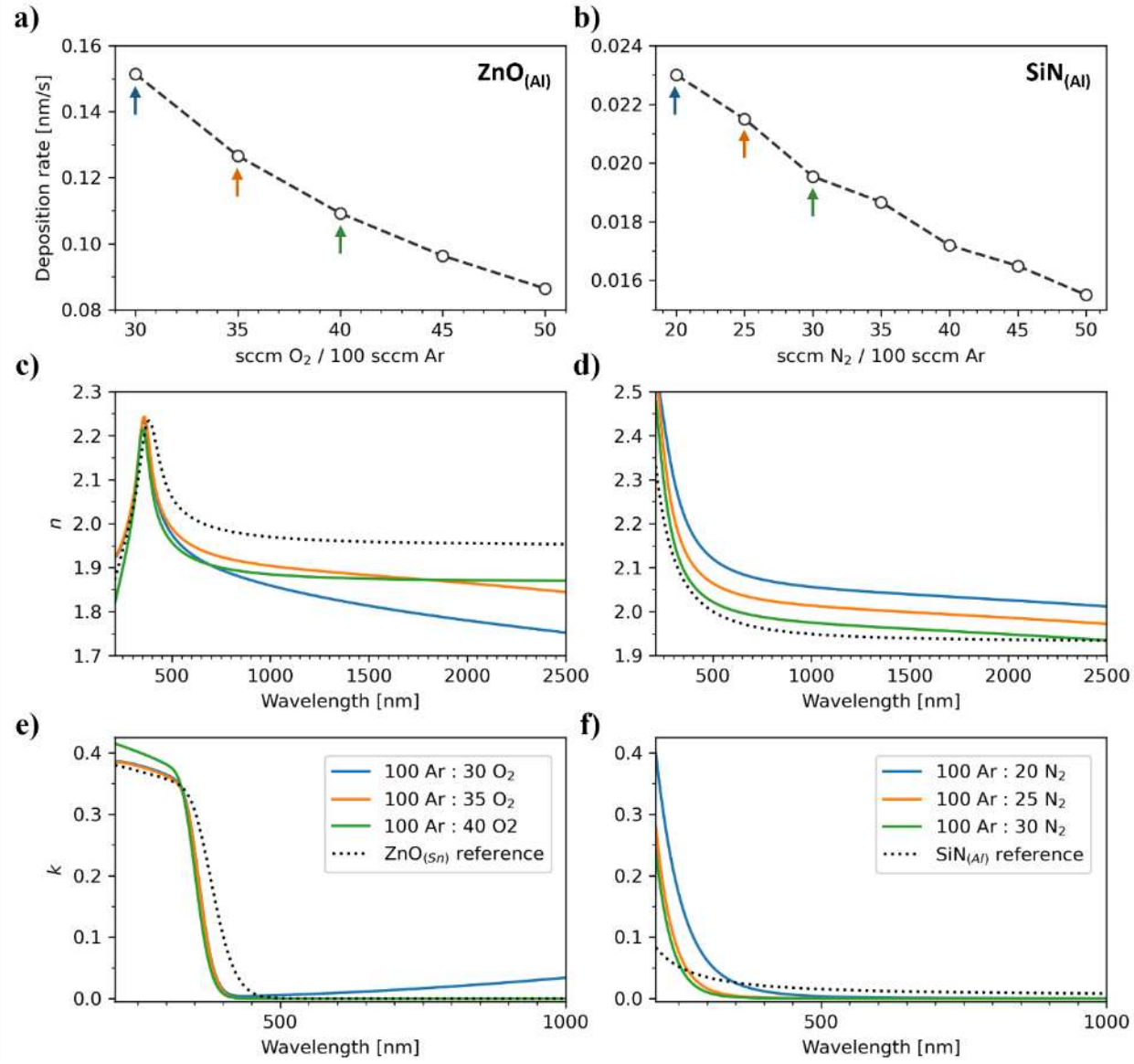


Figure A.1: a), **b)** Deposition rates, **c)**, **d)** refractive indices and **e)**, **f)** extinction coefficients of $ZnO_{(Al)}$ (**(a)**, **(c)**, **(e)**) and $SiN_{(Al)}$ (**(b)**, **(d)**, **(f)**) films deposited with different reactive gas ratios.

A.2 Impact of cleaning on low-E stability

Once coatings with appropriate optical and electrical performance in the as-coated state can be produced, factors influencing their stability can be investigated. Namely, substrate cleaning was found to have a profound impact on low-E durability. It should be noted that preliminary stability tests were performed on samples with a bottom ZnSnO layer, rather than a bottom $SiN_{(Al)}$ layer; while these were both found to be amorphous, and remain amorphous during HT, Kulczyk-Malecka found these to be far poorer diffusion barriers [39]. That being said, this may be preferable for the purpose of optimizing cleaning procedures, as coatings will have a greater sensitivity to any contaminants left behind during cleaning.

Figure A.2 shows the change in transmission for different low-E coatings in which different cleaning steps were used; all samples were washed by hand with either isopropanol (Iso.) or M90 solution, as described in Chapter 3 prior to ultrasound cleaning steps. Unsurprisingly, hand-cleaning samples, followed by agitation and rinsing under DI water and isopropanol was vastly insufficient. While addition of ultrasound cleaning helped in this regard, samples remained highly

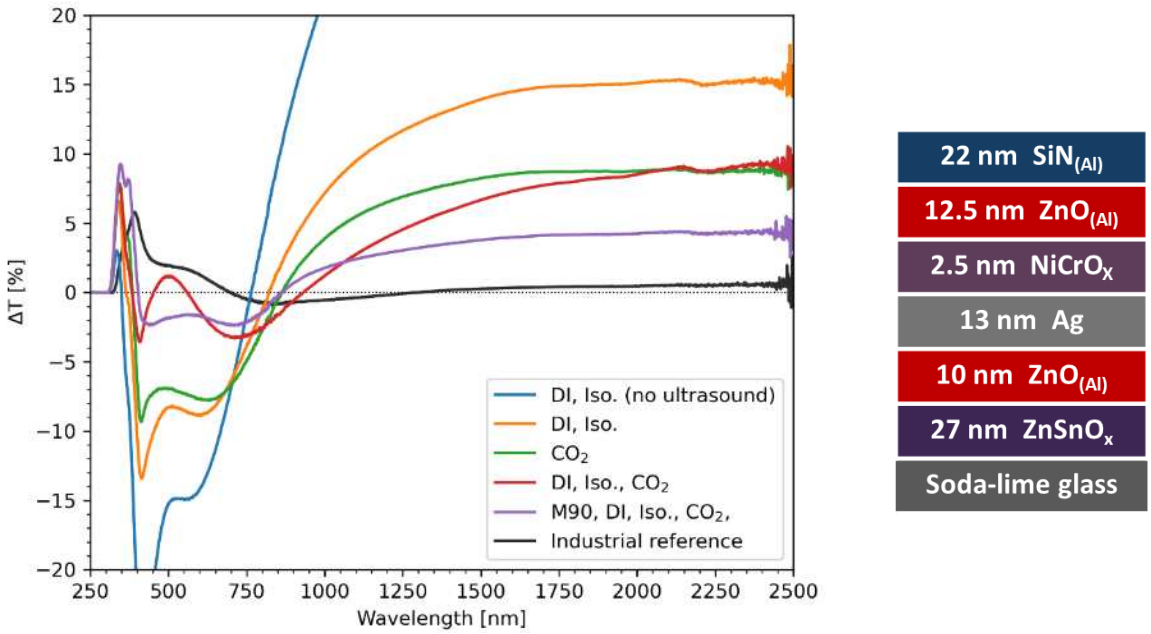


Figure A.2: Δ*T* following 7-minute HT of 3mm low-E glass samples produced with the nominal architecture shown to the right, for different combinations of substrate cleaning methods. Unless specified, all cleaning in liquid solvents was performed in an ultrasound bath.

susceptible to degradation. CO_2 snow cleaning was also tested early on [352], and was shown to yield significant improvements, even when used on its own. However, manually rastering the CO_2 jet made uniformity highly susceptible to user error. Thus, when replacing the bottom ZnSnO layer with $SiN_{(Al)}$, this step was replaced with the addition of an acetone ultrasound bath, yielding the process described in Section 3.1.1. While cleaning optimization never progressed to the point of matching the stability of reference samples provided by the industrial partner, this is attributed to differences in the coating properties, rather than significant contamination remaining following cleaning.

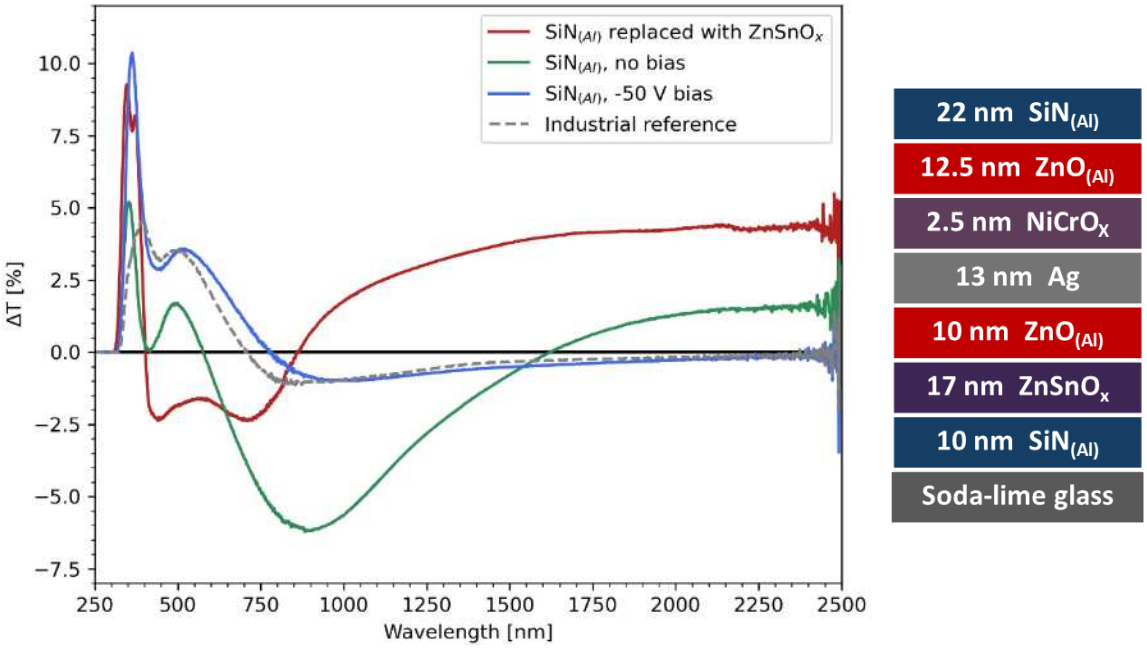


Figure A.3: ΔT following 7-minute HT of 3 mm low-E glass samples produced with the nominal architecture shown to the right, with different modifications applied to the base layer.

A.3 Impact of $SiN_{(Al)}$ stress on low-E stability

While the methodology established above constitutes an essential step in protecting samples from contaminants, by removing those at the substrate surface, appropriate properties of the barrier layers are required to mitigate diffusion of O_2 and Na, as studied in Chapter 4. With the addition of a thin (10 nm) bottom $SiN_{(Al)}$ layer stability is improved, as shown in **Figure A.3** below, but it is still below that of an industrial reference sample with a comparable architecture. It was first with the addition of RF bias during $SiN_{(Al)}$ deposition that comparable results were achieved.

As shown in **Figure A.4** below, wafer curvature measurements found that at 2 mTorr deposition pressure and without bias, $SiN_{(Al)}$ coatings were, essentially, completely relaxed, while those deposited with a -50 V RF bias displayed high compressive stress (≈ -1.7 GPa). While tempting, this should not be interpretated as compressive stress being simply better for, however. In the next section it will be shown that annealing of these films has the potential to result in large defects; this is attributed to the important stress changes observed when cycling the temperature of these films up to 450 °C. On the other hand, increasing the incident energy of film forming particles by decreasing the operating pressure to 1 mTorr results in smaller as-coated compressive stress values (≈ -1.2 GPa), but these were found to offer similar low-E stability, showed no defect formation during HT, and almost no stress changes below 400 °C. Thus, while compressive stress in the $SiN_{(Al)}$ layers can be a useful indicator in trying to improve their ability as diffusion barriers, the mechanisms by which stress is formed, stored, and released must not be discounted.

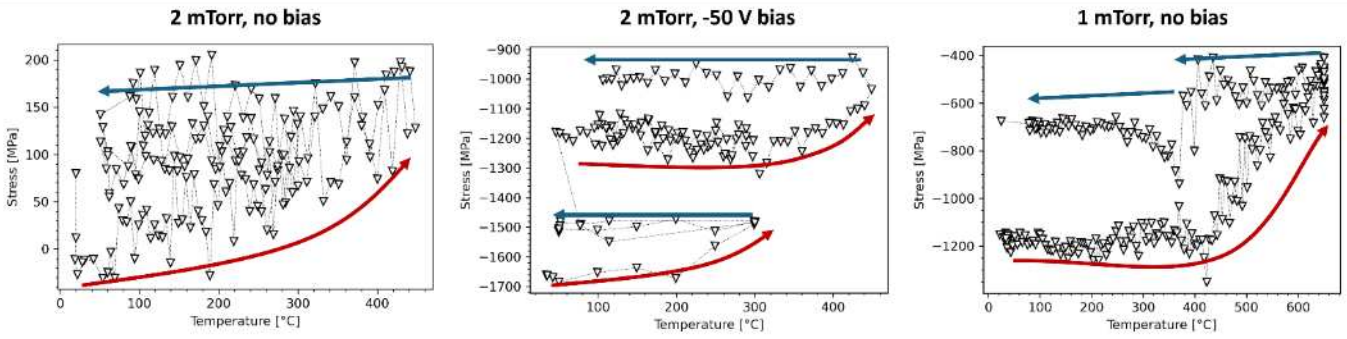


Figure A.4: Stress changes of 40 nm $SiN_{(Al)}$ films as a function of temperature, measured via wafer curvature. Red and blue arrows indicate heating and cooling phases, respectively.

A.4 High temperature stability of dielectrics

Finally, while optical performance and high temperature stability of low-E coatings was achieved even with the usage of biased $SiN_{(Al)}$ layers, as mentioned above, this introduced specific instabilities into the dielectric layers themselves. As these defects were not noticeable when integrated in a full low-E stack, this concern could be dismissed by some. Nonetheless, it highlights the changes induced in the dielectric layers during HT, which should not be ignored given their crucial role in stabilizing the Ag layer.

In addition to the previous stress changes, a brief analysis of the changes in optical properties and film crystallinity during HT was performed for 40 nm single-layer dielectric films deposited on fused silica substates. This revealed relatively minor changes for both $SiN_{(Al)}$ and $ZnO_{(Al)}$ layers, as shown in **Figure A.5** below.

Optical changes in $SiN_{(Al)}$ consist mainly of a decrease of n and k, consistent with a change in stoichiometry, as in **Figure A.1**; note that while it is likely that a gradient in oxidization would be more accurate, this was modelled as a uniform change throughout the film in order to minimize fitting parameters and the reliance on unfounded assumptions. XRD measurements reveal no out-of-plane crystallinity for $SiN_{(Al)}$ films, either before or after HT; as grazing incidence XRD performed on full stacks showed no peaks assignable to $SiN_{(Al)}$, this was taken as sufficient indication that the films remained amorphous, consistent with the interpretation of the optical data above.

For $ZnO_{(Al)}$, the shift between low and high values of k steepens, suggesting a narrower, more defined bandgap, resulting in a broad decrease of n. XRD of as-coated films shows a 001-oriented peak with a strong asymmetry; HT shifts the maxima to larger angles (smaller lattice spacing), but results in a more symmetrical peak, indicating a more consistent structure, once again consistent with the optical properties.

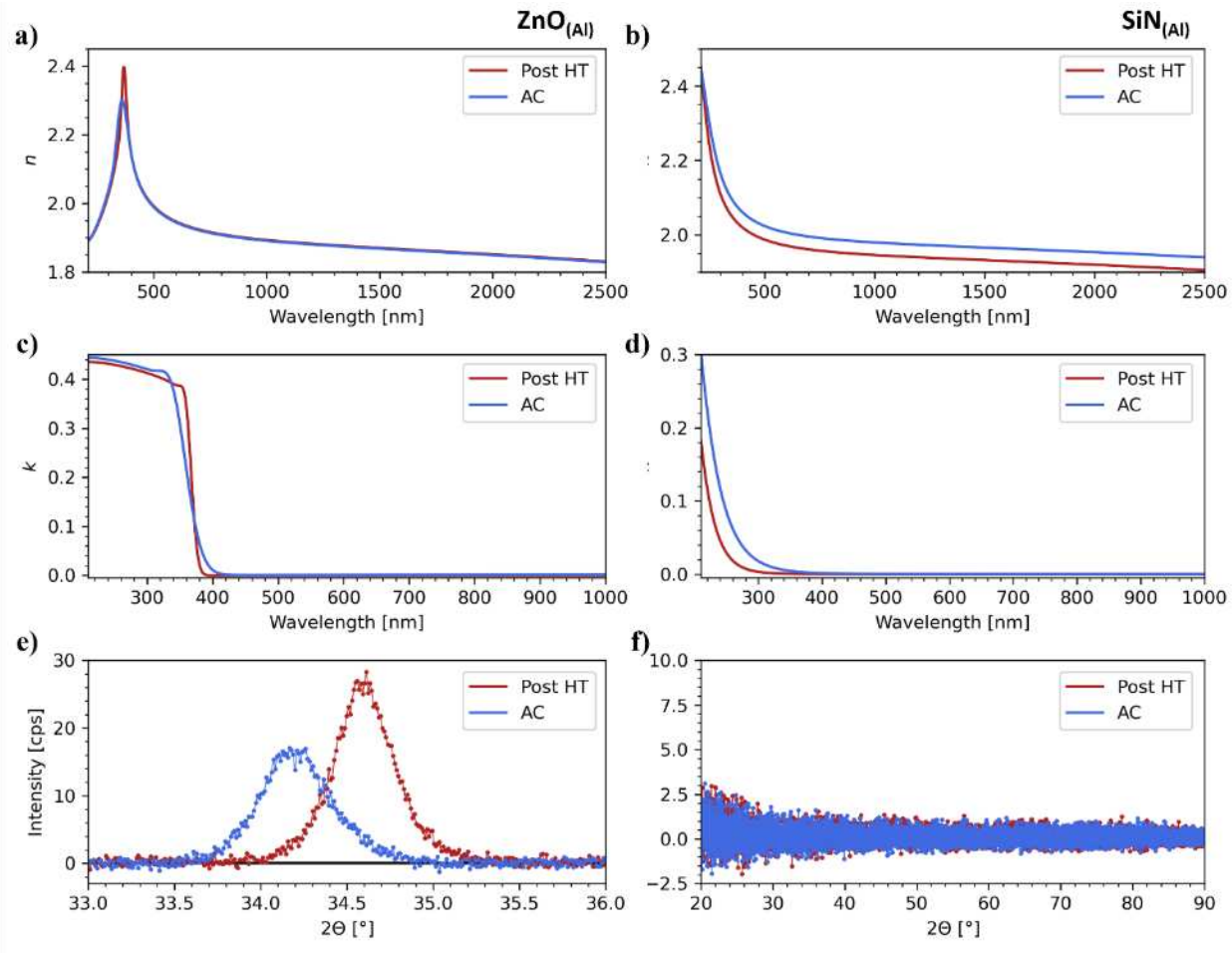


Figure A.5: Analysis of 40 nm thick $ZnO_{(Al)}$ (**(a)**, **(c)**, **(e)**) and $SiN_{(Al)}$ (**(b)**, **(d)**, **(f)**) layers deposited on fused silica substrates, as-coated and following 7 minutes of HT. **a)**, **b)** Refractive indices and **c)**, **d)** extinction coefficients modelled by *ex situ* ellipsometry. **e)**, **f)** XRD diffractograms obtained in Bragg-Brentano geometry.

While these changes are relatively minimal, the stability of individual films does not guarantee their continued stability when integrated to a multilayer architecture. To wit, $ZnO_{(Al)}$-$SiN_{(Al)}$ bilayers present qualitatively different optical changes than either individual film, as shown in **Figure A.6** above. In fact, the behavior is somehow opposite to that of $ZnO_{(Al)}$ single films, suggesting a broadening, and potentially shifting of the bandgap, resulting from different structural changes due to interactions with $SiN_{(Al)}$. The full scope of changes is unclear as the changes proposed here were insufficient to model ellipsometry data, and the analysis of tempered low-E stacks in Chapter 4 does not reveal any outstanding changes which may be at cause. Thus, while

this work focuses on the optical changes resulting from Ag morphological evolution, which have more impact in the visible spectrum, it should be highlighted that glass-dielectric and dielectric-dielectric interactions will require further study in order to achieve single-stock low-E coatings.

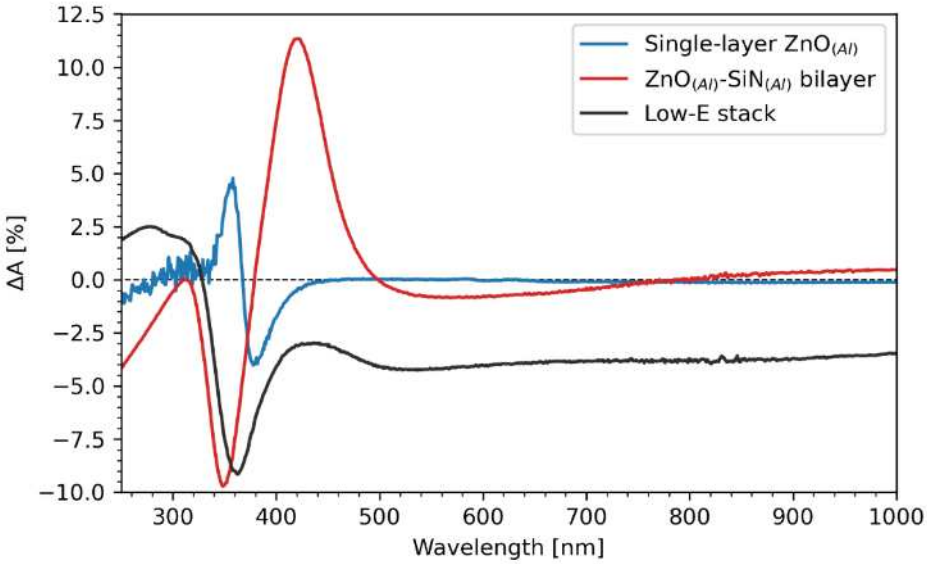


Figure A.6: Change in absorption ($\Delta A = A^{\text{post-HT}} - A^{\text{AC}}$) following 7-minute HT of a 40 nm single layer of $ZnO_{(Al)}$, a bilayer of $ZnO_{(Al)}$ and $SiN_{(Al)}$ (SLG/20 nm $ZnO_{(Al)}$/20 nm $SiN_{(Al)}$), and a low-E stack with the architecture shown in **Figure A.3**.

APPENDIX B SUPPORTING INFORMATION FOR CHAPTER 4

X-ray photoelectron spectroscopy (XPS) was performed using a Thermo Fisher Scientific ESCALAB Xi+ system alongside ion etching to obtain depth profiles of the samples' atomic composition following heat treatment. An Al Kα source was used with a beam size of 400 μm, and depth profiling was performed on a 2.5 mm by 2.5 mm area with a 2000 eV monoatomic Ar ion etch. Given the potential of the high energy etch modifying chemical bonds, and given that significant peak shifts were found as a result of etching despite usage of charge compensation, no binding energy analysis was attempted beyond simple elemental quantification.

Table B.1, below, shows the composition of the different substrates types used in this work. Data is averaged over 7 measurements, acquired following cleaning of the adventitious carbon layer and throughout 420 s of depth profiling with a 2000 eV monoatomic Ar ion etch.

Table B.1: Composition of the substrates used in Chapter 4, as measured by XPS.

	O	**Si**	**Na**	**Mg**	**Ca**	**Sn**	**B**	**Al**	**K**
	O1s	Si2p	Na1s	Mg1s	Ca2p	Sn3d5	B1s	Al2p	K2p
	[at.%]	[at.%]	[at.%]	[at.%]	[at.%]	[at.%]	[at.%]	[at.%]	[at.%]
SLG	62.0 ±1.8	30.4 ±1.3	1.4 ±0.5	2.0 ±0.9	4.1 ±1.5	0.1 ±0.1	-	-	-
BSG	62.2 ±0.9	31.9 ±0.5	0.2 ±0.2	-	-	-	4.2 ±0.5	1.2 ±0.1	0.3 ±0.1

Table B.2: Young's modulus (E), hardness (H), coefficient of thermal expansion (CTE) and transformation temperature (T_t) of SLG and BSG substrates. E and H were measured by nanoindentation; for each sample, two 25-point indentations were made, with final measurements derived from the steady-state portion of both sets of indentations. CTE and T_t are nominal values reported by glass manufacturers [353], [354].

	E	***H***	**CTE**	$\boldsymbol{T_t}$
	[GPa]	[GPa]	[K^{-1}]	[°C]
SLG	79.2 ± 1.7	7.3 ± 0.3	9×10^{-6}	535 ± 15
BSG	63.6 ± 1.6	8.1 ± 0.3	3.25×10^{-6}	525

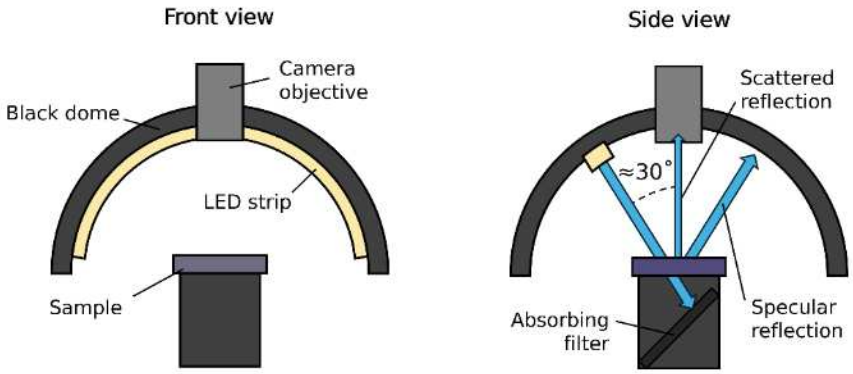


Figure B.1: Schematic representation of the darkfield scratch imaging set-up used in Chapter 4.

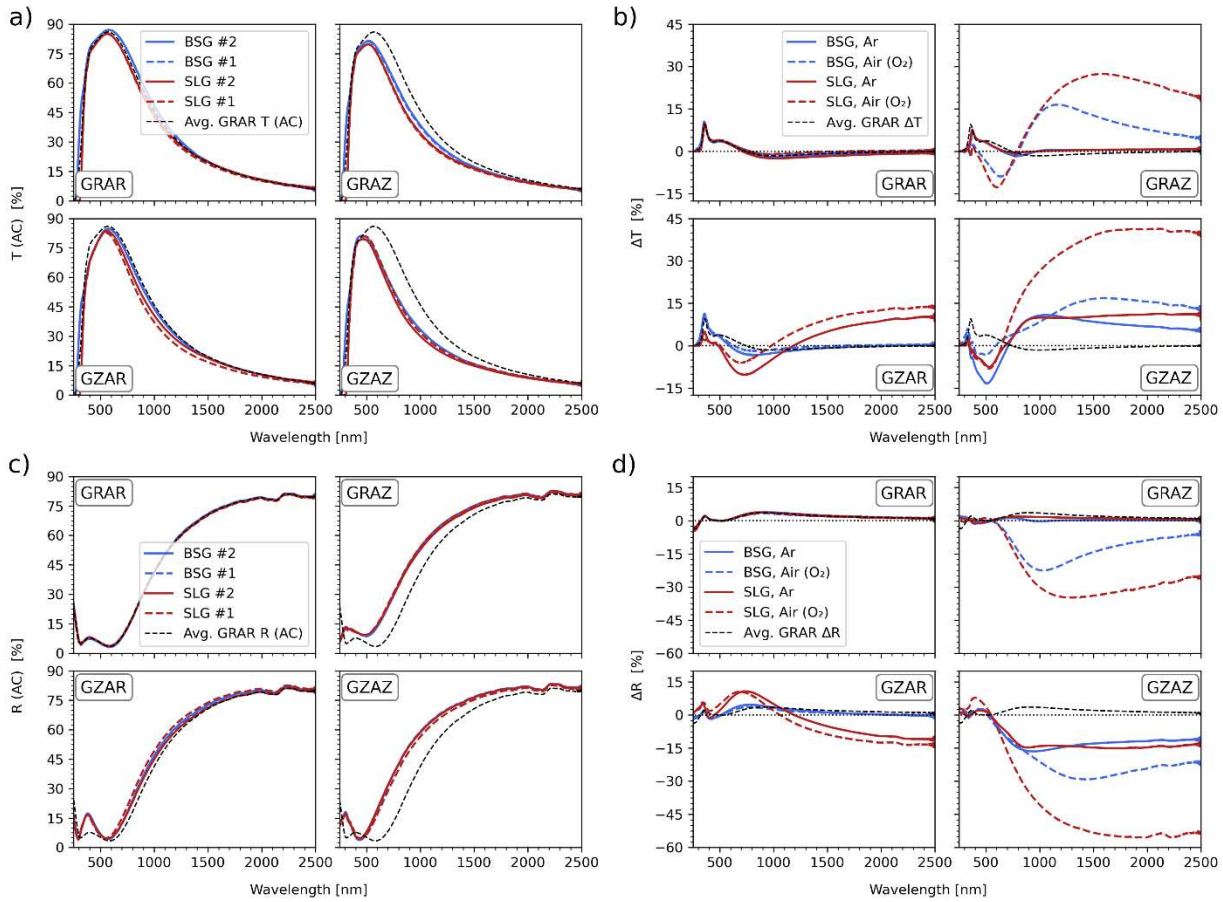


Figure B.2: a) As-coated (AC) optical transmission, **b)** transmission change ($\Delta T = T^{HT} - T^{AC}$), **c)** as-coated reflection, and **d)** reflection change ($\Delta R = R^{HT} - R^{AC}$), for each of the partial stack designs used in Chapter 4, as produced on different substrates and annealed in different atmospheres.

Table B.3: Sheet resistance of low-E stacks and partial stacks produced on various substrates and annealed in different atmospheres, as-coated (AC) and heat-treated (HT) at 650 °C for 8 minutes.

Architecture	Atmos.	Sub.	AC [Ω/□]	HT [Ω/□]
GRAR (Default stack)	**Air (O_2)**	**SLG**	6.51	4.91
	Air (O_2)	BSG	6.31	4.69
	Ar	**SLG**	6.34	4.94
	Ar	BSG	6.39	4.91
GRAZ (Top barrier layer removed)	**Air (O_2)**	**SLG**	6.17	13.1
	Air (O_2)	BSG	6.34	14.2
	Ar	**SLG**	6.38	4.81
	Ar	BSG	6.18	4.61
GZAR (Bottom barrier layer removed)	**Air (O_2)**	**SLG**	5.37	7.00
	Air (O_2)	BSG	5.70	4.57
	Ar	**SLG**	5.83	6.58
	Ar	BSG	5.64	4.46
GZAZ (Both barrier layers removed)	**Air (O_2)**	**SLG**	5.76	160
	Air (O_2)	BSG	5.35	12.0
	Ar	**SLG**	5.32	9.66
	Ar	BSG	5.34	9.34

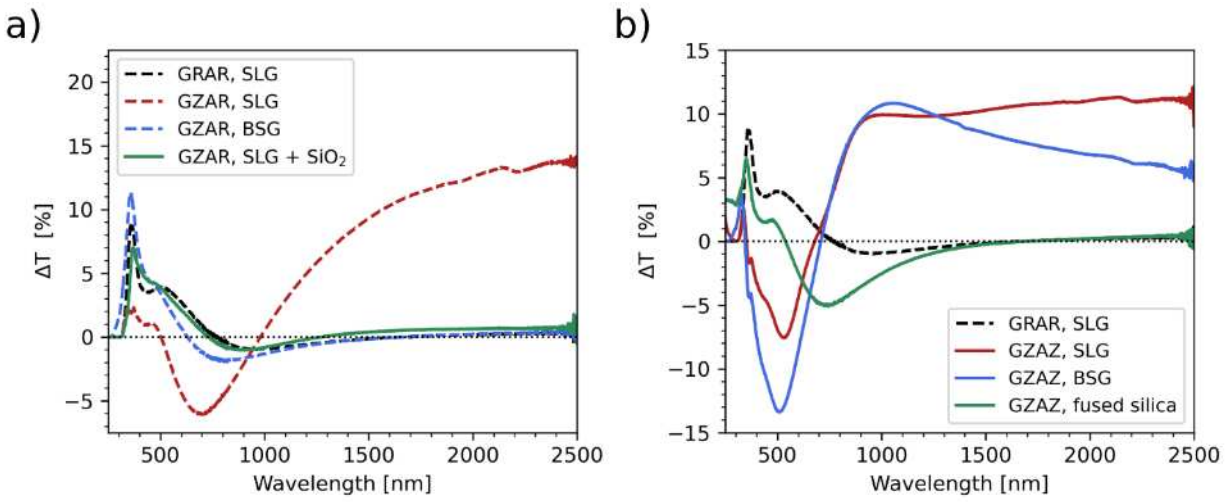


Figure B.3: Optical transmission change ($\Delta T = T^{HT} - T^{AC}$) of various partial stack types annealed in **a)** air, and in **b)** argon. The used substrates are identified in the legend. SLG + SiO_2 and fused silica substrates are described below, and the impact of these results is presented.

SLG + SiO_2 substrates, as used in **Figure B.3a**, correspond to SLG substrates on which a 50 nm SiO_2 layer was deposited by plasma-enhanced chemical vapor deposition. These were subsequently annealed to remove any residual hydrogen remaining from the SiH_4 precursor [355], and wafer-curvature stress measurements confirmed the SiO_2 layer to be highly relaxed following the annealing step. Subsequent deposition and annealing of GZAR-type partial stacks do not result in the characteristic changes observed for bare SLG. As the coefficient of thermal expansion of the substrate is unchanged, and the SiO_2 does not apply meaningful mechanical stress to the substrate, the high temperature degradation of coatings deposited on SLG upon removal of the bottom diffusion barrier layer is attributed to Na diffusion.

In **Figure B.3b**, 1 mm × 2.5 cm × 2.5 cm fused silica substrates, which are completely Na-free, were used in order to test annealing of GZAZ-type stacks in argon. These do not show the characteristic film changes observed for sodium-containing substrates; the deviations from GRAR samples are attributed to different annealing kinetics for the smaller substrates. This reveals that the degradation of GZAZ stacks on BSG is not inherent to the partial stack structure, and is instead attributed to Na diffusion, which simply occurs to a lesser degree than for SLG.

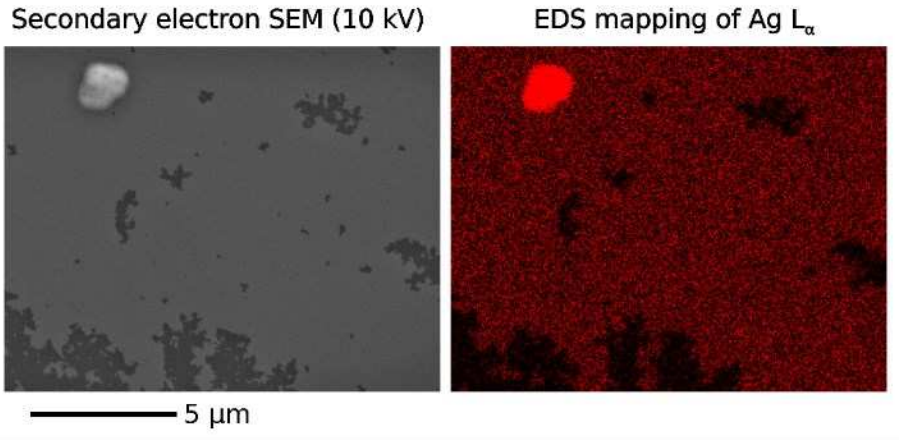


Figure B.4: SEM image of a GZAZ-type stack deposited on BSG and annealed in air, and associated EDS mapping of Ag. An accelerating voltage of 10 kV was used to decrease surface sensitivity and increase the X-ray signal. This reveals that the dark areas are depleted of Ag, as expected from the high contrast found in backscattered electron images in **Figure 4.5e** and **Figure 4.6c-f**.

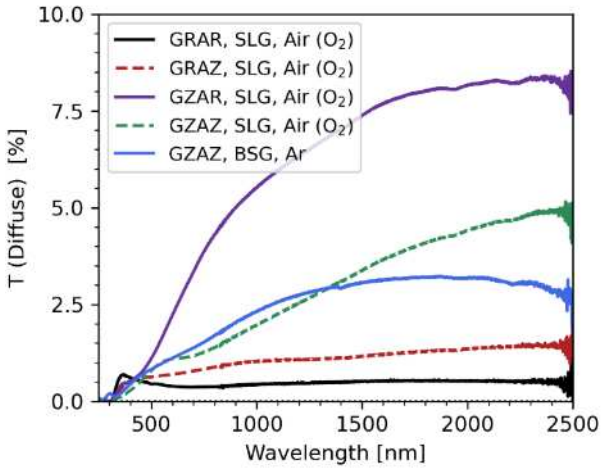


Figure B.5: Diffuse transmission of samples following heat treatment, for different partial stack designs, substrate types, and gas environments. Sodium diffusion, and the resulting formation of large-scale dewetting patterns greatly increase the scattered component. GZAR samples on SLG show particularly high scattering: this is attributed to buckling of the upper dielectrics over fingering instabilities, as shown in **Figure 4.5**.

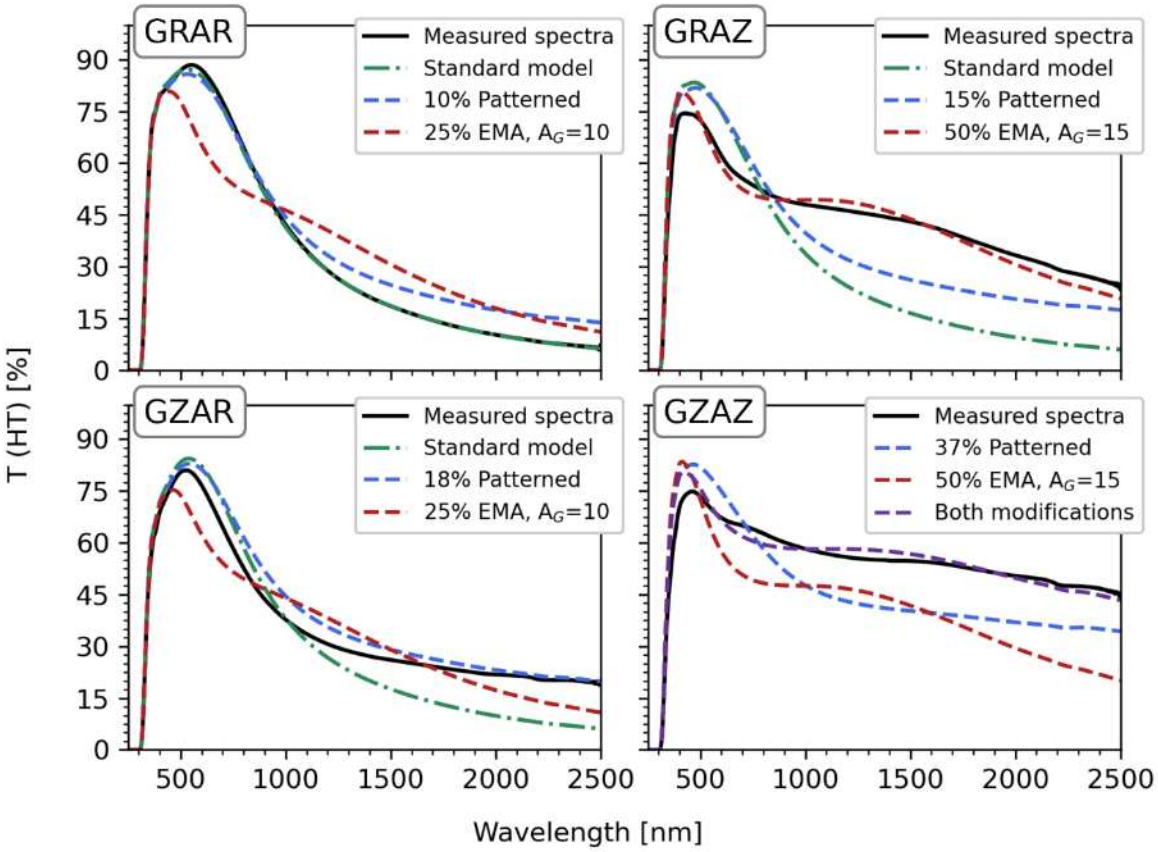


Figure B.6: Comparison of transmission curves of different partial stack designs, deposited on SLG and annealed in air to modelled curves obtained using the *CompleteEASE* software.

The standard model uses fixed dielectric thicknesses and refractive indices, only changing the diffusion barrier thicknesses to 0 nm when appropriate for a given partial stack design. The Ag layer was modelled with fixed thickness and optical properties, using Drude, Gaussian, and Tauc-Lorentz oscillators. Large-scale dewetting was modelled by patterning the Ag layer, decreasing its coverage in the model without adding plasmonic effects. Sub-micron scale dewetting was modelled by adding a Gaussian oscillator to the Ag layer, centered at 1.5 eV and with full width at half maximum of 1.4 eV, to account for plasmonic absorption. These values were obtained by first fitting them independently for each coating, then taking a rough average of the resulting values, allowing one to qualitatively describe the observed changes in each coating type while maintaining a simple parametrization. Then, the resulting Ag optical properties were inserted into a Bruggeman

effective medium approximation (EMA) making it possible to consider that the layer included a certain percentage of void.

The percentage of patterned Ag area, percentage of void in the EMA, and the amplitude, A_G, of the Gaussian are identified for each sample. This figure then reveals that qualitative Ag degradation modes can be identified from the optical spectra based on which type of model most closely resembles the measured transmission. The GRAR sample fits well without modifications to the standard model, the GRAZ sample fits the model associated with sub-micron dewetting, the GZAR sample fits the model associated with large-scale dewetting, and the GZAZ sample requires both types of changes to be implemented. These results are consistent with the SEM and TEM observations shown in **Figure 4.3** to **Figure 4.6** of Chapter 4.

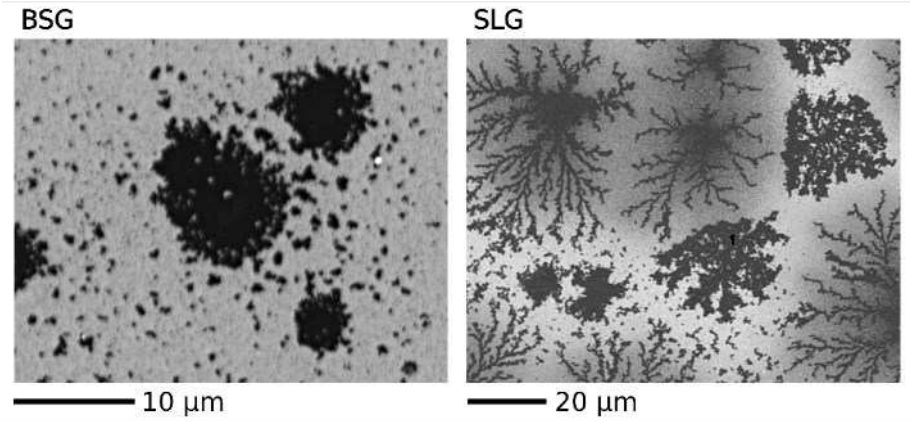


Figure B.7: Backscattered electron mode (10 kV accelerating voltage) SEM images of GZAZ-type partial stacks annealed in air, for BSG (left) and SLG (right), highlighting the irregular edges of the holes in the Ag film for BSG. These are believed to result from the stagnation and widening of fingering instabilities; this is supported by the observation of similar features for select holes in the sample on SLG, as shown above.

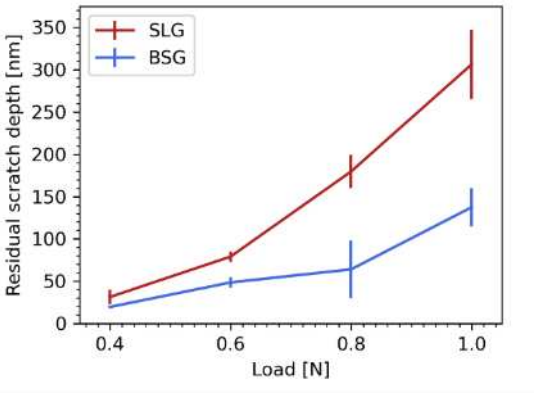


Figure B.8: Residual scratch depth as a function of the applied load, measured by stylus profilometry. Detailed scratch parameters are indicated in Section 4.3.

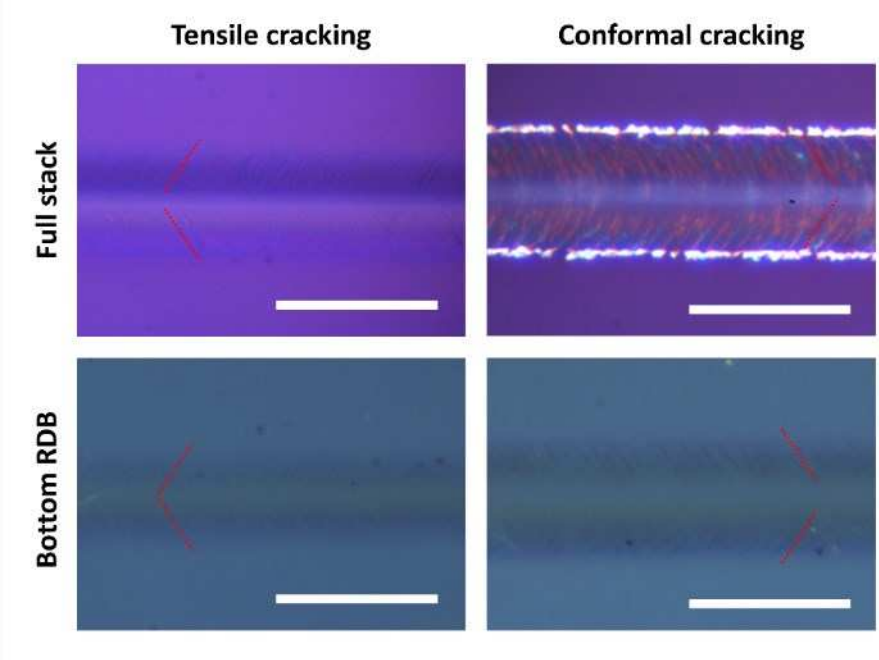


Figure B.9: Optical microscope images of tensile and conformal cracks in full low-E stacks, and of the same samples following acid etching of all but the bottom rigid diffusion barrier (RDB) layer. Proper removal of other layers was confirmed by *ex situ* ellipsometry measurements on a non-scratched area of the sample. Scale bars all correspond to 20 µm. Red dotted lines highlight the crack orientations. All scratches were generated with tip movement going from left to right.

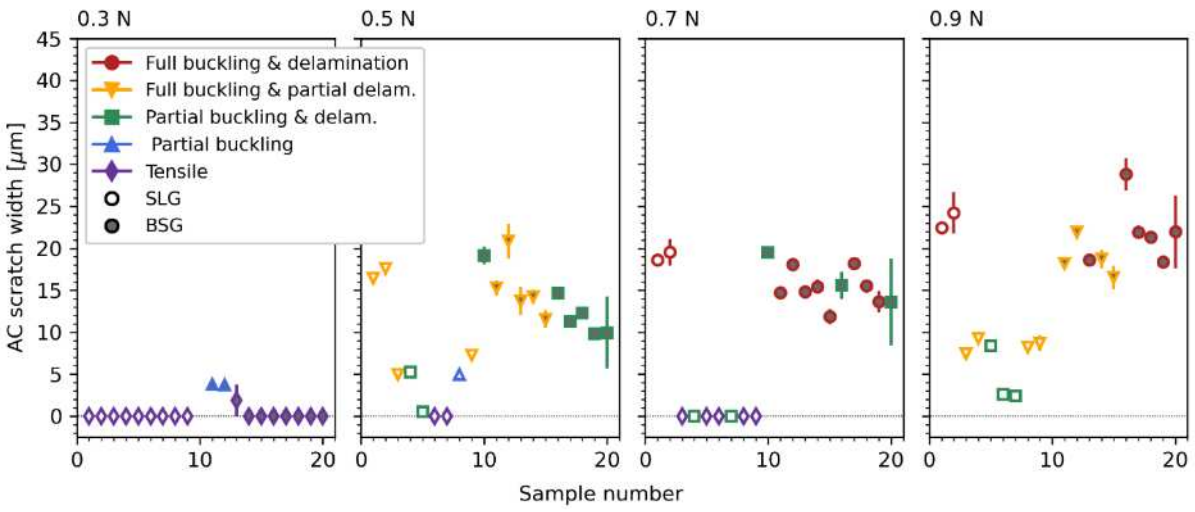


Figure B.10: As-coated (AC) scratch width and defect types of scratches obtained at various constant loads on GRAR-type stacks, shown in **Figure 4.2**. Optical microscope images representative of each defect type are shown in **Figure 4.8**.

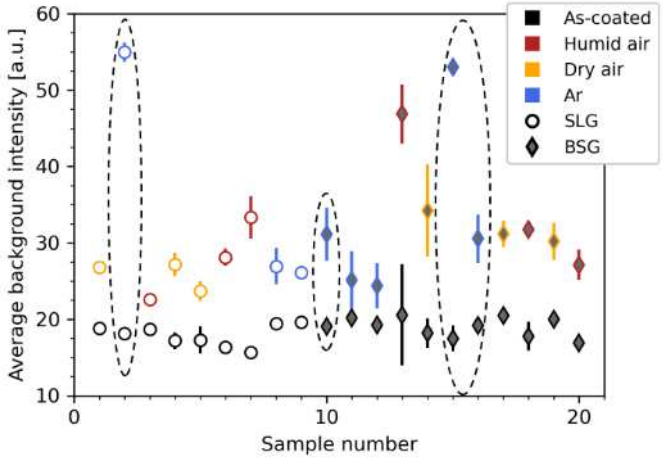


Figure B.11: Average background intensity for each scratched sample, as-coated and following annealing in one of various controlled atmospheres. Circled samples are those which include the circled data points in **Figure 4.10**.

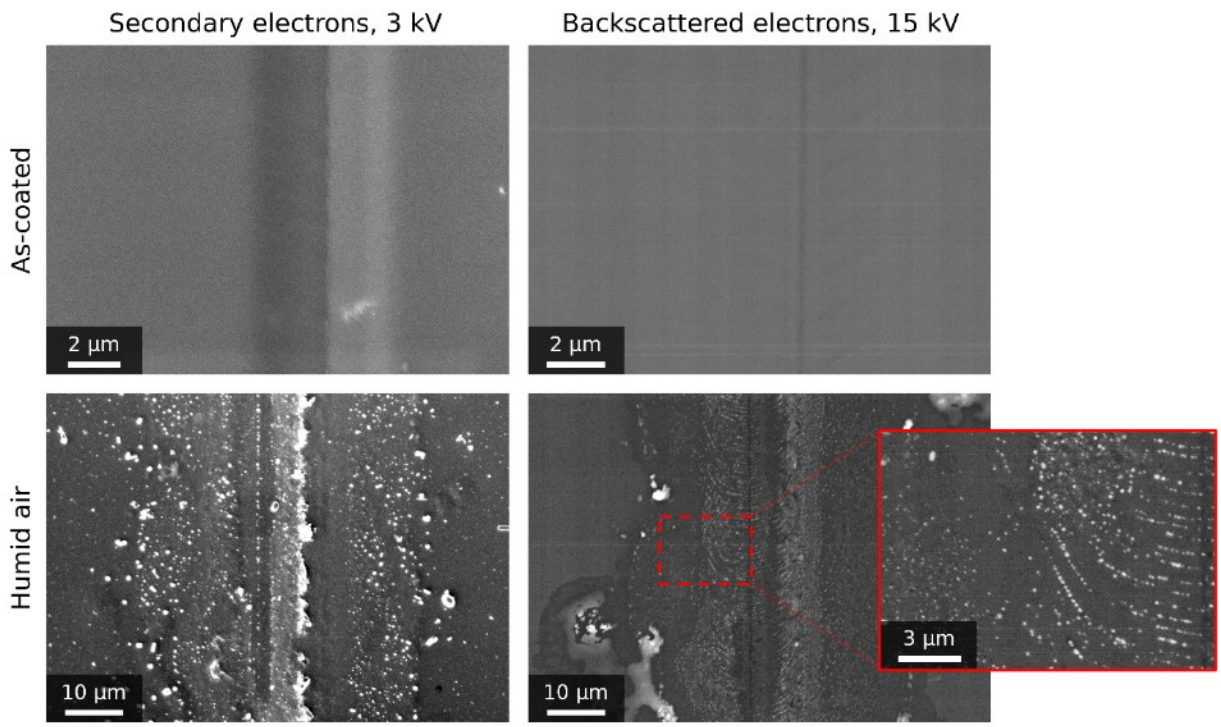


Figure B.12: SEM images of tensile crack structures as-coated (top) and annealed at 650 °C for 8 minutes in humid air (bottom), overcoated with ≈ 50 nm of carbon. For the as-coated scratch, tensile cracks and plastic deformation of the scratch track are faintly visible in secondary electron mode. Backscattered electron observations suggest that there is some dewetting along the tensile cracks and scratch track. The sample annealed in humid air shows a large amount of blisters, particles and other surface features in secondary electron mode. Backscattered electron imaging reveals that these are mostly not Ag, and it shows a wide dewet area in which the formation of small nanoparticles (≈ 150 nm) is observed, similar to those in the buckled areas of scratches annealed in dry air, as shown in **Figure 4.11**.

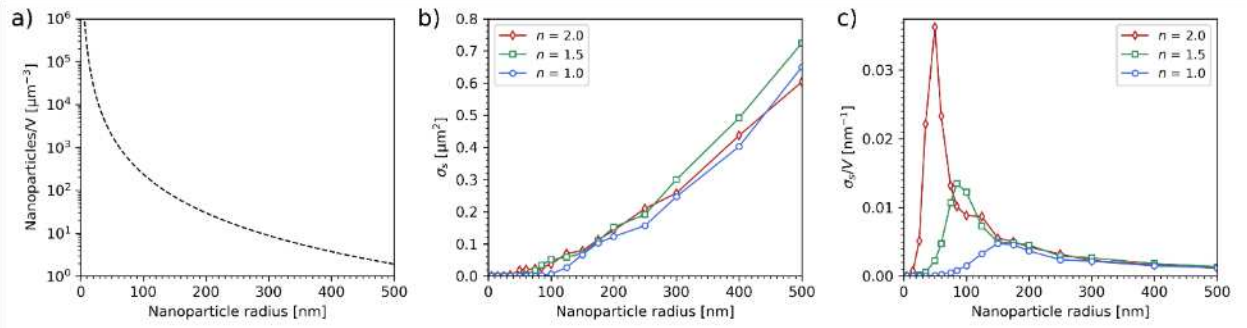


Figure B.13: a) Number of spherical nanoparticles which can be formed per volume of Ag as a function of the nanoparticle radius. **b)** Scattering cross-section at 550 nm, σ_s, of an Ag nanoparticle as a function of the nanoparticle radius, for different refractive indices, *n*, of the surrounding medium. Scattering cross-sections were obtained from Mie theory calculations, obtained using the tool included and described in the following references [274], [356]. **c)** Scattering cross-section per unit volume of Ag dewet into nanoparticles, as a function of the nanoparticles' radius; product of **(a)** and **(b)**. While the scattering cross-section per nanoparticle increases at higher sizes, the amount of nanoparticles which can be formed from a given volume decreases more rapidly. Thus, we find, for the range of refractive indices of the glass, air and dielectric media, that dewetting a fixed volume of Ag into nanoparticles between 50 and 200 nm of radius will result in the highest level of scattering.

APPENDIX C SUPPORTING INFORMATION FOR CHAPTER 5

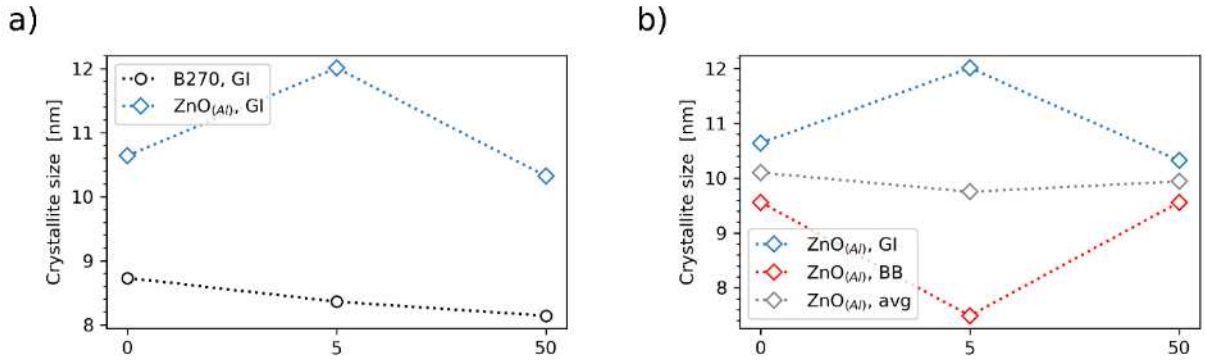


Figure C.1: Crystallite size of 7.5 nm thick $Ag_{(N)}$ coatings deposited on $ZnO_{(Al)}$-coated and uncoated Si substrates as a function of the N_2 concentration in the $Ag_{(N)}$ sputtering gas mixture, obtained from XRD diffractograms. **a)** $Ag_{(N)}$ crystallite size estimated from grazing incidence (GI) geometry measurements. **b)** Comparison of crystallite size estimation of $Ag_{(N)}$ films deposited on $ZnO_{(Al)}$-coated Si substrates for GI and Bragg-Brentano (BB) measurements, as well as their average value (avg).

X-ray diffraction (XRD) measurements were performed using a Bruker Discover D8 system. Crystallite sizes were estimated with the Scherrer equation, using a built-in function in the Bruker *EVA* analysis software. Measurements were performed on 7.5 nm Ag films deposited on Si substrates which were either uncoated or coated with a 10 nm $ZnO_{(Al)}$ seed layer. It is assumed that growth behavior on Si and B270 is representative of growth on Si_3N_4 and other seed layers which do not specifically promote Ag growth patterns.

Bragg-Brentano (BB) geometry measurements were used to evaluate the preferred growth orientation, where 1° grazing incidence (GI) geometry measurements were used to optimize the interaction volume and diffracted signal. Measurements in GI were performed on Si substrates to reduce the amorphous background signal. Only Ag (111) diffraction peaks were considered, as the (200) peaks were not of sufficient intensity to be measured appropriately. While grazing incidence measurements are useful in increasing the interaction volume in such thin samples, given known issues with applying the Scherrer equation to grazing angle XRD [248], these results should be considered with appropriate reserve.

Samples deposited on Si and B270 glass showed no obvious diffraction peaks in BB geometry, whereas those on $ZnO_{(Al)}$ did, confirming the preferential (111)-oriented Ag growth on $ZnO_{(Al)}$ even at low thickness.

Crystallite sizes estimated from GI measurements on Si substrates show a monotonous decrease with increasing N_2 concentration. Crystallite sizes estimated for $ZnO_{(Al)}$ are systematically larger, and while there appears to be an increase in size for $Ag_{(N)}$:5% in GI, the opposite is found for BB measurements; when averaging the results from both measurement geometries, the crystallite size appears to be insensitive to N_2 concentration. The weaker preferred orientation and stronger GI intensity found for $Ag_{(N)}$:5% is not believed to be a feature of these deposition conditions, but rather due to important measurement uncertainty on such thin samples.

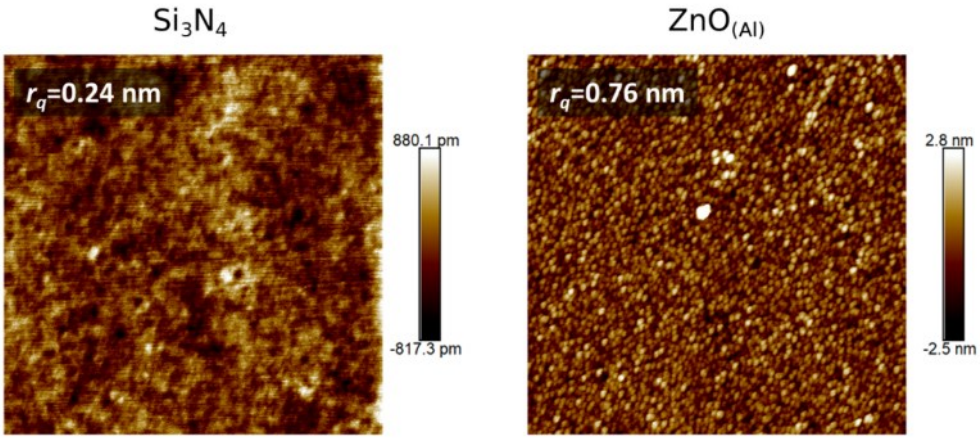


Figure C.2: 1 µm × 1 µm AFM images of 33-nm-thick Si_3N_4 and $ZnO_{(Al)}$ films, annotated with their root mean square roughness, r_q.

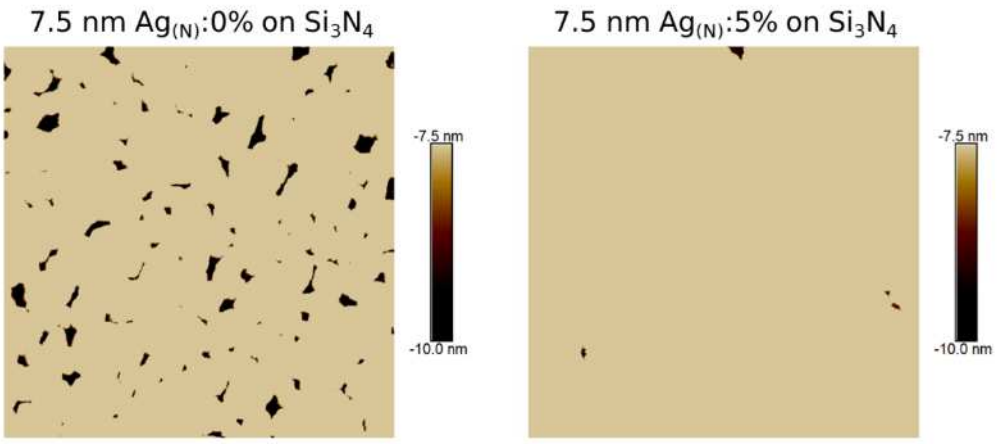


Figure C.3: Threshold analysis of 1 μm × 1 μm AFM images of 7.5 nm Ag films deposited on Si_3N_4 substrates (as shown in **Figure 5.8**), highlighting the increased density of discontinuities present for $Ag_{(N)}$:0%. The median height for each image is set to 0. The corresponding height of the substrate should be -7.5 nm for a smooth and uniform 7.5 nm film. To account for roughness and non-uniformity, we consider that values below -7.5 nm are potentially discontinuous, and values equal to or below -10 nm are fully discontinuous. This threshold was chosen as the majority of datapoints below are within the range of roughness found for the Si_3N_4 substrate. Height values above or below the range of the scale bar are represented in the color of the maximum or minimum of the scale bar, respectively.

It should be noted that the images obtained for 7.5 nm Ag films on ZnO(Al) show no such discontinuities, regardless of the sputtering gas mixture.

APPENDIX D SUPPORTING INFORMATION FOR CHAPTER 6

D.1 Supporting information for Article 2

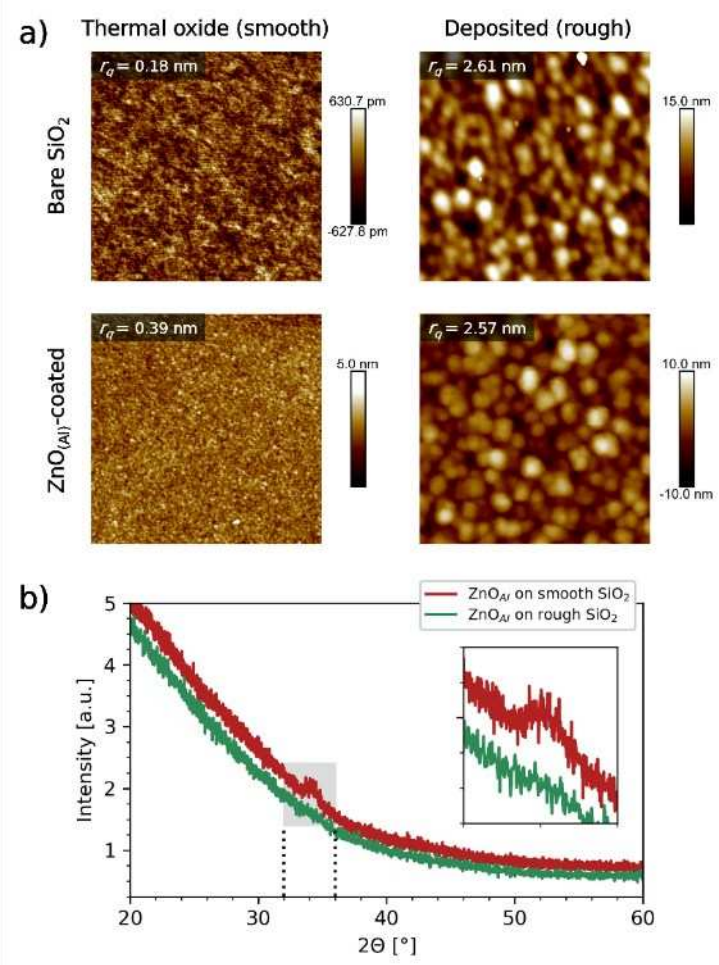


Figure D.1: a) 1 µm × 1 µm AFM images of IE-ISE substrates using 1 µm SiO_2 layers, obtained by wet thermal oxidation (smooth) or magnetron sputtering (rough), bare or overcoated with 10 nm of $ZnO_{(Al)}$. All images are annotated with their root-mean-square roughness, r_q. **b)** Bragg-Brentano geometry XRD diffractograms of 10 nm $ZnO_{(Al)}$-coated IE-ISE substrates, showing (002) $ZnO_{(Al)}$ out-of-plane texture at ≈ 34 ° on smooth substrates, with no discernible features on rough substrates.

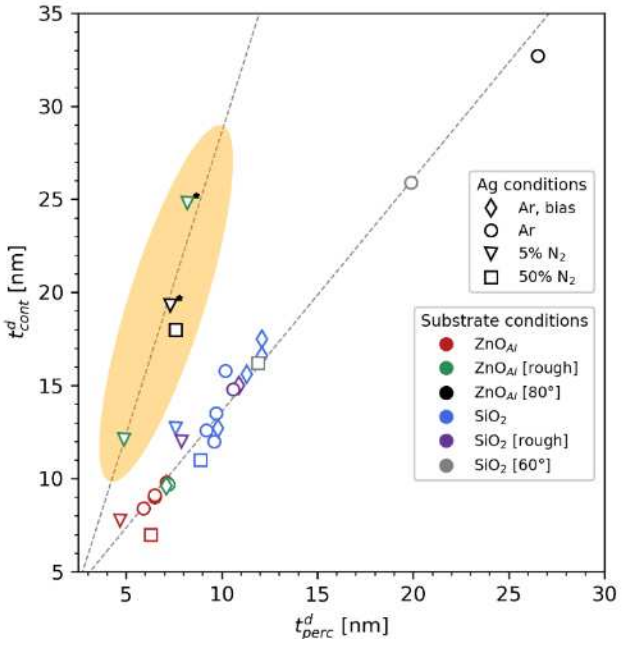


Figure D.2: $t_{cont}{}^{d}$ as a function of $t_{perc}{}^{d}$ measured by IE-ISE on various substrates in different deposition conditions. Trend lines and circling of notable outliers are added for emphasis. Asterisks are used to identify data obtained outside of normal experimental conditions, i.e.: $ZnO_{(Al)}$ heated to 60 °C and rough $ZnO_{(Al)}$ exposed to atmosphere prior to Ag deposition. Due to these deviations, data from these samples is not included in the rest of this work and is only included here to properly demonstrate the secondary trend.

Figure D.2 shows the $t_{cont}{}^{d}$ of the samples studied in this work as a function of $t_{perc}{}^{d}$: almost all films show the same general correlation. A practical impact of this is that the comparative modelling ISE approach method may be used to estimate continuous film formation thicknesses, but only following appropriate calibration, in relevant deposition conditions.

While a different trend is observed for Ag films sputtered in an Ar-N_2 gas mixture on heated or rough $ZnO_{(Al)}$ (which is shown to lack well-defined crystal orientation in **Figure D.1**), a linear relationship is still found; this suggests a different growth regime [19]. The reason for this change in regime is not clear, as while different growth regimes are known to occur, these have been studied in the context of pulsed depositions on weakly interacting amorphous substrates [19], [101]. How this translates to films deposited with a nitrogen surfactant, on a polycrystalline substrate with decent affinity to the film material, only in specific instances (weaker crystallinity for rough substrates, or higher diffusivity for heated ones), requires an analysis beyond the scope of this

paper. Hypothetically, this may be due to a mismatch between the Ag adatom diffusivity versus the size and density of the (001)-oriented crystalline domains on the $ZnO_{(Al)}$ surface: diffusion to preferential sites on the substrate could be promoted over nucleation of new clusters or changes to the coalescence dynamics.

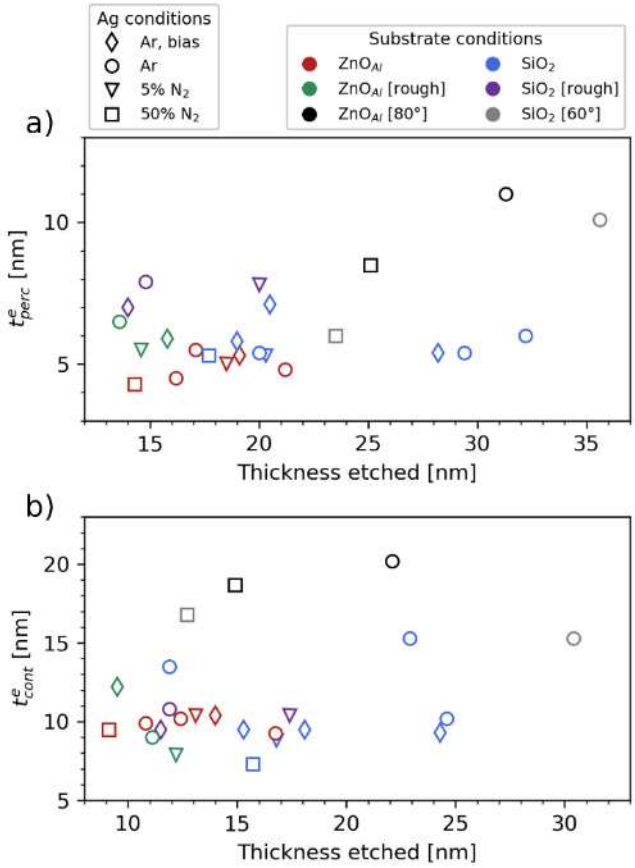


Figure D.3: a) t_{perc}^{e} and **b)** t_{cont}^{e} as a function of the Ag thickness etched between the end of deposition and initiation of breakdown.

Film breakdown thicknesses show no apparent dependence on the total thickness of film material etched, indicating that preferential etching does not play a significant role in film breakdown.

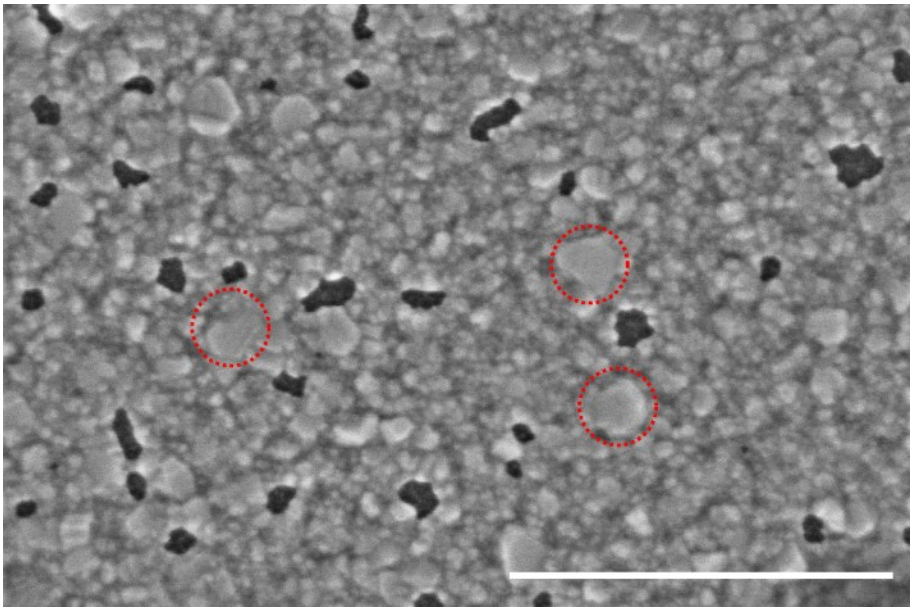


Figure D.4: SEM image of an Ag films produced by deposition on a $ZnO_{(Al)}$-coated Si substrate, up to a thickness of 15 nm, and **s**ubsequent etching to a thickness of 7 nm, as pictured in **Figure 6.1f**. Dotted red circles have a radius of 50 nm; the scale bar corresponds to 500 nm.

From **Figure D.4** it can be seen that no grains are present with radii larger than 50 nm; thus, as discussed in Section 6.4.3, grain boundary grooving cannot entirely account for hole formation during etching.

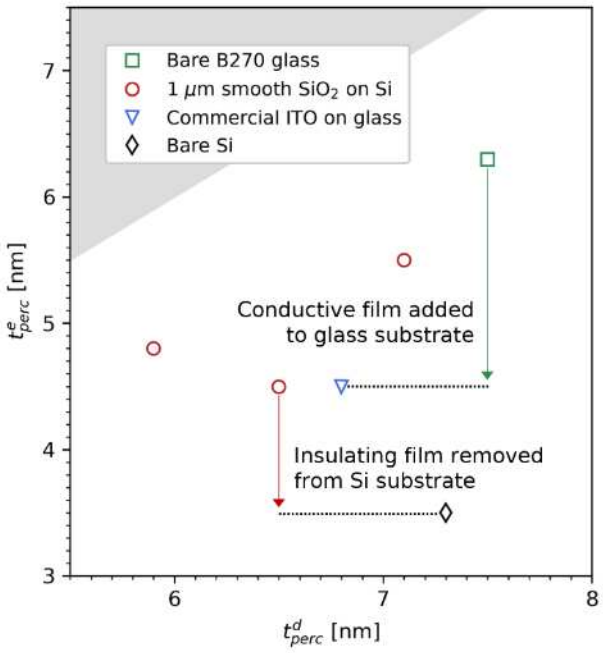


Figure D.5: t_{perc}^{e} and t_{perc}^{d} obtained for Ag films deposited in Ar gas at floating potential, for different $ZnO_{(Al)}$ coated substrates, such that 1 μm smooth SiO_2 on Si describes the smooth $ZnO_{(Al)}$ IE-ISE substrates. All other substrate types do not generate interference enhancement. The grayed area corresponds to where $t_{perc}^{e} > t_{perc}^{d}$.

While preliminary tests varying the pressure and power of the RF bias plasma used to etch the Ag film did not result in any notable changes to the critical thicknesses achievable via etching, these were found to vary as a function of the substrate material. **Figure D.5** compares t_{perc}^{e} and t_{perc}^{d}, deposited in Ar on $ZnO_{(Al)}$ seed layers, with various substrate types.

It is shown that t_{perc}^{d} is comparable for all substrates types, although on the IE-ISE compatible substrates (i.e.: 1 μm smooth SiO_2 on Si, red circles) lower values are observed leading to some variability. While there may be subtle changes in the $ZnO_{(Al)}$ layer obtained on each type of substrate, we attribute this discrepancy to the change in monitoring sensitivity. As a result, we do not believe that there are important differences in the wetting behavior or the resulting morphologies of these films. In contrast, there are important differences in the breakdown behavior as a function of the chosen substrate. Notably, as in **Figure 6.1**, films deposited on bare Si substrates show much lower t_{perc}^{e} than those with thick insulating oxide layers, as used for the previous IE-ISE experiments. A commercial ITO-coated glass substrate (45 Ω/□) was also tested;

in this case, the substrate was affixed to the substrate holder with conductive metallic tape overlapping the ITO coating to maximize conduction between the sample surface and the substrate holder, which is used as the bias electrode for the etching process. Despite the limited conductivity of the ITO coating, a clear decrease of the critical thickness during etching is observed, when compared to the B270 glass substrates, indicating that the substrate's electrical properties can negatively impact the critical thicknesses achieved, possibly via charging or by affecting the electrical field generated by the RF bias at the sample surface. As a result, we believe that using an ion-beam with controllable charge neutralization is a more suitable method to etch Ag films, allowing improved control of the angle and energy of impinging ions, as well as allowing to reduce the impact of the substrate's electrical properties.

D.2 Supporting information for Section 6.7

FDTD simulation methodology

Finite-difference time-domain (FDTD) simulations of the absorption (*A*), reflection (*R*), and transmission (*T*) spectra of multilayer structures were performed in *Lumerical* (Ansys Inc.) software. The simulations were conducted within a rectangular computational domain measuring 1180 nm × 787 nm × 1500 nm, derived from SEM micrographs (1536 px × 1024 px) with a scale of 0.76823 nm·px^{-1}. The stack architectures were based on experimental designs and consisted of five layers, arranged from bottom to top as follows: $SiN_{(Al)}$ (36 nm)/$ZnO_{(Al)}$ (10 nm)/Ag (*t* nm)/$SiN_{(Al)}$ (10 nm)/SiO_2 (73 nm), where *t* represents the Ag layer thickness. The Ag layer's effective thickness was kept constant for different coverages using the relation $f \cdot t$ = 5 nm or 10 nm, where *f* is the SEM-derived Ag coverage ratio. In cases where $f < 1.0$, defects in the Ag layer were filled with a $SiN_{(Al)}$ pseudo-layer, matching the Ag thickness *t* but with an inverted morphology, ensuring positional and structural alignment with Ag defects. The stack was placed on a B270 substrate of identical width and depth to the stack, and monitors placed in the bulk of the glass, effectively simulating the substrate as semi-infinite. The optical parameters (refractive index and extinction coefficient) of each layer were determined using *ex situ* spectroscopic ellipsometry. A plane-wave source was used to irradiate the device with light of wavelengths ranging from 210 nm to 2500 nm. A pair of frequency-domain field and power monitors sampling at 701 points was used

to compute the T and R spectra. To account for backside reflection from the secondary interface between the substrate and air, both forward and forward-reverse light propagation simulations were performed, yielding T_f, R_f, T_{fr}, and R_{fr}. The resulting T, R spectra were then corrected using a custom Python library, *lumflows*, utilizing the same algorithm as *OpenFilters* [305]. The A spectrum was derived using the following relation: $A = 100 - (T + R)$.

Transmission simulations used for comparative purposes were performed with the same input material optical properties and architectures, using the *CompleteEASE* software.

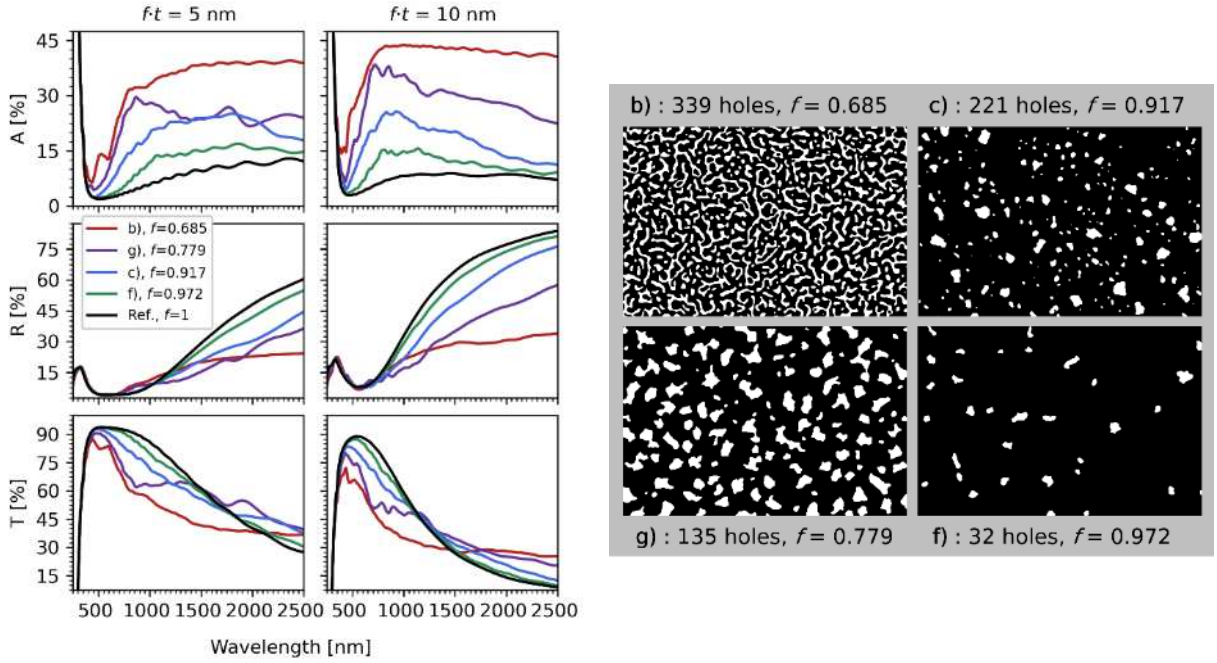


Figure D.6: Left: FDTD-simulated absorption, reflection and transmission of experimentally derived Ag film structures obtained from images **(b)**, **(c)**, **(f)** and **(g)** of **Figure 6.1**, with various Ag coverage ratios (f) and of a theoretical continuous Ag film ($f = 1$), inserted into a B270/$SiN_{(Al)}$ (36 nm)/$ZnO_{(Al)}$ (10 nm)/Ag (t)/$SiN_{(Al)}$ (10 nm)/SiO_2 (73 nm) architecture with $f \cdot t$ = 5 nm or $f \cdot t$ = 10 nm. **Right:** Binary-pattern images used to produce each simulation, all of which have a scale of 1180 nm × 787 nm. Red lines added to hole pattern **(b)** were not included when simulating optical properties; these indicate where holes were segmented for improved fitting to ellipses, prior to calculating the hole size distribution in **Figure 6.8**.

When measuring the hole size distributions for these images, given the wide range of hole shapes, holes were fitted to ellipses using the software *ImageJ* to obtain as representative a hole size distribution as possible. The major and minor axis diameters are each weighted by one half of the hole area, so that each hole is weighted by its total area, and the sum of all histogram elements corresponds to the hole coverage, $1 - f$. While this method does not account for all of the various features encountered in the different hole shapes, it allows one to account for more than one effective size in irregularly shaped holes.[4] In order to apply this approach to the wormlike holes found in sample **(b)**, holes were manually separated into sections with more linear shapes, as indicated by the red lines. For example, a 'V' shaped hole would be separated into two diagonal holes, each of which can be fitted to an ellipse with much greater accuracy. Naturally, this is not a perfect substitution, but allows to better represent large-scale concave shapes. Small concave features at hole edges are not measured by this method. However, these cause variations in the edge-to-edge holes sizes with less effect on the hole area. To account for these variations, histogram bin heights were treated with a weighted moving average; for a given bin, the two immediately adjacent bins were given one-half weight and all other bins were given null weight.

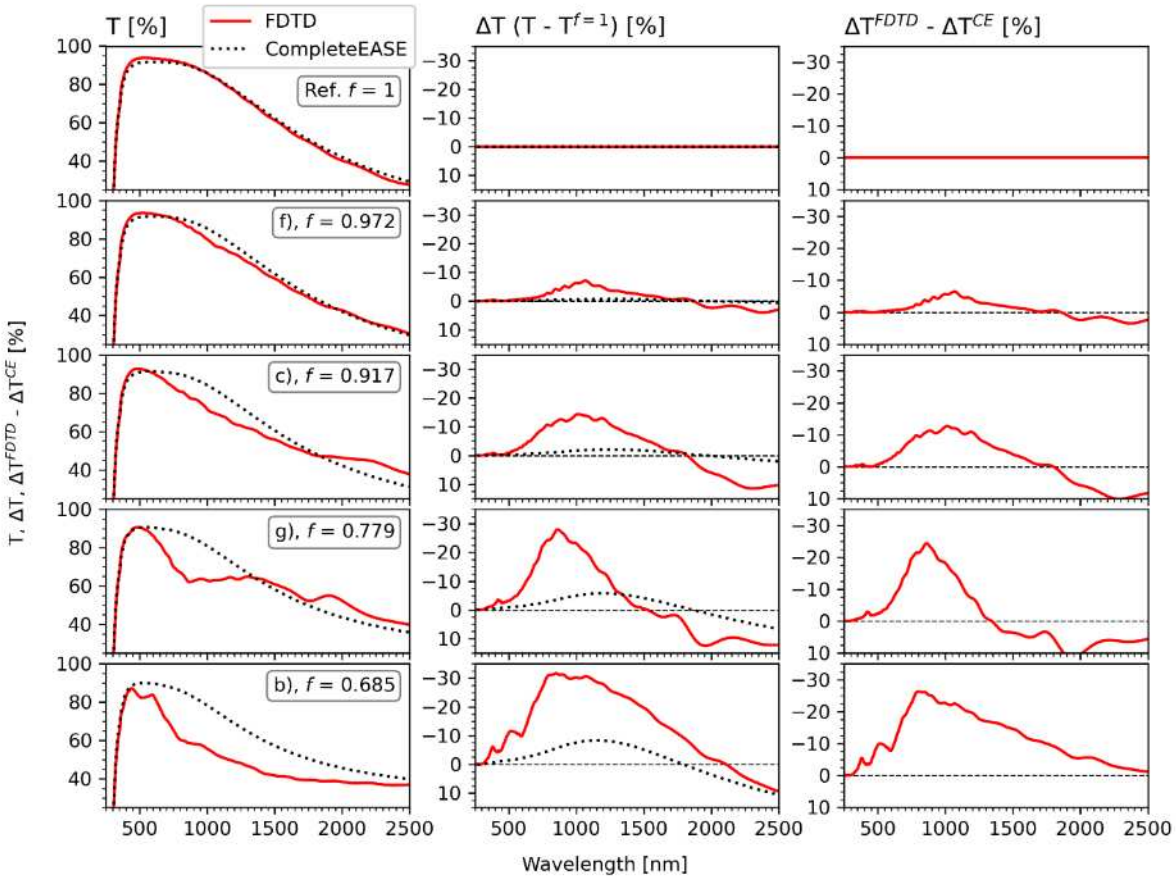


Figure D.7: Demonstration of the processing performed to evaluate the transmission loss attributable to the plasmonic behavior of holes patterns. Transmission spectra (T) of Ag-based AR devices with different Ag coverage ratios f, and Ag thickness t, such that $f \cdot t$ = 5 nm, simulated in FDTD and *CompleteEASE* (CE) simulations (left). The change attributable to hole inclusion (ΔT), with (FDTD) and without (CE) simulation of plasmonic features is obtained by subtracting the transmission of the f = 1 reference from the transmission for a given hole morphology (center). The transmission loss due to plasmonic behavior of holes, $\Delta T^{\text{FDTD}} - \Delta T^{\text{CE}}$, is isolated by subtracting the ΔT obtained with CE simulations from that obtained with FDTD, as the former do not consider plasmonic behavior (right).

Transmission change attributable to the inclusion of a given hole morphology, ΔT, is calculated by taking the difference between the transmission spectra obtained for the f = 1 reference structure and for a given hole pattern, such that $\Delta T = T - T^{f=1}$. To account for changes to optical performance unrelated to plasmonic behavior, the transmission was simulated for each Ag coverage and thickness value in the *CompleteEASE* (CE) software, treating the Ag layer as patterned; as such, changes resulting from partial Ag coverage and thickness changes are considered without

modelling any plasmonic behavior. Therefore, the difference between the ΔT values, ΔT^{FDTD} - ΔT^{CE}, obtained for each type of simulation represents the transmission change attributable to plasmonic behavior of the different hole morphologies.

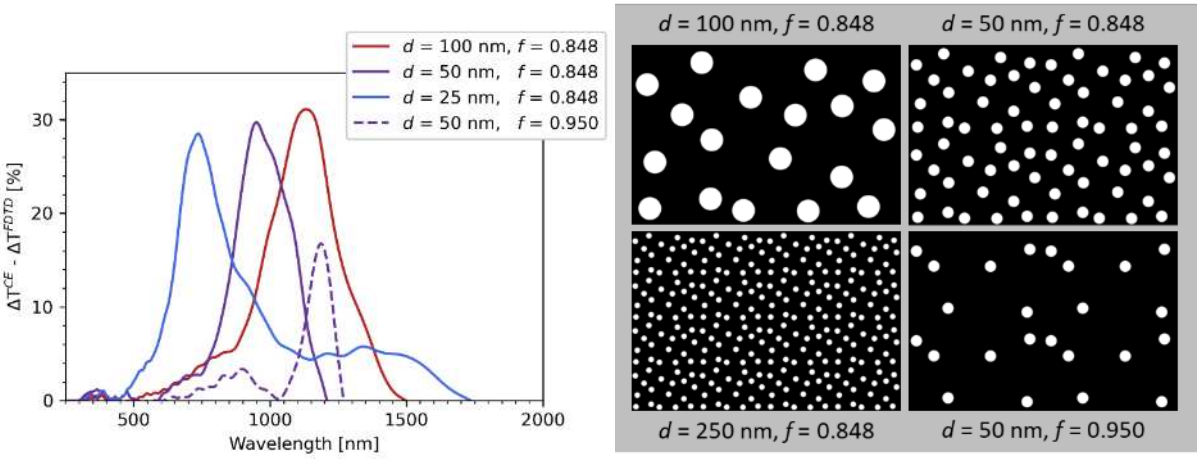


Figure D.8: Transmission loss due to plasmonic behavior of manually generated circular hole patterns with different hole diameters, d, and coverage ratios, f, inserted in the same AR device architecture as for previous simulations. Ag thickness t is kept fixed at 5.89 nm, satisfying $f \cdot t = 5$ nm for the three patterns with $f = 0.848$. **Right:** Binary-pattern images used to produce each simulation, all of which have a scale of 1180 nm × 787 nm. The hole size to spacing ratio was kept constant for the three patterns with $f = 0.848$, as the image with smaller hole sizes were created by stitching together uniformly scaled down copies of the image with 100 nm holes. The image with $d = 50$ nm, $f = 0.950$ was obtained by taking a subset of the holes present in the image with $d = 50$ nm, $f = 0.848$.

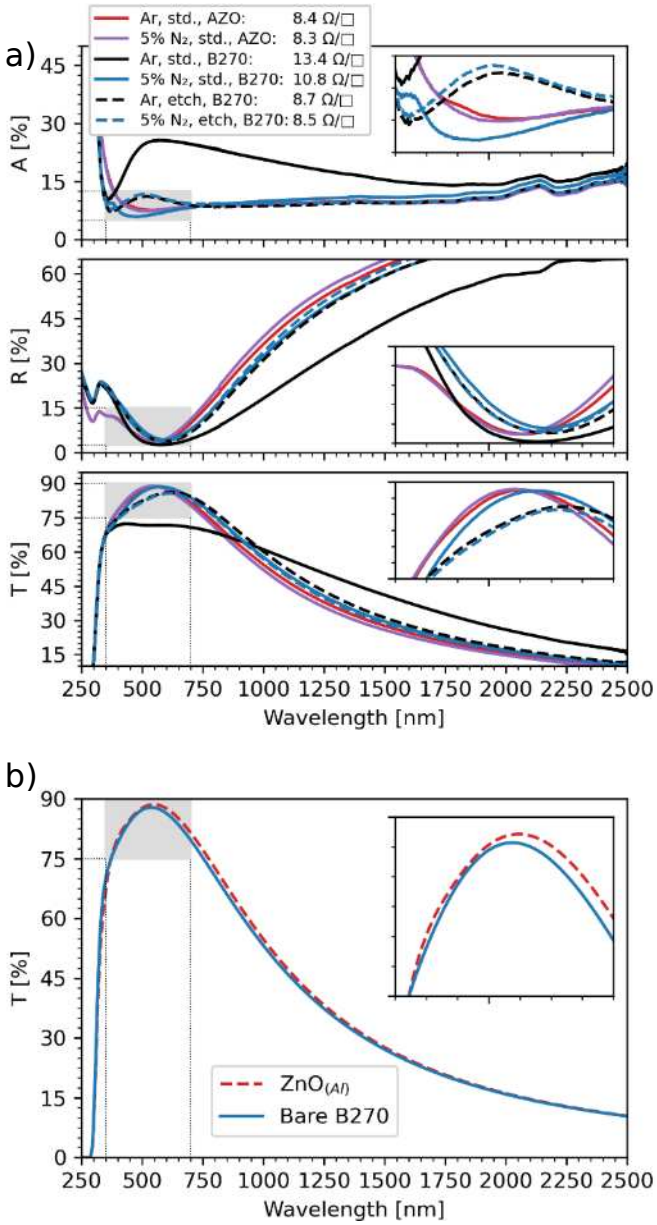


Figure D.9: a) Absorption, reflection, transmission and sheet resistance of optical devices deposited either in a B270/ $ZnO_{(Al)}$ (10 nm)/Ag (9 nm)/$SiN_{(Al)}$ (36 nm) architecture, or with the $ZnO_{(Al)}$ layer removed, thus depositing Ag directly onto the bare B270 glass substrate. Samples deposited onto the glass substrate were fabricated using one configuration with standard deposition and one with post-deposition etching. All sample configurations were deposited using both Ag deposited in pure Ar and Ag deposited in 5% N_2. **b)** Comparison of transmission values for B270 (2 mm)/ $ZnO_{(Al)}$ (10 nm)/Ag (9 nm)/$SiN_{(Al)}$ (36 nm) and B270 (2 mm)/Ag (9 nm)/$SiN_{(Al)}$ (36 nm) coatings modelled in *CompleteEase*, using experimental optical properties obtained by *ex situ* ellipsometry for B270 glass, $ZnO_{(Al)}$, and $SiN_{(Al)}$, and properties from Palik for Ag [14].

Figure D.9a presents spectrophotometry curves and sheet resistance values obtained for various samples obtained via standard deposition on $ZnO_{(Al)}$, compared to ones produced with standard deposition or post-deposition etching on bare B270 glass substrates. Samples with Ag on $ZnO_{(Al)}$ were deposited in a B270/$ZnO_{(Al)}$ (10 nm)/Ag (9 nm)/$SiN_{(Al)}$ (36 nm) architecture. Those with Ag deposition on bare B270 simply had the $ZnO_{(Al)}$ layer removed with no additional modifications, resulting in a B270/Ag (9 nm)/$SiN_{(Al)}$ (36 nm) architecture. The same architecture was used for etched Ag layers. These were deposited at a thickness of 18 nm to ensure continuous film formation prior to etching. **Figure D.9b** presents modelling results which demonstrate that despite the removal of the lower dielectric layer, these architectures should yield comparable transmission values, given the same Ag properties. All configurations were performed with Ag deposited in pure Ar gas and in a mixture with 5% N_2 concentration.

As expected, Ag coatings deposited on $ZnO_{(Al)}$ yield higher performance than those deposited on bare B270 glass substrates. Particularly, Ag directly deposited on B270 in Ar shows vastly lower performance, with a broadband decrease in transmission and nearly a 60% increase in sheet resistance. The addition of N_2 to the sputtering gas mixture greatly improves this, yielding transmission values highly comparable to those on $ZnO_{(Al)}$, although with a sheet resistance still significantly higher. Films deposited and etched show very little dependence of their performance on the deposition sputtering gas mixture, similarly to those produced on $ZnO_{(Al)}$. Both present excellent sheet resistance, within a close margin of those produced on $ZnO_{(Al)}$. However, they also display lower transmission than films deposited on $ZnO_{(Al)}$ or directly deposited on glass with N_2 addition, with clear absorption peaks centered near 500 nm, indicating discontinuity in these films as well.

The increase in absorption is stronger than what is observed between similar samples in **Figure 6.7**; furthermore, the absorption features observed here are narrower, and significantly blue-shifted, resulting in a more noticeable impact in the visible spectrum. This is expected for thicker Ag layers, as shown in **Figure 6.8**. It should also be noted that an absorption peak can be seen at lower wavelengths for films directly deposited on bare glass in 5% N_2: this suggests that absorption features caused by holes in the Ag layer may be obscured by $ZnO_{(Al)}$'s stronger absorption at low wavelengths. Consequently, hole morphologies which result in UV absorption may be difficult to detect on this substrate, for better in the case of trying to remove the optical signal of film discontinuities, and for worse in the case of trying to monitor film discontinuities via optical means.

Finally, these results further solidify the point that in addition to monitoring the critical thicknesses during deposition and etching, studying the hole size and shape as a function of different conditions may lead to significant improvements for etched Ag films, if it enables undesirable optical features to be moved outside of the wavelength ranges of interest. The techniques proposed to decrease the critical etching thicknesses at the end of Section 6.4.3 may be relevant candidates for this end.

In the present context, it suffices to demonstrate that etching post deposition can greatly improve the performance of films which must be deposited in suboptimal conditions, as seen when comparing films deposited in Ar. In more serviceable deposition conditions, as for deposition with 5% N_2, improvements are still possible, depending on what metrics are prioritized; post deposition etching may be preferable to N_2 addition if there are exacting sheet resistance requirements to be met. Improved mitigation of hole formation and control of hole size evolution would enable improvements to be much more widely applicable.

APPENDIX E ADDITIONAL DETAILS PERTAINING TO CHAPTER 7

E.1 Optical changes of SLG during HT and corrections for *in situ* monitoring

Early in the process of achieving low-E coatings that were stable at high temperatures, it was found that ΔT measurements obtained *in situ*, in the Barnstead/Thermolyne furnace described in Section 3.3.1, did not correspond to those obtained by *ex situ* measurements. After verifying that the optical set-up was stable, and that no technical issues caused this mismatch, it was found that it was rather the SLG substrate itself which presented important variations in its optical properties at high temperatures. Interestingly, these are found to be fully reversible.

To account for this effect, *in situ* spectrophotometry data was corrected by subtracting the transmission changes found for bare SLG, ΔT^{SLG}, multiplied by a correction factor accounting for the transmission profile of a low-E coating, f_{corr}, such that $\Delta T^{Corrected} = \Delta T^{Raw} - f_{corr} \cdot \Delta T^{SLG}$. The transmission changes observed *in situ* at the end of the HT of an industrial reference sample and of a bare SLG substrate of equal thickness are shown in **Figure E.1a**. The correction factor, which is intentionally kept general to avoid needing to readjust whenever a different coating is used, or when coating properties change during HT, is shown in comparison to the transmission of the industrial reference sample in **Figure E.1b**.

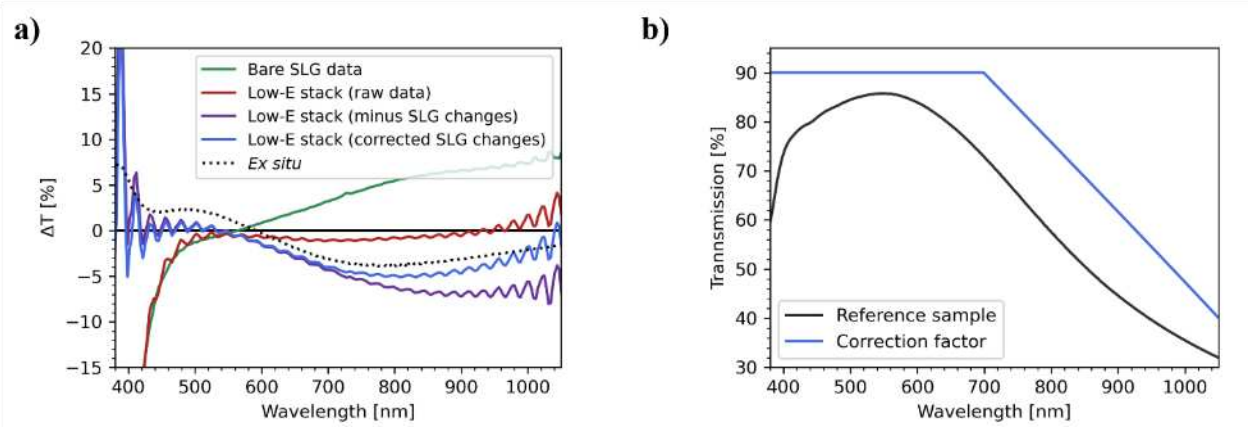


Figure E.1: a) ΔT of bare SLG glass and of a reference low-E stack provided by the industrial partner, obtained *in situ*, comparing different corrections accounting for the transmission changes of soda-lime glass (SLG) at high temperatures to *ex situ* ΔT measurements of the same sample. **b)** *Ex situ* transmission measurement of the industrial reference sample, compared to the generic correction factor used when treating high temperature *in situ* transmission data.

E.2 Etching of encapsulated Ag films

In order to anneal Ag films rapidly by using *ex situ* annealing in a furnace, yet without degrading the film due to atmospheric exposure, Ag films were deposited with various thin encapsulating layers. These films were annealed, then returned to the deposition system with the intent of removing the thin encapsulating layer during the etching process. However, this resulted in extremely slow etch rates and formation of highly plasmonic Ag films, regardless of the encapsulating film material or the annealing conditions.

To wit, results obtained for a sample using a thin aluminum oxide layer to encapsulate the Ag film are shown in **Figure E.2**, below. The Al film was deposited from a 3 in. aluminum target in RF sputtering, with an applied power of 150 W. It was oxidized by exposure to atmosphere but not annealed, in order to demonstrate that the issues encountered are not annealing-related.

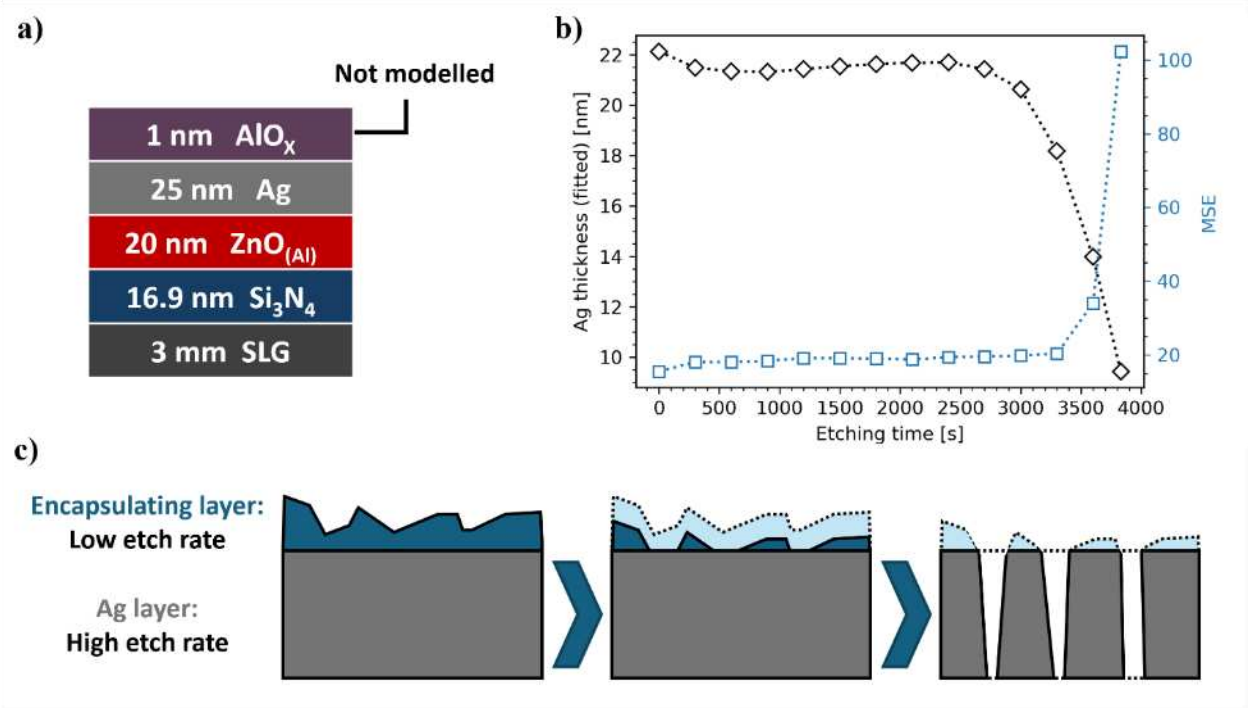


Figure E.2: a) Stack structure used to test the feasibility of etching off Ag encapsulating layers post-HT. **b)** Ag thickness measured via ISE, and associated MSE values, during RF plasma etching of the stack shown in **(a)**. **c)** Schema showing the proposed explanation for the rapid breakdown observed once etching of the Ag layer begins in **(b)**.

Figure E.2b shows the analysis of the etching process using the comparative modelling approach of Chapter 6. Here, the AlO_x is left out from the model. The fitted Ag and resulting MSE are shown as a function of the etching duration. The fitted Ag thickness remains approximately constant, with stable MSE, throughout most of the process, indicating that at this point, the AlO_x barrier remains intact. However, once the Ag thickness starts decreasing, the MSE increases rapidly as well, indicating dewetting while the overall film thickness is still quite high. This is attributed to non-uniformity in the thickness of the Ag film and/or encapsulating layer, and the visibly slow etching rate of the AlO_x layer; as soon as it is removed at a given location, the underlying Ag film will be etched extremely quickly forming holes or trenches wherever the AlO_x layer is removed first. A schematic of this process is shown in **Figure E.2c**.

Thus, while this idea could work in concept, it would require an encapsulating film that is sufficiently dense and that adheres sufficiently well to Ag to make a good encapsulating layer, while having a relatively high etch rate, qualities which seem likely to be at odds. Addition of hydrogen to the sputtering gas was tested in order to attempt to reduce the encapsulating oxides, to no avail. However, as only AlO_x and $NiCrO_x$ were tested, with only a few tests incorporating hydrogen, this should not wholly discourage one from attempting to leverage this approach. Finally, the usage of an ion beam etching with high incident angle, which may smooth the surface during etching, may help in this endeavor.